Politecnico di Torino

Department of Mechanical and Aerospace Engineering
Master's Degree in Aerospace Engineering

TPMS and plate-based AlSi10Mg lattice structures: geometries parametrization and fatigue tests design

Politecnico di Torino

TECHNISCHE UNIVERSITÄT DARMSTADT

Supervisors

Prof. Giorgio De Pasquale

M.Sc. Nikola Milenkovski

Candidate

Mattia Mondin

Academic Year 2024-2025

A nonna di mirabil animo,
saldo ardimento,
incoercibil fede volta all'avvenir.

Captabile puranco intangibile,
lume nell'ombre,
silente soccorso nel mortal peregrinar.

Serbi il cor imperiture reminescenze,
mi sien guida,
ond'io apprenda il gaudio soave dell'esistir.

It should be acknowledged that the research activities required for the preparation of this thesis were carried out at the Fachgebiet Leichtbau und Strukturmechanik (Institute of Lightweight Design and Structural Mechanics) of Technische Universität Darmstadt, located at Otto-Berndt-Straße 2, 64287 Darmstadt (Germany), from July to November 2025.

Abstract

The growing demand for sustainability across the industrial and transportation sectors is driving the development of efficient and lightweight structural solutions. Among these, lattice structures based on triply periodic minimal surfaces (TPMS), such as Gyroid and Primitive, and lattices based on plate-like architectures, such as body-centred cubic (BCC) and face-centred cubic (FCC), have demonstrated significant potential for impact energy absorption and heat exchange applications. However, the absence of standardized procedures for the structural and multi-physical characterization of lattice materials limits an organized comparison of research progresses. While compression-compression and bending fatigue tests have been more commonly investigated by the academic community, static tensile tests and fatigue analysis under tension-compression cycles have not yet been explored to a comparable extent. This thesis aims to establish the fundamentals of tensile experimental characterization of TPMS- and plate-based lattice unit cells, providing reference data and modelling strategies for future fatigue investigations. Sixteen configurations were analysed, all manufactured in AlSi10Mg by laser powder bed fusion (L-PBF) using an EOS M290 system. Four unit-cell topologies—Primitive, Gyroid, BCC, and FCC—were studied at four relative densities: 10%, 15%, 20%, and the minimum achievable with the employed printer, constrained by a minimum wall thickness of 120 µm to ensure printability with the available system. For BCC and FCC lattices, a complete parametric formulation was developed to define cut-outs for unmelted powder removal and to establish relationships between geometry and target relative density, enabling straightforward design adjustments. A tensile-compression fatigue specimen geometry was also proposed, adapted from the ASTM E8/E8M-25 standard, with necessary modifications to accommodate lattice integration. Finite element methods (FEM) simulations under imposed displacement conditions were performed to design the specimens. Results indicated that square cross-section samples are not significantly affected by edge effects, and a general transition-zone design methodology, adaptable to different lattice topologies, was developed. Fracture initiation was predicted to occur within the specimen core, sufficiently distant from both the transition region and the gripping areas. For each lattice shape and density, the numerical simulations with imposed-displacement provided the reaction forces, corresponding to the onset of 50% and 90% of the ultimate tensile stress (UTS). These thresholds were approximated, within an uncertainty range, to the fatigue limit (σ_D) and to the stress limit at 1000 cycles (σ_{1000}), respectively. From these data, Wöhler (S–N) and Haigh diagrams were generated to estimate the samples fatigue failure under specified mean-alternate stress values. This will support the planning of future experimental campaigns. The results of this work establish a methodological and computational framework for the tensile characterization of lattice materials, contributing to the standardization of mechanical testing procedures for additively manufactured TPMS and plate-based structures.

Contents

List of Figures

List of Tables

Chapter 1

Introduction and State of the Art

In this Master's thesis, sheet-TPMS (Triply Periodic Minimal Surfaces) and plate-based lattices have been examined with particular attention to their structural mechanical characteristics, since their intrinsically lightweight architecture makes them promising candidates for advanced engineering applications. Additionally, strength and fracture behaviour are important even in cases where the primary purpose is not structural, as when cellular materials are employed for thermal insulation, flotation, or filtration [1]. This work has been carried out in collaboration between DIMEAS, Department of Mechanical and Aerospace Engineering at Politecnico di Torino (Italy), and the Fachgebiet Leichtbau und Strukturmechanik (LSM – Institute of Lightweight Design and Structural Mechanics) at Technische Universität Darmstadt (Germany).

To ensure a clear understanding of all the concepts involved, the discussion begins with fundamental notions of cellular materials, before introducing lattice structures and, subsequently, the specific TPMS and plate-based unit cells under investigation: Primitive, Gyroid, body-centred cubic (BCC), and face-centred cubic (FCC).

1.1 Cellular solids

Cellular solids: structures and properties [1] is considered a foundational manual for cellular materials. It was written in 1997 by two prominent figures of the scientific and academic community, namely Lorna J. Gibson, professor at the Massachusetts Institute of Technology (MIT), Department of Materials Science and Engineering [2], and Michael F. Ashby, emeritus fellow of the University of Cambridge, Department of Engineering [3]. The book presents a description of the structures of honeycombs and foams and their mechanical, thermal, and electrical properties. The word *cell* has its origins in Latin, as the ancient Romans called *cella* a small compartment and *cellarium* a cluster of cells. In the meaning of *basic unit of plant and biological structure* was first used by Robert Hooke in his book Micrographia (1664) [1]. From *cellarium*, the concept of *cellular solids* developed, as the scientific community is interested in the assembly of cells. Ashby and Gibson provided a definition for this class of materials: « *a cellular solid is one made up of an interconnected network of solid struts or plates which form the edges and the faces of the cells* ». Later in the book, another definition is proposed: « *from a geometrical point of view it is helpful to think of cellular structures as vertices, joined by edges, which surround faces, which enclose cells*».

At a first level, cellular materials can be classified into three main groups according to their topology: honeycombs, foams, and lattice structures, even though the last represented a not fully developed concept in those years [4]. Honeycombs are considered 2D structures, as all the walls share a common generator, while foams are 3D configurations, as walls have random

orientations. Moreover, foams can be composed of closed cells, sealed to each other, or open ones, interconnected among them. Finally, lattice structures can be considered a particular family of foams, well organised in space. However, this categorization is far from exhaustive and complete: even when the cell shape is fixed, different arrangements are possible, which deeply influence mechanical properties. In order to organise and recognise similar patterns, and with the geometrical definition of cellular structures in mind, the concepts of *edge-connectivity* and *face-connectivity* can be defined; the former as the number of edges that meet at a vertex, the latter as the number of faces that meet at an edge [1]. Connectivity can be used for further classification of cellular solids with the same cell shape but different packing.

Foam configurations have been employed since the beginning by nature, in wood, which has been found in Egyptian artifacts dated more than 5000 years ago, or cork, which has been used for bungs in wine bottles since Roman times, or still in bones, sponges, and corals, mantis shrimp, abalone shells, bamboo, and bird beaks [1, 5, 6], just to name a few. Wood and balsa usually have a well-organised closed-cell structure, almost as regular as bees' honeycombs [1]. Others, for example bones and sponges, are based on struts instead of plates. In the last centuries, these natural cellular solids have been paired with man-made ones, which are currently employed in a variety of applications such as impact absorption, packaging and cushioning, thermal insulation, floatability, and structural applications. The low thermal conductivity of closed-cell foams is exploited from the cheapest coffee cups to extremely expensive rocket technologies; even ships carrying liquefied natural gas, which due to political and economic issues are frequently mentioned today, rely on such thermal insulation. The large compressive strains withstandable find applications in the field of energy absorption concerning fragile item transportation as well as bird strikes onto leading edges of aircraft wings [4]. Marine buoyancy was one of the earliest markets of cellular materials. Pliny the Elder (AD 77) mentioned the use of cork as a material for fishing floats in his writings [1], while nowadays polymer foams are used in safety jackets, thanks to their ability to preserve excellent buoyancy properties even after damage. In structural applications, balsa wood served as the core of sandwich panels for some bombers during World War II, and today aluminium or Nomex® honeycomb structures play that role. As can be easily inferred, cellular materials constitute an important class of engineering materials that, even though currently not neglected, unlike at the end of the last millennium [1], had not received full and complete research attention.

Cellular solids properties depend on two separate sets of parameters [1]. They are firstly determined by *relative density*, or its complementary, *porosity*. The concept is straightforward: once defined as ρ^* the density of the cellular material, and ρ_s that of the solid material the walls are made of, relative density is simply the ratio of the former to the latter. In this regard, relative density can also be determined through the *mixture rule*: considering the cellular material as an inhomogeneous matter, made of empty volumes (neglecting the air mass) and solid struts or plates, the density of the cell results from weighting its constituents according to their volume fractions. However, cellular solids cannot have any relative density, as Ashby and Gibson stated that a threshold of 30% marks the border between the former and porous solids. Properties of cellular materials can be tuned through proper design of the relative density, and a much wider range of values, compared to those of bulk materials, is achievable. For instance, Ashby and Gibson plotted in an Ashby chart Young's modulus and density of many classes of materials, in order to highlight that, while for solid materials a factor between 10^2 and 10^3 separates the lowest and highest elastic moduli within a single family (that of polymers, for example), it increases up to 10^4 by simply foaming.

The other set of parameters is cell *shape* and *size*, with the former being much more significant. For instance, it determines the isotropy or anisotropy of mechanical performance, while the latter exerts a weak influence on most mechanical and thermal properties [1]. Recently, many studies

have investigated the influence of these parameters, as well as the impact of manufacturing techniques on the final structures. In this regard, García-Gutiérrez et al. [7] (Mexico) observed a significant influence of topology, especially at high porosity levels: for 10% relative density, the proper cell choice can lead to stiffness increases of up to 126%. Ziaie et al. [8] (Ireland) investigated TPMS and experimentally found that unit cell size plays a minimal role in affecting mechanical properties. The same conclusions were reached by Forés-Garriga et al. [9] (Spain), who found almost no stiffness dependence on cell size, under the condition that the geometry is perfectly scaled. Nevertheless, even if the majority of the papers agree with Ashby and Gibson's model, not the entire academic community does. Mahapatra et al. [10] (India, UK) identified an inverse proportionality between mechanical properties and cell size. With respect to specific strength and stiffness, Alagha et al. [11] (Jordan, UAE) measured better performance at smaller cell sizes.

(a) SC unit cell.

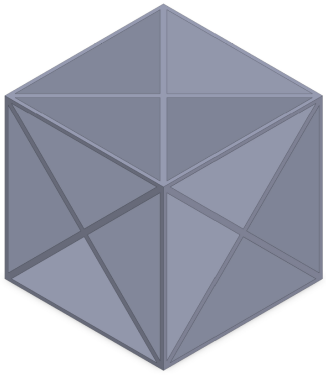

(b) BCC unit cell.

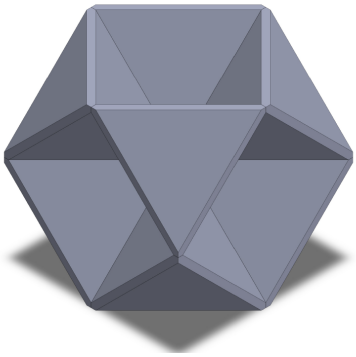

(c) FCC unit cell.

Figure 1.1: Plate-based unit cells as designed in [12].

1.1.1 Lattice materials

Lattice materials are cellular solids based on three-dimensional cells, which have recently aroused interest in the scientific literature. Cells can be open or closed, strut-, shell- [13], or plate-based, and differ from foams thanks to their periodic structural arrangement. In Xin et al. [14] (China), it is also reported that some authors classify lattice materials into random and non-random ones, but this categorization, being rare in the reviewed literature, is not used in this thesis. Pseudo-periodic lattices also exist: these are cases in which the cell is subjected to small adjustments, such as the same topology but different size or thickness [14, 15]. Further

categorizations concern the way lattices are generated, manually or mathematically. The latter technique relies on algorithms and constraints to create a lattice configuration [16]. Lattice materials constitute well-organised structures whose mechanical properties can be tuned through design; in contrast to random foams, they offer superior stiffness and controllable mechanical responses [17], and for this reason, they are often denoted as *architectured* materials [18]. Many efforts have been and continue to be devoted to their design in an attempt to generate ever more performant metamaterials [13]. In this regard, Sun et al. [17] (China) generated novel plate-based architectures to achieve high specific energy absorption and low peak crushing forces.

Plate lattices are an emerging subclass of sheet-based cellular materials [19], and are generally designed by emulating Bravais crystal structures, specifically the simple cubic (SC), BCC and FCC arrangements [12]. Chua et al. [12] (Singapore, UK) incorporated plates along the slip planes in the SC and FCC lattices, and along the close-packed planes in the BCC one, as shown in Fig. 1.1. BCC and FCC cells are the same employed in this thesis; additionally, strut-based SC, BCC and FCC, as commonly reported in literature [20, 21], have been added for completeness in Fig. 1.2. They have found applications in many sectors, from sound [12, 22] and energy absorption, benefitting from high strength-to-stiffness ratios, to medical implants exploiting their biocompatibility. Plate-based lattices have repeatedly exhibited superior stiffness and strength compared to truss and TPMS lattices, given similar porosity. Bonatti et al. [23] (Switzerland, USA) found that 316L shell-based TPMS have superior mechanical properties compared to truss lattices with the same density. Additionally, it is known that even optimal truss-lattice materials cannot achieve the theoretical Hashin-Shtrikman stiffness bounds [13], while the latest studies revealed that plate lattices can [13, 24].

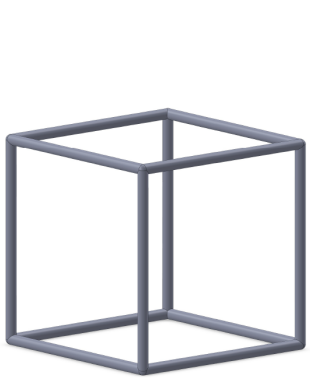

(a) SC unit cell.

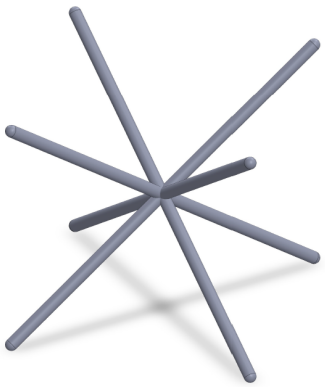

(b) BCC unit cell.

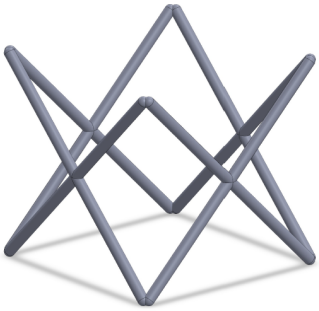

(c) FCC unit cell.

Figure 1.2: Strut-based unit cells as reported in [20, 21].

1.1.2 Triply periodic minimal surfaces

TPMS are part of the lattice materials group. Alagha et al. [11] refer to TPMS as *shellular* (shell lattice) structures, associated with continuous and smoothly curved shells. On the contrary, Xin et al. [14] consider TPMS lattices an autonomous family [14]. Their geometrical patterns and mathematical foundations have been investigated for more than 250 years [25], and at least for several decades [26]. However, only recent advancements in Additive Manufacturing (AM) have enabled the fabrication of these structures with sufficient precision [26]. The synergy between these intricate architectures and AM continues to drive significant progress in materials science and engineering [27]. The paper by Pehlivan [27] (Turkey) also refers to TPMS as *metamaterials*, because their special properties and functions arise from their unique, engineered geometry rather than the material itself. Jiang et al. [28] (China) describe TPMS as *algebraic surfaces* found in nature, defined by implicit functions. Biological examples include beetle shells, butterfly wing scales, and trabecular bone [10], or weevils and crustacean skeletons [29]. TPMS are described through mathematical equations, and the resulting geometries are characterised by periodicity along the three independent directions and zero mean curvature [14]. Mathematically, the exact representation of a TPMS surface is given by eq. (1.1), known as *Enneper-Weierstrass representation*, where ω_o is a fixed point and ω a variable point in the complex plane, i the imaginary unit, θ the so called *Bonnet angle* and $R(\tau)$ the *Weierstrass function* [30].

$$\begin{cases} x = e^{i\theta}\mathrm{Re}\displaystyle\int_{\omega_o}^{\omega} (1-\tau^2)R(\tau)\,d\tau \\ y = e^{i\theta}\mathrm{Re}\displaystyle\int_{\omega_o}^{\omega} i(1+\tau^2)R(\tau)\,d\tau \\ z = e^{i\theta}\mathrm{Re}\displaystyle\int_{\omega_o}^{\omega} 2\tau R(\tau)\,d\tau \end{cases} \tag{1.1}$$

However, TPMS employed in lattice structures are only approximations of the these formulas [28]. Indeed, they assume a mathematical representation in the form of implicit periodic surfaces, such as those described by eq. (1.2). In this formulation, r denotes the position vector in Euclidean space. The vector h_k refers to the k-th grid vector in reciprocal space, whereas A_k represents its corresponding amplitude coefficient. The parameter λ_k specifies the wavelength of the periodic term, and P_k indicates its phase. The quantity c is a constant [28]. This equation can also be conceived as a set of trigonometric functions forming a system, which assumes the form $\varphi(x, y, z) = c$. Al-Ketan et al. [31] (UAE) denoted them as *level-set equations*.

$$\varphi(r) = \sum_{k=0}^{K} A_k \cos\left(\frac{2\pi\, h_k \cdot r}{\lambda_k} + P_k\right) = c \tag{1.2}$$

What follows are the implicit equations for the approximated representation of the Schwarz-Primitive (commonly known as Primitive [9]), eq. (1.3), Schoen-Gyroid (Gyroid [9]), eq. (1.4), and Schwarz-Diamond (Diamond [9]), eq. (1.5), unit cells, from [31].

$$\varphi(x, y, z) = \cos(X) + \cos(Y) + \cos(Z) = c \tag{1.3}$$

$$\varphi(x, y, z) = \sin(X)\cos(Y) + \sin(Y)\cos(Z) + \sin(Z)\cos(X) = c \tag{1.4}$$

$$\varphi(x, y, z) = \cos(X)\cos(Y)\cos(Z) - \sin(X)\sin(Y)\sin(Z) = c \tag{1.5}$$

In these formulas, $X = 2\alpha\pi x$, $Y = 2\beta\pi y$, and $Z = 2\gamma\pi z$ are conceived to guarantee the periodicity of the lattice and to control the cell size dimension through the coefficients α, β, and γ. The constant c controls the thickness. When the level-set function is computed at $c = 0$, the resulting iso-surfaces divide the domain into subregions of equal volume. The size of these subdomains can be adjusted by modifying the iso-value: increasing or decreasing the constant shifts the surface along the normal direction, thereby expanding or contracting the volumes [31]. Furthermore, if one of these regions is completely filled with material, the resulting structure is referred to as a *network-solid*, whereas if the partitioning surface itself forms the solid phase, the structure is termed a *sheet-solid* [13]. Some examples of both types are shown in Fig. 1.3. Sheet-TPMS lattices have demonstrated higher fatigue strength compared to skeletal-TPMS lattices. In fact, Soro et al. [32] (Australia, France) reported that fatigue fracture of the struts always occurred at nodes, where local stress concentrations exist.

To easily describe TPMS physical behaviour, Bobbert et al. [29] (The Netherlands, Belgium, Denmark) use a parallel with soap films, which span a surface of minimal area between given boundaries. Actually, studies on the surface tension of soap films date back to the mid-19th century, when Plateau discovered stable surfaces of minimal area enclosed by a closed curve [10]. The zero mean curvature provides TPMS lattices with the advantage of reducing notches and stress concentrations [14]. Additionally, this property brings another advantage, namely the self-supporting nature of these cells [9]. Indeed, lattice structure fabrication typically omits support structures due to their difficulty in removal from within the lattice [15]; for TPMS structures, this can be done without compromising the quality of the result.

1.2 The role of Additive Manufacturing

« *Foams can be made out of almost everything: metals, plastics, ceramics, glasses, and even composites* » [1]. However, traditional mechanical forming processes, such as brazing, press forming, mold casting, metal wire spinning, sheet lamination, and gluing (for honeycomb), limit the topological complexity achievable due to fabrication difficulty. In the field of foams, in 1997, Ashby and Gibson wrote that it was not possible to produce higher-order hierarchical materials with cells at even more levels of scale [1]. Scientists were aware of the great theoretical potential of these configurations, but they were impossible to fabricate. In recent times, the production market has been completely revolutionised under the pressure of industrial demand [33]. The fourth industrial revolution envisioned the emergence of advanced technologies, with the potential for replacing traditional manufacturing processes while maintaining the same cost-effectiveness and efficiency as mass production [15], due to complete control over geometric features [34]. Additionally, only the progress of AM has made possible the fabrication of advanced structures that were previously unfeasible or prohibitively expensive [35], such as the lightweight fan blades developed by Wang et al. [36] (China). Beyond any doubt, additive manufacturing is currently recognised as a strategic pillar of a worldwide transformation towards industry [9], on the path to guaranty optimization of material use, flexibility, and millimetre-level precision [14].

In the field of metallic AM, Powder Bed Fusion (PBF) and Directed Energy Deposition (DED) technologies are the most widespread. The former refers to a group of additive manufacturing techniques that use a bed of powdered material, typically metal, although polymers can also be employed, which is selectively fused layer by layer using a heat source. With regard to this, Selective Laser Melting (SLM) employs a laser as the energy source, while Electron Beam Melting (EBM) uses an electron beam. SLM typically operates in an inert gas atmosphere (often argon, a good cost-benefit compromise) and is suitable for producing highly detailed and precise parts, particularly for small, complex geometries. EBM, on the other hand, works

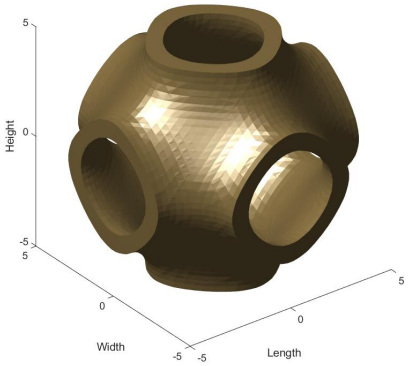

(a) Sheet-solid Primitive unit cell.

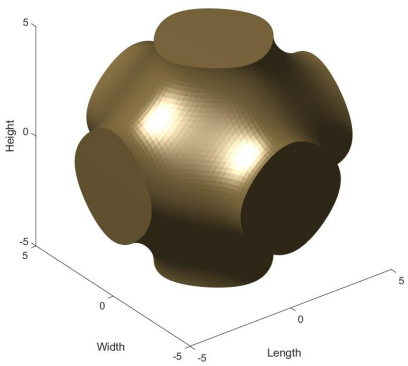

(b) Network-solid Primitive unit cell.

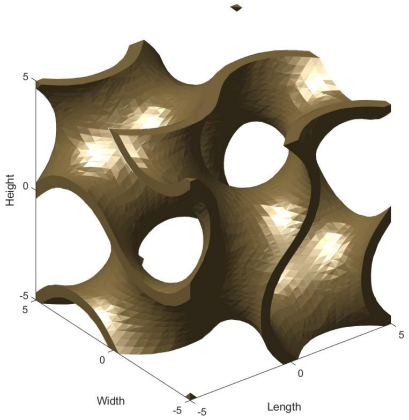

(c) Sheet-solid Gyroid unit cell.

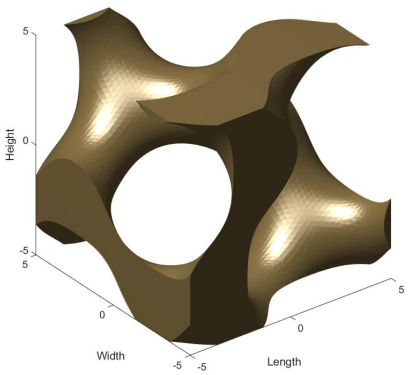

(d) Network-solid Gyroid unit cell.

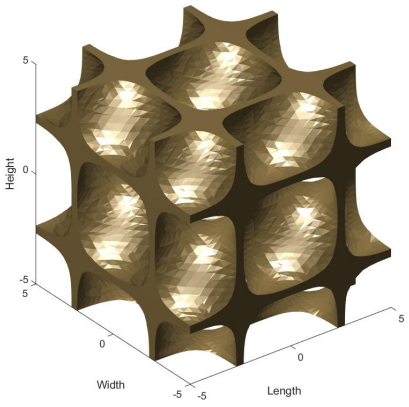

(e) Sheet-solid Diamond unit cell.

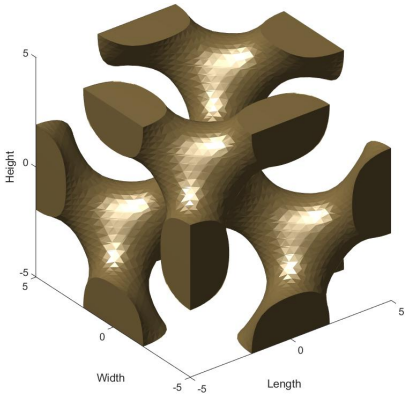

(f) Network-solid Diamond unit cell.

Figure 1.3: Examples of sheet- and network-solid TPMS cells designed through MSLattice.

in a high-vacuum environment to prevent the electrons from interacting with other particles, and is suitable for larger parts, especially those requiring high material density and mechanical strength. DED offers greater flexibility both in terms of material and energy source. The process involves focusing an energy source, which could be a laser, an electron beam, or a plasma arc, onto a metal feedstock in wire or powder form. The material is then melted and deposited layer by layer, enabling the creation or repair of metal parts with complex geometries. DED is particularly effective for part repair, coating deposition, and the production of large components. PBF technologies have the advantage that, if the mass involved is not excessive, the whole powder volume serves as a supporting structure layer after layer [9], reducing the need for additional support structures.

On the other hand, the use of AM processes also introduces a huge number of parameters impacting the final product. When combining this variability with the ever-expanding portfolio of lattice designs, the number of possible combinations explodes. Even just the selection of optimal printing settings is extremely challenging and involves laser power, hatch distance, scanning speed and strategy, powder quality, and particle size. In this regard, Mahapatra et al. [10] claim that the interaction between the process, design, and material is essential for accurately predicting the structural behaviour of lattice structures. Furthermore, AM process parameters that lead to good quality results for bulk materials, generally do not perform in the same way for lattice structures, requiring systematic investigations of the impact of these parameters through a methodology called design of experiment (DOE) [27]. The energy input is considered the most important factor: many studies have addressed the topic and found that both excessive and insufficient values can negatively affect printing quality [14]. Another factor is the printing direction: samples produced in a flat orientation, hence on the bed, show optimal mechanical properties [27]. The printing parameters also influence the presence of volume and surface defects (pores, unmelted particles, lack of fusion (LOF), cracks), often caused by complex thermal cycles that traditional manufacturing technologies generally do not introduce [37]; these issues are particularly relevant as they impact failure initiation. Kelly et al. [26] (USA, Germany) analysed the influence of laser parameters on compressive and tensile loading of Ti6Al4V SLM-printed Gyroid structures. Many post-processes have been proposed to reduce the influence of the aforementioned defects, such as shot peening, laser peening, and water jet peening, which, by inducing residual stresses within the surface of the fabricated parts, are beneficial for enhancing fatigue life [37]. Singh et al. [38] (UAE, USA) suggest chemical etching, electro-polishing, and ultrasonic and nanocrystalline surface treatments to improve surface roughness. Xin et al. [14] suggested that sandblasting and abrasive flow machining can improve the fatigue life of as-built materials by up to 400%. However, the impact of these defects on fatigue life is the subject of controversial discussion. Schultheiß et al. [39] (Germany) reported inconsistent results with improved surface finishing and therefore suggest that fatigue life enhancement should be addressed by tackling internal defects and microstructural properties. Soro et al. [32] reported expecting significant positive effects from hot isostatic pressing (HIP) for tension-tension fatigue, which is more detrimental than tension-compression, allowing this post-process to close internal undesired pores. At the same time, the authors found that fatigue crack initiation always occurs at the surface, pointing out the importance of its condition. Xin et al. [14] claim that irregularly shaped LOF reduces fatigue life in the Low Cycle Fatigue (LCF) regime, while surface defects serve as crack nucleation points in the High Cycle Fatigue (HCF) regime.

1.3 State of the Art

Lattice materials find application in a wide variety of fields, including automotive, biomedical implants and tissue engineering [32], and energy absorption, just to name a few, where their

lightweight and customizable structural properties are crucial for reducing weight while maintaining strength and functionality. Additionally, research literature is full of investigations about the use of lattices in the aerospace field, such as for anti-icing systems of aircraft's wings [40]. The paper by Wang et al. [41] (China) is an example of the exploitation of TPMS cells in the aeronautical sector. The authors designed fan blades filled with TPMS lattices, obtaining a lighter engine without compromising mechanical performance and impact resistance. Engineers at nTop are reported to have developed air-cooled heat exchangers for aerospace applications utilizing TPMS lattice structures with 85% volume reduction and converting around 40 parts into a single one [15]. Sultan Kilic et al. [42] (Turkey) studied ballistic applications for Diamond TPMS and FCC plate-based unit cells. Coluccia et al. [43] (Italy, Germany) studied the energy absorption and crushing load efficiency of strut-based lattices. Further applications are cited in the literature: contact membrane distillation and reverse osmosis applications are cited in [44], nuclear fusion in [45] and cooling of injection molds in [46].

1.3.1 Fatigue

During long-term use, lattice structures are frequently subjected to cyclic loading, a condition that makes fatigue resistance a critical property [14]. The application of lattice structures in as many fields as briefly mentioned above forces these structures to be able to withstand complex loading conditions over extended use. For instance, it is worth remembering that fatigue fracture accounts for 50% to 90% of aircrafts' structural failures. Even in 2007, a serious in-flight incident was caused by this failure mechanism [14]. Additionally, in the aeronautical field, not only are the structural requirements extreme, but also the environmental conditions. This is even more valid in the astronautical field, such as that related to satellite operations. As a consequence, sufficient fatigue resistance is mandatory. In the direction of investigating this field, the paper by Xin et al. [14] constitutes a comprehensive review of failure mechanisms and life prediction of AM metallic lattices. The authors highlight how fatigue is affected by several factors: manufacturing uncertainties and deviations from computer-aided design (CAD) geometries, unit cell arrangement, additive manufacturing-induced directionality, surface roughness, and volume porosity, as well as LOF defects, voids, cracks, unmelted or partially melted surface particles and inclusions. Additionally, fatigue life along the building direction is lower than that in the non-building direction, by a factor of two thirds. Increasing relative density generally plays a role in enhancing the fatigue life of lattices, bringing its behaviour closer to that of bulk materials, as well as larger cell sizes and wall thickness. The damage evolution process in lattice material is characterised by progressive failure of cells and subsequent stress redistribution in the non-failed ones [1].

Since 1997, when the manual by Ashby and Gibson was published, the compressive behaviour of cellular materials has received far more attention than the tensile one. Indeed, it is sufficient to observe the section subdivisions in the book to notice an unequal distribution in the number of pages. Nowadays, in the more specific field of lattice structures, the scientific literature still presents the same feature: a large portion of the research concerning fatigue of lattice structures focuses on compression-compression loading conditions, and even when the static mechanical behaviour is investigated, quasi-static compression tests and simulations decisively prevail [5, 28, 39]. Several authors agree with this statement [10], even if some exceptions exist [1]. Pelegatti et al. [47] (Italy) suggest that other loading regimes are less explored due to a number of experimental challenges encountered when testing these materials in the tensile regime. Khan et al. [15] (Italy) attribute it to the lack of specific standardization, which favours

[1] Pehlivan [27] claims the contrary, for example that TPMS structures have been extensively studied for their mechanical properties using tension tests, but he is truly part of a tiny minority.

compression-compression fatigue analyses due to their simplicity [15]. Regardless of the reason, in the real world structures are subjected to complicated load conditions over their lifetime, and different fatigue regimes can occur [48], including tension and compression stress and bending deformation, which makes it unreasonable to focus on a single design [5]. In the field of medical applications, which could be considered the Ti6Al4V world, implants are frequently loaded in tension [32]; moreover, stress concentration as well as bending loads can induce local tensile stresses [26].

However, when leaving the world of compression-focused studies, a few examples of three- and four-point bending, tensile-compression, tensile-tensile, and torsional quasi-static or fatigue studies can be found. Schultheiß et al. [39] studied the flexural behaviour of Gyroid architectures via rotating bending tests, Jiang et al. [28] the torsional resistance and torsional fatigue of several TPMS, García-Gutiérrez [7] the flexural properties of different shell-TPMS, skeletal-TPMS, and strut-based cells through a cantilever beam configuration, Han et al. [49] (China) investigated the three-point bending of several TPMS structures, Shaikh et al. [44] (USA) chose three-point bending for TPMS structures when investigating the effect of processing conditions (laser power, scan speed, and scanning strategy) on Diamond and Gyroid architectures, and the same configuration is used in the studies of Ren et al. [5] (China). Coluccia et al.(Italy) [50] developed a strain-based method for the fatigue failure analysis of truss-based lattice structures, applied to all-face-centred-cubic cells additively manufactured with 316L stainless steel. The method was employed for a case of four-point bending cyclic load and validate through experimental tests. The same authors [51] applied a multiscale-based methodology for the fatigue analysis of AM lattice structures, applying homogenization and de-homogenization techniques, and then validating the procedure through experimental test, on a four-point bending configuration. In the tensile field, Demir et al. [25] (Turkey) conducted tensile tests on polylactic acid (PLA) Primitive, Diamond, and Gyroid lattice structures produced via fused filament fabrication (FFF). Falkowska et al. [52] (Poland) focused on tension-compression fatigue tests of Diamond TPMS lattices built using Ti6Al4V. Lietaert et al. [48] (Belgium) studied Ti6Al4V Diamond scaffolds for biomedical applications under quasi-static tensile tests and tension-tension, tension-compression, and compression-compression fatigue tests. Pelegatti et al. [47] investigated, through quasi-static tensile tests and tension-compression fatigue analysis, skeletal Gyroid and FBCCZ strut-based lattices made of 316L steel. Soro et al. [32] studied quasi-static tension and tension-tension fatigue analysis of Ti6Al4V TPMS lattice structures and found that the fatigue performance of the cells (Diamond, Gyroid, Primitive) is superior to conventional strut-based ones. Pirotais et al. [18] (France) write that thin-walled TPMS structures are the most promising for fatigue resistance compared to conventional strut-based lattices and studied the behaviour of Ti6Al4V SLM-built samples through high-cycle uniaxial fatigue tests. The paper by Mahapatra et al. [10] focuses on the experimental evaluation of tensile properties of acrylonitrile butadiene styrene (ABS), pure and reinforced with short Kevlar fibres, TPMS structures. Regarding the Gyroid architecture, the authors recognise its superior mechanical performance and versatility in many fields.

1.3.2 TPMS Heat transfer

Lattice materials are characterised by a high surface-to-volume ratio and excellent heat transfer capacity, making them ideal candidates for heat exchangers and catalytic reactor technologies [14]. They exhibit outstanding heat dissipation performance [46], but also thermal properties are highly dependent on geometrical topology: for instance, sheet-TPMS Primitive cells are characterised by the best conductivity [46, 53]. TPMS lattices have been heavily investigated in recent years due to their superior thermo-mechanical characteristics compared to

stochastic foams at the same volume fraction [53]. In this regard, Doostmohammadi et al. [46] (Iran, Italy) investigated new designs for TPMS structures intended for thermal applications, obtaining up to 15% higher heat conductivity than base TPMS architectures. TPMS-walled heat exchangers (HX) are receiving increasing attention as they show significant potential for industrial applications. In fact, compact HXs are cost-effective, lightweight, efficient and characterised by low pressure drop [54]. The power requirements for pumping fluids and gases through the lattices are reduced compared to traditional foams, due to the lattices' periodicity and consequent high permeability [35, 53]. Moreover, TPMS-walled HXs show higher Nusselt numbers than conventional ones [55]. All these characteristics make them optimal candidates for aviation, automotive, defence, high-power electronics, water recovery, and nuclear and small energy production systems. Furthermore, TPMS geometry is intrinsically characterised by large turbulent kinetic energy (TKE) in the fluid field. Due to these property, there is no need to apply passive heat transfer enhancement devices, such as vortex generators or rough surfaces, to improve performance. Aluminium heat exchangers have been successfully printed [54]. The cell orientation affects heat transfer performance and was studied by Liu et al. [54] (USA). Relative density is also important when dealing with thermal properties. The studies by Muhli et al. [53] (Canada) concluded that lattices with porosity lower than 45% lose their effectiveness for heat transfer applications, becoming more similar to a solid than a lattice structure.

1.4 Structure of the thesis and motivation

1.4.1 Material choice

The choice of material mainly depends on the manufacturing process employed. The designed specimens are intended to be produced through SLM. This choice, which can also be seen as a constraint, limits the range of applicable materials. Indeed, in the field of SLM, several but not infinite, metallic alloys can be used. Many researchers employ Ti6Al4V [32], a titanium alloy highly appreciated in biomedical implants thanks to its stability in the body environment and biocompatibility. However, titanium is relatively expensive and also has a quite high density, around 1.7 times that of aluminium. Another metal frequently employed, although less than titanium, is 316L steel, which has a very high density, as its main constituent is iron. Boron-steel alloy has been used by [34], 17-4PH stainless steel by [53], Inconel 625 by [56]. Finally, some works rely on AlSi10Mg aluminium alloy [38, 57, 58], which has been shown to give excellent results when processed through SLM. Lattice structures were also built using other aluminium alloys such as Al12Si and Al 7075 [4]. In the end, the choice has fallen on AlSi10Mg, which is the most employed among aluminium alloys in the field of lightweight structures [4] and is currently the most widely produced alloy for SLM [42]. This alloy has recently experienced increasing interest due to its weldability, necessary in the SLM process, although it has been used in the aerospace industry for decades [59]. The addition of silicon enhances the material's specific heat and thermal conductivity, surpassing that of ferrous materials, leading to extended heating durations and reduced operating temperatures [60]. Finally, even though this thesis focuses solely on numerical simulations, the validation of the results is essential for employing the developed numerical models in future works; consequently the importance of extensive experimental studies [35]. Selecting AlSi10Mg facilitates the comparison of simulated and experimental data.

1.4.2 Cells choice

As previously done in other works [11, 61], it has been decided to focus on two different families of cells, namely two sheet TPMS architectures and two plate-based ones. As claimed

by several authors, both classes have demonstrated better mechanical performance compared to strut-based lattices [11]. Additionally, while some authors have found even better properties for plate-based than TPMS cells, producing the specimens through SLM requires the application of cut-outs to the plate-based cells, which improve manufacturability but have a detrimental effect on the mechanical characteristics. As a result, the superior performance of plate-based over TPMS structures can no longer be taken as certain, and a comparison becomes necessary. Finally, TPMS structures appear to exhibit superior mechanical properties at lower relative densities, whereas plate-based lattices tend to perform better at higher relative densities [11].

In the field of TPMS, Primitive and Gyroid architectures have been selected. First of all, they are, together with Diamond, the most studied cells [44]. This point simplifies the comparison of the results with previous research works; similar considerations can be found in [62]. Additionally, the two cells are quite different from each other, which makes their comparison rational. Gyroid is known for its great fatigue performance, thanks to its morphology, which ensures a more even distribution of stresses and strains. Singh et al. [38] performed compression-compression fatigue tests and found that 30% relative density Gyroid samples, selectively laser melted with AlSi10Mg powder, outperformed I-WP ones. On the other hand, Qiu et al. [62] (China, Australia) observed that Primitive architecture exhibits the best printability. Indeed, this difference, difficult to simulate in finite element analysis, can conversely impact potential experimental tests. Furthermore, Primitive cells have a very high degree of spatial symmetry, which Gyroid lacks, but also a lower surface-to-volume ratio [62], which could be beneficial in reducing surface defects [63]. Finally, in industrial applications, for instance HXs, Primitive cells experience a lower pressure drop, while Gyroid has an intrinsically large TKE production [54] in thermal applications, which could be beneficial, and once again makes a comparison between the two cells rational.

According to [19], FCC and BCC have straightforward manufacturability, which makes them ideal candidates for further investigation. Jiang et al. [64] (USA) found the longitudinal stiffness to be similar between the BCC and FCC cell types, but the BCC yield strength to be slightly higher. Other authors highlighted the great performance of FCC plate lattices, which exhibit high force uniformity and the highest shear modulus [19], as well as the best overall energy absorption [65]. However, while previous research has extensively compared the mechanical behaviour of TPMS structures, only limited studies have dealt with plate lattices [11]. Therefore, due to the lack of research, the choice of these cells has also been based on the possibility of having references from previous works. In this regard, BCC and FCC (plate-based) are currently the most studied cells at LSM, and strategies, such as those for the cutout design, can be more easily shared on these architectures. Indeed, it is often useful to proceed in small steps and establish a baseline that can later be used for further studies [26].

Considering all these factors, the decision to investigate the tensile behaviour of Primitive and Gyroid, as well as BCC and FCC lattices, with the aim of providing a foundation for subsequent tension-compression or tension-tension fatigue studies, appeared well justified. This approach enables the comparison of architectures spanning a wide range of mechanical characteristics, which could prove advantageous for guiding topology selection in practical industrial applications.

1.4.3 Contribution

To the best of my knowledge, the tensile behaviour of sheet TPMS (Primitive and Gyroid) and perforated plate-based (BCC and FCC) architectures manufactured via SLM using AlSi10Mg aluminium alloy has not been systematically investigated. While extensive studies exist on lattice structures, they overwhelmingly focus on compression-dominated loading conditions,

quasi-static compression tests, or compression-compression fatigue scenarios. Tensile loading, tension-tension, and tension-compression fatigue conditions, which are critical in real-world applications such as aerospace and heat exchanger designs, remain significantly underexplored, even though the importance of a full understanding of the loading scenarios has been highlighted by many authors. Moreover, although TPMS structures like Primitive and Gyroid have been widely studied, the comparison between these sheet-based lattices and plate-based architectures (BCC and FCC) under tensile loading is limited. Plate-based cells have shown potential for superior mechanical performance at higher relative densities, yet manufacturability challenges, such as the need for cutouts in SLM fabrication, have constrained their systematic investigation.

This thesis primarily aims to fill the gap in knowledge regarding the tensile behaviour of sheet TPMS (Primitive and Gyroid) and perforated plate-based (BCC and FCC) lattices manufactured via SLM using AlSi10Mg aluminium alloy. The numerical investigation of their response under quasi-static tensile loading not only addresses this underexplored area but also establishes a necessary foundation for subsequent studies on tension-compression and tension-tension fatigue behaviour. The work systematically considers both the influence of different cell shapes and the effect of relative density, spanning the maximum porosity allowed by the SLM process as well as 10%, 15%, and 20% relative density, thereby providing a comprehensive understanding of how these factors affect mechanical performance and fatigue potential.

To enable this investigation, the thesis also addresses critical design and fabrication challenges that have previously limited systematic studies. A reproducible specimen design methodology is developed, including the rational, standardized design of cut-outs for BCC and FCC cells to ensure efficient powder removal during SLM fabrication without compromising mechanical performance. By integrating these methodological improvements, the work supports the rational selection of lattice topologies and densities for industrial applications and provides a solid basis for future experimental and numerical research into the mechanical and fatigue behaviour of lightweight lattice materials.

Chapter 2

Software assessment

In this chapter, the design of TPMS and plate-based unit cells is described. In order to perform this activity, appropriate software had to be tested, chosen, and properly used. It might seem a very easy and quick task; however, the reality is quite the opposite. For instance, different software or codes, apparently designed to perform the same operations, can lead to very different results depending on variations in geometric and mass characteristics. For this reason, the chapter has been titled *Software assessment*, even though its content extends far beyond what these two words might suggest. Indeed, while for TPMS unit cells I have used already existing tools provided to me by LSM researchers, who studied the limitations that I will later highlight and developed some Python^{TM} codes to overcome them, the plate-based design has been almost entirely carried out by me, from the CAD modelling to the volume calculation. As a consequence, the second part of the chapter is dedicated to the detailed description of all these passages.

2.1 TPMS unit cells

2.1.1 Literature review

As already mentioned in the introduction, the two TPMS architectures that have been studied are Primitive and Gyroid. There are many software available for the design of these cells, both open source and proprietary ones. In the scientific literature on the subject, it is frequently cited *nTop*, formerly nTopology [66]. I here reported a few authors that have relied on it for their works, but the entire list would be pretty long. Muhli et al. [53] used nTop in their research focused on the dimensional assessment of uniformly periodic porosity Primitive TPMS lattices; Shaikh et al. [44], for Gyroid modelling [44] and Rezapourian et al. [67] (Estonia, USA), whose work studied Ti6Al4V split-P TPMS lattices for bone tissue engineering. Professor De Pasquale and Daniela Barra (Italy) also wrote a manual, which has recently witnessed the publication of its fifth edition, with the declared aim of being a «*Comprehensive Reference Manual for Beginners and Intermediate Users with Step-by-Step Design-Based Approach*»[68]. Therefore, it appears clear that nTopology is established as one of the most used proprietary software for TPMS lattice design. However, the scientific literature often refers to open-source software as well. In this field, *MSLattice* and *MaSMaker* represent possible solutions. Zhang et al. [69](China), created the TPMS structure they needed (Primitive, Gyroid, Diamond, I-WP, F-RD and Neovius), through MSLattice. Pehlivan relied on this software for his work on polymer-based TPMS. The software is a MATLAB®-based tool, projected by Dr. Oraib Al-Ketan, scientist at New York University Abu Dhabi [70]. Detailed description of the software is reported in a dedicated paper [31], a very short one in App. A.1.

Even if MaSMaker, differently from MSLattice, relies on Python programming language [71], it is pretty similar to the latter from the user viewpoint. The first version of the software only included Gyroid architecture [72], while the new one, MaSMaker 2.0, has expanded the range to Primitive, Diamond, Split-P, Neovius, and Lidinoid. Its functions are explored by Pérez-Barrera et al. [73] (Mexico), in a dedicated paper, but a short presentation can also be found in App. A.2. Recently, Sabic et al. [74] (Poland) relied on MaSMaker for the design of PLA Gyroid scaffolds and their evaluation for long bone fracture. In the field of fluid flow and heat transfer, Guillermo et al. [75] (Mexico) used the software to design Gyroid structures. Later in this chapter, the limitations of the cited open-source software, with particular attention to the specific requirements for this thesis work, will be addressed.

Due to their mathematical description, TPMS lattices are really adapted to be modelled through programming. Scientific literature reports, for instance, the implementation of Python and MATLAB codes suitable for TPMS design. In the field on nuclear energy and heat exchange, Martin et al. [71] (USA) relied on a Python code, partially in-house built and partially taken from an open-source project, for creating the cells they need. In García-Gutiérrez et al. [7], a combination of software was used. TPMS structures (Gyroid and Primitive) were modelled using a level-set approximation in MATLAB 2020, then the exported mesh in a .stl file is decimated through Autodesk® Fusion 360(TM) 2022 and hence the model exported to SolidWorks® 2019 to be subjected to a solidification process to get a .step file. In Wang et al. [76] (China), Primitive and Gyroid bone scaffolds were modelled using MathMod-9.1 and SolidWorks. The last two cited examples highlight the limitations of traditional CAD software for TPMS modelling, given their necessity to be coupled with additional tools for an effective design process.

2.1.2 Modelling process

TPMS lattices were generated using Python-based tools developed at LSM. These codes were created to overcome limitations observed in commonly used open- source TPMS modelling software, such as MSLattice and MaSMaker.

As described in [31], MSLattice produces sheet-network lattices by first generating a zero-thickness implicit surface defined by the level-set function of the chosen TPMS architecture. The physical thickness is then introduced by offsetting the surface along its normal direction of the *iso-value* c according to:

$$-c \leq \phi(x, y, z) \leq c \tag{2.1}$$

While the methodology is conceptually straightforward, the resulting STL quality is strongly dependent on the chosen resolution. Thin-walled structures, particularly at low relative densities, require very fine meshes to avoid artifacts, which leads to large STL files and significant computational cost. Fig. 2.1 these issues: increasing the grid-point resolution improves accuracy but also increases file size considerably (from 5.31 MB to 14.7 MB). A similar trend is observed with MaSMaker, which also relies on level-set voxelization. As shown in Fig. 2.2, low voxel resolution leads to noticeable geometric distortion and inconsistent wall thickness, particularly critical for lightweight designs. Increasing voxel density improves fidelity but again results in large STL files (up to 9.91 MB in the example shown).

To avoid these drawbacks, the modelling in this thesis relies on the LSM-developed Python codes, which are designed to decouple geometric accuracy from STL resolution. The internal data representations ensure that even coarse-resolution STL exports preserve correct wall thickness and topology, allowing reliable refinement during later processing in Materialise Magics without excessive file sizes. Fig. 2.3 demonstrates that both low- and high-resolution meshes generated with these codes maintain adequate surface quality while producing significantly

smaller files than the equivalent MSLattice output. This makes the method well suited for modelling TPMS structures with very thin walls, where open-source tools typically struggle.

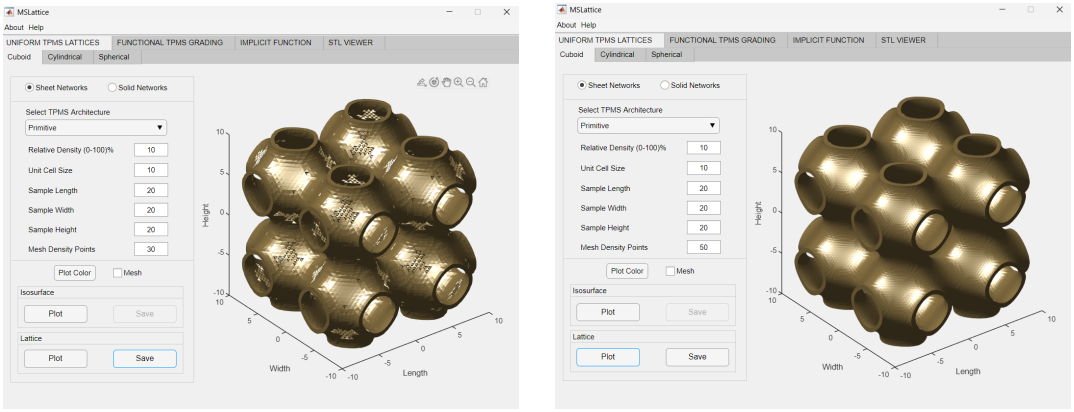

(a) Grid points: 30 for each unit cell. (b) Grid points: 50 for each unit cell.

Figure 2.1: Primitive unit cell: example of generation through MSLattice.

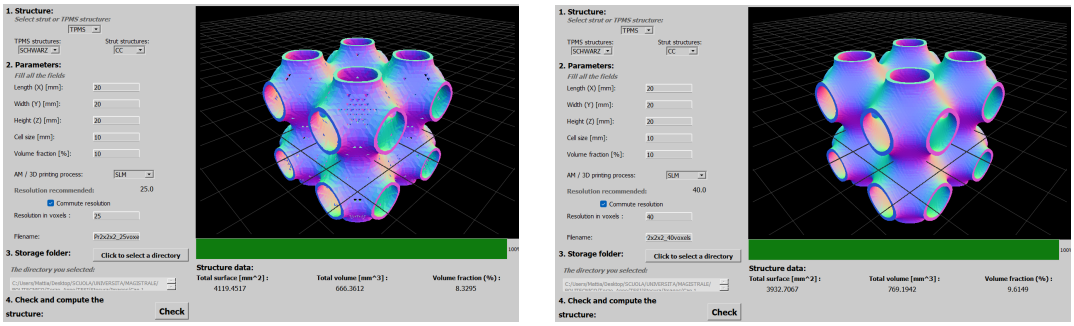

(a) Voxels: 25 for each unit cell. (b) Voxels: 40 for each unit cell.

Figure 2.2: Primitive unit cell: example of generation through MaSMaker.

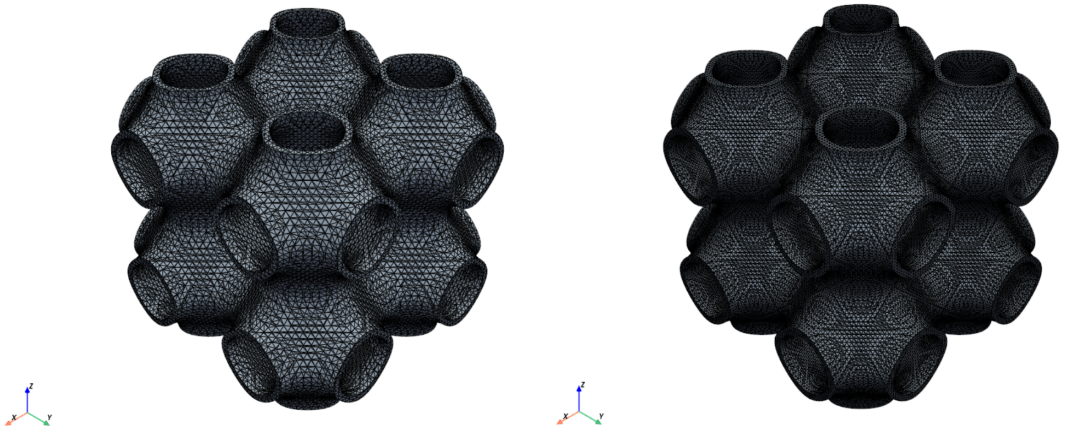

(a) Grid point: 30 for each unit cell. (b) Grid point: 50 for each unit cell.

Figure 2.3: Primitive unit cell: example of generation through LSM-developed codes.

In summary, due to their mathematical nature, TPMS geometries benefit greatly from pro-

grammatic generation rather than traditional CAD operations. The in-house codes developed at LSM provide a consistent and efficient modelling workflow that is robust across varying thicknesses and resolutions, and therefore they form the basis for all TPMS unit cells used in this thesis.

Finally, for what concerns the gradation process, the three tools explored, namely MSLattice, MaSMaker, and LSM-developed Python codes, implement a linear gradation. For instance, MSLattice implements such gradation for sheet-network structures by describing the iso-value as a linear function along one of the Cartesian coordinates, of the type $c = Ax + B$, where x is the axis along which gradation is imposed, A and B are constants that depend on the initial and final relative densities, and c follows eq. (2.2) [31]. MaSMaker details are not available in its paper [73], while the details of LSM-developed Python codes cannot be disclosed as they are still part of ongoing reserach.

$$-c(x, y, z) < \phi < -c(x, y, z) \tag{2.2}$$

Here, the main advantage of LSM-developed codes is the possibility of grading the sample on both sides and of having a core homogeneous section. On the contrary, MSLattice and MaSMaker (without modifications to the source code, and hence relying solely on the downloadable already-executable version) are limited to one-sided gradation, and there is no possibility of grading only a specific section. Fig. 2.4 is self-explanatory. It is worth noting that this setting is particularly useful when dealing with specimens to be tested, as it allows, in a single step, both the modelling of the test section and the transition zones.

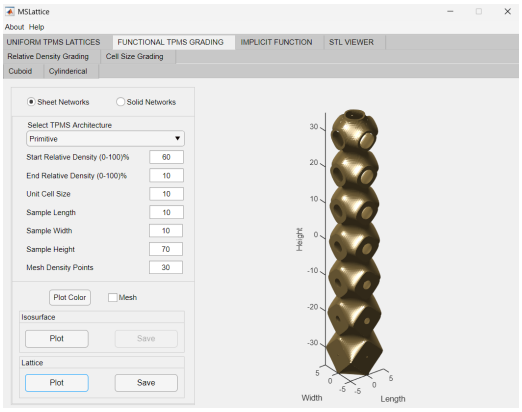

(a) MSLattice.

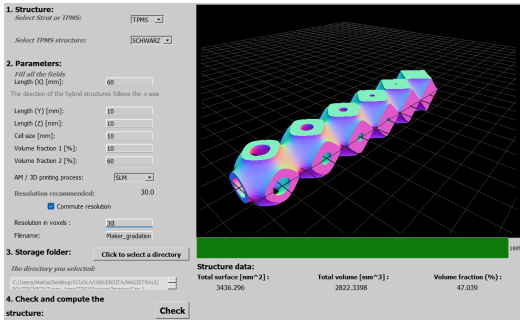

(b) MaSMaker.

(c) LSM-developed Pyhton codes.

Figure 2.4: Primitive unit cell gradation: examples of gradation obtained with different software.

2.2 Plate-based unit cells

2.2.1 Literature review

In Par 2.1.1, many works have been cited. Indeed, on one side, due to the TPMS geometry, which is hard to reproduce with traditional CAD software, and on the other side thanks to the efforts that the scientific community has made in searching for and designing effective modelling solutions, there is extensive literature on this specific aspect of the subject. On the contrary, concerning plate-based unit cells, such as BCC and FCC, which also are analysed in this thesis, a similar quantity of material does not exist, since for these structures traditional CAD software perform very well. In Li et al. [77] (China, Australia), the section *Design and methods* does not report any specific CAD software used for modelling the hybrid lattice structures under study. The same occurs for Zhang et al. [65] (China), whose authors conducted studies on the energy absorption performance of several plate-based lattices and also in Abdelmageed et al. [19] (UAE). However, it is also possible to find papers in which the CAD software employed are explicitly declared. This is the case of Medhin et al. [78] (UAE), where the authors relied on Creo Parametric 10.0 for their work focused on the ductility and energy absorption of hybrid plate-based lattice structures. In Ghosh et al. [79] (USA), the authors used Autodesk Inventor Professional 2019 to investigate the behaviour of stereolithography-built lattices under compression loads. Anyway, for this thesis I relied on SolidWorks 2024, mainly for practical reasons, as I was already familiar with the software and held an educational licence for it. Nonetheless, this does not constitute an arbitrary choice. Indeed, many authors have recently employed it. These include, just to name a few, Alagha et al. [11], in a paper dedicated to both TPMS and plate-based lattices, Wang et al. [41] and Kilic et al. [42], who investigated the ballistic behaviour of selective laser melted AlSi10Mg using FCC and Diamond lattice structures.

2.2.2 BCC unit cell: modelling process

BCC and FCC plate-based unit cells require the design of cut-outs. Indeed, while Primitive and Gyroid sheet-TPMS are intrinsically open, and the unmelted material can be easily removed at the end of the printing process, this is not the case for BCC and FCC. In fact, these structures require the addition of holes to remove the unused powder (PBF) or resin (digital light processing - DLP) in order to enable to exploit the full potential of lightweight structures. Bonatti et al.[13] (Switzerland, USA) highlighted the problematic, correctly stating its root are not only in the close-shape geometry, but also in the fabrication technology used. Issue arise when dealing with powder-bed or liquid-bath additive technique. Actually, many authors addressed this problematic and identified several solutions. Xue et al. [80] (China) studied plate-based hybrid configurations fabricated via selective laser sintering (SLS) using nylon powder. A 2 mm-diameter hole was placed at the centre of each plate (the cell size is around 20 mm), to allow the removal of unused powder; indeed, the unmelted one can induce unnecessary attachments and geometrical deviations. Still in the field of polymeric materials, Schneider and Kumar [61] (UK) examined the energy absorption properties of several truss-, shell- and plate-based lattice structures. The authors ran numerical simulations and performed experimental tests under quasi-static compressive loads, adopting three different additive manufacturing processes, namely material jetting (MJ), SLS and DLP. In order to remove the unused resin, they designed holes with a radius of 0.250 mm at the centre of each bounding surface for plate-lattice structures fabricated via DLP. SC lattices, fabricated through SLS and MJ, were modified to integrate 0.350 mm radius holes. Li et al. [77] analysed an hybrid cell composed of SC-plate and BCC-truss basic configurations. The cells, produced with thermoplastic polyurethane (TPU) via SLS processes, had a size of 20 mm and adopted a central hole with

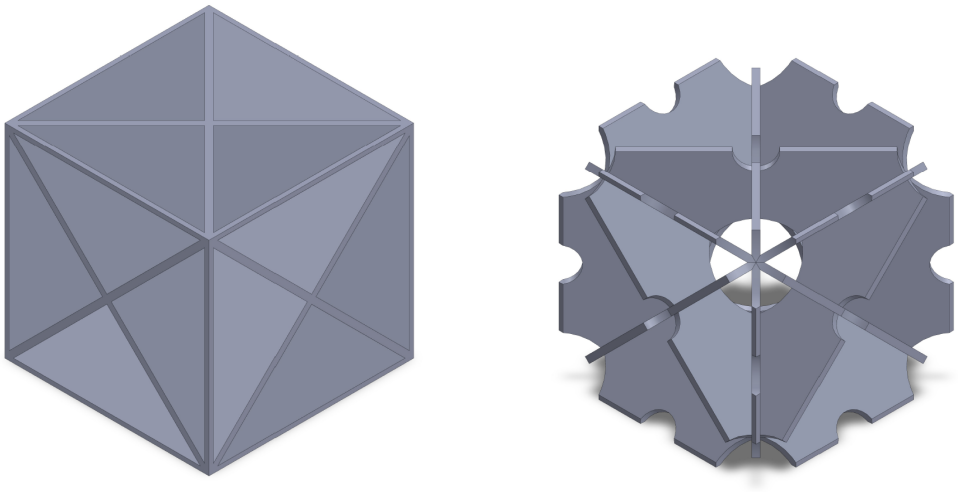

(a) Unit cell without cut-outs. (b) Unit cell without cut-outs.

Figure 2.5: Geometry of the designed BCC unit cell.

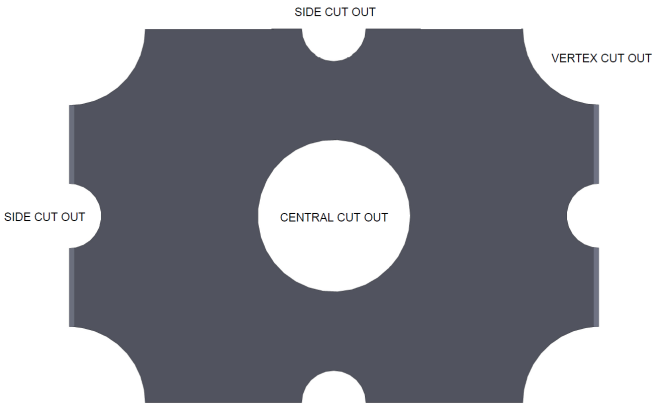

Figure 2.6: BCC unit cell: fundamental patch with cut-outs.

a diameter of 3 mm. Chua et al. [12] (Singapore, UK) employed spherical vertex cuts for the BCC and FCC cells, and Li et al. [22] (Singapore), for FCC. Heidenreich et al. [81] (Switzerland, USA), fully aware of the problem of entrapped powder within plate-based closed cells, decided to pursued an alternative path that guided them to «*the development of plate-lattices made from perforated plates*». Specifically working with a SC-BCC plate hybrid architecture, they designed a unit cell that has no limitations in powder removal. Ghosh et al. [79], working with photolithographic manufacturing, faced the creation of closed pockets between plates, with the consequence of inevitable resin entrapment. Even if aware of the possibility of relying on holes, also these authors decided to rely on alternative geometries. In particular, they modelled a partially strut- and partially plate-based configuration, so to get an open cell. Finally, Jiang et al. [64] had a still different idea. Instead of modifying the cell geometry, they suggest to change the production process and apply fused filament fabrication (FFF).

In this paragraph, they are described, also with the help of pictures, the modelling steps and the equations that have led to the final design of the BCC cell. In Fig. 2.5, the BCC unit cell is shown, with (on the right) and without (on the left) cut-outs. The volume is a cube with a

side length of 10 mm, and the thickness can be varied as a parameter. Indeed, for conventional plate-based lattices, the unit cell geometry can be completely described using two independent parameters: the cell size and the relative density [12], the latter being substituted by wall thickness, in this thesis. The BCC cell is quite easy to model: once the smallest element has been identified, the one displayed in Fig. 2.6, it is sufficient to pattern and/or mirror it in the other directions to obtain the final shape. The more complicated phase concerns the choice of the holes dimensions, which rises the number of independent geometrical parameters to three [12]. Indeed, the equations for the side holes can be implemented directly in SolidWorks, as they are explicit relations. On the contrary, those governing the vertex and central cut-outs are not, and I implemented them in MATLAB 2022. Based on previous experience at LSM, it was decided to design these cut-outs so that a sphere with a radius of $R_{sp} = 0.50$ mm can always pass through them. As a consequence, the third independent parameter becomes R_{sp}, which is an innovative approach compared to the examples reported in the scientific literature, where one or more fixed radii are chosen. In addition, it was decided that these holes must be created using cylindrical cuts. The choice of not using spherical ones lies in the consideration that, while the lateral surfaces of cylindrical holes are straight and parallel, and therefore prevent any kind of powder stagnation during the removal phase, the spherical ones are characterised by bowl-shaped lateral surfaces that could trap the powder. In conclusion, these elements (the sphere-based approach and its radius of 0.50 mm, as well as the cylindrical extruded cut) constrain the geometry. The axes of the different cylinders are perpendicular to the front face sheet of the fundamental element and pass through the midpoints of the planar sides, the vertices, and the centre of the plate, as shown in Fig. 2.6. Eq.(2.3) calculates the radius of the side cut-out, where t is the thickness of the plate. It has been obtained from geometric considerations and from the corresponding equations derived from Fig. 2.8. The location of this type of holes is reported in Fig. 2.7. Formally, they are two different kinds of cut-outs, but in practice they are governed by the same equations. One appears within the cell itself, which I will refer to as the *side-central cut*, while the other is formed when the lattice is created, and I will refer to it as the *side-side cut*.

$$Rs = \sqrt{2} * Rsp + \frac{t}{2} \tag{2.3}$$

With reference to Fig. 2.8, the constraint is defined by the long red segment, which should have the same dimension of the sphere, according to the approach described above. The two grey face sheets are perpendicular to each other, and the entire structure displayed is symmetric; hence, the long red segment and the green one are inclined at 45° with respect to each other. As a consequence, they are proportional by a factor of $\sqrt{2}$. Then, considering the short red segment, namely the thickness (t), it is also inclined at 45° with the horizontal direction. Consequently, it is the hypotenuse of an isosceles triangle, whose height (h) is equal to:

$$h = \frac{t}{2} * tan(45) = \frac{t}{2} \tag{2.4}$$

Finally, the side cut-out radius is given by the sum of the green and blue segments, which corresponds exactly to eq.(2.3). Additionally, in Fig. 2.9 it is possible to visualise the sphere approach for this type of cut-outs.

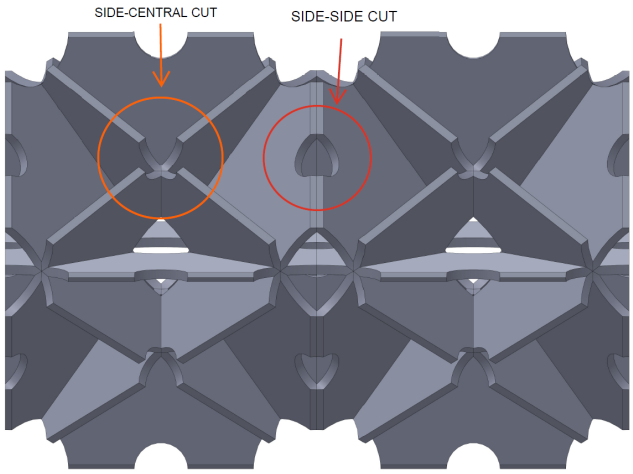

Figure 2.7: BCC unit cell - side cut-outs: location.

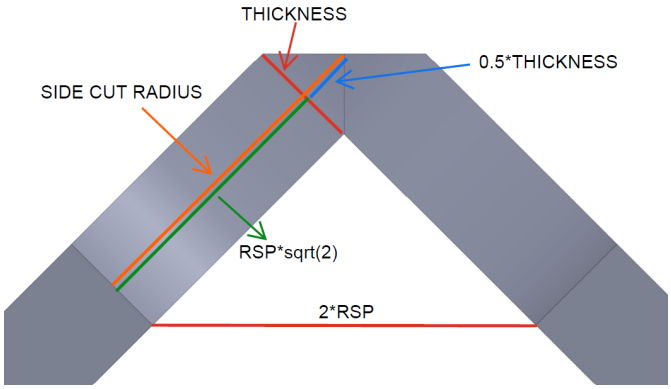

Figure 2.8: BCC unit cell - side cut-outs: sketch for dimension calculation.

(a) Front view.

(b) Top view.

Figure 2.9: BCC unit cell - side cut-outs: visualisation of the sphere approach.

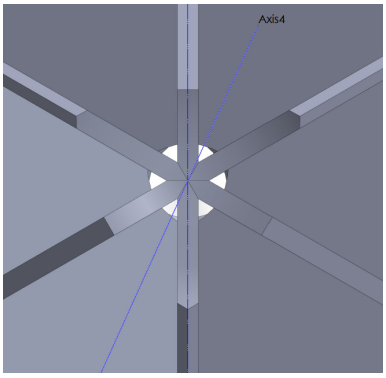

(a) Location considering a single unit cell.

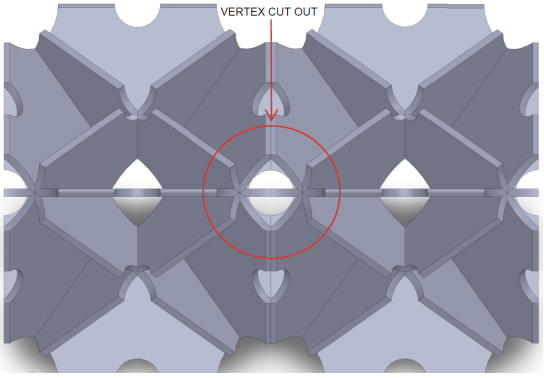

(b) Location considering two adjacent unit cells.

Figure 2.10: BCC unit cell - vertex cut-outs: location.

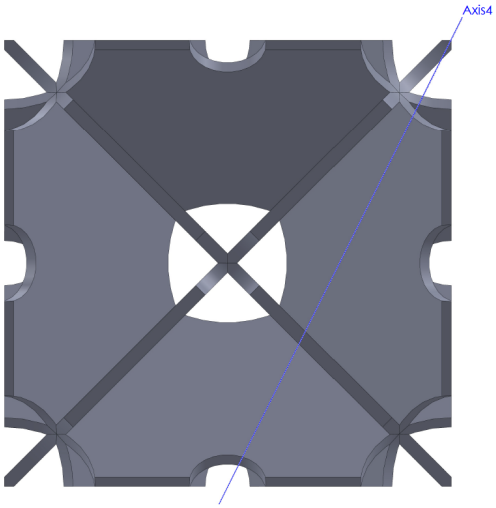

Figure 2.11: BCC unit cell - vertex cut-outs: Axis 4 visualisation.

As mentioned before, the case of the central and vertex cuts is more complicated. Actually, for these two shapes the equations are the same, and a careful observation of the central hole quickly reveals that it is composed of eight vertex cuts, a statement whose full effects will be discussed in Ch. 3, when dealing with the density calculations. In Fig. 2.10, the location and shape of this cut are displayed.

The procedure for determining the cut-out radius is described here step by step. First of all, it is necessary to observe the axis highlighted in blue and denoted as *Axis 4* in Fig. 2.11. It can be identified as the intersection of *Plane 5* and *Plane 6* in Fig. 2.12a, with the first coincident with the cubic face sheet, and the latter created as follows: Plane 6 must contain the AB segment of Fig. 2.12b and the homologous segment at the opposite vertex cut. Plane 6 can also be obtained through an alternative method. In this case, it is necessary to rotate one of the inclined face sheet planes by 30° around the axis connecting the point denoted as M in Fig. 2.12b and its homologous point at the opposite vertex cut. Alternatively, *Axis 4* can be drawn by connecting the upper-right vertex of the uncut unit cell with the midpoint of the bottom edge, both being on the shown face sheet in Fig. 2.11. All the equivalent strategies mentioned above lead to the identification of the axis, namely *Axis 4*, which has the particular geometrical characteristic of

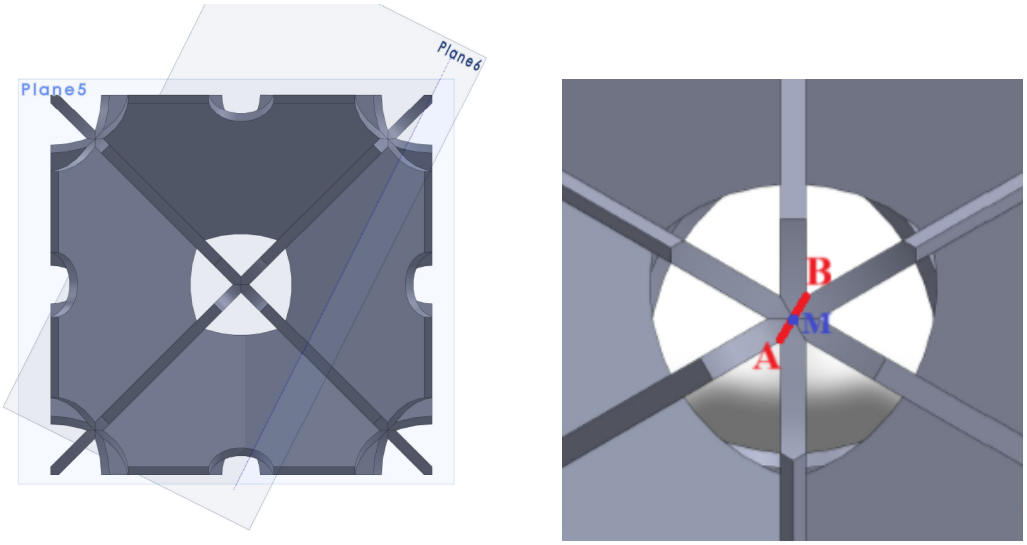

(a) Plane 5 and Plane 6. (b) Segment AB and point M.

Figure 2.12: BCC unit cell - vertex cut-outs: Axis 4 construction.

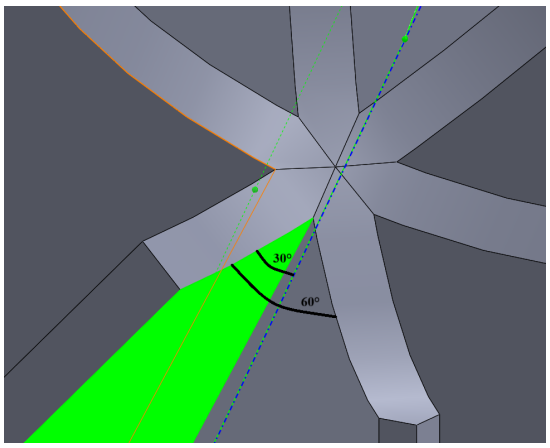

Figure 2.13: BCC unit cell - vertex cut-outs: Plane 6 splits in two congruent angles the one of the curvilinear triangle.

being at an equal minimum distance from each side of the curvilinear triangle resulting from the cut and encircling the hole. With regard to this, it is worth noting that, in this way, Plane 6 creates two equal dihedral angles, whose lateral surfaces are Plane 6 and the BCC unit cell geometry, as displayed in Fig. 2.13. At this point, a clear analogy can be drawn with the intersection of the angle bisectors of a planar triangle, the incenter, and the inscribed circle. In this geometry, *Axis 4* becomes the axis along which the *inscribed* sphere can pass, tangent to the curvilinear triangle.

In Fig. 2.14, the geometrical configuration described in words until now has been graphically represented for better visualisation. This scheme leads to the following system of equations:

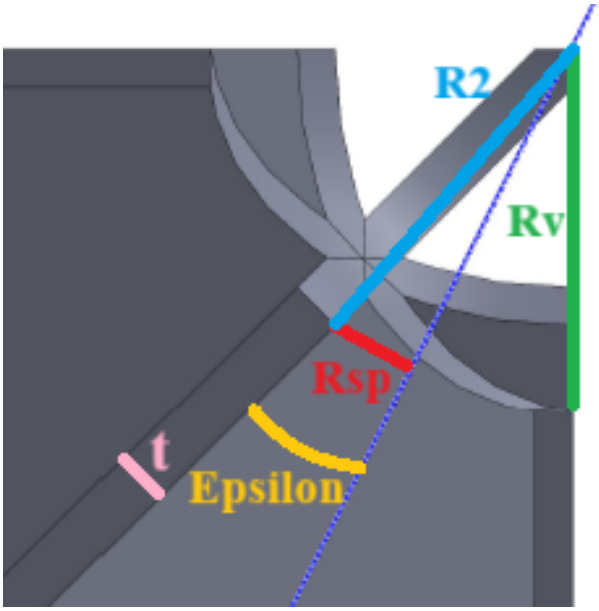

Figure 2.14: BCC unit cell - vertex cut-outs: sketch for dimension calculations.

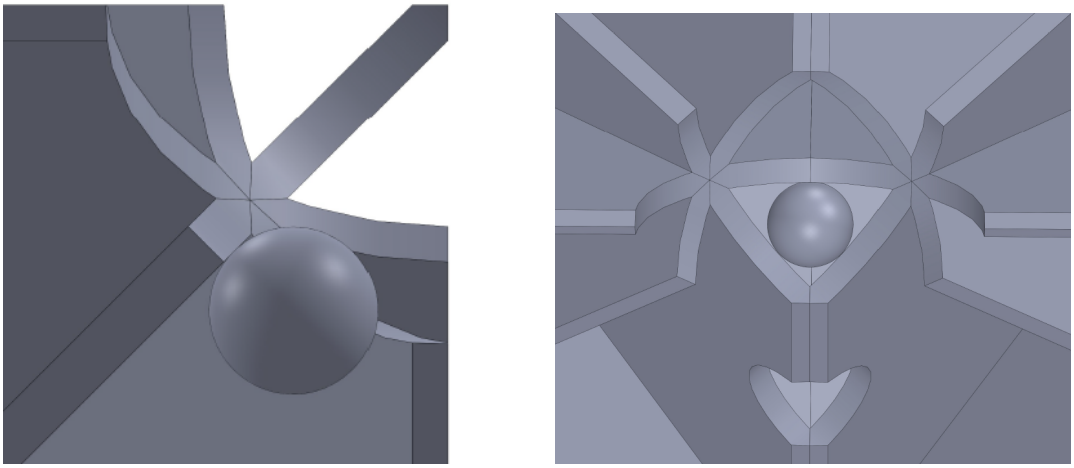

(a) Side view. (b) Normal view.

Figure 2.15: BCC unit cell - vertex cut-outs: visualisation of the sphere approach.

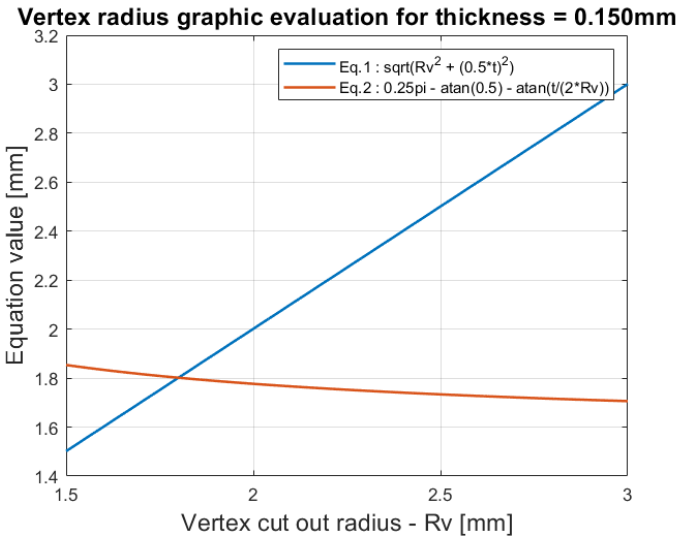

Figure 2.16: BCC unit cell - vertex cut-outs: example of graphic calculation of Rv.

$$\begin{cases} R_2 = \sqrt{R_v^2 + \dfrac{t^2}{4}} \\ R_{sp} = R_2 * sin(\varepsilon) \\ \varepsilon = \dfrac{\pi}{4} - arctan(0.5) - arctan(\dfrac{t}{2 * Rv})[\text{rad}] \end{cases} \tag{2.5}$$

This system of equations has no analytical solution and it could be solved graphically by plotting the two equations that represent $R_2(R_v)$ and considering their intersection, as shown in Fig. 2.16, or it could be solved through numerical methods, such as the *fsolve* function available in MATLAB. In the latter case, the system of equations must be rewritten in the form $F(X) = 0$, specifically yielding eq.(2.6). The implementation of both methods is reported in App. B. Additionally, in Fig. 2.15 it is possible to visualise the sphere approach for this type of cut-outs.

$$F = \left(R_v^2 + \frac{t^2}{4}\right) * (sin\varepsilon)^2 - Rsp^2 = 0 \tag{2.6}$$

The two solutions can also be used sequentially; for instance, a good strategy is to use the graphical method for a rough estimation of the solution, thereby providing the MATLAB function *fsolve* with an initial guess already close to the exact result.

2.2.3 FCC unit cell: modelling process

In this paragraph, they are described, also with the help of pictures, the modelling steps and the equations that have led to the final design of the FCC cell. In Fig. 2.17, this cell is shown with (on the right) and without (on the left) cut-outs. The volume is a cube with a side length of 10 mm, and the thickness can be varied as a parameter. Although this cell requires more effort to model than the BCC one, the approach is exactly the same: once the smallest element has been identified, it is sufficient to pattern and/or mirror it in the other directions to obtain the final shape.

Due to the higher complexity, the steps and the equations that lead to the fundamental element shown in Fig. 2.18 are presented. First, it is necessary to sketch an equilateral triangle,

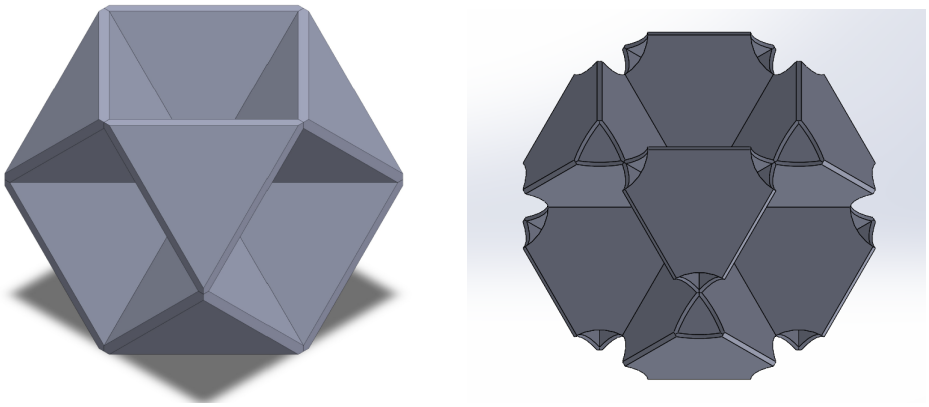

(a) Unit cell without cut-outs. (b) Unit cell with cut-outs.

Figure 2.17: Geometry of the designed FCC unit cell.

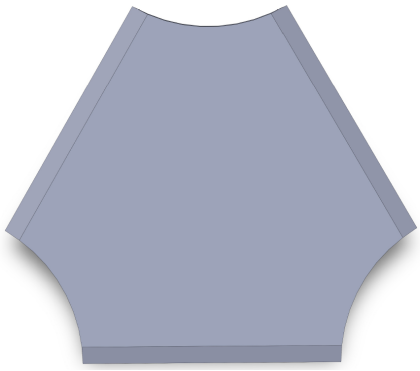

Figure 2.18: FCC unit cell: fundamental patch with cut-outs.

whose side must be chosen so that the unit cell side will be 10 mm. To achieve this, with reference to Fig. 2.19, eq.(2.8) can be obtained. Basically, as a consequence of the chamfering of the tetrahedron edges, the side length of the triangle is reduced from both sides of the black segment shown in detail in Fig. 2.19b. This consideration, combined with the final tetrahedron arrangement shown in Fig. 2.19c, leads to eq.(2.8). Then, a smaller equilateral triangle must be drawn on a plane parallel to that of the larger triangle and shifted upwards by the desired wall thickness. The choice of the side dimension of this polygon must take into consideration that a loft between the two triangles must be created and that the slope of the inclined lateral surfaces that will appear must be equal to $\alpha/2$. This step is necessary because the face sheets of a regular tetrahedron, built with four equilateral triangles, are inclined at an angle of α (given by eq.(2.7)) relative to each other. The shorter side is therefore determined through eq.(2.9), and Fig. 2.20 supports the associated set of equations. Once the triangular face sheet has been designed, it is necessary to chamfer its edges to allow the assembly of eight tetrahedrons into an FCC unit cell. To achieve this goal, the edges cannot be sharp. In addition, cutting the cell as represented in Fig. 2.21 must result in a very regular organisation of perpendicular and parallel lines. In Fig. 2.21, the incorrect geometry is shown on the left, while the correct one is shown on the right. This is achieved through the imposition of a proper equation among the several variables involved. The resulting relation is given by eq.(2.11).

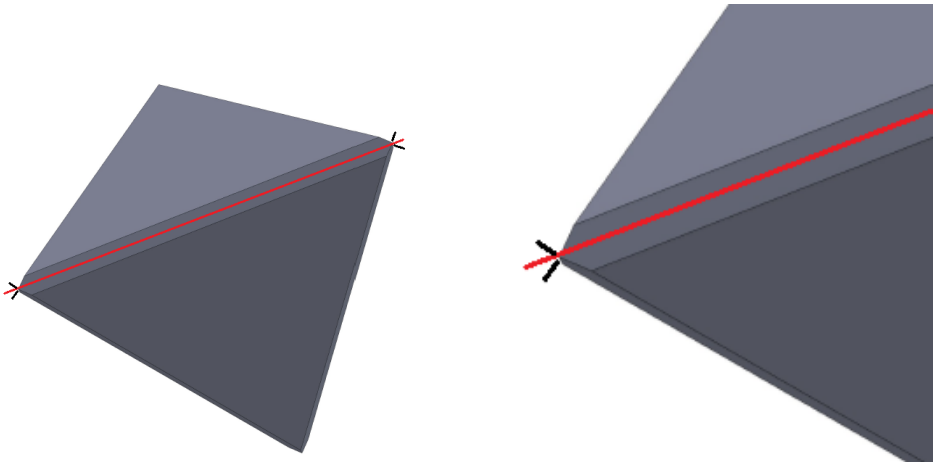

(a) Single tetrahedron without cut-outs. (b) Single tetrahedron without cut-outs, detailed view.

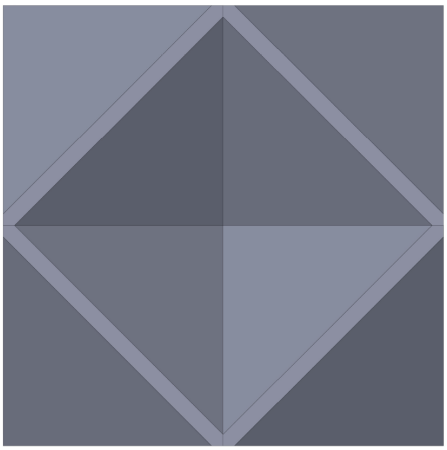

(c) Top view of the entire unit cell.

Figure 2.19: FCC unit cell: sketch for calculating of the length of the fundamental element side.

$$\alpha = arccos\left(\frac{1}{3}\right) \tag{2.7}$$

$$Side = \frac{\sqrt{2}}{2} * (Size_{cell} + 4 * Indent_{cut}) \tag{2.8}$$

$$Side_{short} = Side - 2 * \frac{Indent}{tan30^o} \tag{2.9}$$

$$Indent = \frac{t}{tan\frac{\alpha}{2}} \tag{2.10}$$

$$Indent_{cut} = \frac{t}{2 * sin\frac{\alpha}{2}} \tag{2.11}$$

Then it comes the time to design the holes. Extruded cuts for the FCC unit cell are cylindrical as well, for the same reasons that guided this choice for the BCC unit cell. Their location has been chosen at each vertex of the triangular face sheet, as this allows complete and straightforward powder removal. This choice is logical and, in fact, has its roots in everyday life: it

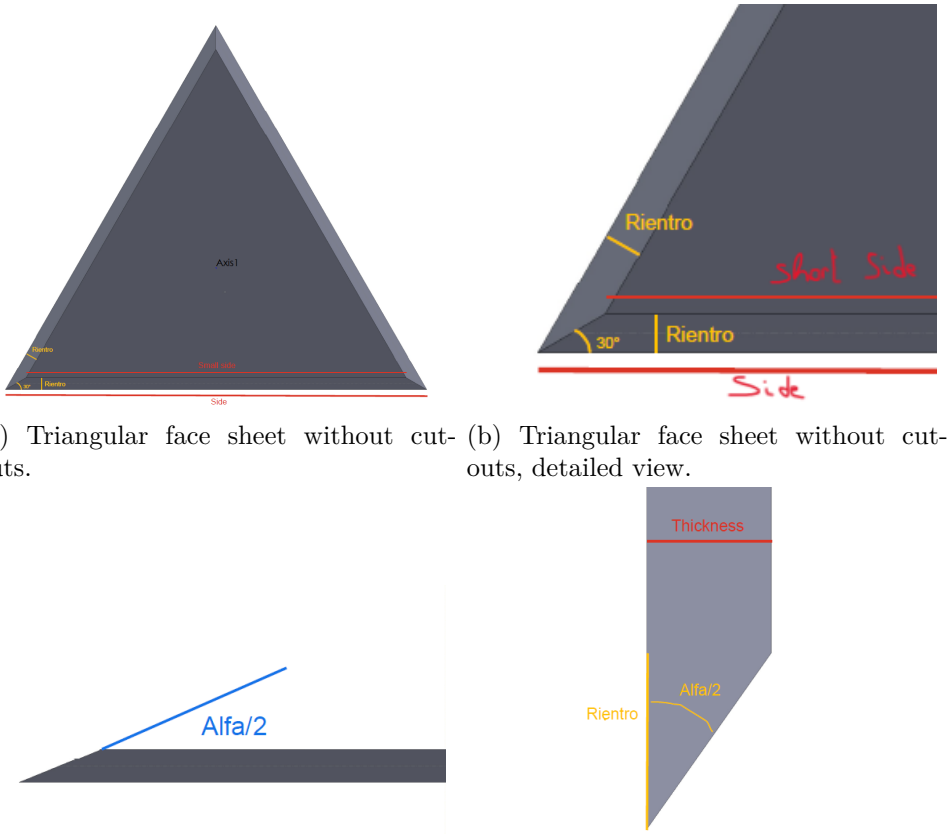

(a) Triangular face sheet without cut-outs.

(b) Triangular face sheet without cut-outs, detailed view.

(c) Lateral side slope.

(d) Lateral side slope, detailed view.

Figure 2.20: FCC unit cell: sketch for calculating of the length of the fundamental element side.

resembles the cut generally made on a Tetra Pak bottle to extract all its contents. Meanwhile, Chua et al. [12] and Li et al. [22] made the same choice. Specifically, the authors of the latter paper investigated the compressive behaviour of FCC plate-based lattices fabricated in steel using SLM. To optimize the mechanical performance, they used Finite Element Modelling to identify low stressed regions, which resulted the vertex ones. Therefore, they introduced cut-outs there, implementing them as spherical subtractions with a radius of 0.900 mm. The cylinder axis is perpendicular to the face sheet and passes through the vertex of the chamfered edge. It should be noted that this is an arbitrary choice; a parametric study could be conducted to evaluate the influence of different positions on mechanical performance. From one side, this would constitute a separate research project and, therefore, until additional data become available, it remains a very reasonable design. On the other side, it is the choice currently implemented as LSM. The radius of the extruded cut is determined using the sphere-based approach previously described. This methodology, applied to the FCC architecture, is shown in Fig.2.22.

As can be seen from Fig. 2.23, the vertex cut is still described by curvilinear triangles, even in this case. Specifically, the actual hole has three curvilinear sides of equal length. Consequently, it can be expected that, in some way, the 1:2 ratio that usually characterises the diagonals of equilateral triangles also appears for this hole. Empirically, many trials can be performed, and this is precisely the situation that occurs each time. Therefore, it is possible to impose a length equal to $3 * Rsp$ on the black segment shown in Fig. 2.23a. Subsequently, the projection on the plane of the black segment in Fig. 2.23b must be determined. The corresponding equation is

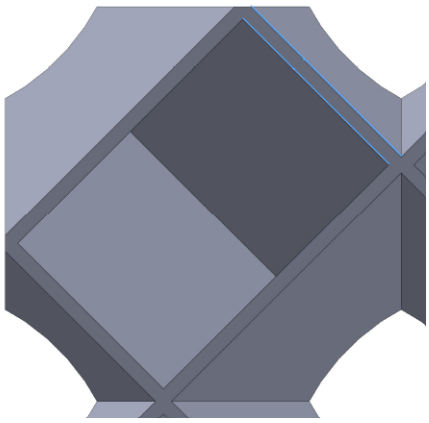

(a) Wrong internal structure arrangement.

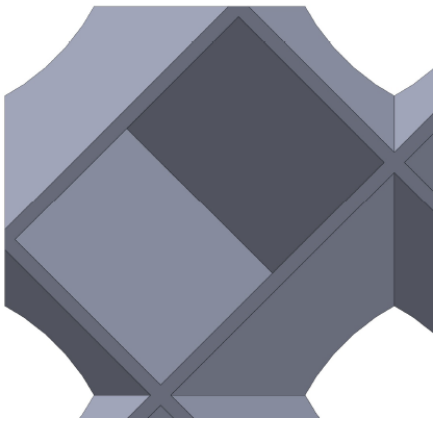

(b) Correct internal structures arrangement.

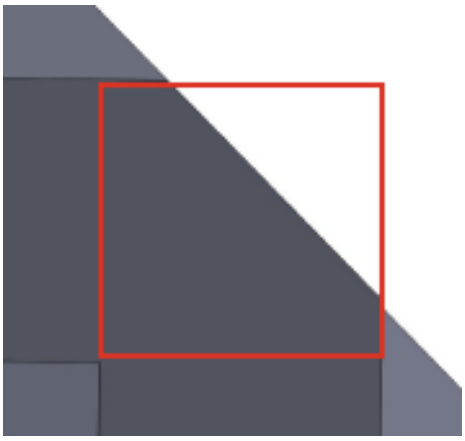

(c) Wrong external structure arrangement.

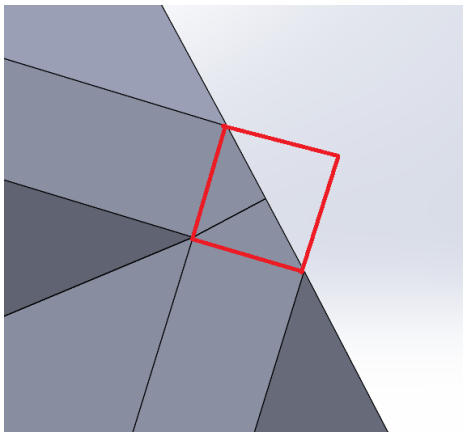

(d) Right external structure arrangement.

Figure 2.21: FCC unit cell - chamfered edges: sketch in support of the geometry parametrization.

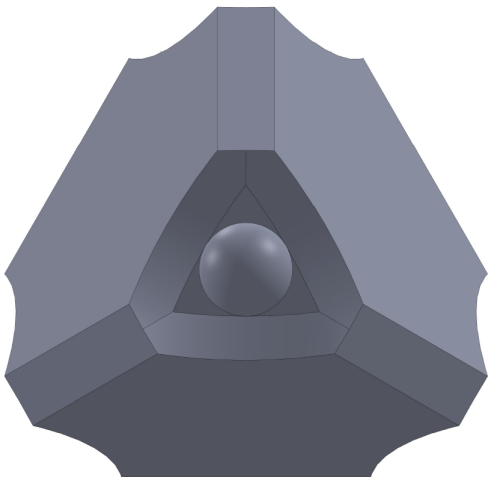

Figure 2.22: FCC unit cell - vertex cut-outs: visualisation of the sphere approach.

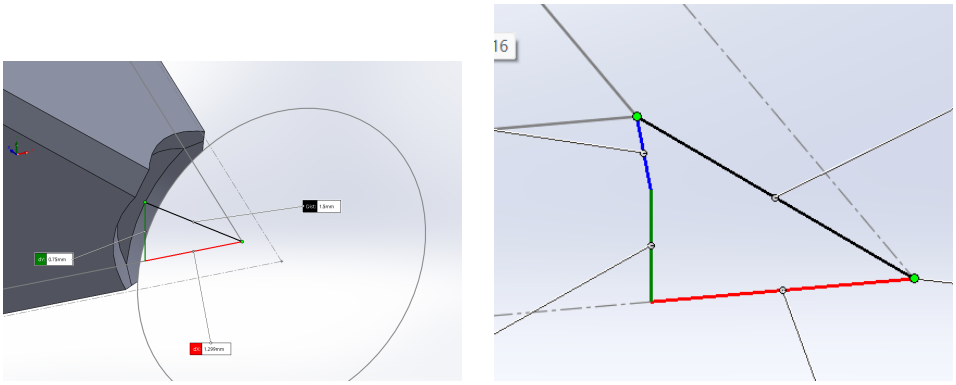

(a) Visualisation of significant lengths defining the cut.

(b) Visualisation of significant lengths near the vertex.

Figure 2.23: FCC unit cell - vertex cut-outs: sketch for dimension calculations.

relatively simple: the blue segment has a length equal to half the thickness and its opposed to an angle of $\alpha/2$ created by the green segment and the hypotenuse of the corresponding right triangle. The length of the green segment (Lg) is therefore given by eq.(2.12). The angle between the projection of the black segment and the red segment is 30°. Hence, this projection measures the green segment divided by $\sin 30°$.

$$L_g = \frac{t}{2 * tan\frac{\alpha}{2}} \tag{2.12}$$

Thus, the desired projection is determined as follows:

$$\begin{aligned} L_p &= \frac{t}{2 * tan\frac{\alpha}{2} * sin30^o} \\ &= \frac{t}{tan\frac{\alpha}{2}} \end{aligned} \tag{2.13}$$

Finally, the radius of the cylindrical extruded cut for the FCC unit cell is determined as follows:

$$\begin{aligned} R_v &= 3 * Rsp + \frac{t}{2 * tan\frac{\alpha}{2} * sin30^o} \\ &= 3 * Rsp + \frac{t}{tan\frac{\alpha}{2}} \end{aligned} \tag{2.14}$$

In conclusion, for the BCC unit cell, almost every equation can be directly implemented into SolidWorks to obtain a parametrised model, with thickness, cell dimensions and R_{sp} as the parameters. However, the vertex cut-out radius must be determined using another software, such as MATLAB, which is capable of solving implicit non-linear equations. For the FCC unit cell, all the equations are explicit and can therefore be directly incorporated into the CAD model, resulting in a fully parametrised model as a function of the aforementioned parameters.

Chapter 3

Geometrical design of lattice samples for tensile tests

In this chapter, both TPMS and plate-based lattice specimens are designed for tensile-compression fatigue tests. In Ch. 2, the geometric features of the studied cells have already been modelled and parametrized, with CAD and Python codes available. The leading design variables are the cell size, the sphere radius and, respectively, the thickness and the iso-value. A total of sixteen specimens must be designed, corresponding to the Primitive, Gyroid, BCC, and FCC architectures, each produced with relative densities equal to: the lowest one compatible with the manufacturing process[1], 10%, 15%, and 20%. The final geometry consists of a lattice test section and two bulk ends, connected through graded interfaces. The cell size has been fixed at 10 mm, following the outcomes of previous research conducted at LSM.

The chapter is subdivided into three main sections. The first provides a review of the literature on specimens design for tensile-compression fatigue tests. The second focuses on establishing the relationships between thickness and relative density. Finally, the third section describes the designed specimens and explains the rationale behind each design choice. Additionally, the final section briefly describes the working mechanism of the code used to determine the parameters that define the geometric dimensions of the transition regions.

3.1 Literature review

When dealing with the design of specimens for tensile and fatigue tests, many sources and standards must be consulted. Indeed, several standardization institutions, such as the American Society for Testing and Material (ASTM), the British Standard Institution (BSI), and the International Organization for Standardization (ISO) have invested efforts in producing extensive documentation on the topic. Regarding metallic materials, such as aluminium alloys, important references are ASTM E8/E8M-25, E606/E606M-21, E468/E468M-23a, E466-21, BS ISO 1099:2017, BS EN 3987:2009, and ASTM STP 566. These documents contain plenty of information, from specimen design to testing machines, from recording systems to failure criteria. However, they are written for bulk materials, even if specific design and tests for samples fabricated via additive manufacturing processes are provided. When it comes to lattice structures, such as the TPMS and plate-based configurations analysed in this thesis, no standard practices currently exist [14]. Khan et al. [15] wrote about the lack of specific standardization for fatigue experiments with lattice structures, linking this situation to the large interest in

[1] According to the experience developed at LSM, it is possible to print lattice structures whose wall thickness is at least 0.120 mm.

uniaxial compression-compression cycle loading. Indeed, *this approach is favoured by its simplicity*. This opinion is shared by Doroszko and Seweryn [82] (Poland), with particular remark on the difficulty of this kind of analysis and tests. As a consequence, the design of the tests must refer to the aforementioned standards just as guidelines, which provide the fundamental framework to be adjusted according to the prevailing circumstances. This flexibility is already included in some norms. For instance, BS EN 3987:2009 [83], *Aerospace series - Test methods for metallic materials - Constant amplitude force - controlled high cycle fatigue testing*, with reference to notched specimens, does not put prescriptions on the design of these samples, recognising the specialised nature of the field; it simply underlines that the chosen configuration and the research objectives must be coherent. It is also possible to consult the scientific literature, namely published papers, to check what has been previously chosen by scientists and engineers. This paragraph is organised as follows: in the first part, the fundamental guidelines that can be extracted from the standards and manuals are cited; in the second section, examples and choices from the scientific literature are reported, firstly for TPMS and then for plate-based architectures.

3.1.1 Standards

Standard E606/606M-21 [84], *Standard Test Method for Strain Controlled Fatigue Testing*, and Standard E466-21 [85], *Standard Practice for Conducting Force Controlled Constant Amplitude Axial Fatigue Tests of Metallic Materials*, as well as most of the standards that have been consulted, underline the importance of assuring the alignment of the longitudinal axis of the specimen with the direction of the applied force during each cycle. This care is necessary to minimize bending strain, which in turn leads to more repeatable test results; the lower the material ductility, the greater the influence and thus the importance of this aspect. Many standards also provide a quantification for the acceptable bending, stating that the corresponding stress must not exceed 5% of the range of maximum or minimum stress imposed during the test [85]. BS ISO 1099:2017 [86], *Metallic materials - Fatigue testing - Axial force-controlled method*, provides the corresponding values in terms of strain. The standard BS EN 3987:2009 prescribes inspections of the alignment of the load train assembly no later than one year or 100 tests, whichever occurs sooner. Also the gripping part of the sample, namely the section connecting the specimen to the testing machine, is mainly constrained by bending considerations [84]. Finally, the good practice of reducing as much as possible the distance between grips, is recommended to minimize bending.

Concerning extensometers, the norm [84] requires that the chosen technology must allow accurate measurement of deformation in the gauge section. Regarding specimen design, a minimum diameter (d) of 6.35 mm is recommended in the test section for cylindrical samples, with the gauge section length in the range $3d \pm d$. STP 566 [87], *Handbook of Fatigue Testing*, prescribes a gauge length lower than $4d$ to prevent buckling of the structure. Strategies to concentrate higher stresses in the test section and to guide failure to this section must also be adopted. Therefore, the shoulder radius should be as large as possible, consistent with the limitations on sample length; values in the range $4d \pm 2d$ are suggested. Standard E466-21 prescribes similar sample dimensions to those reported by E606. For cylindrical samples, the gauge section should have a diameter in the range 5.08 - 25.4 mm, a length of 2 to 3 times the diameter to avoid excessive slenderness and buckling during tensile-compression fatigue tests, and a grip cross-sectional area 1.5 to 4 times larger than that the gauge section. The blending fillets between the test section and the ends are larger than in E606, with a minimum radius of $8d$, to minimize the theoretical stress concentration factor K_f. The norm also cautions against gauge sections with sharp edges, which are inherently weak for metallographic reasons, since the grain struc-

ture cannot be confined by neighbouring grains in these regions. Similarly, BS EN 3987:2009 states that failures caused by initiation at a corner of the test section, in the case of rectangular cross-section samples, must be considered invalid. Both examples align with the widespread consideration that edge effects should be negligible on the specimens' mechanical behaviour.

3.1.2 TPMS unit cells

Some authors relied on cylindrical dog-bone specimens, particularly in the case of small unit cells. For instance, Soro et al. [32] analysed Schwartz-P, Diamond, and Gyroid unit cells produced via SLM with Ti6Al4V, and designed cylindrical specimens with a minimum relative density of 30-33%. This density varies linearly along the longitudinal direction, in order to model a smooth transition between the gauge section and the bulk ends. Xin et al. [14] reported the possibility of density-gradient transition zones. Araya et al. [88] (Costa Rica, Finland) also used cylindrical specimens. The authors studied the tensile behaviour of TPMS structures, specifically the Gyroid cell, considering relative densities from 10 to 50%, in steps of 10%. The specimens have the typical dog-bone shape; the test section has a diameter of 12 mm and a height of 18 mm. The relative density varies along the longitudinal direction to ensure that stresses concentrate in the middle of the sample, while the grip sections are bulk. On the contrary, Doroszko et al. [82], relied on flat dog-bone specimens in their studies on the cycling behaviour of Ti6Al4V Diamond structures under fully reversed load conditions. Falkovska et al. [52] also dealt with the fatigue behaviour of Ti6Al4V Diamond structures, fabricated via Laser Powder Bed Fusion (L-PBF). Tensile-compression fatigue tests under fully reversed constant-amplitude loading conditions were carried out, considering four different relative densities, namely 19, 27, 50, and 66%. The specimens have the typical dog-bone shape and do not present any bulk section. The test section has a thickness of 6 mm, a width of 8 mm, and a length of 23.40 mm. Boniotti et al. [89] (Italy, France) provide a case of square cross-section samples. The authors studied strut-based lattices in which each side contained 4 unit cells, as they claimed that « *previous studies have shown that the mechanical properties of these two structures are almost unaffected by the dimension of the section if there are at least 4×4 cells* ». The specimens for fatigue experimental tests under tension-tension loads have a height of 4 unit cells in the test section and two layers of graded cells for each side, between the grips and the gauge section. The cell side measures 2.4 mm. Bigger cells are used by Kelly et al. [26]. The authors, studied the mechanical behaviour of Ti6Al4V sheet-based Gyroid structures, fabricated via SLM, under tensile and compression, static and cycling loading conditions. The unit cell has a size of 4 or 6 mm; the gauge section is a cube of 6 mm per side, for both cell dimensions. The samples present the dog-bone shape and only the core is made of lattice structures; in fact, transition and grip sections are bulk. Pelegatti et al. [47] worked with smaller unit cells than [89]. Their paper deals with skeletal-Gyroid cells made of additively manufactured 316L steel. The unit cell side is 2 mm and the sample has lattice gauge and transition sections, and bulk grips. The specimen cross-section is a square of 6×6 cells. The test section has a height of 15 cells, while two layers for each side are graded to create a smooth transition between the core and the grips. They perform static tests and fatigue analysis under fully reversed constant-amplitude loading conditions. They reported that literature suggested using 7 cells per side to guarantee reliable results, but their FE analyses proved that, at least for their stress and strain ranges, the difference with 6 is negligible.

Some authors designed specimens referring to international standards. This is the case of several works on polymer materials, which relied on ASTM D638. Pehlivan [27], who studied the tensile properties of three polymer-based TPMS cells (Gyroid, Neovius, and Diamond)

using dog-bone specimens, designed the samples according to D638, where only the test section is a lattice structure, while both the transition and end sections are bulk. Demir et al. [25] also dealt with the tensile properties of polymeric TPMS lattices, modelled according to D638-22 [90]. Mahapatra et al. [10] analysed Gyroid and Diamond lattices built through 3D printing in acrylonitrile butadiene styrene (ABS), pure and reinforced with short Kevlar fibres. Tensile samples were fabricated according to D638-14 [91]: the test section has a length of 57 mm, a width of 13 mm, and a core thickness of 3, 4, or 5 mm, according to the cell size. Two different sample arrangements were employed, both with bulk transition and grip sections and lattice core. The reinforced samples also have an upper and lower face sheet, creating a sandwich structure in the test section. An example of non-application of the international standards can be found in Doroszko et al. [82]. The authors had to adjust the geometry and dimensions of the specimens based on the configuration and capabilities of the facilities at their disposal. Similarly, Pelegatti et al. [47] worked with 6×6 cell sections instead of 7×7 ones due to size limitations imposed by the experimental equipment.

3.1.3 Plate-based unit cells

Considering the situation for BCC and FCC, the field of compression behaviour has been more explored than bending and tensile characteristics, but in any case less than what has been done for TPMS structures. Specimens are generally designed without referring to international standards. In this context, Wang et al. [41] are an exception. The authors studied three unit cells, namely plate-based BCC and FCC, and Gyroid, using 2×2×2 cells cubic samples, whose side is 30 mm, designed according to ASTM D695-15 [92]. In the field of polymeric materials, the paper by Alagha et al. [11] deals with the mechanical behaviour of SC-FCC-BCC, a combination of the three cell architectures. The authors first assessed the influence of the number of unit cells per direction (models with 1, 2, 3, and 4), with a fixed cell size of 14 mm. Once the results proved that two unit cells per side are sufficient to reach convergence of the FE analysis, they relied on 2×2×2 cells cubic samples for the remaining numerical simulations and experimental tests. The same, but single unit cells (SC, BCC, and FCC), have been studied by Abdelmageed et al. [19], who also assessed the influence of the number of cells and, differently from Alagha et al. [11], concluded that «*The FCC and the BCC structures achieve stable responses with 3×3×3 cells configurations*». The SC architecture follows the same rule, with the difference that misleading results are associated with the 4×4×4 configuration, which is therefore suggested to avoid for this cell shape. Zang et al. [65] investigated the compression performance of AlSi10Mg SC, BCC, and FCC plate-based lattices, with densities from 6 to 22% in steps of 4%. The necessity of samples composed of at least four unit cells per direction, even if specifically referring to the Energy Absorption Performance (EAP), is reported by these authors as well. The cell size adopted is 10 mm. Jiang et al. [64] studied BCC, FCC, and hybrid BCC-FCC plate-based cells, made of 316L steel, also choosing a cell size of 10 mm and performing compression tests on single cells. Ghosh et al. [79] focused on partially strut- and partially plate-based open cell configurations, performing compression tests on 40x40x40 mm^3 samples, with four cells for each side (4×10 mm). Smaller cells are used by Heindenreich et al. [81] (4×4×4 mm^3 cells) and by Schneider and Kumar [61] (3.33 to 10 mm). The authors examined the energy absorption properties of several truss-, shell-, and plate-based polymeric lattice structures in various configurations, namely cubic samples with a side of 20 mm, filled with 2 to 6 unit cells per side. Xue et al. [80] performed quasi-static compression tests on 2×2×2 cells samples fabricated via nylon powder SLS technique. Larger cells were used by Medhin et al. [78] (20 mm) and Li et al. [77], who analysed a hybrid cell composed of SC-plate and BCC-truss basic configurations, adopting the same cell size. Their lattice was produced via

SLS using TPU.

3.2 Density evaluation

This paragraph is dedicated to the density determination of the designed samples. The motivation for that is the extreme dependency of the mechanical performance to the relative density and, hence, the necessity of creating tools for its reliable and quick determination. Indeed, these calculations are very significant, considering that the specimens, apart from the unit cell employed, are mainly comparable or distinguishable from each other by the relative density. In this regard, Ashby and Gibson [1], already in 1997, underlined the necessity of equations to relate the cell dimensions and shape to the density. Here too, as in the rest of the thesis, the work can be split into that for TPMS and that for plate-based architectures.

3.2.1 TPMS unit cells

TPMS unit cells have a very intricate geometry and, thus, their volume is far from being computable through analytical formulas. Therefore, approximate methods must be exploited. A good approximation is to calculate the midsurface (which remains fixed) and then multiply it by the average thickness, obtaining a result which, especially for low-density samples, represents a good approximation, within a margin of error of a few percentage points, due to the non-uniform thickness distribution in TPMS cells. For instance, Bonatti et al. [13] studied shell-lattices obtained from smoothing the topology of tube-lattices and compared the relative densities of different cells. They considered a constant average thickness and evaluated the surface areas of the midplane, providing formulas for them. However, this is not the approach implemented here. Through LSM-developed Python codes, it is possible to associate the iso-value with the corresponding relative density, hence obtaining the desired value. In addition, the possibility of continuously grading the TPMS specimens leads to the necessity of knowing the density-iso-value pair just for the test section, as the transition to the grips interface is automatically computed from these numbers. Schneider et al. [61] calculate the Gyroid relative density from the CAD geometry using MATLAB.

3.2.2 Plate-based unit cells

On the contrary, plate-based BCC and FCC architectures are composed of simpler shapes. To support this statement it is sufficient to recall that, apart from the necessity of determining equations to relate the parameters selected by the user with the dimensions dependent on them, traditional CAD software are entirely appropriate tools for modelling these cells. In fact, for the analysed cells, analytical formulas for their volume calculation exist. I have used those from LMS, eq.(3.1) and eq.(3.2), for BCC and FCC respectively (L is the cell size, t the thickness). They are based on the calculation of the fundamental patch volume, to be multiplied by its numerosity in the unit cell. Nevertheless, a few examples are also reported in recent scientific works, such as Schneider et al. [61] and Xue et al. [80]. A significant issue is the presence of cut-outs. Indeed, the equations originally provided are no longer valid for perforated plates. The strategy I am going to describe is based on an approach similar to that used for the fundamental patch. Specifically, the volume removed with cut-outs is computed and multiplied by the number of occurrences. Common volumes, simultaneously subtracted from multiple elements, are treated to ensure they are counted once and only once. This process involves basic arithmetic operations as well as the evaluation of integrals and certain approximations. The implemented MATLAB code can be consulted in App. C. The obtained

Thickness [mm]	SolidWorks Vol. [mm^3]	MATLAB Vol. [mm^3]	Rel. Error
0.100	70.0125	70.0120	-7.14E-06
0.200	132.9293	132.9277	-1.20E-05
0.400	237.2617	237.2523	-3.96E-05
0.700	339.1555	339.0930	-1.84E-04
1.000	374.1074	373.8854	-5.93E-04

Table 3.1: BCC unit cell - A few examples of the density errors.

Thickness [mm]	SolidWorks Vol. [mm^3]	MATLAB Vol. [mm^3]	Rel. Error
0.100	54.7750	54.7748	- 3.65E-06
0.200	103.0393	103.0393	$<$ 8.73E-07
0.400	179.3409	179.3409	$<$ 5.02E-07
0.700	240.5895	240.5895	$<$ 3.74E-07
1.000	233.7522	233.7522	$<$ 3.85E-07

Table 3.2: FCC unit cell - A few examples of the density errors.

results have been repeatedly verified (changing the plate thickness) against those provided by the *mass property* function of SolidWorks 2024, resulting in relative errors lower than 10^{-4} for the range of thicknesses employed, as can be read from Tab. 3.1 and 3.2. A few examples are reported in Tab.3.1 and 3.2. The errors are defined through eq.(3.3), considering the SolidWorks calculations as exact. These data are used to plot the dependency of the errors on the relative density and the thickness value.

$$BCC_{Vol} = 2\sqrt{2}(3L^2 - 6\sqrt{2}Lt + 8t^2)t \tag{3.1}$$

$$FCC_{Vol} = 2\sqrt{3}(2L^2 - 3\sqrt{3}Lt + 5t^2)t \tag{3.2}$$

$$Rel_{Err} = \frac{MATLAB_{Vol} - SolidWorks_{Vol}}{SolidWorks_{Vol}} \tag{3.3}$$

As can be seen from Fig. 3.1, the magnitude of the relative errors increases with thickness for the BCC architecture. This behaviour is a direct consequence of the approximations that have been carried out. On the contrary, the FCC unit cell shows the opposite trend, namely the relative error decreases as thickness increases. This is due to the characteristics of eq.(3.3): if the numerator remains unchanged (nonzero because of the uncertainty introduced by the finite number of significant digits) and the denominator increases, the result can only decrease. The curve also highlights two additional aspects: at very low thicknesses, the code does not provide an exact result, even if the error is extremely negligible; moreover, if the thickness exceeds 0.822 mm, the relative error begins increasing again. This occurs because the maximum achievable density has been reached, and any further increase in thickness causes the larger cut-outs to outweigh the volume gain. The combination of these two parameters results in a decrease of the relative density, and hence of the denominator. Finally, for both unit cells, the scripts consistently underestimate the density compared to the values obtained with SolidWorks. Density limitations are also discussed in [82]; the authors analysed samples with different relative densities and identified both geometrical and mechanical constraints associated with these values. Specifically, the upper limit of 66% was chosen to ensure that the Diamond cell remains

identifiable and does not degenerate into a simple porous medium, while the lower limit of 18.5% was set to prevent failure under very small loads.

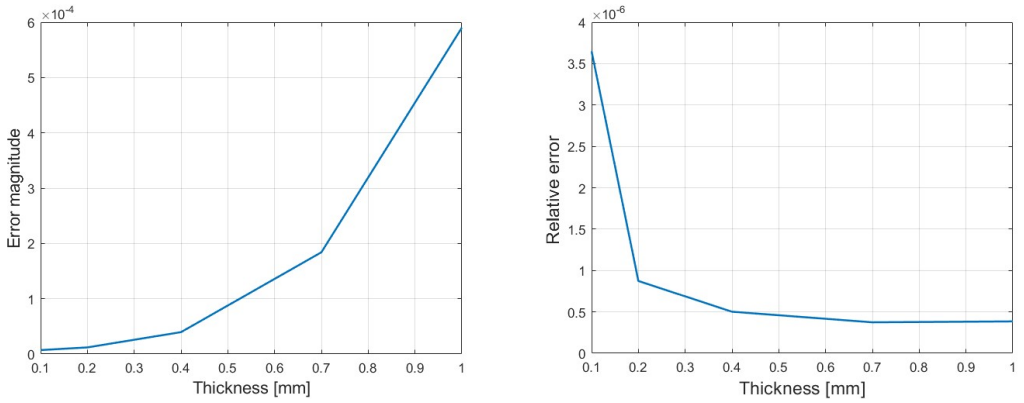

(a) Script for BCC unit cells.

(b) Script for FCC unit cells.

Figure 3.1: Density calculation for plate-based unit cells: Visualisation of the error dependence on thickness, comparing results from in-house developed code with SolidWorks reference data.

In Ch. 2, the different types of extruded cuts have already been introduced. In the following sections, they are revisited and analysed in depth, with particular attention to their volume and, consequently, their influence on density. First, the BCC architecture will be examined, followed by the FCC one.

BCC Unit cell

In Fig. 3.2, the *side-central* cut-out is shown, both in its negative form (the hole created) and in its positive form (the volume removed). Essentially, it corresponds to the intersection of two perpendicular disks, each with radius R_c and thickness t [2]. The volume of a single disk is determined through eq.(3.4). Of course, both disks must be considered, but it is equally important to count the volume of their intersection V_{int} only once. The derivation, which has been adapted from [93], considers that two cylinders of radius R_c, one aligned along the x-axis and the other along the y-axis, intersect each other; the common volume corresponds to the region lying below the lowest surface at every point. These cylinders are described by the ineqs.(3.5) and (3.6).

$$V_{disk} = \frac{\pi * R_c^2 * t}{2} \tag{3.4}$$

$$y^2 + z^2 \leq R_c^2 \tag{3.5}$$

$$x^2 + z^2 \leq R_c^2 \tag{3.6}$$

The mathematical translation of the intersection is a system, in which both inequalities must be simultaneously satisfied. Hence, by rewriting the inequalities as functions of z and applying the *minimum* function, ineq.(3.7) is obtained.

$$z^2 \leq min(R_c^2 - x^2, R_c^2 - y^2) \tag{3.7}$$

[2]The nomenclature is used consistently throughout the thesis. When the meaning of a symbol is not specified, it has been introduced in a previous paragraph or chapter.

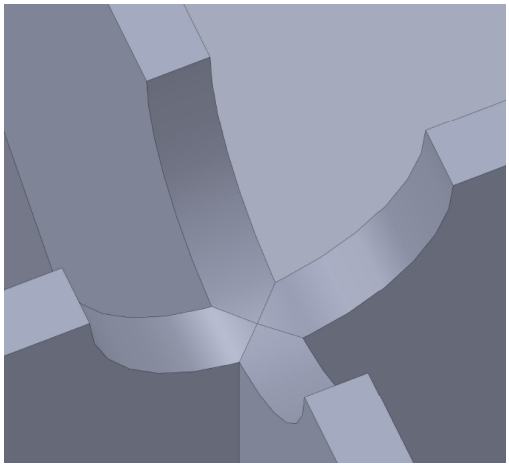

(a) Hole created through the cut.

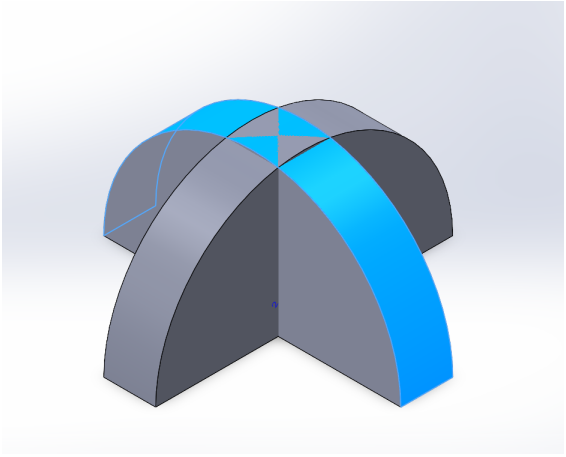

(b) Removed volume through the cut.

Figure 3.2: BCC unit cell: shape of the side-central cut-out.

This can be split in two systems, as follows:

$$\begin{cases} z^2 \leq R_c^2 - x^2 \\ R_c^2 - x^2 \leq R_c^2 - y^2 \end{cases} \tag{3.8}$$

$$\begin{cases} z^2 \leq R_c^2 - y^2 \\ R_c^2 - y^2 \leq R_c^2 - x^2 \end{cases} \tag{3.9}$$

It is immediate to notice that, apart from the employed symbols, the systems represent the same quantities. In other words, this is a case of dummy variables. Therefore, only one system needs to be studied, for instance syst.(3.8). Working on its first inequality, it results in two inequalities: the first one still referring to the calculations, while the second one arises from the necessity of imposing existence conditions on the square root argument. The main steps are reported here.

$$\begin{cases} -\sqrt{R_c^2 - x^2} \leq z \leq +\sqrt{R_c^2 - x^2} \\ R_c^2 - x^2 \geq 0 \\ R_c^2 - x^2 \leq R_c^2 - y^2 \end{cases} \tag{3.10}$$

$$\begin{cases} -\sqrt{R_c^2 - x^2} \leq z \leq +\sqrt{R_c^2 - x^2} \\ -R_c \leq x \leq R_c \\ y^2 \leq x^2 \end{cases} \tag{3.11}$$

$$\begin{cases} -\sqrt{R_c^2 - x^2} \leq z \leq +\sqrt{R_c^2 - x^2} \\ -R_c \leq x \leq R_c \\ -|x| \leq y \leq |x| \end{cases} \tag{3.12}$$

The third inequality of syst.(3.12) represents the area enclosed between the bisectors of the first–third and second–fourth quadrants, when the first one is rotated clockwise in the xy-plane around the z-axis. Alternatively, for our purposes, if coupled with the proper limitations along the x and y directions, it corresponds to the two light blue triangles in Fig. 3.2b. Therefore, it is necessary to calculate the area under the disk lateral surface, with the following limits:

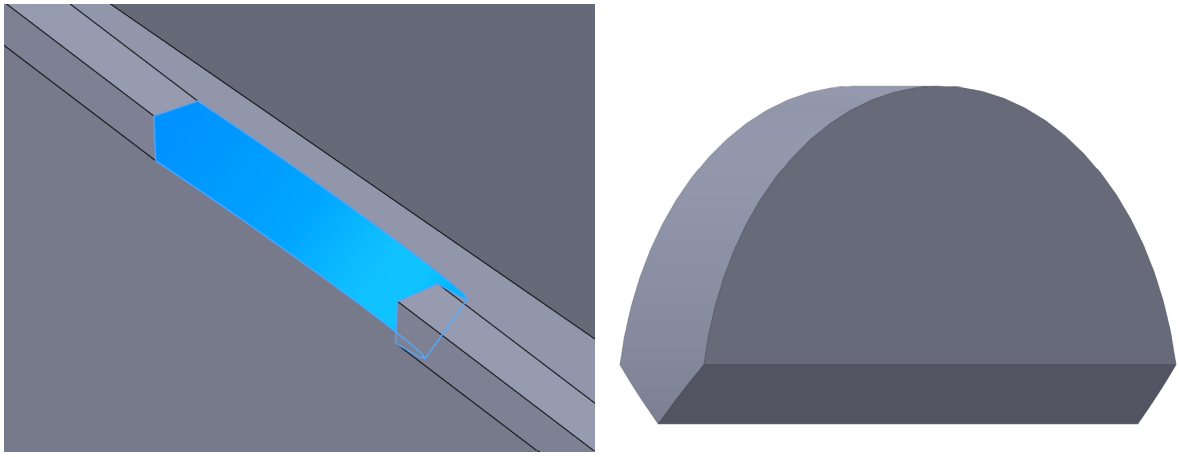

(a) Hole created through the cut. (b) Removed volume through the cut.

Figure 3.3: BCC unit cell: shape of the side-side cut-out.

- x goes from $-\frac{t}{2}$ to $+\frac{t}{2}$;
- y goes from $-|x|$ to $+|x|$;
- z goes from 0 to $\sqrt{R_c^2 - x^2}$.

Additionally, taking into account the symmetry and the dummy variable, the x interval can be modified as follows: $x \in (0, \frac{t}{2})$, and the result has to be multiplied by four. This process leads to eq.(3.13).

$$V_{int} = 4 * \int_0^{\frac{t}{2}} dx \int_{-|x|}^{|x|} dy \int_0^{\sqrt{R_c^2 - x^2}} dz \tag{3.13}$$

The integral in eq.(3.13) can be solved analytically. This calculation leads to eq.(3.14).

$$V_{int} = \frac{8}{3}\left[R_c^3 - \sqrt{\left(R_c^2 - \frac{t^2}{4}\right)^3}\right] \tag{3.14}$$

Finally, the whole volume is determined through eq.(3.15). It can be easily inferred from Fig. 2.7 that each BCC unit cell has six of these holes.

$$\begin{aligned} V_{tot} &= 2 * V_{disk} - V_{int} \\ &= \pi * R_c^2 * t - \frac{8}{3}\left[R_c^3 - \sqrt{\left(R_c^2 - \frac{t^2}{4}\right)^3}\right] \end{aligned} \tag{3.15}$$

Let's now analyse the second type of holes. In Fig. 3.3, the *side-side* cut-out is shown, both in its negative form (the hole created) and in its positive form (the volume removed). Essentially, it corresponds to half of a disk, with chamfered edges along the flat side.

A reasonable approach consists in considering the volume in Fig. 3.3b as composed of two main portions: the one delimited by the external circular surface, referred to as *disk*, and the remaining part (Fig. 3.4a) characterised by the chamfered surfaces. The latter can itself be further subdivided into three portions: a central *prism* with a triangular base, and two very thin

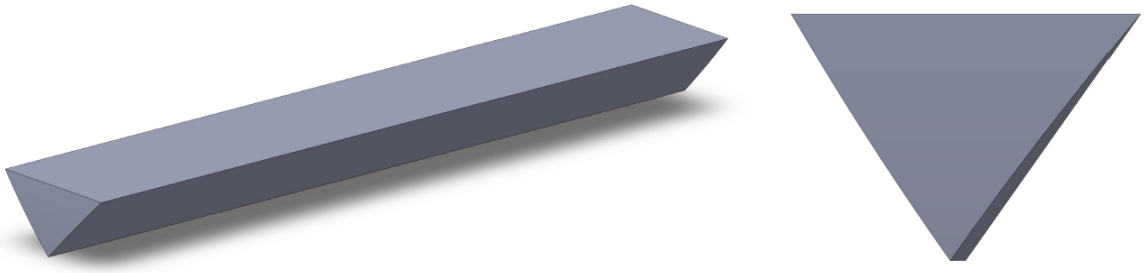

(a) Prism. (b) Single cap.

Figure 3.4: BCC unit cell: subvolumes of the side-side cut-outs.

external volumes, referred to as *caps* (Fig. 3.4b). The prism volume is given by eq.(3.19), while the volume of each cap is determined through eq.(3.20). Naturally, the calculations could be simplified by exploiting the symmetry of the shapes and performing the volume determination on only half or one-fourth of each portion.

The volume of a prism is calculated as the product of the base area A_b and the height h. Since the base is a triangle, and the inclined edges produced by the chamfers are inclined at 45° with the horizontal, the triangle has a base of length t and a height equal to half of it. The prism height is $2X_f$, which corresponds to the distance between points A and B in Fig. 3.5, measured along the x axis. The external surface of the *disk* is mainly described by the equations of a cylinder, since the cut is produced using one of these solids. Considering the *disk* as lying on the xy plane, point B has coordinates $(X_f, \frac{t}{2})$. Using the equation of a circle of radius R_s, eq.(3.16), and solving for the x coordinate, eq.(3.17), it is then possible to calculate X_f, eq.(3.18).

$$x^2 + y^2 = R_s^2 \tag{3.16}$$

$$x = \pm\sqrt{R_s^2 - y^2} \tag{3.17}$$

$$X_f = \sqrt{R_s^2 - \left(\frac{t}{2}\right)^2} \tag{3.18}$$

$$\begin{aligned} V_{pr} &= A_b * h \\ &= \frac{1}{2}\left(t * \frac{t}{2}\right) * 2 * X_f \\ &= \frac{1}{2}t^2 X_f \end{aligned} \tag{3.19}$$

Each side cut has two *caps*, which can be split into two symmetric halves. To compute the volume, an integral must be written. The x coordinate goes from X_f to the radius R_s. The y coordinate goes from 0 to the external surface, described by eq.(3.16). Considering just one half of the cap, the z coordinate goes from 0 to $y \tan 45°$, as can be observed in Fig. 3.6.

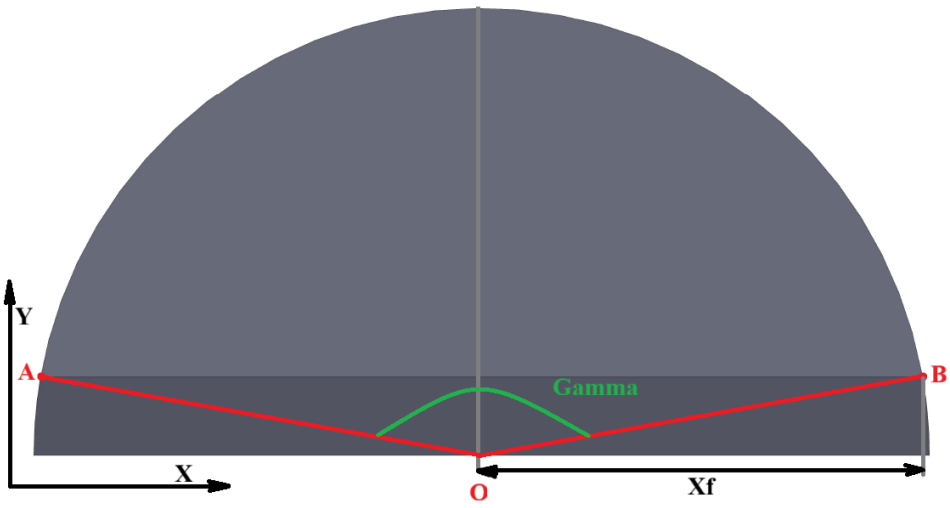

Figure 3.5: BCC unit cell - side-side cut-outs: sketch for volume calculations, front view.

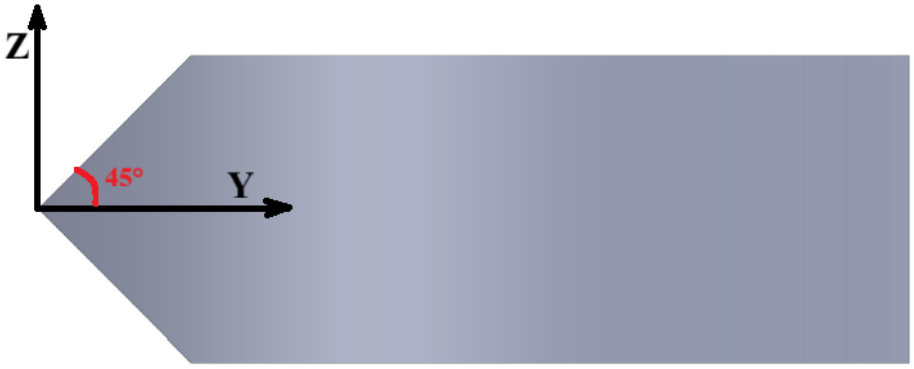

Figure 3.6: BCC unit cell - side-side cut-outs: sketch for volume calculations, lateral view.

$$
\begin{aligned}
V_{cap} &= \int_{X_f}^{R_s} dx \int_0^{y_{max}} dy \int_0^{ytan45^\circ} dz \\
&= \int_{\sqrt{R_s^2-(t/2)^2}}^{R_s} dx \int_0^{\sqrt{R_s^2-x^2}} dy \int_0^{y} dz \\
&= \int_{\sqrt{R_s^2-(t/2)^2}}^{R_s} dx \int_0^{\sqrt{R_s^2-x^2}} y dy \\
&= \frac{1}{3}\left[R_s^3 - \left(R_s^2 + \frac{t^2}{8}\right)\sqrt{R_s^2 - \frac{t^2}{4}}\right]
\end{aligned}
\tag{3.20}
$$

To obtain the volume of the *disk*, it is necessary to calculate the angle γ using eq.(3.21). The volume of the combination of the two parts, *disk* and *excess*, shown in Fig. 3.7, is computed through eq.(3.22). The excess volume is simply a prism, whose volume is given by eq.(3.23).

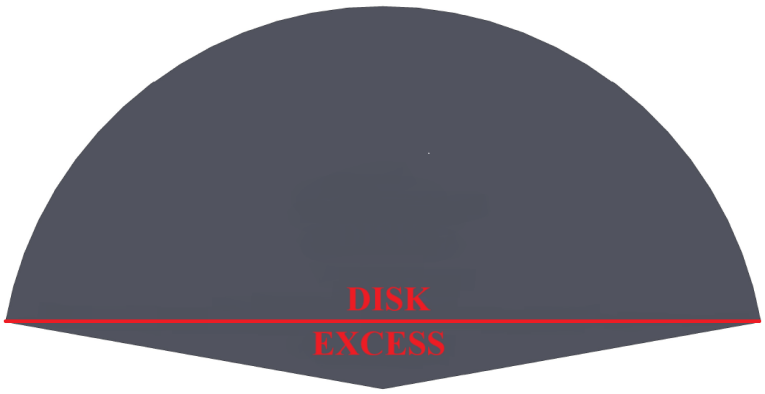

Figure 3.7: BCC unit cell - side-side cut-outs: sketch for volume calculations, disk and excess visualisation.

$$\gamma = \pi - 2 * arctan \frac{0.5 * t}{Xf} \tag{3.21}$$

$$V_{disk} = \frac{\gamma}{2} * R_s^2 * t \tag{3.22}$$

$$\begin{aligned} V_{pr2} &= A_b * h \\ &= \frac{1}{2} * \frac{t}{2} * 2X_f * t \\ &= \frac{1}{2} t^2 X_f \end{aligned} \tag{3.23}$$

Finally, combining all these formulas, the total volume of the side cut is determined through eq.(3.25). It can be easily inferred from Fig. 2.7 that each BCC unit cell has twelve of these holes.

$$V_{tot} = V_{pr} + 4 * V_{cap} + V_{disk} - V_{pr2} \tag{3.24}$$

$$= \frac{\gamma}{2} R_s^2 t + \frac{4}{3} \left[R_s^3 - \left(R_s^2 + \frac{t^2}{8} \right) \sqrt{R_s^2 - \frac{t^2}{4}} \right] \tag{3.25}$$

Let's now analyse the third type of holes. In Fig. 3.8, the *vertex* cut-out is shown, both in its negative form (the hole created) and in its positive form (the volume removed). Essentially, it corresponds to the combination of three of the fundamental elements shown in Fig. 3.9, with chamfered edges along the flat side. These elements are essentially a quarter of a disc, with thickness t and radius R_v, and one chamfered edge. The approach to determine its volume is relatively straightforward: the volume of the quarter is first calculated as if the edge were not chamfered and then the excess volume V_{ch}, obtained through eq. (3.26), is subtracted. The net volume is given by eq. 3.27.

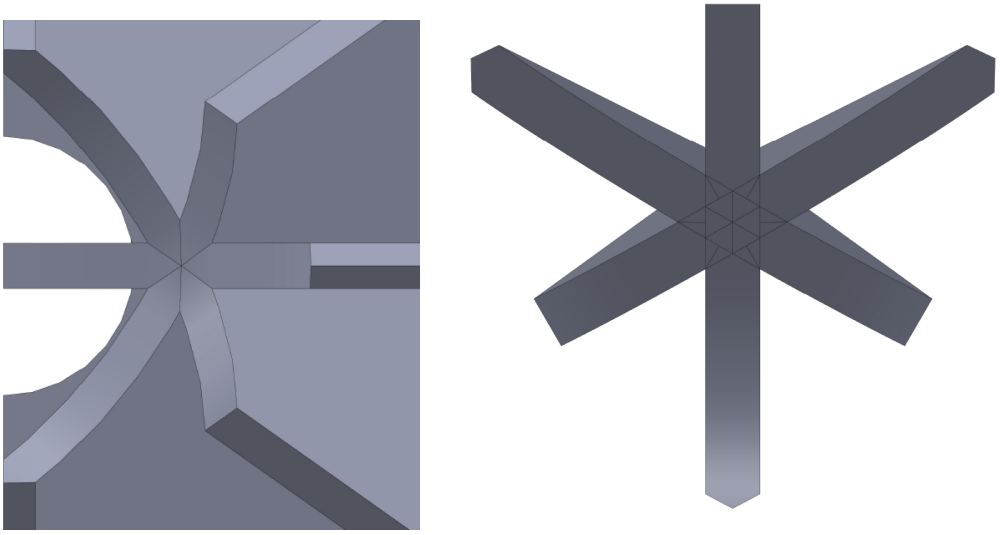

(a) Hole created through the cut. (b) Removed volume through the cut.

Figure 3.8: BCC unit cell: shape of the vertex cut-out.

$$V_{ch} = \int_0^{t/2} \int_x^{t/2} \int_0^{\sqrt{R_v^2 - x^2}} dz\, dy\, dx \tag{3.26}$$

$$V_v = \frac{\pi R v^2 t}{4} - 2V_{ch}; \tag{3.27}$$

The hard part in the calculations of the volume of the BCC vertex cut-out lies in the intersection between the three fundamental elements. In this regard, two different intersections are shown in Fig. 3.10a and Fig. 3.10b. The former is the common volume between two elements, which will be denoted as *2E-Intersection*, and the latter among three, which will be denoted as *3E-Intersection*. The volume of the cut-out is therefore calculated as three times V_v, minus three times the 2E-Intersection, plus once the 3E-Intersection. This peculiar calculation guarantees that each part of the hole is counted once and only once. In this regard, a careful analysis of the geometries allows to understand that each fundamental element contains twice the 2E-Intersection, and hence it is added six times, whereas only three are required. However, the aforementioned subtraction eliminates the 3E-Intersection, which needs to be restored.

As previously done for the other geometries, both the 2E- and 3E-Intersections have been split into simpler and smaller subvolumes. They are now described and associated with the corresponding volume equations. In Fig. 3.11, the main subdivision of the 2E-Intersection is shown, respectively in the left and right images, with a plane perpendicular to the longitudinal external edges. The smaller volume can be further split into the cube in Fig. 3.12a, the larger triangular-base pyramid in Fig. 3.12b, the two smaller square-base pyramids in Fig. 3.12c, and the triangular-base pyramid in Fig. 3.12d. The corresponding equations must be determined through many geometric considerations, but in the end, all the geometric equations can be calculated analytically.

The cube has a side equal to $\frac{t}{\sqrt{2}}$, and its volume is obtained through eq. (3.28). The larger pyramid has a right triangle, with side $t\sqrt{2}$, as its base and a height h_{p1}, obtained through eq. (3.29). The angle derives from the inclination of the diagonal connecting the two opposite vertices of the cubic cell. The corresponding volume is calculated through eq. (3.30). The two smaller pyramids have a square base with side $\frac{t}{\sqrt{2}}$ and the same height; the volume of each of

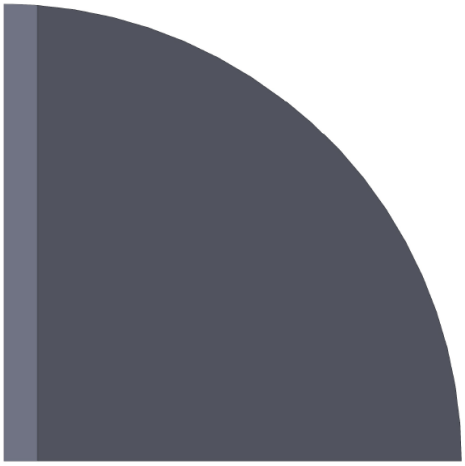

Figure 3.9: Fundamental element of the BCC vertex cut-out geometry.

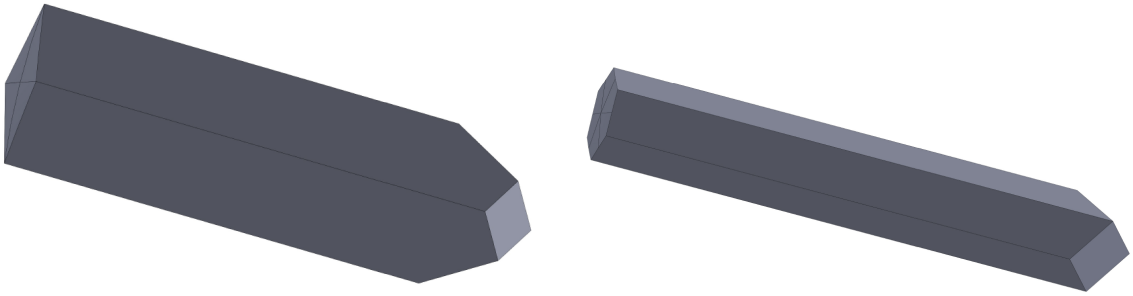

(a) Two-elements intersection.

(b) Three-elements intersection.

Figure 3.10: BCC unit cell - vertex cut-out: visualisation of the intersections.

them is determined through eq. (3.31). Finally, the last pyramid has a triangular base with sides $2t$ and $t \cdot \tan(30°)$, and a height equal to $\frac{t\sqrt{6}}{6}$. Its volume is obtained through eq. (3.32).

$$V_{cube} = \frac{\sqrt{2}}{4}t^3 \tag{3.28}$$

$$h_{p1} = \frac{\sqrt{3}}{9}tcos(arctan(\frac{1}{\sqrt{2}})) \tag{3.29}$$

$$V_{pyr_1} = \frac{\sqrt{3}}{9}t^3cos(arctan(\frac{1}{\sqrt{2}})) \tag{3.30}$$

$$V_{pyr_s} = \frac{\sqrt{2}}{6}t^3 \tag{3.31}$$

$$V_{pyr_2} = \frac{\sqrt{2}}{18}t^3 \tag{3.32}$$

The above equations, as can be seen, are analytical and do not present any approximation. The difference with the SolidWorks results lies in the part under the cylindrical surface. Indeed,

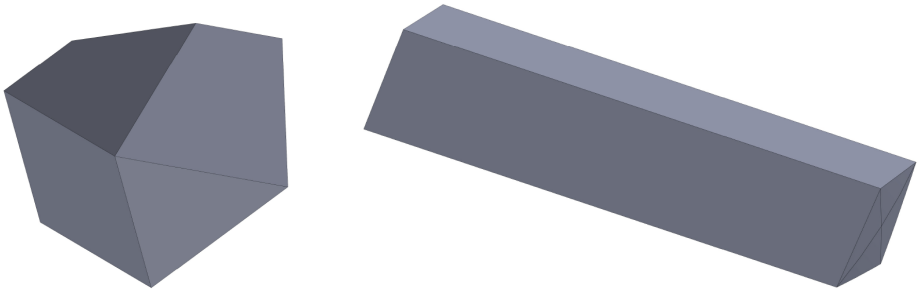

(a) Smaller subvolume. (b) Bigger subvolume.

Figure 3.11: BCC unit cell - vertex cut-out: 2E-Intersection main subvolumes.

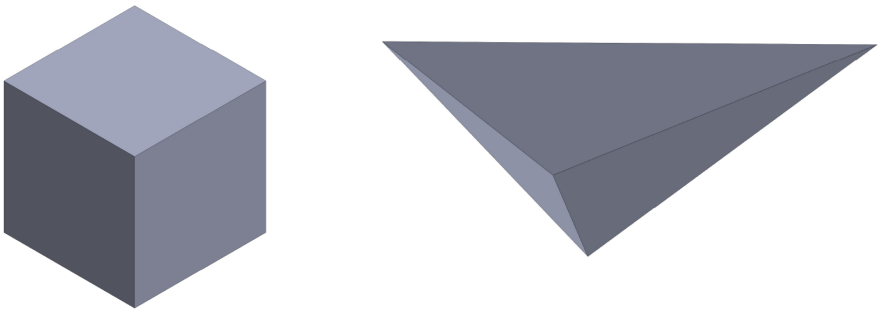

(a) Cube. (b) Larger triangular-base pyramid.

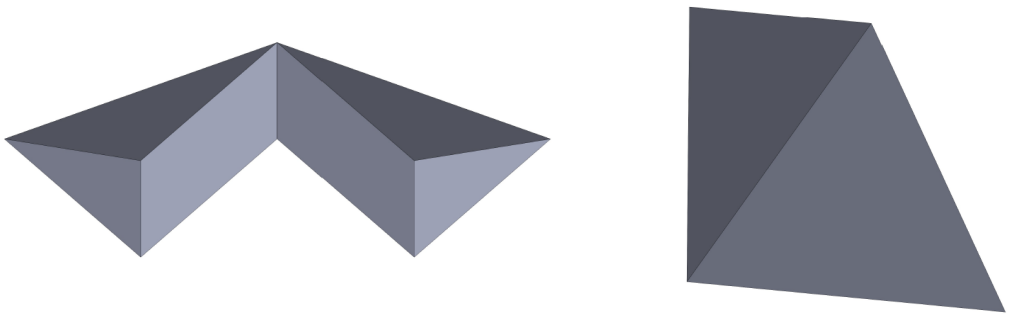

(c) Smaller square-base pyramids. (d) Triangular-base pyramid.

Figure 3.12: BCC unit cell - vertex cut-out, 2E-Intersection: further subdivision of the smaller subvolume.

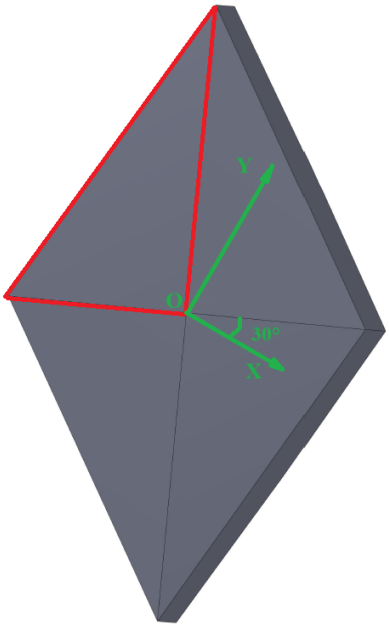

Figure 3.13: BCC unit cell - vertex cut out, 2E-Intersection: visualisation of the integration limits on xy plane.

here the intersection between the two cylinders is neglected and hence the volume to subtract is not determined through the consideration of the lower surface at each point. This is possible because the difference, as already described through tables and graphs, is extremely limited. The integration is performed through the volume integral of eq. (3.33), considering the integration limits shown in Fig. 3.13. The x variable goes from minus half the thickness to zero, the y variable ranges from the lower side, whose inclination is 30°, to the upper side, with an inclination of 120°, and z is constrained by the cylindrical surface $\sqrt{R_v^2 - y^2}$.

However, in this way, the volume is over-estimated, as z is considered starting from zero. Therefore, it is necessary to subtract the excess volume. This is calculated as the product of the base (four times the triangle that defines the integration limits) and the distance from the origin, which simple geometry allows to calculate as $h_d = \frac{\sqrt{6}}{2}t$. The resulting formula is given by eq. (3.34).

$$V_{sf} = 4 \int_{y_{\min}}^{y_{\max}} \int_{-\frac{t}{2}}^{0} \sqrt{R_v^2 - y^2}\, dx\, dy \tag{3.33}$$

$$V_{2E-Exc} = \sqrt{2}t^3 \tag{3.34}$$

Finally, the entire volume of the 2E-Intersection is given by the following equation:

$$V_{2E-Int} = V_{sf} + V_{cube} + V_{pyr_1} + V_{pyr_1} + V_{pyr_s} - V_{2E-Exc}; \tag{3.35}$$

A very similar procedure is followed for the 3E-Intersection. In Fig. 3.14, the main subdivision of the 3E-Intersection is shown, respectively in the left and right images, with a plane perpendicular to the longitudinal external edges. The smaller volume can be further split into the same cube as in the 2E-Intersection and the three pyramids shown in Fig. 3.15. The cor-

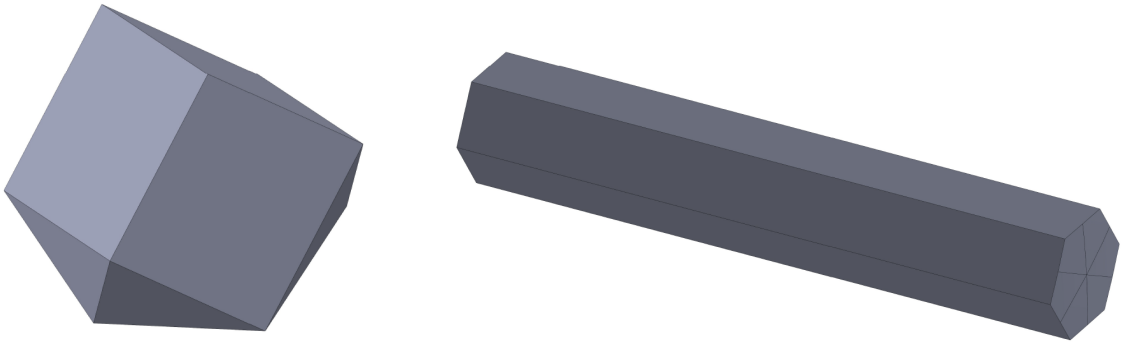

(a) Smaller subvolume. (b) Bigger subvolume.

Figure 3.14: BCC unit cell - vertex cut-out: 3E-Intersection main subvolumes.

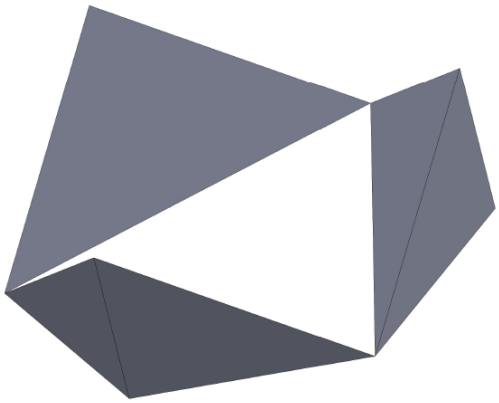

Figure 3.15: BCC unit cell - vertex cut out, 3E-Intersection: the three pyramids.

responding equations must be determined through many geometric considerations, but in the end, all the geometric equations can be calculated analytically.

The three pyramids have a triangular base with side t and height $\frac{t}{2}\tan(30°)$, and a height $h_{pexa} = \frac{\sqrt{6}}{6}t$. The corresponding volume (for a single pyramid) is calculated through eq. (3.36).

$$V_{pyr_{exa}} = \frac{\sqrt{2}}{72}t^3 \tag{3.36}$$

The above equations, as can be seen, are analytical and do not present any approximation. The difference with the SolidWorks results lies in the part under the cylindrical surface. Indeed, here the intersection between the three cylinders is neglected and hence the volume to subtract is not determined through the consideration of the lower surface at each point. This is possible because the difference, as already described through tables and graphs, is extremely limited. The integration is performed through the volume integral of eq. (3.37), considering the integration limits shown in Fig. 3.16. The x variable goes from zero to half the thickness, the y variable ranges from the lower side, whose inclination is $-30°$, to the upper side, with an inclination of $30°$, and z is constrained by the cylindrical surface $\sqrt{R_v^2 - y^2}$.

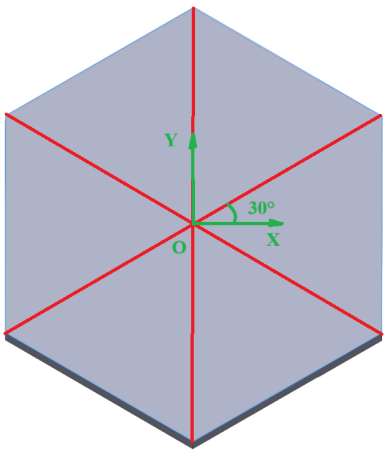

Figure 3.16: BCC unit cell - vertex cut out, 3E-Intersection: visualisation of the integration limits on xy plane.

However, in this way, the volume is over-estimated, as z is considered starting from zero. Therefore, it is necessary to subtract the excess volume. This is calculated as the product of the base (six times the triangle that defines the integration limits) and the distance from the origin, which simple geometry allows to calculate as $h_{exa} = \frac{\sqrt{6}}{3}t$. The resulting formula is given by eq. (3.38). However, in this way, only five sixths of the cube are removed, and therefore one sixth does not need to be restored.

$$V_{exa} = 6 \int_{y_{\min}}^{y_{\max}} \int_{0}^{\frac{t}{2}} \sqrt{R_v^2 - y^2}\, dx\, dy \tag{3.37}$$

$$V_{3E-Exc} = \frac{\sqrt{2}}{2} t^3 \tag{3.38}$$

Finally, the entire volume of the 3E-Intersection is given by the following equation:

$$V_{3E-Int} = V_{exa} + \frac{5}{6} V_{cube} + 3 * V_{pyr_{exa}} - V_{3E-Exc} \tag{3.39}$$

As the final equation, the vertex cut-out volume is determined by the sum of three times the fundamental element volume, minus three times the 2E-Intersection volume, plus once the 3E-Intersection volume.

$$V_{V-cut} = 3V_v - 3V_{2E-Int} + V_{3E-Int} \tag{3.40}$$

FCC Unit cell

In Fig. 3.17 it is possible to observe one the pieces removed from each face sheet, when extruding the vertex cut-out. Every face sheet presents 3 of these, every single tetrahedron 12 and hence each unit cell 96. It has a thickness t and is not symmetric with respect to the xy plane. Indeed, when cutting it along this plane, two portions with very similar configurations but different dimensions are obtained. They are referred to as *big* and *small*, shown in Fig. 3.18b and Fig. 3.18a, respectively. In the equations, the big portion is denoted with subscript 1 and 3, and the small with subscript 2 and 4. Despite being asymmetric along the xy plane, the shape has a plane of symmetry, so only half of its volume needs to be considered.

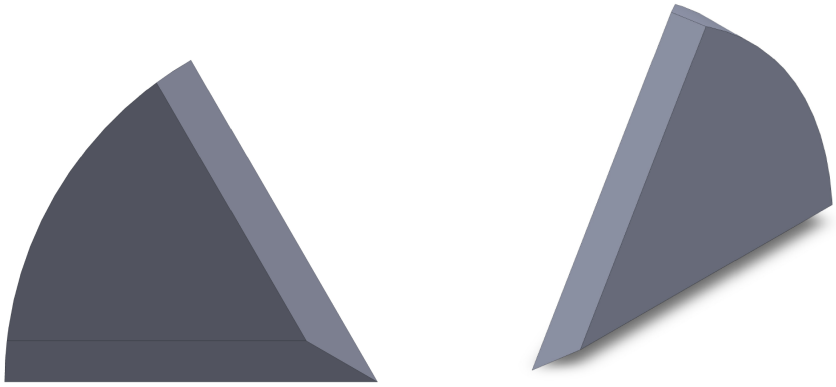

(a) Front view. (b) Inclined view.

Figure 3.17: FCC Unit cell - vertex cut-outs: shape of the removed material from each face sheet.

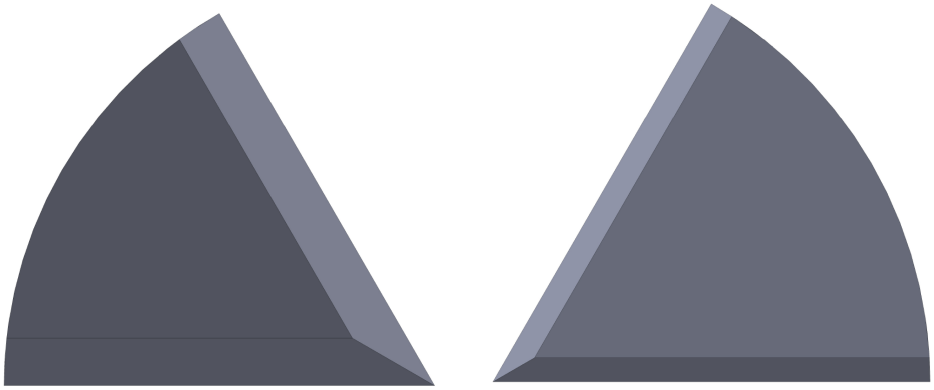

(a) Portion facing the inside volume of the tetrahedron, denoted as *small*.

(b) Portion facing the external environment, denoted as *big*.

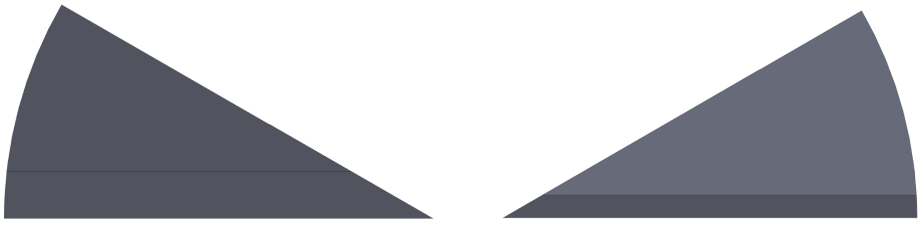

(c) Half of the *small* portion.

(d) Half of the big *big* portion.

Figure 3.18: FCC Unit cell - vertex cut-outs: shape of the removed material from each face sheet, additional images.

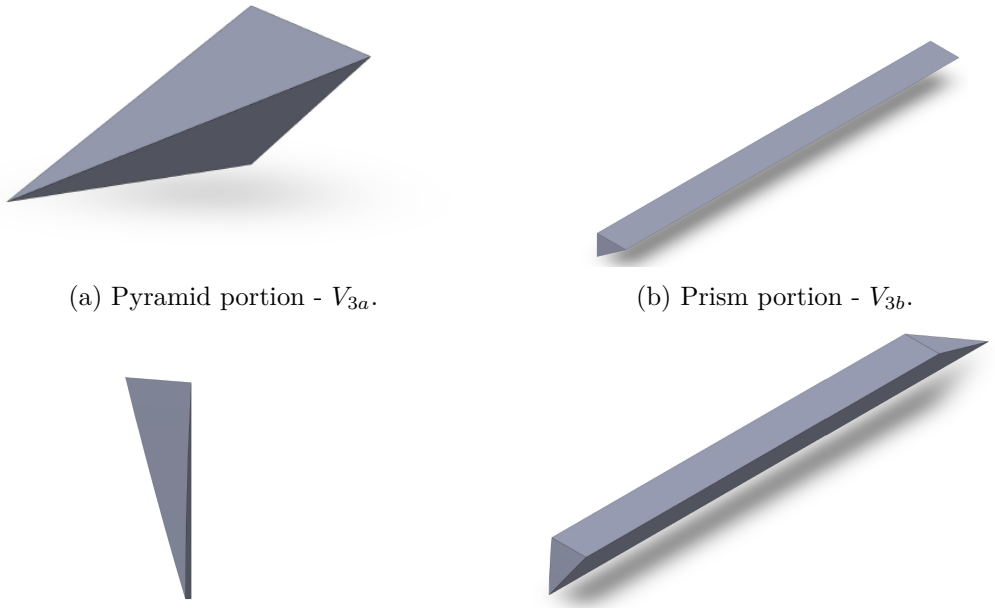

(a) Pyramid portion - V_{3a}.

(b) Prism portion - V_{3b}.

(c) Cap portion - V_{3c}.

(d) Combination of pyramid, prism and cap portion, which together form V_3.

Figure 3.19: FCC Unit cell - vertex cut-outs: shape of the subvolumes.

Each half can be split into two portions: one resembling a slice of a cylinder disk, and a slender portion. The slender portion is further divided into three pieces: the pyramid shown in Fig. 3.19a, the prism in Fig. 3.19b, and the remaining volume, referred to as the cap, in Fig. 3.19c. This approach is valid for both the small and the big portions; almost all the equations involved are formally the same, differing only in the dimension values. The pyramid volume is calculated in eq.(3.57), the prism volume in eq.(3.58), and the cap volume in eq.(3.60). The pyramid base is a right triangle with sides Sn_1 and dy_1, shown in Fig. 3.20c, corresponding to the horizontal polygon. Its area A_b is computed as half of the product of the two sides and the sine of the included angle. The pyramid height is half of the plate thickness. The prism has a rectangular base with sides dy_1 and R_{12}, where R_{12} is given by eq.(3.51). In that equation, R_v is reduced by the projection of Sn_1 along the x axis and X_v, the x coordinate where the axis of the extruding cylinder passes. The equations are valid even if an alternative choice to that of Ch. 2 is adopted, provided that it is along the radius and not closer; this allows minor flexibility without changing the code and derives from an initially different choice for the location of the extruding cylinder axis. For the prism, as for the pyramid and cap, the height is half the thickness. Finally, the cap volume calculations follow the same approach as eq.(3.20). It is necessary to identify the limits of integration and then compute a triple integral. The x coordinate goes from dx_1 to X_{ff}, lying on the external circumference described by eq.(3.52). The y coordinate is limited by Y_v and the external circumference, and the z coordinate varies from 0 to $(y - Y_v)\tan\delta$. The integrals are numerically evaluated in MATLAB.

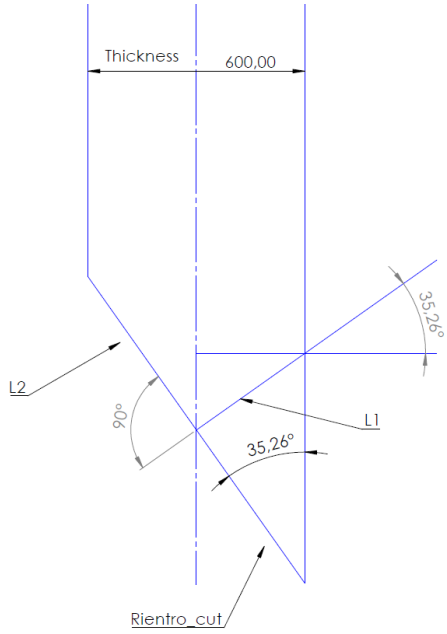

(a) Thickness and slope visualisation.

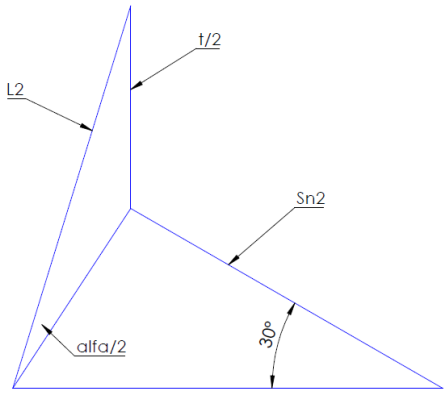

(b) Slope-related calculation for the *big* portion.

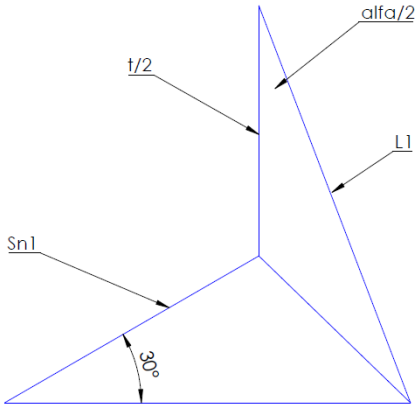

(c) Slope-related calculation for the *small* portion.

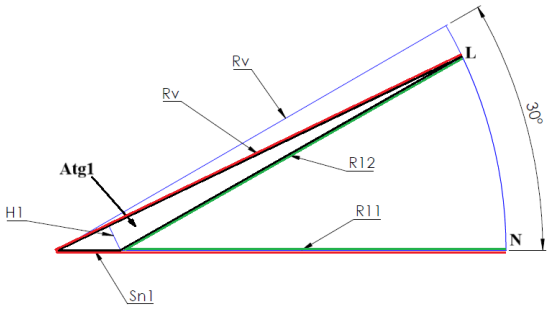

(d) Front visualisation for *Atg* area calculations.

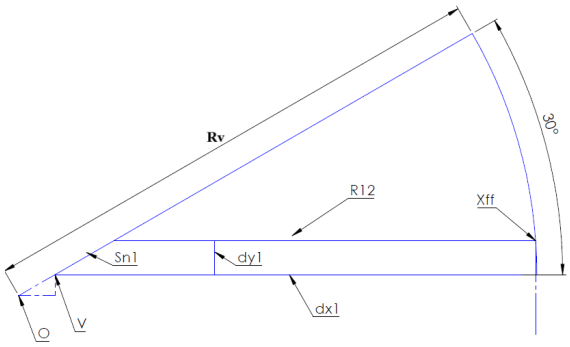

(e) Front visualisation for the determination of the limits of integration.

Figure 3.20: FCC Unit cell - vertex cut out: sketches for dimension calculations.

$$
\begin{aligned}
l_1 &= Indent_{cut} * tan\frac{\alpha}{2} \\
&= \frac{t}{2 * cos\frac{\alpha}{2}}
\end{aligned} \tag{3.41}
$$

$$
\begin{aligned}
l_2 &= Indent_{cut} \\
&= \frac{t}{2 * sin\frac{\alpha}{2}}
\end{aligned} \tag{3.42}
$$

$$
\begin{aligned}
Sn_1 &= l_1 * \frac{sin\frac{\alpha}{2}}{sin(30)} \\
&= \frac{t}{2 * cos\frac{\alpha}{2}} sin(30) \\
&= t * tan\frac{\alpha}{2}
\end{aligned} \tag{3.43}
$$

$$
\begin{aligned}
Sn_2 &= l_2 * \frac{cos\frac{\alpha}{2}}{cos(30°)} \\
&= t * cotan\frac{\alpha}{2}
\end{aligned} \tag{3.44}
$$

$$
\begin{aligned}
dy_1 &= l_1 * sin\frac{\alpha}{2} \\
&= \frac{t}{2} tan\frac{\alpha}{2}
\end{aligned} \tag{3.45}
$$

$$
\begin{aligned}
dy_2 &= l_2 * cos\frac{\alpha}{2} \\
&= \frac{t}{2} cotan\frac{\alpha}{2}
\end{aligned} \tag{3.46}
$$

$$
\begin{aligned}
dx_1 &= \sqrt{R_v^2 - (Y_v + dy_1)^2} \\
&= \sqrt{\frac{t}{tan\frac{\alpha}{2}}\Big[6Rsp + \frac{t}{tan\frac{\alpha}{2}} - Y_v tan^2\frac{\alpha}{2} - \frac{t}{4} tan^3\frac{\alpha}{2}\Big] + (9Rsp^2 - Y_v^2)}
\end{aligned} \tag{3.47}
$$

$$
\begin{aligned}
dx_2 &= \sqrt{R_v^2 - (Y_v + dy_2)^2} \\
&= \sqrt{\frac{t}{tan\frac{\alpha}{2}}\Big[6Rsp + \frac{3}{4}\frac{t}{tan\frac{\alpha}{2}} - Y_v\Big] + (9Rsp^2 - Y_v^2)}
\end{aligned} \tag{3.48}
$$

$$
\tag{3.49}
$$

$$
\begin{aligned}
R_{12} &= dx_1 - Sn_1 * cos(30) - X_v \\
&= dx_1 - \frac{\sqrt{3}}{2} tan\frac{\alpha}{2} t - X_v
\end{aligned} \tag{3.50}
$$

$$
\begin{aligned}
R_{22} &= dx_2 - Sn_2 * cos(30) - X_v \\
&= dx_2 - \frac{\sqrt{3}}{2} cotan\frac{\alpha}{2} t - X_v
\end{aligned} \tag{3.51}
$$

$$
(x - X_v)^2 + (y - Y_v)^2 = R_v^2 \tag{3.52}
$$

$$
X_{ff} = X_v + \sqrt{R_v^2 - Y_v^2} \tag{3.53}
$$

$$
\begin{aligned}
\delta_1 &= arctan\frac{\frac{t}{2}}{dy_1} \\
&= arctan(cotan\frac{\alpha}{2}) \\
&= \frac{\pi}{2} - \frac{\alpha}{2}
\end{aligned} \tag{3.54}
$$

$$
\delta_2 = \frac{\alpha}{2} \tag{3.55}
$$

$$
\begin{aligned}
V_{3a} &= \frac{1}{3} A_b * h \\
&= \frac{1}{6} Sn_1 * dy_1 * sin(60) * \frac{t}{2} \\
&= \frac{\sqrt{3}}{48} t^3 * tan^2(\frac{\alpha}{2})
\end{aligned} \tag{3.56}
$$

$$
\begin{aligned}
V_{4a} &= \frac{1}{3} A_b * h \\
&= \frac{1}{6} Sn_2 * dy_2 * sin(60) * \frac{t}{2} \\
&= \frac{\sqrt{3}}{48} t^3 * cotan^2(\frac{\alpha}{2})
\end{aligned} \tag{3.57}
$$

$$
\begin{aligned}
V_{3b} &= A_b * h \\
&= \frac{dy_1 * \frac{t}{2}}{2} * R_{12} \\
&= \frac{t^2}{8} tan\frac{\alpha}{2} R_{12}
\end{aligned}
$$

$$
\begin{aligned}
V_{4b} &= A_b * h \\
&= \frac{dy_2 * \frac{t}{2}}{2} * R_{22} \\
&= \frac{t^2}{8} cotan\frac{\alpha}{2} R_{22}
\end{aligned} \tag{3.58}
$$

$$V_{3c} = \int_0^{(y-Y_v)*tan\delta_1} dz \int_{Y_v}^{\sqrt{R_v^2-x^2}} dy \int_{dx_1}^{X_{ff}} dx \tag{3.59}$$

$$V_{4c} = \int_0^{(y-Y_v)*tan\delta_2} dz \int_{Y_v}^{\sqrt{R_v^2-x^2}} dy \int_{dx_2}^{X_{ff}} dx \tag{3.60}$$

Once these structures are analysed, it remains to compute the volume of those slices, which we might be induced to think are circumferences, but actually are not. Indeed, in Fig. 3.20d, it appears that R_{11} and R_{12} are two different quantities. Consider the slice created by R_v, the arc of circumference between the points L and N, and the side given by the sum of R_{11} and Sn_1. This is exactly a slice of a cylindrical disk, as the sum aforementioned is equal to R_v when the vertex V and the origin O coincide; otherwise, some adjustments have to be made. In the extruded cut, this slice does not have a constant thickness because of the portion highlighted as Atg_1 in Fig. 3.20d. However, let us pretend it is so. The curvilinear triangle with the red sides is actually a real slice of a circumference, because both its sides have an equal length of R_v. However, we are interested in determining the surface bounded by the green segments, which is obtained by subtracting Atg_1 from the larger slice. The triangle with black sides is an extension that can be calculated in two different ways, as done in eq.(3.62). Exploiting this characteristic, it is possible to invert the formulas to determine h_1, which is used to compute the angle γ. Finally, the extension of the surface we need is computed and multiplied by half of the thickness to get the volume. The same procedure, with different dimensions, is employed for the opposite side.

$$\begin{aligned} Atg_1 &= \frac{R_v * h1}{2} \\ &= \frac{Sn_1 * R_{12} * sin(30°)}{2} \\ &= \frac{t}{4} tan\frac{\alpha}{2} R_{12} \end{aligned} \tag{3.61}$$

$$\begin{aligned} Atg_2 &= \frac{R_v * h2}{2} \\ &= \frac{Sn_2 * R_{22} * sin(30°)}{2} \\ &= \frac{t}{4} cotan\frac{\alpha}{2} R_{22} \end{aligned} \tag{3.62}$$

$$\begin{aligned} h_1 &= \frac{2 * Atg_1}{R_v} \\ &= \frac{t}{2} tan\frac{\alpha}{2}\frac{R_{12}}{R_v} \end{aligned} \tag{3.63}$$

$$\begin{aligned} h_2 &= \frac{2 * Atg_2}{R_v} \\ &= \frac{t}{2} cotan\frac{\alpha}{2}\frac{R_{22}}{R_v} \end{aligned} \tag{3.64}$$

$$\gamma_1 = arcsin\frac{h_1}{Sn_1} \tag{3.65}$$

$$\gamma_2 = arcsin\frac{h_2}{Sn_2} \tag{3.66}$$

$$\begin{aligned} V_1 &= t\left(\frac{\gamma_1}{2}R_v^2 - Atg_1\right) \\ &= \frac{t}{4}\left(2\gamma_2 R_v^2 - tan\frac{\alpha}{2}R_{12}t\right) \end{aligned} \tag{3.67}$$

$$\begin{aligned} V_2 &= t\left(\frac{\gamma_2}{2}R_v^2 - Atg_2\right) \\ &= \frac{t}{4}\left(2\gamma_2 R_v^2 - tan\frac{\alpha}{2}R_{22}t\right) \end{aligned} \tag{3.68}$$

$$\tag{3.69}$$

Finally all volumes, from V_1 to V_{4c} are put together, has the sum constitutes the volume of the removed material. There are twelve of this elements for each tetrahedron, 96 for each FCC unit cell.

3.3 Specimens design

In this section the design of the specimens is described in details. Initially, in the first paragraph, the attention is posed on the *general* design: this means that the approach that guided the final configurations and the main features are common to all the samples. However, for reasons that are going to be described, some adjustments have to be made in order to achieve the desired densities or to lead the failure location within the gauge section, as prescribed by every standard that can be consulted. Therefore, the second paragraph deals with the design of *specific* specimens.

3.3.1 General specimen design

In the design of the specimens both the guidelines extracted from the standards, the insight highlighted by the academic papers and the constraints posed by the specific research I am working on, guided the final choice. In this research the constraints are posed by the unit cell size and the additive manufacturing process chosen for fabrication. All the architectures studied, hence Primitive and Gyroid for TPMS, and BCC and FCC for plate-based lattices, have been designed with a unit cell size of 10x10x10 mm^3, selected for coherence with previous research activities carried out at LSM. Indeed, the interest lies in lower relative densities and due to the machine which is supposed to be use for production, there is a practical lower limit of around 0.120 mm for stable, printable wall thickness. Choosing a 10 mm cell size allows to achieve the targeted low densities without violating this manufacturing constraint. Concerning the production phase, an EOS M290 (EOS GmbH, Germany) is supposed to be used, with AlSi10Mg aluminium alloy powder. It implements the selective laser melting technology and has a 250x250 mm^2 printing plate, which mainly limits the sample longitudinal dimension.

Finally, given the will of studying very lightweight structures, 10, 15 and 20% relative densities have been chosen. In addition, to assess the mechanical properties of extremely lightweight configurations, at the limit of printability, cells with a wall thickness of 0.120 mm have been modelled. Details are reported in Tab.3.3, 3.4, 3.5 and 3.6.

Rel. density [%]	Iso-value
4.30	0.1500
10.0	0.3496
15.0	0.5244
20.0	0.6990

Table 3.3: Primitive unit cell: relative densities and the corresponding iso-values for the test section.

Rel. density [%]	Iso-value
4.87	0.1500
10.0	0.3096
15.0	0.4640
20.0	0.6181

Table 3.4: Gyroid unit cell: relative densities and the corresponding iso-values for the test section.

Rel. density [%]	Thickness [mm]	R_v [mm]	R_s [mm]
8.32	0.120	1.7611	0.7671
10.0	0.146	1.8001	0.7801
15.0	0.229	1.9246	0.8216
20.0	0.322	2.0641	0.8681

Table 3.5: BCC unit cell: relative densities and the corresponding thicknesses and cut-outs radii for the test section.

Rel. density [%]	Thickness [mm]	R_v [mm]
6.50	0.120	1.6697
10.0	0.193	1.7729
15.0	0.314	1.9441
20.0	0.472	2.1675

Table 3.6: BCC unit cell: relative densities and the corresponding thicknesses and cut-outs radii for the test section.

In order to assess the influence of edge effects and transition zones, simulations on reduced-dimension specimens have been carried out for all cell architectures, but only for a single density. Although the detailed description of this phase is postponed to Ch. 4, as the FE model needs

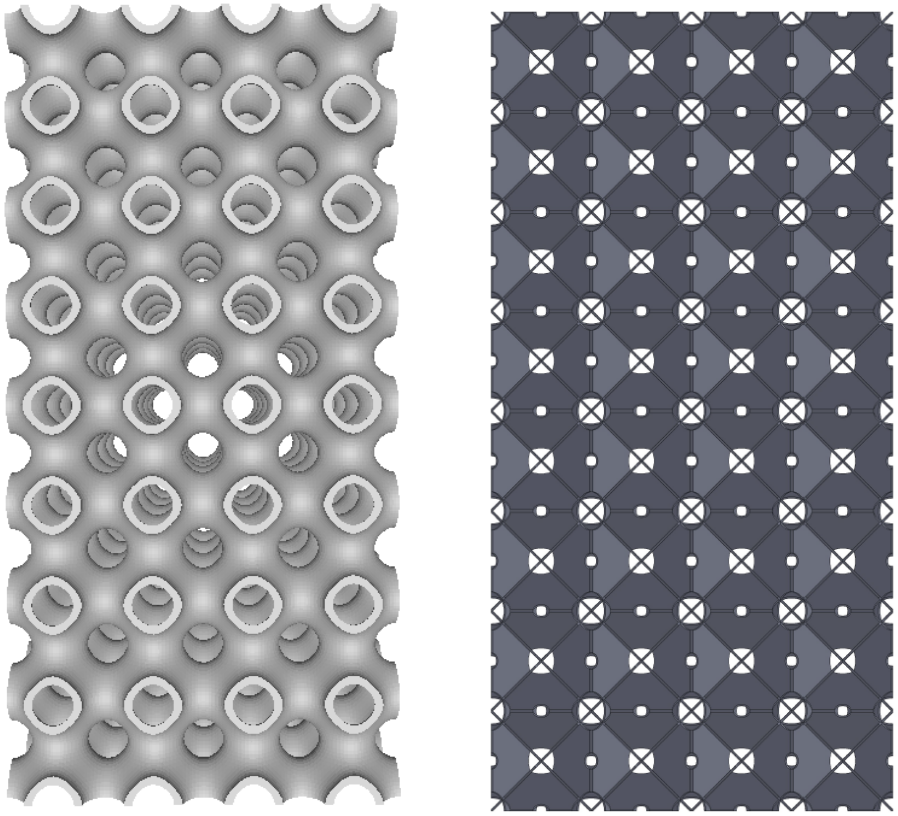

(a) Primitive unit cell. (b) BCC unit cell.

Figure 3.21: Full dimension test section examples for two different type of cells.

to be presented, the results will be briefly foreshadowed at this stage. All the specimens simulated are characterised by failure initiations within the specimens rather than at the edges, which are relatively unloaded, even though the specimens have a square cross-section. On the opposite side, the design and fabrication of cylindrical samples, similar to those prescribed by international standards for testing bulk materials, is potentially possible but would lead to poorer outcomes both in terms of printing quality and alignment with the research objectives. Specifically, cylindrical samples could be printed horizontally, but this would require additional supports that must be removed after fabrication. This process could negatively affect the external surface quality and, consequently, degrade the mechanical properties, especially fatigue-related ones. In the context of obtaining cylindrical specimens, two main strategies can be identified. The first is to model a structure with a square cross-section and then cut and extract the desired cylindrical volume. Nonetheless, this approach does not eliminate the presence of external edges; while the original edges disappear, new ones are created, leading to a mixture of full unit cells inside and partial ones at the external surface. Such configuration could potentially result in highly non-uniform mechanical properties. The second possibility is to arrange the cells so that they directly form a circular cross-section. Nevertheless, this choice introduces additional issues, as the cells would be distorted and deformed compared to their initial configuration, thereby altering the properties that the research aims to investigate. In conclusion, for these reasons, and based on the support of FE simulations, it has been decided to rely on square cross-section samples.

For the purpose of obtaining reliable mechanical properties, a minimum of four unit cells

per direction has been chosen, in agreement with previously cited studies [65, 79, 89]. The combination of this value with the acceptable ratios among the three main sample dimensions, as prescribed by standards, guided the choice of the test section volume, which resulted in 4x4x8 unit cells. A couple of examples are shown in Fig. 3.21. Indeed, for the necessity of keeping the specimens printable, which forces the minimization of their length, the lower height-to-width ratio has to be adopted. For instance, due to dimension constraints, flat samples cannot be employed. When considering a thickness of four cells, a width of at least double, which then must be multiplied by two to get the minimum height, the specimen would easily exceed the machine plate dimensions, even prior to the application of transition regions and grips.

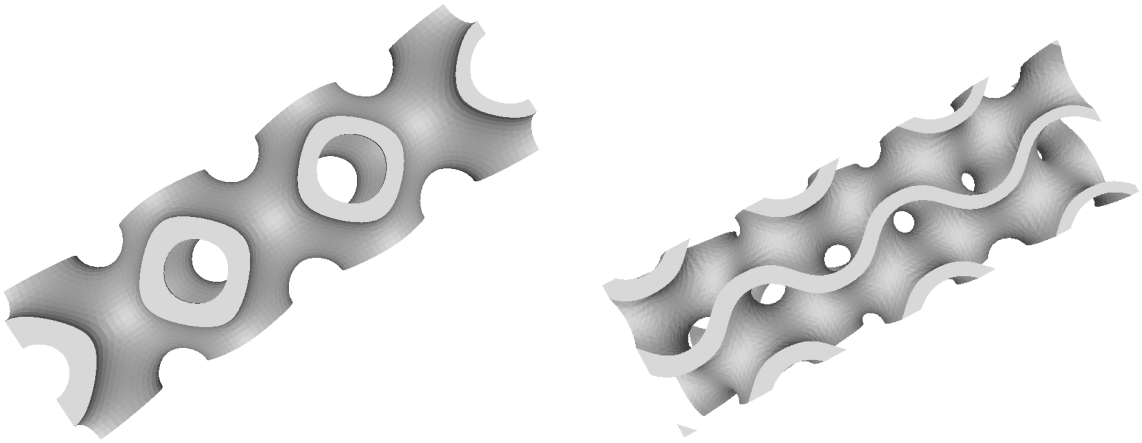

(a) Primitive unit cell. (b) Gyroid unit cell.

Figure 3.22: Example of columnar (1x3 cells) transition zones for two different types of cells.

Transition zones are another important aspect to address. The general approach used to design them is quite simple: a density gradient is applied to increase the stiffness and strength of these regions compared to the test section. Specifically, these linking sections are designed to gradually double the density, from the test section interface to the grip interface[3]. For Primitive and Gyroid specimens, the density gradient is linear and the iso-value increases continuously, thanks to the possibility of directly implementing the gradation using the mathematical description of these structures; a couple of examples are shown in Fig. 3.22. In contrast, BCC and FCC plate-based configurations are not described by mathematical functions, and therefore it is practically impossible to grade them continuously along their length. For this reason, a stepwise approach has been chosen. These cells have been cut through a horizontal plane into two equal volumes, an upper and a lower one, exploiting their symmetry. Then, different thickness values (and corresponding cut-outs radii) have been applied to each part, and the process is repeated for all the transition layers[4]. In practice, this theoretically straightforward process is not fully applicable to all shapes due to cut-outs, which limit the maximum relative density achievable by BCC and FCC unit cells to 37.33% and 24.63%, respectively, as can be seen from the graphs in Fig.3.23. Moreover, simulations of BCC configurations highlighted the need for adjustments to the geometry of these cells. The assessment and selection of the final design required significant time and computational effort, with some compromises being necessary. Nonetheless, transition zones serve a specific purpose: to prevent fracture at the interface between them and the grips

[3]For plate-based lattices, the mechanism is exactly this, while for TPMS architectures the iso-value, rather than the density, is doubled. However, these two parameters correspond closely, so that, as a rule of thumb, doubling the iso-value leads to doubling the relative density.

[4]A detailed description of this process can be found in Par. 3.4, while the MATLAB codes are in App. C.

or test section. Therefore, the adjustments made do not affect the quality of the results. ASTM norms provide guidance for the length of transition zones based on the specimen diameter. Specifically, ratios between the radius of the fillet and the gauge section diameter are specified, as well as ratios for the grip and gauge diameters. However, the printability of these samples must also be considered. As shown in Fig. 3.24, the global length required would be excessive. As a first trial, two cell layers for the transition zones, as in [47], have been considered and simulated.

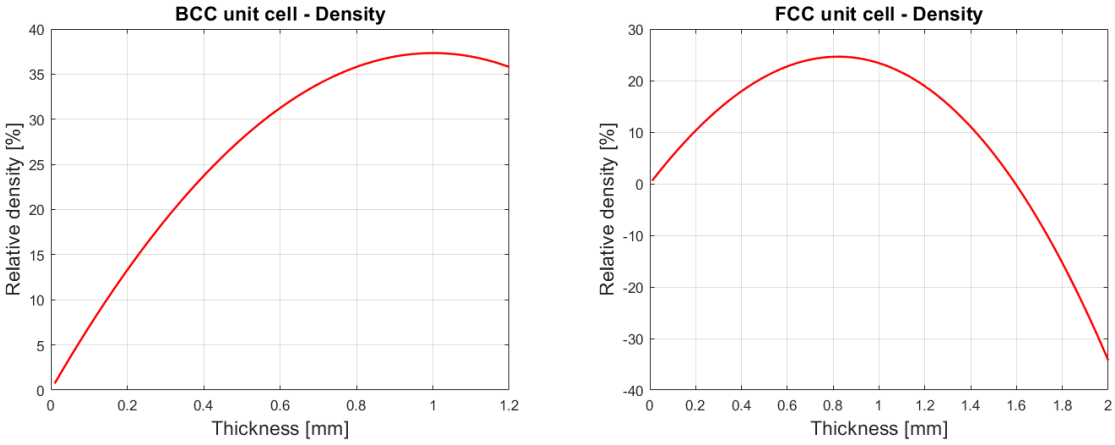

(a) BCC unit cell.

(b) FCC unit cell.

Figure 3.23: Graphic visualisation of the relation between relative density and thickness for the original designed of BCC and FCC plate-based cells.

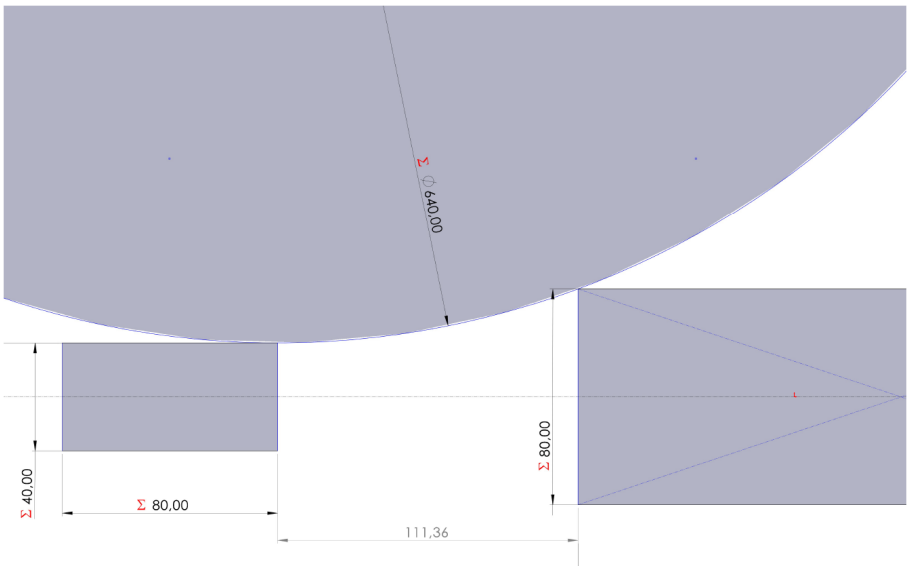

Figure 3.24: Blending fillet as it would be applying ASTM E466-21.

According to the simulation results, Gyroid and FCC cells do not show any issues, while Primitive and BCC cells exhibit minor problems. Specifically, although the main failure, that is the one leading to complete specimen failure, occurs entirely within the test section, secondary fractures appear near the interface between the test section and the transition, even if still within

the test section[5]. To address these issues, simulations with three-layer transition sections were performed, showing no significant changes in the structural behavior. Consequently, since the main failure complies with all ASTM recommendations and post-failure results are not fully reliable, a double-density approach with three-layer transition zones has been implemented, using a lower density gradient compared to the two-layer configuration.

Two different grips geometries have been designed: a traditional one and an innovative one, whose effectiveness must be determined through experimental tests. The first grip, shown in Fig. 3.25a, is composed of a 4 mm-thick plate, a truncated cone with a larger radius of 20 mm and a smaller radius of 10 mm, and a cylindrical end 30 mm long. The plate has the same dimensions as the samples' cross section, and the truncated cone lateral surface has an inclination of 45°, which allows it to be printed without additional supports. On the other side, this choice ensures a smooth reduction of the cross-sectional area. The modified version, shown in Fig. 3.25b, is designed for tensile tests to allow better alignment of the samples during the initial stages of testing, when the forces applied by the clamping mechanism are still quite low. Distortions due to residual stresses may arise during production, and especially for low-density as-built specimens, these could lead to failure due to bending moments. Xin et al. [14] wrote that under axial loading, it typically happens that the outermost cells of lattice materials fail under the effect of bending loads caused by misalignment. This type of grip is intended to mitigate the effects of such distortions. The sphere radius is 12.5 mm, corresponding to a 25% increase compared to the cylinder radius. The flat surfaces visible in the figure result from the intersection of the sphere with a horizontal plane, producing a circle equal to the cylinder cross section.

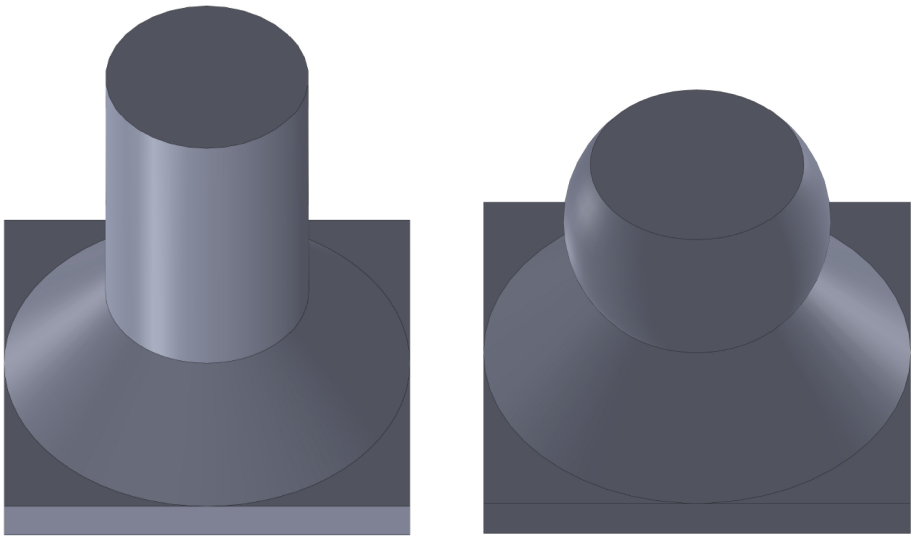

(a) Grip with cylindrical end. (b) Grip with spherical end.

Figure 3.25: Geometry of the designed grips.

In conclusion, the designed samples are 4x4x14 unit cells (one is 13), with a test section of 4x4x8 unit cells, whose proportions and mechanical behaviour are expected to conform to ASTM standards, and transition zones of 4x4x3 unit cells (one is 2.5).

[5]Post-failure results are not completely reliable, as explained in Ch. 4.

3.3.2 Specific specimens design

In this paragraph, the specific design of each specimen is described. In Fig. 3.26 and 3.27, the test sections of the 15% relative density specimens are shown. There is not much to add, except for the Primitive cell. The height of that sample corresponds to 8 cells, as in all the other configurations, but it starts and ends with half of a cell. In this specific example, it represents the interface between the test section and the transition regions, but the same general configuration also characterises the interface between the transition regions and the grips. Simulations have been conducted and show that failures occur within the gauge section even when the interface is a full layer instead of half a layer. Nonetheless, this configuration is preferable, as it seems less prone to cause detachment from the grips.

The specific characteristics of the transition regions differ significantly. Primitive and Gyroid specimens are designed exactly as described in Par. 3.3.1, without any adjustment. In contrast, plate-based specimens require much more attention. As already mentioned, the BCC architecture, with the designed cut-outs, has a maximum achievable relative density. This characteristic only influences the design of the transition region in the 20% specimen. When doubling the relative density, the 40% value cannot be reached. However, due to the limited difference (less than 7%) and considering all the points discussed in Par. 3.3.1, the last layer simply has a relative density of 37.33%, corresponding to a 1.00 mm thickness, instead of 40. Relative density limitations have a greater impact on FCC architectures. Specimens with 6.50 and 10% relative density follow the general density gradient approach exactly. The 15% specimen was initially designed to reach a 30% relative density at the interface with grips, implementing three, instead of four, vertex cuts per cell. Finally, the 20% relative density specimen is designed with different cut-outs to achieve a higher density. For this sample, the cut-outs are cylindrical holes with radius $Rsp = 0.500$ mm, placed in the middle of each plate, as in other studies [61, 77, 80].

Several simulations have been run for BCC-based specimens. The vertex cut-outs guide the failure location, and it was necessary to move them further from the interface between the transition and test regions. To achieve this, three main solutions were analysed. First, a layer was added to the initial two-layer transition configuration to assess whether a lower density gradient (the same density step spread over six layers instead of four) would be beneficial. This solution provided no significant improvement; however, it was adopted for the reasons discussed in Par. 3.3.1. As a second trial, the edges between the touching half-cells were chamfered to reduce stress concentration in these areas. Again, no significant benefits were observed. It is worth mentioning that, due to the very small dimensions of these geometrical details, only the FE simulations could be influenced, while the difference virtually disappears because of the finite sensitivity of the printing apparatus. Finally, considering that the vertex cuts were responsible for the unwanted behaviour, a very particular design was chosen, as shown in Fig. 3.28. Starting from the test section interface, the first layer has the same dimensions as the test section; the second layer also has the same thickness and cuts' radius, but the external edges are continuous. This feature is achieved by implementing the extruded cuts only on the inclined plates and not on the vertical ones. From the third to the sixth layer, the geometry follows that of the second layer, with modified edges, and the dimensions change. The corresponding thickness and cuts' radius are computed considering the initial density as that of the test section and the final density as double, but splitting the gap into only four steps. The code does not change and does not account for the geometry variations; it is therefore the same for all BCC samples' densities.

As previously stated, FCC-based specimens with 15 and 20% relative density are subjected to geometry variations. In this case, the implemented codes take the geometry variations into

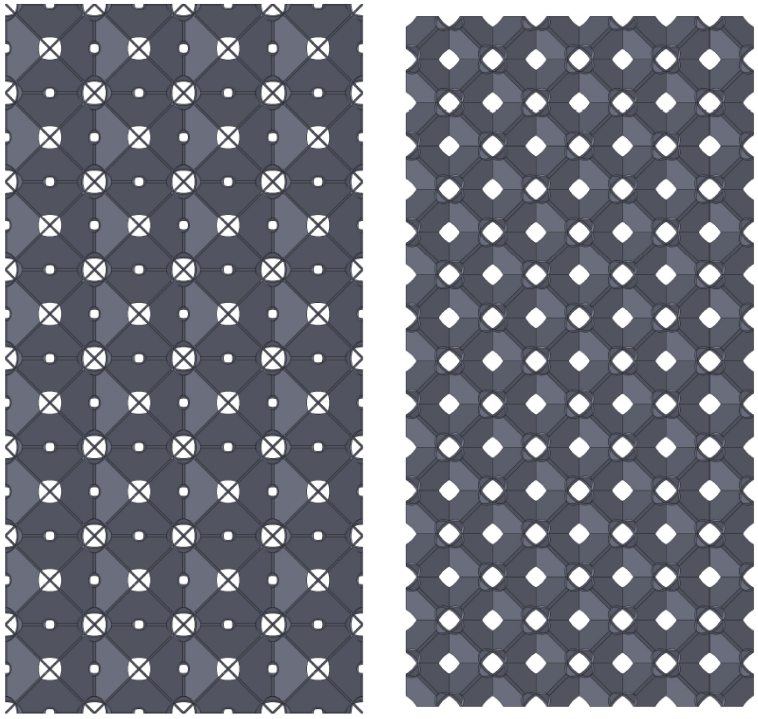

(a) BCC unit cell. (b) FCC unit cell.

Figure 3.26: Plate-based architectures: full dimension test sections for 15% relative density.

account. This choice was made to reduce the differences with the 6.50 and 10% relative density configurations, reflecting the intention not to change both the geometry and the code.

For the 15% relative density, two adjustments have been made. A column of the transition region (a sixteenth of it) is shown in Fig. 3.29a. As can be seen, each tetra, which corresponds to an eighth of the unit cell, has only three vertex cuts. The external one has been removed. This procedure allows the basic geometry to remain almost unchanged while reaching the 30% relative density value. Indeed, this configuration has a maximum achievable density of 30.79%, as shown in Fig. 3.29b. In addition, the height of only this transition region is set to 2.5 unit cells, to ensure a better interface with grips. As a result, the entire specimen is 10 mm shorter than all the others. Indeed, a higher density not only implies thicker plates but also larger cut-outs, and the interaction of these geometric features could drastically reduce the interface area between the cells and the grips. To avoid the risk of failure at these locations, this limitation has been introduced. The final relative density is therefore 27.5 instead of 30%, because the sixth layer has been removed.

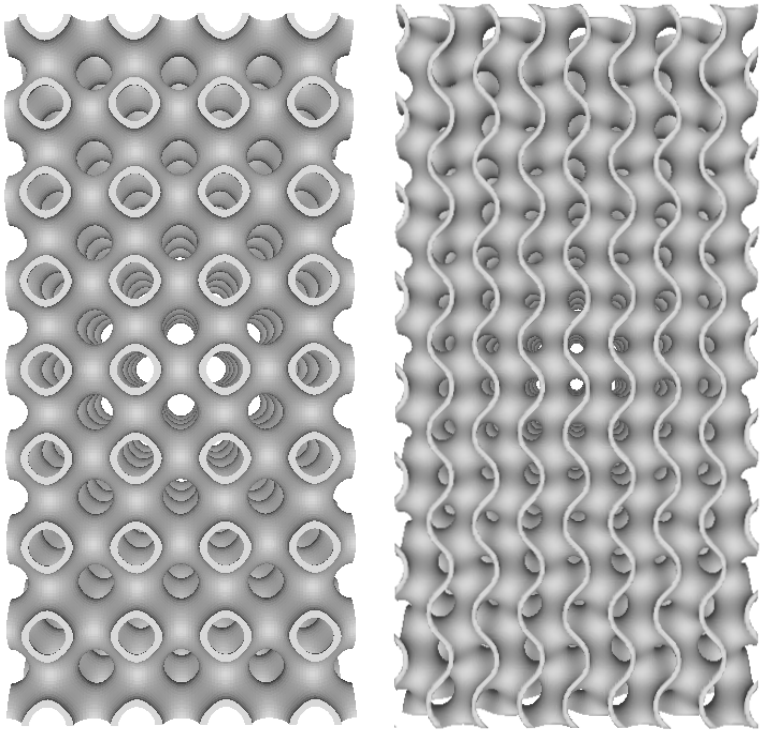

(a) Primitive unit cell. (b) Gyroid unit cell.

Figure 3.27: TPMS architectures: full dimension test sections for 15% relative density.

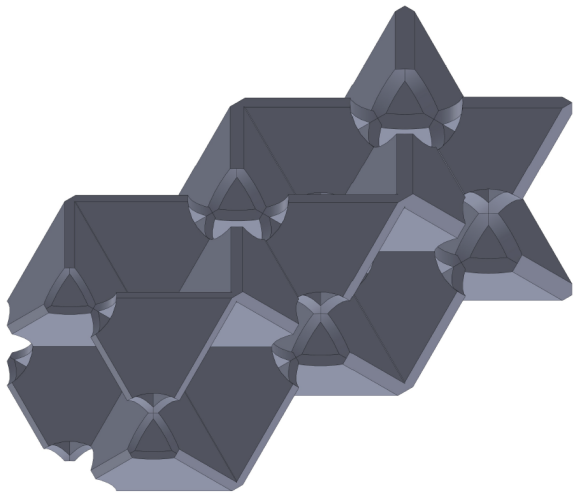

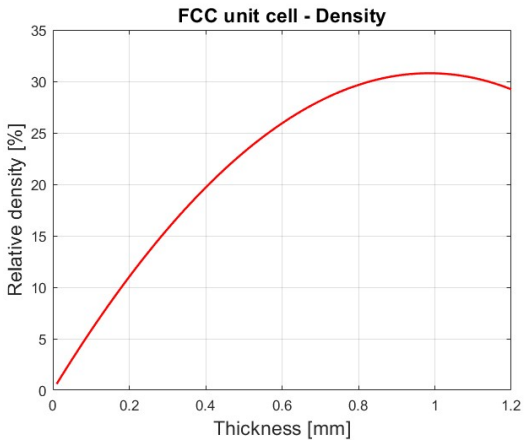

(a) Example of columnar (1x2.5 cells) transition zone, with only three cut-outs for each tetrahedron.

(b) Graphic visualisation of the relation between relative density and thickness, when only three cut-outs for each tetrahedron are employed.

Figure 3.29: FCC unit cell - 15% rel. density specimen: transition region and density limitation.

For the 20% relative density, the transition zone structure is as follows: the first layer still includes the vertex cuts, although only two of them. Such a design choice is required by the need to ensure a smooth interface with the test section, avoiding an excessively abrupt transition. The thickness remains unchanged compared to that of the test section, resulting in a relative

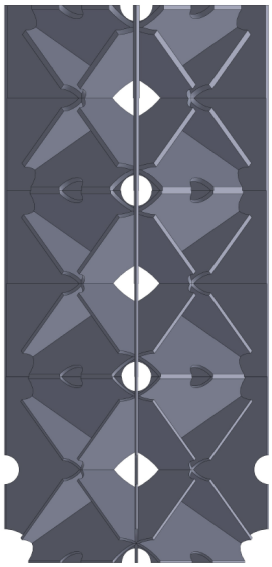

Figure 3.28: BCC unit cell: example of columnar (1x3 cells) transition zone with continuous external edges.

density of 24.44%. The remaining layers, from the second to the sixth, have cut-outs in the middle of each plate, as previously described. Their relative density is calculated considering this feature, and the double-density approach is implemented in its general form. A column of the transition region (a sixteenth of it) is shown in Fig. 3.30a. This configuration has a maximum achievable density of 89.93%[6].

(a) Example of columnar (1x3 cells) transition zone, where cut-outs are placed in the middle of each face sheet.

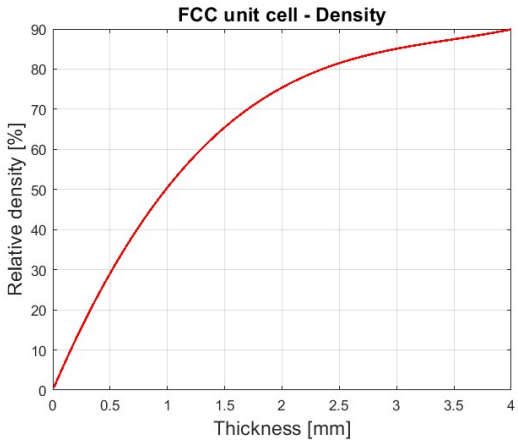

(b) Graphic visualisation of the relation between relative density and thickness, when cut-outs are placed in the middle of each face sheet.

Figure 3.30: FCC unit cell - 20% rel. density specimen: transition region and density limitation.

Finally, in Tab. 3.7, a summary of the main geometric and physical characteristics of all the designed specimens is presented. The number of cells and dimensions are given in the following

[6]This result has been obtained by applying a maximum thickness-to-cell-side ratio of 0.4, limit found by researchers at LSM.

order: the first two numbers correspond to the in-plane dimensions of the cross-section, while the third refers to the longitudinal length. The cell size is 10*10*10 mm^3.

CELL	**Test section rel. density** [%]	**Test section dimensions** [N. of cells]	**Trans. zone end rel. density** [%]	**Trans. zone dimensions** [N. of cells]	**Total length** [mm]
BCC	8.32	4*4*8	16.6	4*4*3	140
	10.0	4*4*8	20.0	4*4*3	140
	15.0	4*4*8	30.0	4*4*3	140
	20.0	4*4*8	37.3	4*4*3	140
FCC	6.50	4*4*8	13.0	4*4*3	140
	10.0	4*4*8	20.0	4*4*3	140
	15.0	4*4*8	30.0	4*4*2.5	130
	20.0	4*4*8	40.0	4*4*3	140
Primitive	4.30	4*4*8	8.60	4*4*3	140
	10.0	4*4*8	20.0	4*4*3	140
	15.0	4*4*8	30.0	4*4*3	140
	20.0	4*4*8	40.0	4*4*3	140
Gyroid	4.87	4*4*8	9.74	4*4*3	140
	10.0	4*4*8	20.0	4*4*3	140
	15.0	4*4*8	30.0	4*4*3	140
	20.0	4*4*8	40.0	4*4*3	140

Table 3.7: Summary of the sample dimensions.

3.4 Plate-based cell gradation

In this paragraph, the fundamental mechanism of the implemented MATLAB codes for calculating the necessary dimensions of the plate-based specimens' transition zones is described. These samples are graded through a step approach and three-cell layers transition regions have been adopted. When considering only half of the cells, these layers double and become six. The user selects the initial and final densities, the number of layers to be used, the architecture of interest (BCC or FCC), and the radius of the sphere (*Rsp*) to implement the sphere-based cut-out approach. Additionally, the user must choose an initial thickness value and a guess for the BCC vertex cut-out radius (x_0). An appropriate choice of these two parameters can improve the efficiency of the code, reduce computational effort, and consequently shorten the time required to obtain a solution. Specifically, the initial thickness must be lower than that of the first transition layer; otherwise, the code will not work. The closer this value is to the correct one, approaching from below, the fewer unnecessary calculations the code performs. The parameter x_0 is necessary for the proper functioning of the MATLAB function *fsolve*. For the dimensions used in this research, setting $x_0 = 2$ has always led to convergence. However, verification through the graphical method is always recommended.

Once the user has entered these parameters, the code performs the following operations. It calculates the density increment by dividing the density interval by the number of half-cell layers. Then, it creates a vector containing the desired density values for each of these layers. Within a *while* loop, it applies the formula for BCC (or FCC, as required) relative density

calculations and compares the results with the desired density for the thinner layer. As long as the current value remains below the target, it increases the thickness by 0.001 mm at each cycle, updates the cut-outs dimensions, and repeats the steps until that density is exceeded. It then saves the corresponding thickness value (and also R_v for BCC) and repeats all the operations for the next layer, continuing until all layers are processed. At the end of this procedure, the saved vector contains thickness values corresponding to densities slightly higher than the desired ones, and the respective relative errors are computed. To obtain the thickness values that correspond to densities slightly below the desired ones, it is not necessary to repeat the entire process; instead, the excessive values are simply decreased by 0.001 mm, the corresponding densities are recalculated, and the errors determined. Finally, the defect and excess errors are compared, allowing the selection, case by case, of the thickness value that minimizes the density discrepancy. At the end of the calculations, the user obtains the vector containing the thickness values to be used in SolidWorks for each layer and, only for the BCC cells, the vector containing the corresponding R_v values, since all the other dimensions are already linked to these through equations directly implemented in the CAD models.

Chapter 4

Finite Element Analysis

In this chapter, the model used for finite element simulations is described. This includes choosing the material behaviour and the damage mechanism, selecting the appropriate mesh parameters, applying loads and boundary conditions and implementing a certain type of analysis. Whenever possible, a brief review of the literature supports the description of the adopted settings. Secondly, the initial analyses, whose results guided the mesh size selection and the design of the specimens, are addressed, and their outcomes are briefly outlined. Finally, the definitive simulations have been run and the corresponding results are discussed. Indeed, by imposing an uniaxial displacement along the longitudinal direction, the tensile behaviour of samples is simulated, with particular interest in determining stress-strain diagrams, Young's moduli, yield and ultimate tensile strength (UTS), stress and strain distribution and consequently failure mode and initiation.

4.1 Definition of the Finite Element Model

This section deals with the choice of the fundamental settings involved in all the finite element analyses which have been run. Each topic is described, for clarity reasons, in a dedicated paragraph. Many choices have benefited from previous research carried out at LSM and those experiences have been exploited to build the finite element models. Where this methodology was not applicable, namely for loads and boundary conditions, which are more related to the specific research, the standard ASTM E8/E8M-25 has guided their selection. Finally, in order to provide the imposed settings with stronger foundations, a brief literature review has been conducted, looking for similar choices in other scientific works.

4.1.1 Material and damage mechanism model

As already mentioned, the material that is supposed to be used in the experimental activities, and thus that has been simulated in the FE analyses, is the aluminium alloy denoted as *AlSi10Mg*, common in lightweight applications and suitable for processing through SLM technologies. The chemical composition, as stated in EOS documentation [94], is reported in Tab. 4.1 and the physical and mechanical properties in Tab. 4.2. However, this served just as a reference and guideline. Actually, this metal alloy has already been employed at LSM for previous works, and thus this thesis benefits from already acquired data. These properties are those with which the material bilinear model, shown in Fig. 4.1, is built. The software (Abaqus[1]) linearly interpolates between the imposed yield and ultimate tensile strength [95]. The linear-

[1] Abaqus® Version 2023. Dassault Systèmes.

elastic behaviour is described, for isotropic materials as many metal alloys are[2], through two values out of a set of free. In this case, Young's modulus E and Poisson's coefficient ν are known, so the shear modulus G can be determined through eq.(4.1) [59]. When the stresses exceed the yield strength σ_y, the mechanical behaviour changes. A simple but reliable model to describe it is a linear work-hardening curve, as the one given by eq.(4.2). The slope of this second segment is the tangent modulus E_T and is computed through eq.(4.3) [96].

$$G = \frac{E}{2(1+\nu)} \tag{4.1}$$

$$\sigma = \sigma_y + E_T \varepsilon \tag{4.2}$$

$$\begin{aligned} E_T &= \frac{\sigma_{UTS} - \sigma_y}{\varepsilon_U - \varepsilon_y} \\ &= \frac{\sigma_{UTS} - \sigma_y}{\varepsilon_U - \dfrac{\sigma_y}{E}} \\ &= \frac{\sigma_{UTS} - \sigma_y}{\varepsilon_U^{pl}} \end{aligned} \tag{4.3}$$

Element	Min. [wt.%]	Max. [wt.%]
Al	Balance	
Si	9.0	11.0
Fe	-	0.55
Cu	-	0.05
Mn	-	0.45
Mg	0.20	0.45
Ni	-	0.05
Zn	-	0.10
Pb	-	0.03
Sn	-	0.05
Ti	-	0.15

Table 4.1: AlSi10Mg chemical composition (EOS).

After defining the material's elastic and plastic behaviour, a damage initiation model must be specified. For this purpose, a Johnson-Cook model has been selected. The ductile criterion is a phenomenological approach used to predict the onset of damage resulting from void nucleation, growth, and coalescence, and it is typically applied to ductile metals, as the name implies. The *Johnson-Cook* criterion represents a specific form of the ductile criterion, in which the equivalent plastic strain at damage initiation, $\bar{\varepsilon}_D^{pl}$, is described by the following equations [95]:

$$\bar{\varepsilon}_D^{pl} = \left[D_1 + D_2 e^{-D_3 \eta}\right] \left[1 + D_4 ln\Big(\frac{\dot{\bar{\varepsilon}}^{pl}}{\dot{\varepsilon}_0}\Big)\right] \Big(1 + D_5 \hat{\theta}\Big) \tag{4.4}$$

[2]Actually, AM fabrication processes can induce directionality dependence in the mechanical properties of structures.

Quantity	Value
Average density	≥ 2.67 g/cm^3
Vert. σ_y	230 MPa
Horiz. σ_y	270 MPa
Vert. σ_{UTS}	460 MPa
Horiz.σ_{UTS}	450 MPa

Table 4.2: AlSi10Mg physical and mechanical properties (EOS) - As built.

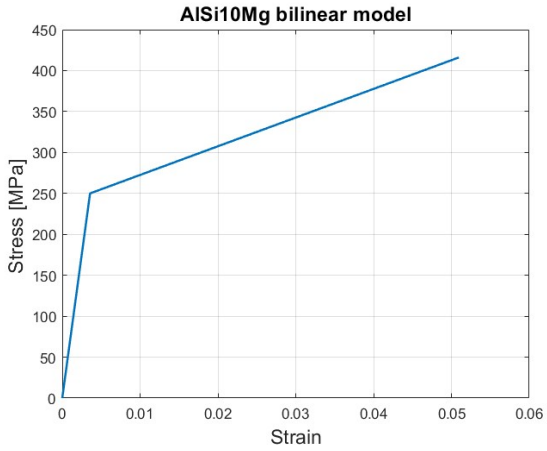

Figure 4.1: AlSi10Mg bilinear material model employed in the analyses.

$$\hat{\theta} = \begin{cases} 0 & \text{for } \theta < \theta_{transition} \\ \dfrac{\theta - \theta_{transition}}{\theta_{melt} - \theta_{transition}} & \text{for } \theta_{\text{transition}} \leq \theta \leq \theta_{melt} \\ 1 & \text{for } \theta > \theta_{melt} \end{cases} \tag{4.5}$$

where D_1 to D_5 are the failure parameters, $\dot{\varepsilon}_0$ the reference strain rate and $\hat{\theta}$ the non-dimensional temperature, defined as a function of the actual relationship with the transition and melting temperatures. In the simulations run, no temperature effects are considered. Additionally, the numerical values of the employed Johnson-Cook parameters are reported in Tab. 4.4. In this case, they have not been directly determined at LSM, but resulted from previous literature review; they have supported numerical simulations run during previous research and have already

Quantity	Value
Density	2.69 g/cm^3
E	70.0 GPa
ν	0.35
σ_y	250 MPa
σ_{UTS}	416 MPa
E_T	3.50 GPa
ε_U^{pl}	0.045

Table 4.3: AlSi10Mg physical and mechanical properties implemented (LSM).

produced reliable results. Also several authors employed this damage model. Just to name a few, in the field of plate lattices by Sun et al. [17] and He et al. [97] (USA), in that of strut-based lattices by Sultan Kilic et al. [42] and Noronha et al. [98] (Australia), and in that of TPMS by Ziaie et al. [8], Yan et al. [99] (China, UK) and Liu et al. [100] (China).

Quantity	Value
D_1	$\geq$ -5.0
D_2	0
D_3	0.0432
D_4	0
D_5	0
θ_{melt}	933 K
$\theta_{\text{transition}}$	466.5 K
$\dot{\varepsilon}_0$	1
$\bar{u}_f^{pl}$	0.01

Table 4.4: Johnson-Cook damage initiation and evolution parameters implemented.

Finally, a mechanism for damage evolution must be defined. This mechanism treats damage as a gradual reduction of the material's stiffness, eventually leading to failure [95]. A linear softening damage evolution based on plastic displacement has been adopted. After the damage initiation criterion is satisfied, the damage variable D increases linearly with the effective plastic displacement $\bar{u}^{pl}$, as described by eq.(4.6). Here, L denotes the characteristic element length. The documentation notes that Hillerborg, in 1976, suggested using a stress-displacement relationship instead of stress-strain for modelling material behaviour after damage begins, to mitigate mesh dependency [95]. Complete failure occurs when $\bar{u}^{pl} = \bar{u}_f^{pl}$, where $\bar{u}_f^{pl}$ represents the plastic displacement at failure, which is defined by the user when configuring the model.

$$\dot{\bar{u}}^{pl} = L\dot{\bar{\varepsilon}}^{pl} \tag{4.6}$$

4.1.2 Mesh

In this paragraph, the choice of the mesh is addressed. As could be easily imagined, previous works in the field of TPMS and plate-based lattice structures have been carried out at LSM, and therefore the general settings of the finite element models benefit from those experiences. Due to the complex geometry, and following LSM-best practices, a solid tetrahedral mesh has been used for all the specimens, apart from the grips, for which a solid hexahedral mesh has been applied. The choice of this mesh, guided by the aforementioned reasons, also finds examples in the literature on the topic. It was also adopted, just to name a few, by Rezapourian et al. [67] for split-P cells, by Sultan Kilic et al. [42] and Jiang et al. [64], whose authors used a tetrahedral mesh for strut-based lattices combined with hexahedral elements for bulk components, by Alagha et al. [11] and by Schneider et al. [61] in the field of plate-based lattices, by Zhang et al. [69] and Doroszko et al. [82] for studies on TPMS structures. The automatic discretization (unstructured mesh) in Abaqus produced acceptable results regarding mesh quality, even if a few elements had to be adjusted.

In order to connect the two meshes, a node-to-surface *tie* constrain has been applied. It enforces kinematic compatibility, meaning displacements remain continuous across the interface. For best accuracy, the main surface should be chosen as the one with the coarser mesh [101]. Therefore, in the FE models employed, these have been selected to be the grip' surfaces. Ad-

ditionally, a good practical rule is to avoid tying meshes in the actual region of interest, as it could degrade the stress distribution. Therefore, in the case here described, although the mesh scale changes significantly, the tie is located at the interface between the graded ends and the solid tabs, while the region of main interest is the central lattice section. This placement makes the tie acceptable for the purposes of this thesis. An example is shown in Fig. 4.2.

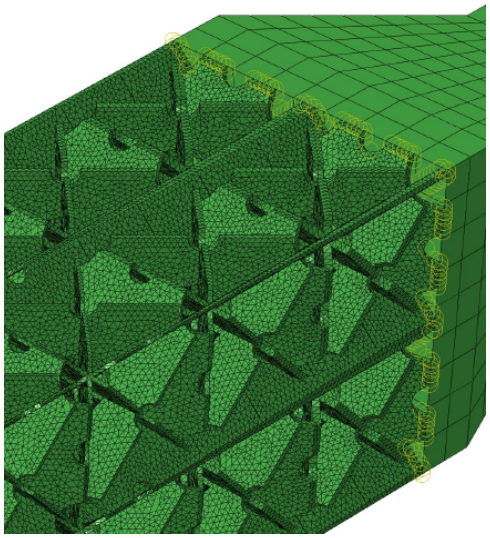

Figure 4.2: Example of the interface between the grip and the transition region, where the tie constraint is applied.

Before proceeding with the description of the mesh seed sizes, it is necessary to highlight an important constraint that has significantly affected this thesis[3]. The maximum number of elements that could be used was around 2 million, not due to software limitations, but due to hardware constraints. Indeed, the computers employed were adequate but not *workstations*. Previous experiences at LSM had repeatedly observed this limit. Theoretically, before starting the simulation of a full model, it is a good guideline to perform a *mesh sensitivity* or *verification study*. Many studies include this procedure [4, 19, 67, 102]. Therefore, not one but two of these studies, aiming to verify the impact of very fine meshes, have been carried out. While the results show reliable predictions for the elastic behaviour of the structures, this was not the case for UTS values and failure predictions. In the end, the final choice fell on a mesh with an approximate global size of 0.35, constant for all the specimens, roughly corresponding to two million tetrahedral elements. A finer mesh is not employable for the cited limitations. In Abaqus, seeds specify where nodes are likely to be placed and serve to control the intended density of the mesh [103]. More intuitively, they may be regarded as a user-defined target spacing along edges during meshing: they provide guidance to the mesher rather than imposing an exact element size. An example of mesh seeds application, with this dimension, is shown in Fig. 4.3. Previously, other authors faced limitations and were forced to make the most cost-effective choice. Zhang et al. [65] chose the element size to balance computation time and numerical accuracy; similarly, Sultan Kilic et al. [42], whose selection resulted from a trade-off between accuracy, computational efficiency, and processing time, and so did Bonatti et al. [13], Abdelmageed et al. [19], and many others. For the grips, an approximate global size of 1.60, automatically computed by the software, was selected.

[3]The details of these studies are reported at Par. 4.2.1.

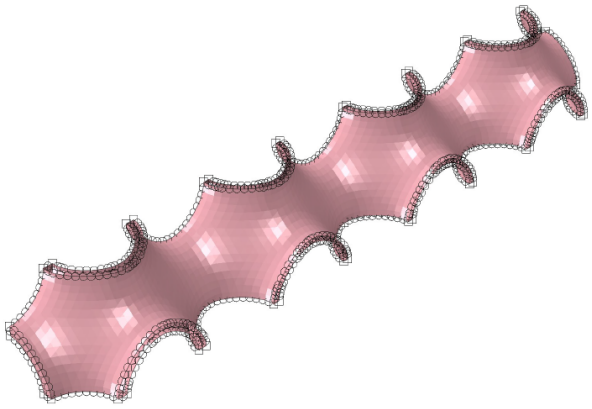

Figure 4.3: Fourth of a column of Primitive unit cells: example of seeds application.

4.1.3 Loads and boundary conditions

As already mentioned, loads and boundary conditions have been selected relying on ASTM E8/E8M-25 [104] as guideline. Specifically, the displacement rate has been set according to the section *Control Method C – Crosshead speed control method for determining yield properties*, thus applying a constant crosshead speed equal to 0.015 mm/mm per minute. The entire length of the specimen, namely the distance between the two grips (for specimens not having reduced sections [104]), has been considered for the strain rate calculations. In support of this choice, the total internal energy (ALLIE) and total kinetic energy (ALLKE) curves have been plotted for every analysis. Their behaviour shows the longitudinal displacement is applied with a proper slow speed, with the latter value being negligible from the very beginning to failure[4]. As usually happens in experimental tests, only one crosshead is moving, while the other is clamped. The former has the displacement applied along the positive z direction only, while the latter has all its degrees of freedom, both rotational and translational, blocked. Being the displacement rate quite low, this choice should not lead to results particularly different from the case of perfectly symmetric application. Finally, in order to reduce the computational time required, many simulations[5] have been carried out on just one fourth of the specimen, hence exploiting its symmetry. In these cases, symmetric boundary conditions have been applied on the lateral surfaces, considering the proper symmetry plane.

4.1.4 Analysis type

With respect to the analysis type, *Dynamic Explicit* simulations have been run, according to the good results obtained during previous investigations at LSM. Indeed, this type of analysis handles material degradation and element deletion much more robustly than Static General. There are no convergence issues when elements distort or fail, which is why it has been selected for this damage-driven problem. Additionally, it can implement both a linear and a large-deformation theory, making it suitable for very different simulations, from those characterised by strains and rotations that could be assumed to be small, to large ones [105]. These analyses employed a procedure consisting of a large number of small time increments. In the simulations run, the large deformation setting has been chosen, with the incrementation automatically computed by the software. Moreover, with this type of analysis a mass scaling factor is generally

[4]Wang et al. [41] report that as long as the kinetic energy of the lattice structure remains below a 20th of the total energy, the effects of inertia forces can be neglected.

[5]This is the case of all the definitive and part of the initial simulations.

used to speed up the simulation time. Its influence is discussed at Par. 4.2.2. The application of mass scaling was also adopted by Bonatti et al. [13] and by Schneider et al. [61], who studied several lattice structures (strut-, plate-, and TPMS architectures) and applied a 0.00001 factor. On the contrary, Qiu et al. [62] explicitly avoided the use of mass scaling, but did not provide any justification.

4.2 Initial simulations

In this section, the *initial* finite element analyses are presented. The term initial emphasizes that these simulations were conducted during the first half of the thesis work; consequently, they differ in several aspects from the final tensile simulations. Such differences could concern the investigated densities, the imposed displacement rate and the geometry of the samples. Nevertheless, these analyses remain both meaningful and reliable, as they provided the groundwork on which the design of the specimens has been based. Indeed, specimen design, numerical simulations and density selection are deeply interrelated activities rather than strictly sequential steps. As a consequence, even though the thesis should be structured to maximize clarity and logical flow, frequent cross-references to preceding and subsequent sections are unavoidable. Moreover, some adjustments and modifications during the course of the work are inevitable, reflecting the iterative and exploratory nature of the research process.

4.2.1 Mesh sensitivity

At the very beginning of the simulations, a mesh sensitivity study on two different samples was conducted. Its goal was to assess the effect of mesh size, thus leading to an informed choice of the mesh seeds value, even though constrained by the available computers. The mesh sensitivity studies were among the first to be run; therefore, the specimen design was not definitive and the corresponding simulations were not conducted according to standard practices. In this regard, only the energy curves were observed to check the quasi-staticity of the simulations, namely the predominance of internal energy over kinetic energy; just a couple of examples are displayed in Fig. 4.4, as the trend is the same for all the models. During this stage, the idea was to analyse the behaviour of only the test section, in order to isolate the mesh impact from other potential influencing parameters, such as the effects of transition regions or grips. Therefore, only a 2x2x4 uniform unit cells sample was adopted. It is clearly of reduced dimension and specifically corresponds to a reproduction of the definitive gauge section at a 1:2 scale. An example is shown in Fig. 4.5a. Additionally, it was necessary to conduct this study pragmatically: meshing 16 specimens (4 unit cells $\times$ 4 densities) with 15 different mesh seeds, and then simulating each one, would have resulted in an enormous time investment and was virtually impossible.

Therefore, only a very lightweight Gyroid specimen was analysed, generated with an iso-value of 0.189, which approximately corresponds to 6.11% relative density. A mesh seed size from 0.50 to 0.250 was applied, in steps of 0.125. The bottom surface was clamped, while the nodes of the top were linked through a rigid connection and displaced by 1 mm in 10 s (not standard), as shown in Fig. 4.6 and 4.7a. Finally, stress and strain curves were plotted. Unfortunately, the results did not show convergence. Indeed, failure occurred later each time the mesh seed size was reduced, thereby increasing the maximum reaction force and the strain at failure. However, this large difference in failure was coupled with only small variations in the Young's modulus, as shown in Fig. 4.8a. This indicates that there is room for a change of the damage model and/or a better setting of its parameters, but the elastic behaviour, and hence the Young's modulus calculations, is expected to be predicted accurately. After this first attempt, a second study was conducted to reach even finer meshes. Therefore, it was necessary to reduce the specimen

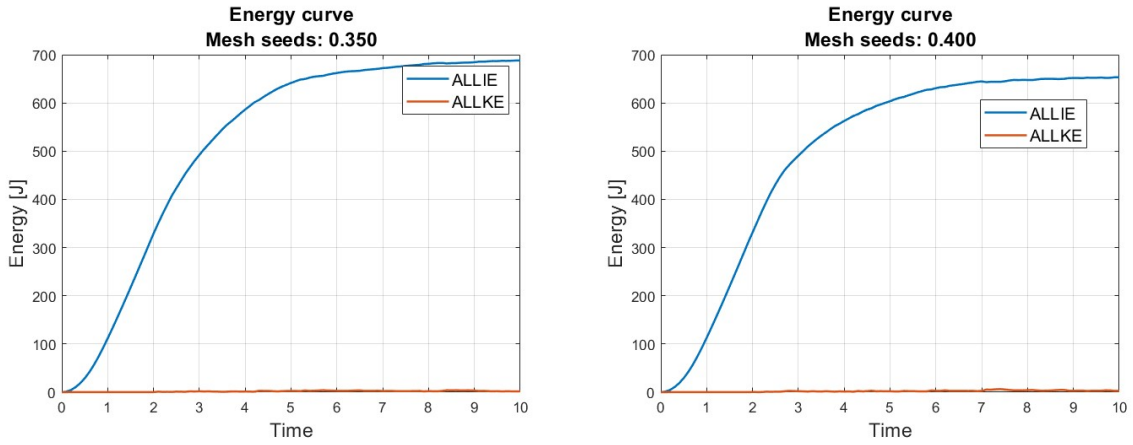

(a) 0.350 mm mesh seeds.

(b) 0.400 mm mesh seeds.

Figure 4.4: Mesh sensitivity analysis: ALLIE and ALLKE curves built for two different simulations.

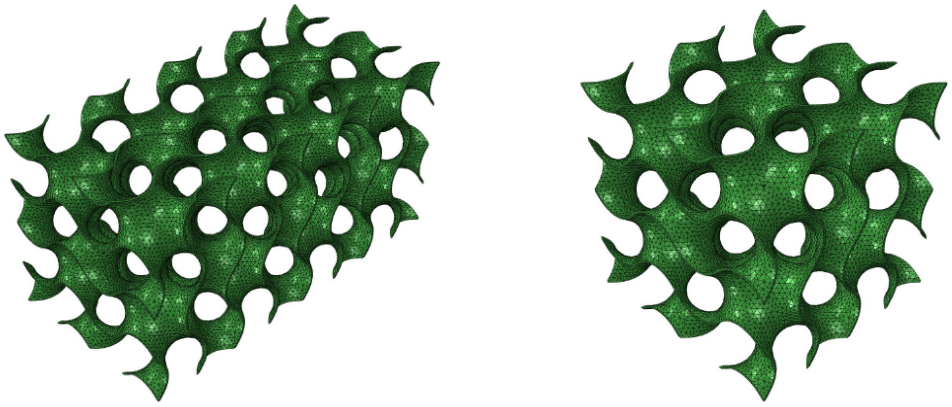

(a) Specimen with 2x2x4 cells, employed for the first study.

(b) Specimen with 2x2x2 cells, employed for the second study.

Figure 4.5: Mesh sensitivity analysis: geometries of the samples employed.

dimensions, in order to postpone the aforementioned limitation due to the maximum number of elements. Samples of 2x2x2 unit cells, with symmetric boundary conditions applied to the bottom surface and displacement applied to the top, were used. An example of the specimen is shown in Fig. 4.5b, and of the loads and boundary conditions configuration in Fig. 4.7a. This strategy allowed the use of seed sizes from 0.50 to 0.200, in steps of 0.125. Unfortunately, the results did not differ from those obtained in the previous mesh sensitivity study, as clearly visible in Fig. 4.8b. One possible rationale behind the differences in the predicted plastic behaviour, depending on the mesh refinement, lies in the local yielding of small portions of the structure. Local stresses above the yield strength lead to premature damage of some elements in the structure. In this regard, Zheng et al. [34] investigated the static tensile, compressive and bending characteristics of Primitive unit cell, finding that local plasticity may occur in the structure as a consequence of local stresses below the general yield of the structure. Going back to the main flow, the consequence could be that the finer the mesh, the smaller the damaged volumes, and hence the higher the ultimate tensile strength and strain at failure, as smaller portions of the structure are affected by degradation. This hypothesis can justify both the

stable behaviour of the elastic region and the non-convergent behaviour of the plastic region. If this explanation is correct, it would be inappropriate to treat this issue as a convergence problem. Instead, it would likely be related to the material model itself, which would need experimental testing to be properly calibrated. Future research in this direction could be very beneficial.

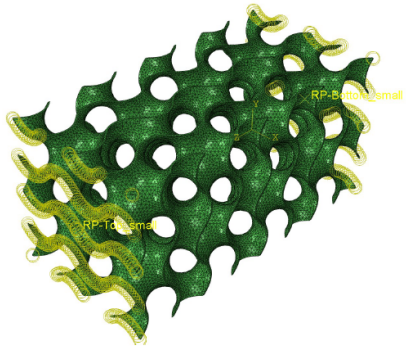

Figure 4.6: Mesh sensitivity analysis: visualisation of the nodes being constraint to the reference points.

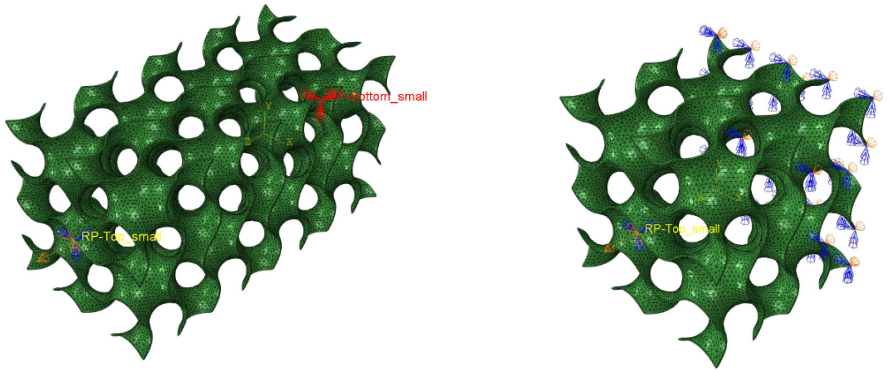

(a) Case of the specimen with 2x2x4 cells, employed for the first study.

(b) Case of the specimen with 2x2x2 cells, employed for the second study.

Figure 4.7: Mesh sensitivity analysis: visualisation of the employed loads and boundary conditions.

In conclusion, the mesh size selection was guided mainly by computer constraints. Indeed, it is the finer mesh reachable with the available hardware. Additionally, the difference between the Young's modulus determined using the two finest meshes (0.275 and 0.250 for the first analysis, 0.225 and 0.200 for the second) show only a marginal variation in the Young's modulus: respectively 1.19 and 1.11%, suggesting that the possibility of applying a even finer mesh should close the distance with convergence. Bonatti et al. [13] relied on a similar error threshold of (1% difference in stiffness).

In conclusion, for this thesis a global approximate size of 0.35 was chosen, representing the best compromise achievable. It leads to roughly 2 million elements for each final specimen simulation, representing the finest mesh that could be employed. Once again, these results should be reliable for the Young's Modulus calculation and stress distribution when not too close to the failure point, while comparisons with experimental results are fundamental to assess the failure characteristics.

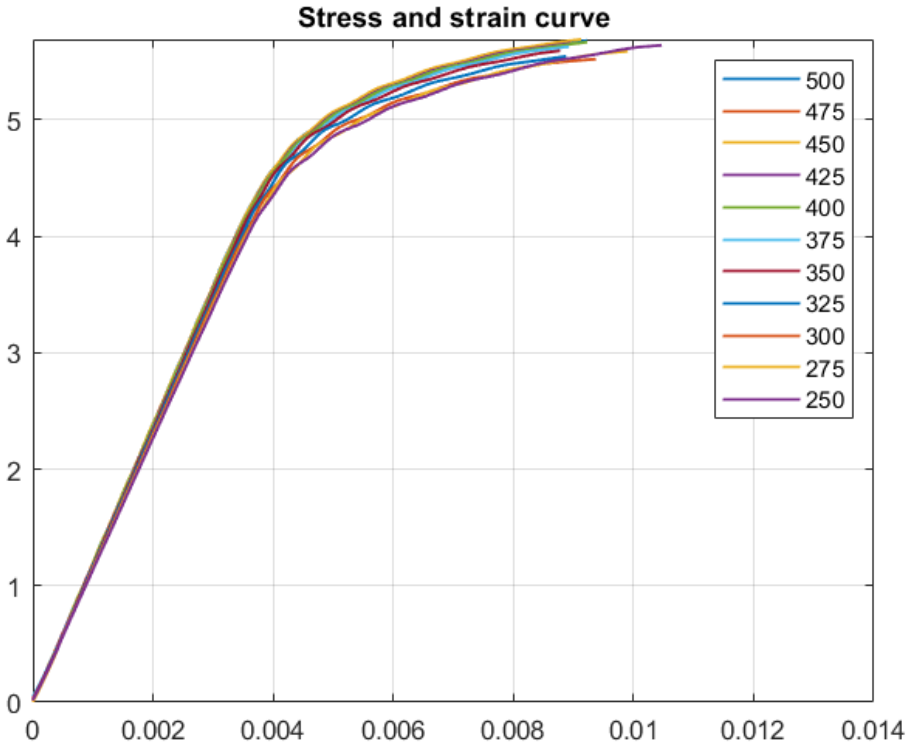

(a) Case of the specimen with 2x2x4 cells, employed for the first study.

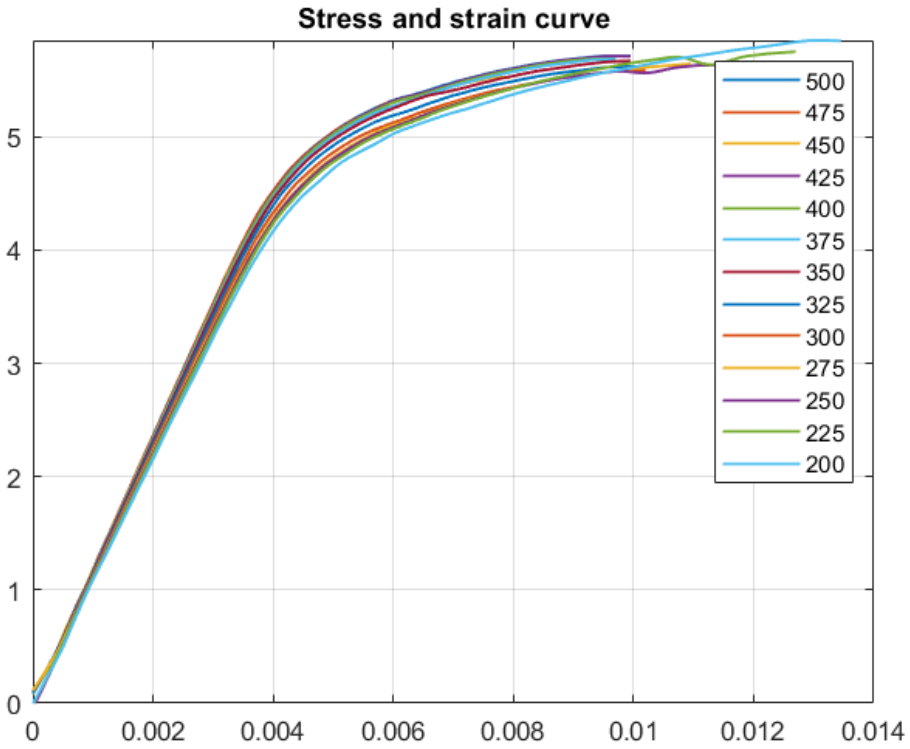

(b) Case of the specimen with 2x2x2 cells, employed for the second study.

Figure 4.8: Mesh sensitivity analysis: generated stress and strain curves, for the different mesh seeds values.

4.2.2 Mass scaling

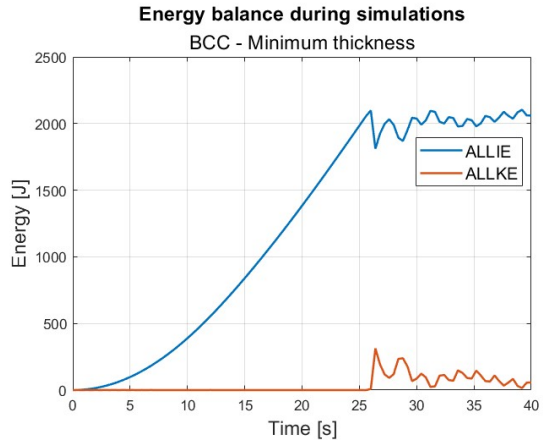

(a) BCC unit cell specimen - 8.32% rel. density.

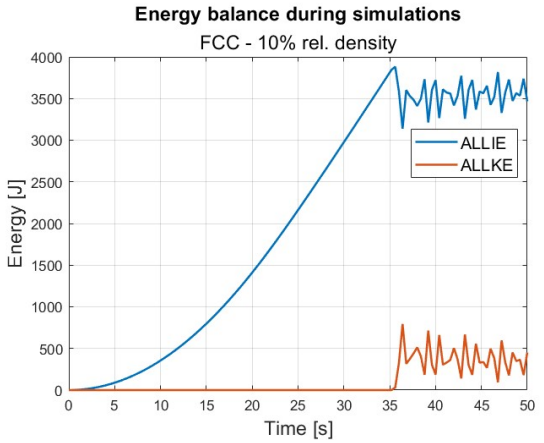

(b) FCC unit cell specimen - 10% rel. density.

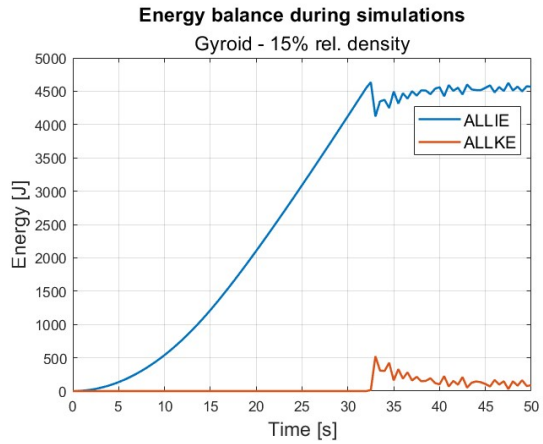

(c) Gyroid unit cell specimen - 15% rel. density.

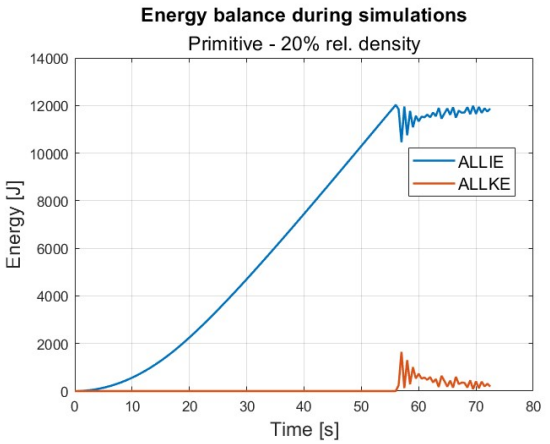

(d) Primitive unit cell specimen - 20% rel. density.

Figure 4.9: Mass scaling: assessing its impact through a comparison with ALLIE and ALLKE curves.

As previously mentioned, Dynamic Explicit analyses are appropriate for the simulated configurations, which include large strain and elements failure and deletion. Nevertheless, the drawback is the potentially long runtime due to very small stable time increments. This is why it is generally applied a carefully chosen mass scaling, with the aim of artificially increase the stable time increment and significantly speed up the simulation while keeping inertial effects negligible. Abaqus documentation [105] indicates that a modest degree of mass scaling is generally acceptable for quasi-static analyses, a criterion that is met by the simulations performed in this thesis. It is nevertheless essential to verify that the introduced mass and the associated rise in inertial forces do not significantly influence the accuracy of the solution. From a theoretical standpoint, these effects can be considered negligible as long as the kinetic energy of the lattice structure stays below roughly 5% of the total mechanical energy [41]. In line with LSM best practices, an initial mass-scaling value of 0.0001 was selected. Given the aforementioned hardware limitations, maintaining the simulation time within a manageable threshold was essential. Nevertheless, since no numerical setting should be adopted without appropriate justification, a brief assessment of its influence on the simulations was carried out. This evaluation aimed to determine whether the computational time could be reduced, or the stress oscillations mitigated,

by employing alternative scaling factors of 0.001 or 0.00001, respectively. The comparison was carried out at a later stage than the mesh sensitivity analysis, resulting in the implementation of imposed displacement rates as described in Par. 4.1.4 on definitive specimens, with symmetric boundary conditions applied on the two lateral sides. Attempts with different cell types and densities were made using a 0.001 mass scaling factor, thanks to the low time investment required, but only a single simulation was performed when decreasing the mass scaling factor to a tenth of the implemented value. Indeed, after a few hours the simulation was stopped because simple arithmetic operations indicated that several days would be required for each specimen, and hence that choice was considered unfeasible. Some results are shown in Fig. 4.10. As can be clearly observed, keeping the mass scaling factor sufficiently small is fundamental, as a too high value leads to unrealistic abrupt changes in the stress distribution. The value used for the final simulations, 0.0001, is still not perfect and produces some oscillations in the stress and strain curves, but these are negligible compared to the global trend. However, for the implemented factor and until fracture occurs, the trend remains quite clear, and through a linear interpolation of the collected data, the Young's modulus value can be extracted with good precision, representing the best compromise between computational cost and quality of the results.

A final consideration can be made for the maximum reaction force, which is almost independent of mass scaling effects, and for the plastic region of the graph, which experiences a decrease in the oscillations' amplitude. It is also fundamental to mention that, because of mass scaling, the behaviour after fracture is no longer reliable. Stress and strain curves become unrealistic, and the kinetic energy, even if it still remains a fraction of the internal energy, gains more importance, particularly at low densities, as displayed in Fig. 4.9.

4.2.3 Transition regions

In this paragraph, the simulations run for designing the transition regions of the definitive specimens are presented. They include the analysis of the double-density approach verification, length effects (two or three unit cell layers) assessment, and the BCC transition section unit cell geometry selection. At Sec. 3.3, the principal results of these analyses have already been briefly described, as they were employed for the final design of all the specimens. However, a few more details will be presented. The following specimens have been simulated[6]:

- BCC unit cell
  - reduced dimensions with 0.150 mm plate thickness (10.24% rel. density), with 3 layers of transition zones;
  - reduced dimensions with 0.150 mm plate thickness, with chamfered edges between transition layers;
  - reduced dimensions with 0.150 mm plate thickness, with continuous external edges in the transition regions;
  - full dimensions with 0.178 mm plate thickness (11.97% rel. density);
- FCC unit cell

[6]It is important to mention that the densities could appear unusual, as they are not the same as those considered in the main body of the thesis. The reason behind this is that the effective densities were not fixed from the beginning. In fact, a previous hypothesis was to use 10, 20, and 30% relative density specimens, another one 5, 12, and 19%. Moreover, the minimum printable thickness was initially set to 0.150 mm (which resulted in approximately 0.176 and 0.189 iso-values). In later stages, results from investigations at LSM suggested that 30% was too high and 5% probably too low, and that the minimum printable thickness could be set to 0.120 mm; hence, the final choice was made.

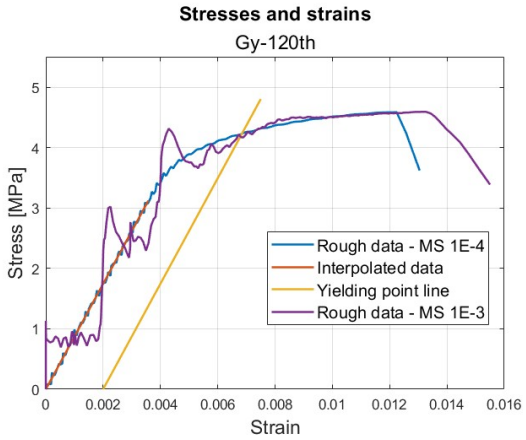

(a) Gyroid unit cell specimen - 4.87% rel. density.

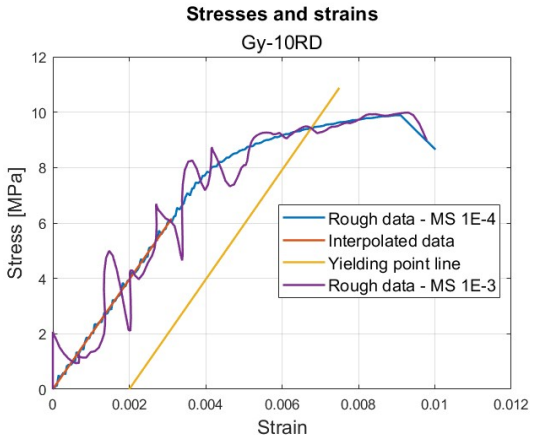

(b) Gyroid unit cell specimen - 10% rel. density.

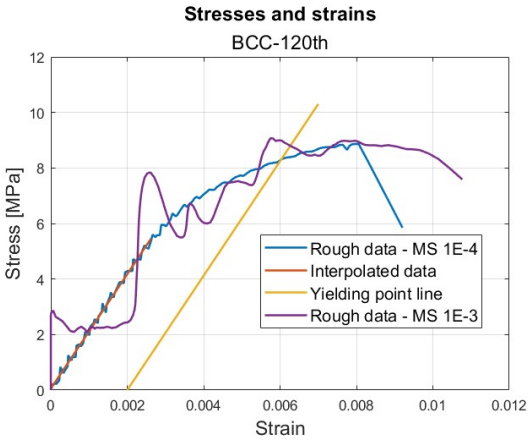

(c) BCC unit cell specimen - 8.32% rel. density.

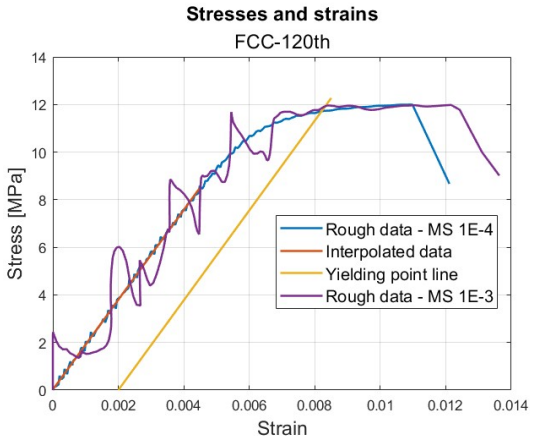

(d) FCC unit cell specimen - 6.50% rel. density.

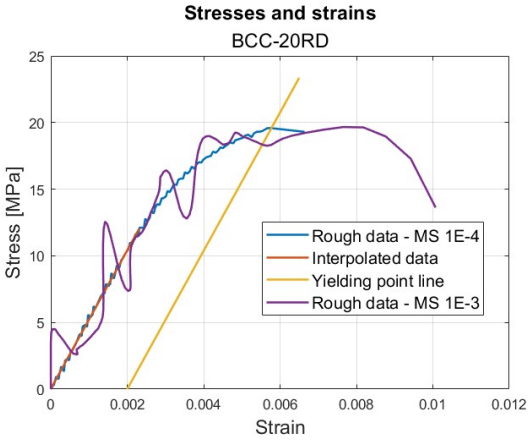

(e) BCC unit cell specimen - 20% rel. density.

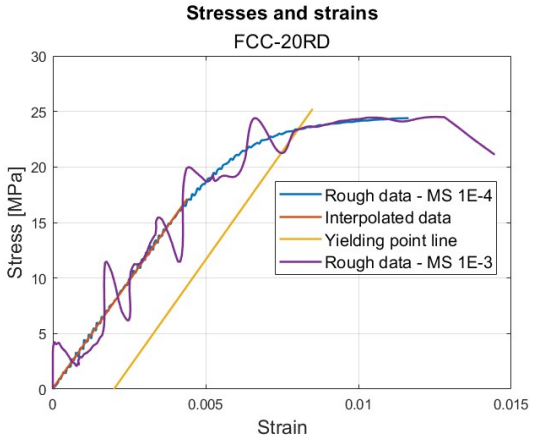

(f) FCC unit cell specimen - 20% rel. density.

Figure 4.10: Mass scaling effect on stress and strain curves.

  - reduced dimensions with 0.150 mm plate thickness (7.97% rel. density);
  - full dimensions with 0.239 mm plate thickness (12.01% rel. density);

- Primitive unit cell
  - reduced dimensions with 0.176 iso-value (5.27% rel. density), with 2 layers of transition zones;
  - reduced dimensions with 0.176 iso-value, with 3 layers of transition zones;
  - reduced dimensions with 0.176 iso-value, with 3 layers of transition zones and a different grip interface;

- Gyroid unit cell
  - reduced dimensions with 0.189 iso-value (6.11% rel. density);
  - full dimensions with 0.189 iso-value.

With regards to the transition regions investigations, the initial simulations were run on very lightweight samples (0.150 mm thickness, or very low iso-values such as 0.176 and 0.189), because these are more prone to fail, especially at the interface with the grips, as the contact surface is in some way proportional to the density. Additionally, test sections at a 1:2 scale relative to the definitive ones were adopted. Actually, the transition regions, of two layers, should have followed the same scale, but printing limitations made this unfeasible. To summarise, simulations were run on 2x2x8 reduced-dimension samples (hence without symmetric boundary conditions), with small grips (20x20 mm plates instead of 40x40 mm), as shown in Fig. 4.11, with imposed displacement as described in Par. 4.1.4. Grips were later adapted to include a thinner plate, as they were over-dimensioned.

Failure mode description

- *FCC*: Fracture occurs completely inside the test section, specifically in the fifth cell from the bottom, slightly shifted towards the top, where the displacement is applied. Moreover, failure propagates from inside the specimen, not from the external edges; this indicates that the specimen design conforms to the applicable standards. The reaction force magnitude measured at the reference points (one at the top, one at the bottom) is identical, confirming that the loads are correctly transmitted through the entire structure. The displacement applied at failure is 0.767 mm, corresponding to a global strain of approximately 0.01, which is the value applied for the Johnson-Cook damage evolution model. The interfaces, both between grips and transitions and between transitions and test sections, are not damaged.

- *Gyroid*: Fracture occurs completely inside the test section, specifically in the fourth cell from the bottom, slightly shifted towards the bottom, where the specimen is clamped. Moreover, failure propagates from inside the specimen. The reaction force magnitude measured at the reference points (one at the top, one at the bottom) is identical. The displacement applied at failure is 0.633 mm, corresponding to a global strain of approximately 0.008, which is close to 0.01 but not exactly the same. Interfaces are not damaged.

- *BCC*: Fracture occurs completely inside the test section, specifically at the interface between the fifth and sixth cells from the bottom, slightly shifted towards the top. For this cell, the fracture is guided by the vertex cut-outs. Indeed, in more than one of these

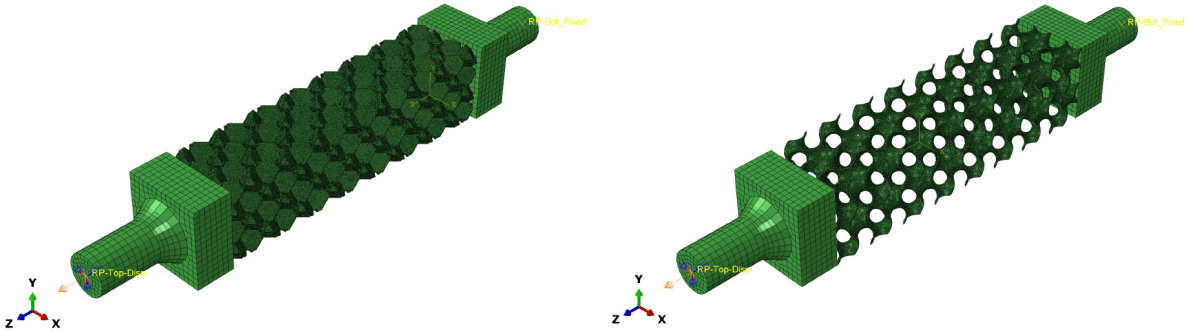

(a) FCC unit cell. (b) Gyroid unit cell.

Figure 4.11: Two examples of reduced dimensions samples, employed for the initial simulations.

locations, specifically on the vertical plate, fracture initiation can be localized. In particular, apart from the one leading the main failure (the one that splits the specimen in two parts, for better understanding), the interfaces between transition and test sections are also subjected to damage; however, these do not evolve into complete failure. The reaction force magnitude measured at the reference points (one at the top, one at the bottom) is identical. The displacement applied at failure is 0.443 mm, corresponding to a global strain of approximately 0.0055. This value makes the BCC unit cell the most brittle among those studied until this point.

- *Primitive*: Fracture occurs completely inside the test section, specifically in the fifth cell from the bottom, slightly shifted towards the top. The failure takes place approximately in the middle of the unit cell, with a specific pattern: external cells fail in parallel but not at the same z-coordinate as the central ones, because the cell fails where its cross section is smaller. As for the BCC cell, apart from the main failure, the interfaces between transition and test sections are also damaged, even if they do not evolve into complete failure. The displacement applied at failure is 1.21 mm, corresponding to a global strain of approximately 0.015. This value makes the Primitive unit cell the least brittle among those studied until this point.

Based on these outcomes, FCC and Gyroid unit cells do not require, at least theoretically, design changes. The double-density approach for modelling the transition zones works and leads to failure properly located inside the specimens' test sections. On the contrary, this is not the case for BCC and Primitive cells, which required further investigations.

For the Primitive cell, it was studied whether a longer transition region (2x2x3), with a smoother increment of density along its longitudinal direction, could be beneficial or would not change the result. However, the situation was approximately the same as described in this paragraph for the 2x2x2 specimen; only the displacement at failure is higher because the entire specimen had a length of 10 cells. The design was also adjusted to change the interface with the grips, as shown in Fig. 4.12, but these changes appeared to have no impact on the fracture pattern or location.

On the contrary, the BCC-based specimens were more prone to adjustments, thanks also to the cut-outs, which could be modified, and the stepwise density gradation. Three possible solutions were analysed: a longer transition region, as for the Primitive architecture; the implementation of chamfered edges between the density steps, to avoid discontinuities; and a modification of

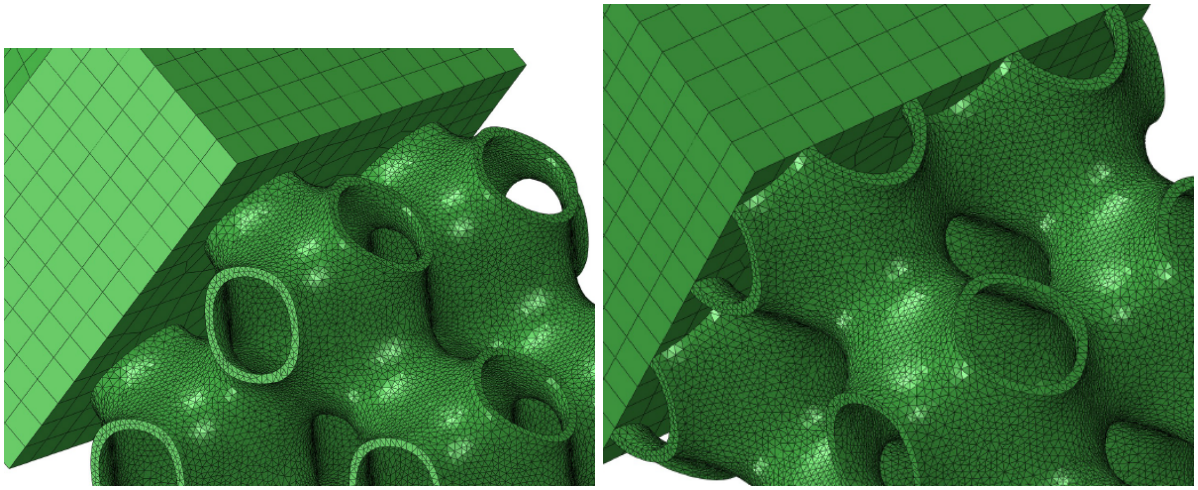

(a) Full cell interface, which is expected to be weaker.

(b) Half cell interface, which is expected to be stronger.

Figure 4.12: Primitive unit cell: different interfaces with grips.

the vertex cuts. The main results and considerations are reported below:

- *Three layers*: As in the case of Primitive unit cells, this solution was studied with the aim of smoothing the density gradient along the transition sections. The specimen is composed of 2x2x10 cells, and the main failure appears between the fifth and sixth cells, namely exactly in the middle of the test section. However, secondary fractures still appear at the interfaces between test and transition zones, even if, as already suggested by the chosen vocabulary, they are less intense than the one leading to failure. No significant differences arise compared to the two-layer transition model, making this modification insufficient and thus not final.

- *Chamfered*: The specimen is composed of 2x2x8 cells, and the main failure appears between the fourth and fifth cells, namely exactly in the middle of the test section. However, secondary fractures still appear at the interfaces between test and transition zones, even if, as already suggested by the chosen vocabulary, they are less intense than the one leading to failure. No significant differences arise compared to the smooth transition model, making this modification insufficient and thus not final.

- *Modified edges*: The specimen is composed of 2x2x9 cells, and the main fracture is located at the interface between the fifth and sixth cells. There is also a secondary and minor fracture close to the interface between the test section and the transition zone. As already mentioned for BCC architecture, fractures appear only where vertex cut-outs are located, and not in correspondence with other types of holes. The chosen design performs very well in this regard. The transition zone is made of 2.5 cells, but the thickness variations affect only two of them. Therefore, the secondary failure appears one entire cell away from the last thickness change and half a cell away from the closest modified edge. Thanks to these adjustments, these minor fractures are entirely located within the test section, even though the margin is small. Consequently, this design proves to be the best among the three solutions investigated.

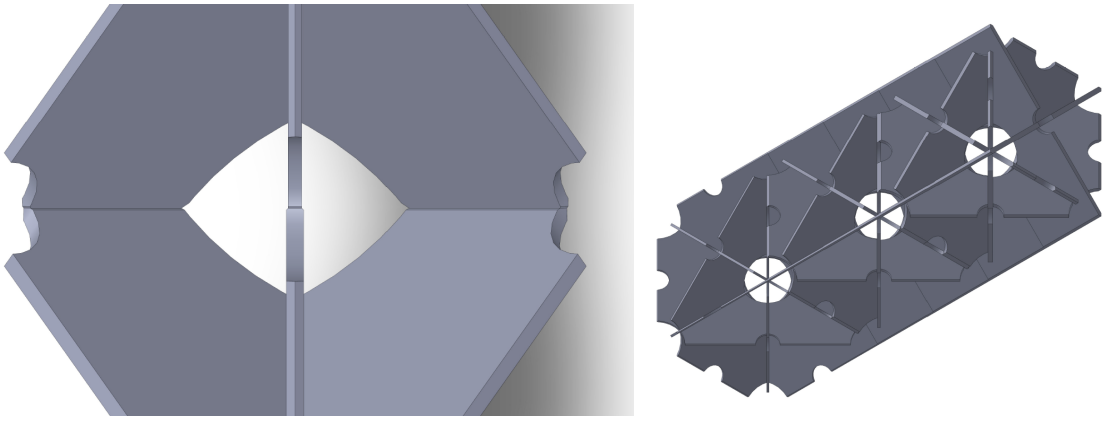

(a) Chamfered edges between steps: detail view of the geometry.

(b) Modified external edges.

Figure 4.13: BCC unit cell: different geometries for transition regions.

Final considerations

In conclusion, the following considerations for BCC and Primitive architectures were made:

- the main fracture was predicted to appear in the test section, in compliance with the regulatory requirements;
- the smaller fractures did not evolve into a complete failure of the specimen;
- longer transition regions would lead to unprintable samples;
- for the BCC architecture the modification of the external edges is the most promising solution;
- for the Primitive architecture no adjustments of the cell geometry were identified that would not risk completely changing its mechanical behaviour.

In conclusion, for all the aforementioned reasons, and those already mentioned in Sec. 3.3, the Primitive transition regions have a height of 3 cell layers, like almost all the other specimens, and no geometrical adjustments. Similarly, the BCC transition regions have a height of 3 cell layers, like almost all the other specimens, with continuous external edges.

As very last step of these initial simulations, all the unit cells with the studied thicknesses (0.150 mm) and iso-values (0.176 and 0.189), and the designed transition regions, were analysed on a quarter of the definitive specimen design (as the one shown in Fig. 4.14), applying symmetric boundary conditions. This additional step was used to verify and assess once again the theoretical correctness of the chosen designs.

4.3 Tensile simulations

In this section, the results of the tensile simulations, whose model has already been described in the first section of this chapter, are presented. In particular, the first paragraph focuses on the stiffness of the different cells, comparing the various topologies at equal volume fraction and, within the same architecture, assessing the influence of relative density. The second paragraph deals with yield strength and ultimate tensile strength. Again, the investigation of the influence

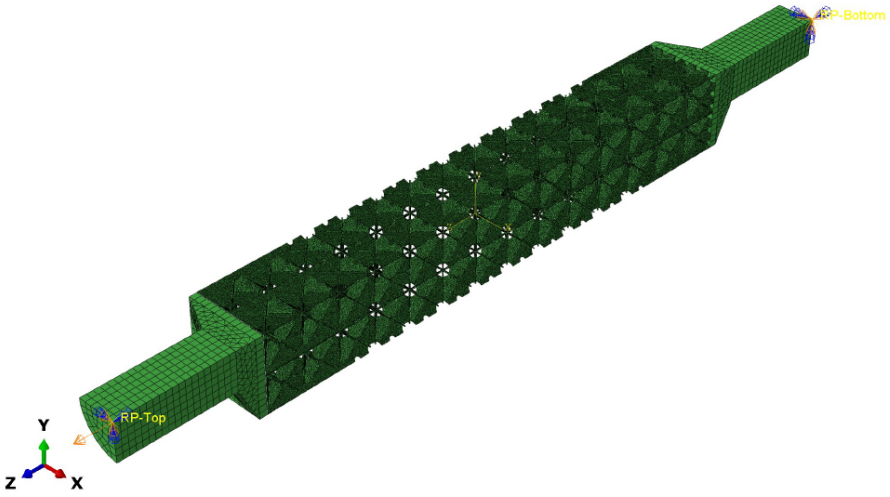

Figure 4.14: Example of full dimension specimen. It is a fourth of it because symmetric boundary conditions are applied on the two later face sheets.

of different topologies and porosities allows comparisons and performance evaluation of the cells. Finally, the last paragraph describes the failure shape and its localization within the specimen and the cells.

Displacement values are extracted from Abaqus at two nodal surfaces defined in the model. Specifically, these surfaces correspond to the cross sections located at the two extremities of the test section, as shown in Fig. 4.15. For each node, the displacement value is extracted, the top and bottom values are subtracted, and the net displacement is obtained. Then, to derive a single displacement value used to plot the stress–strain curve of each specimen, the net displacements at all nodes are averaged over the cross section. Force values, which unlike the displacements remain constant along the specimen, are extracted from a reference point at the top.

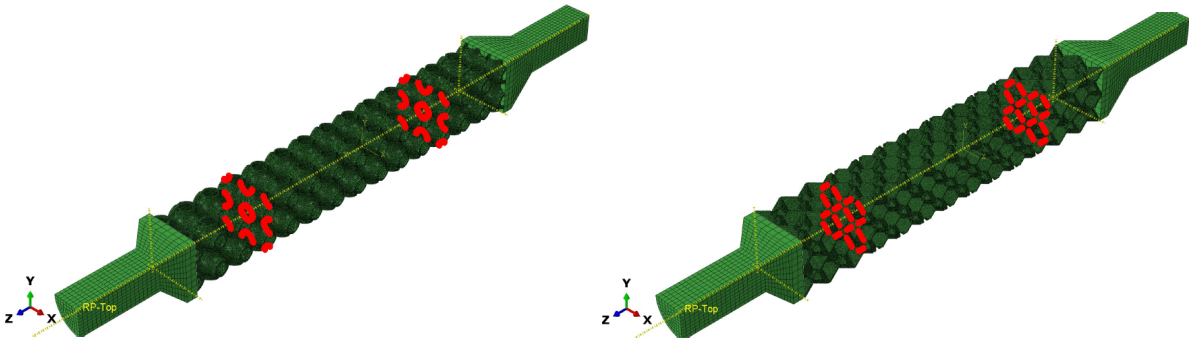

(a) Example with Primitive unit cell specimen.

(b) Example with FCC unit cell specimen.

Figure 4.15: Nodal surfaces for displacement data extraction.

Nominal stresses are determined by dividing the force by the initial cross-sectional area of the sample. Nominal strains are calculated by dividing the displacement by the initial height of the test section. Several authors who investigated the mechanical performance of TPMS and plate-based lattices have employed the same procedure [62, 106].

To assess the influence of relative density, it is appropriate to compare specific properties. These are defined by dividing the mechanical properties by the mass of the test section, which has been determined through Abaqus. This approach is reported and adopted in the paper by Alagha et al. [11].

4.3.1 Young's Modulus

In this paragraph, the stiffness results are presented. As already discussed, the mass scaling factor generates small oscillations in the stress–strain curves. To obtain smoother curves, a local smoothing has been applied. Specifically, the MATLAB function *smooth* was used with the *lowess* option and a parameter of 0.05. This function performs data smoothing through a local regression that reduces noise while preserving the underlying trend. With the *lowess* method, the algorithm fits a first-degree locally weighted regression to subsets of the data, assigning greater weight to points closest to the evaluation location [107]. The selected span value specifies that 5% of the data is included in each local fit, thus controlling the degree of smoothing: it averages the curve locally while maintaining its overall shape. The Young's moduli are obtained in the initial phase of deformation by linearly fitting the data collected during the first five seconds of the tensile simulations; a similar procedure was adopted by Zheng et al. [34].

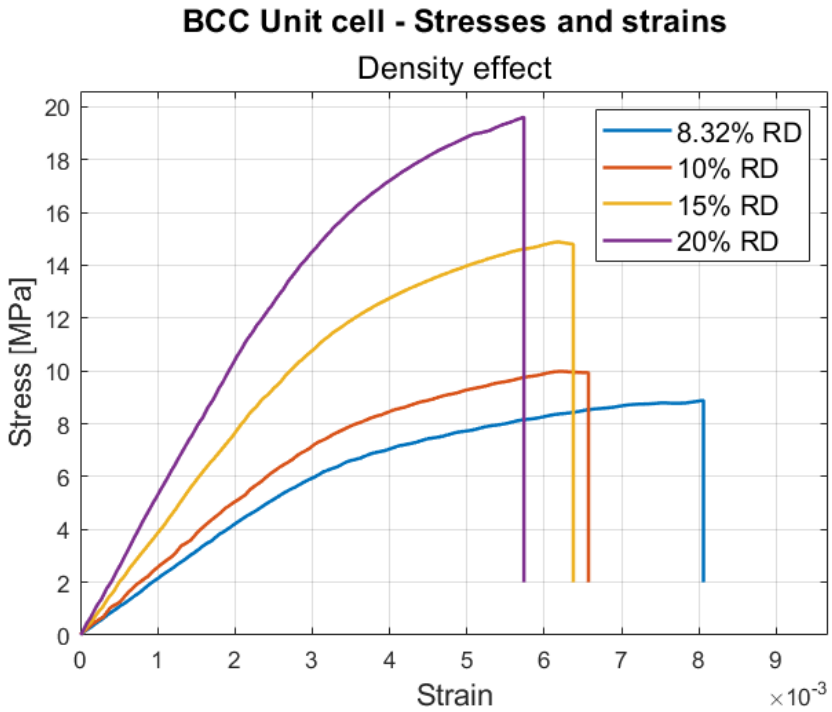

Figure 4.16: Stress and strain curves: impact of different porosities, for the BCC cell.

In Fig. 4.16 - 4.19, the stress-strain curves are shown and organised by topology to highlight the influence of relative density. Similarly, but limited to the common relative density values, the curves grouped according to the volume ratio are reported in Fig. 4.20 - 4.22, in order to emphasise the effect of the cell geometry. These curves exhibit a typical elasto-plastic response, with an initial linear elastic region followed by strain hardening. Soro et al. [32], who investigated TPMS lattices with Primitive, Gyroid and Diamond cells, although of skeletal type, observed similar curve shapes. Moreover, except for the Primitive cell, yield stress and ultimate tensile

strength are very close, as shown in the charts of Fig. 4.23 - 4.26, which confirms that these architectures predominantly display a brittle behaviour. In this regard, Kelly et al. [26], who examined the tensile response of Ti6Al4V Gyroid samples (50–90% porosity), reported the absence of a yield region, namely elastic deformation directly followed by failure. As expected, higher relative density values improve the stiffness [11, 25, 26]. Indeed, a linear trend can be identified for every topology, as clearly visible in Fig. 4.27 - 4.30. This linear behaviour is also reported in [10].

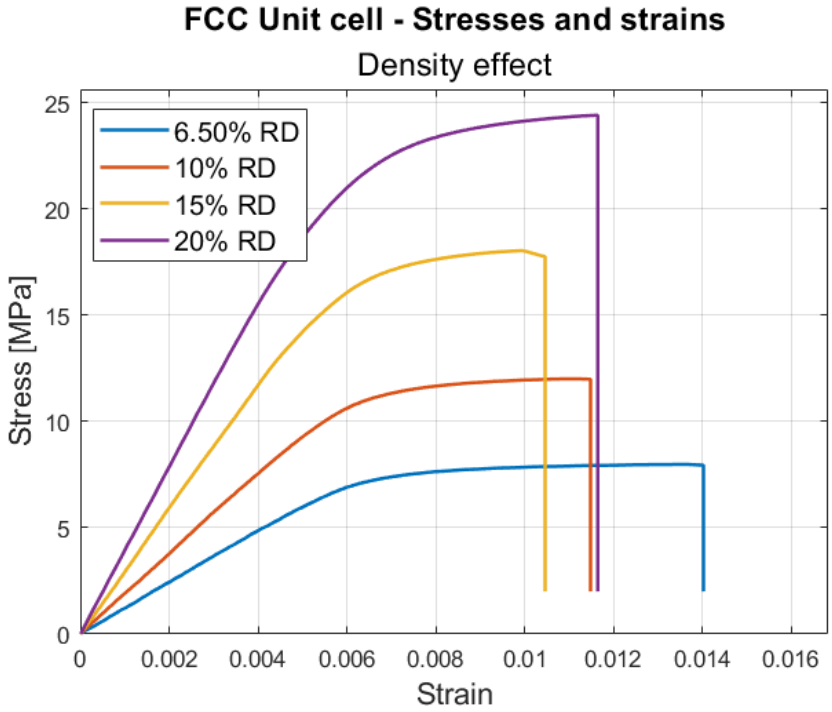

Figure 4.17: Stress and strain curves: impact of different porosities, for the FCC cell.

Generally, when comparing two different alloys, the one with lower stiffness typically exhibits greater ductility. This behaviour has also been found in lattice structures. Indeed, Zhuo et al. [108] (Norway, Germany) investigated the compressive performance of sheet-TPMS Gyroid samples, fabricated by SLM using the Inconel alloy 718, and experienced that lower porosities lead to higher stiffness and lower ductility. Nevertheless, for the curves in Fig. 4.16 - 4.19, this trend is not strictly observed for the analysed metamaterials. Indeed, only the BCC architecture follows the expected *higher stiffness–lower ductility* behaviour, while the 20% FCC specimen and the 10% TPMS ones deviate from this general trend.

The curves in Fig. 4.20 - 4.22 and the bars in Fig. 4.31 - 4.33 facilitate the identification of both common features and distinguishing characteristics of the different cell architectures. It is generally accessed that plate-based lattice materials exhibit higher stiffness values, compared to truss and TPMS lattices [11, 24]. The bar charts presented in this and the following chapter indicate that the results obtained in this thesis are consistent with that observation, also because it is necessary to consider that cut-outs are reducing the cells' performance compared to those achievable with closed geometries. At every density, the Primitive shape is the least stiff and most ductile cell, whereas the BCC cell is the stiffest and most brittle. The Gyroid and FCC architectures display very similar stiffness; upon closer examination, the former has a slightly higher Young's modulus, while the latter exhibits slightly greater ductility. Relative density

also influences the mechanical performance among the different architectures. Indeed, while at 10% volume fraction the stiffness of BCC cells is about 2.5 times that of the Primitive cell, and that of the Gyroid almost twice, these differences decrease as the relative density increases. In this context, it is worth noting that, according to García-Gutiérrez et al. [7], mechanical properties are particularly influenced by topology at low relative densities. The highest withstandable strain is observed in the Primitive 4.30% relative density specimen, which reaches a deformation of 2.4% at failure. The heaviest sample of the same geometry still achieves a strain at failure of 2.0%. In contrast, the BCC cell reaches a strain at failure ranging between 0.57% and 0.81%. Finally, the FCC and Gyroid architectures show similar values: the former ranges from 1.05% to 1.40%, while the latter, slightly more brittle, ranges from 0.91% to 1.22%.

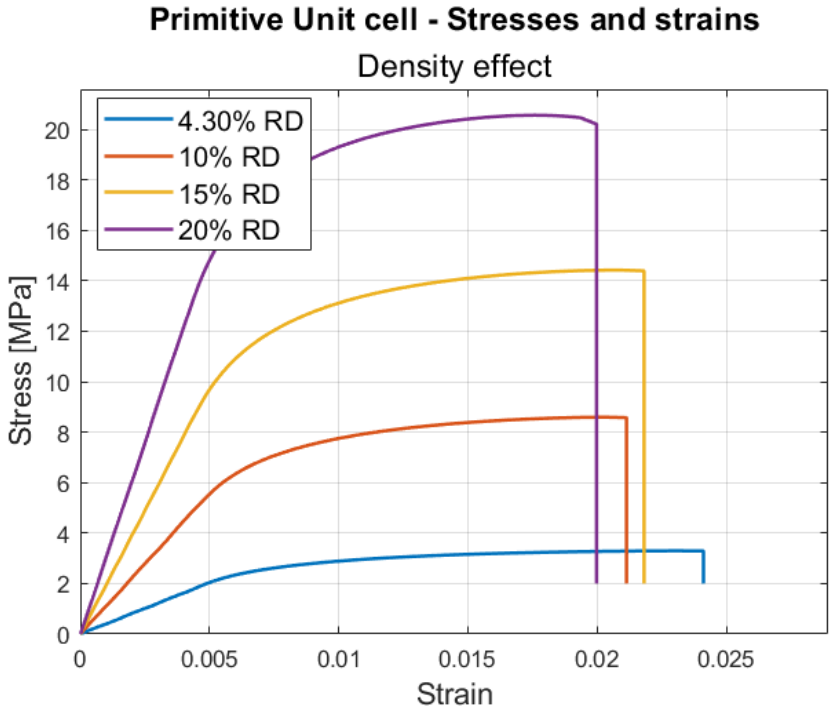

Figure 4.18: Stress and strain curves: impact of different porosities, for the Primitive cell.

Finally, the specific Young's modulus values exhibit a positive linear trend, as shown in Fig. 4.34 - 4.37. Plate-based architectures show a weaker dependence, with variations of about 5% across the extreme studied densities, whereas for TPMS cells the specific Young's modulus increases linearly and significantly with volume ratio. Alagha et al. [11] reported minimal effects on specific stiffness for TPMS Diamond and plate-based hybrid BCC–FCC–SC cells.

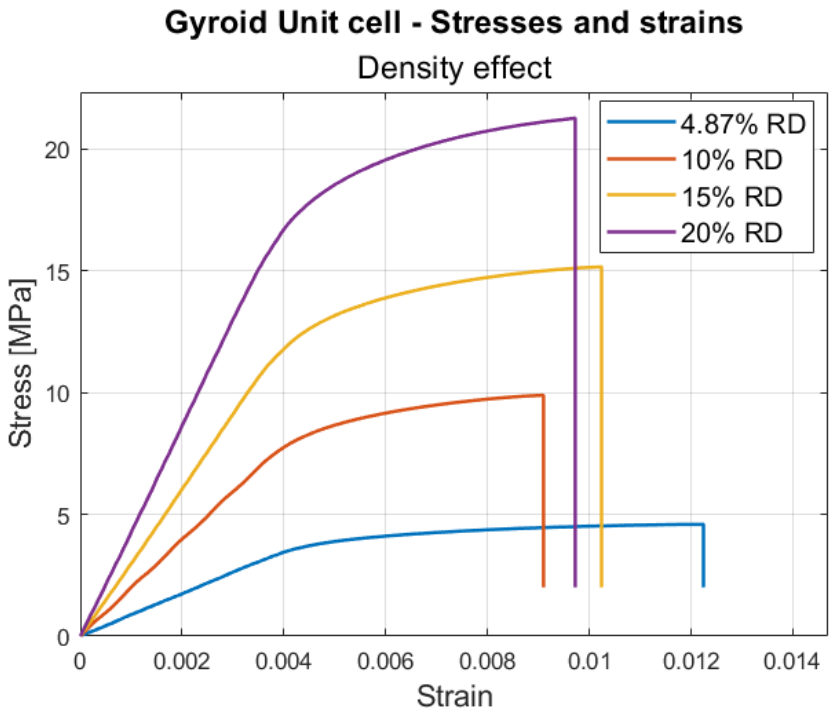

Figure 4.19: Stress and strain curves: impact of different porosities, for the Gyroid cell.

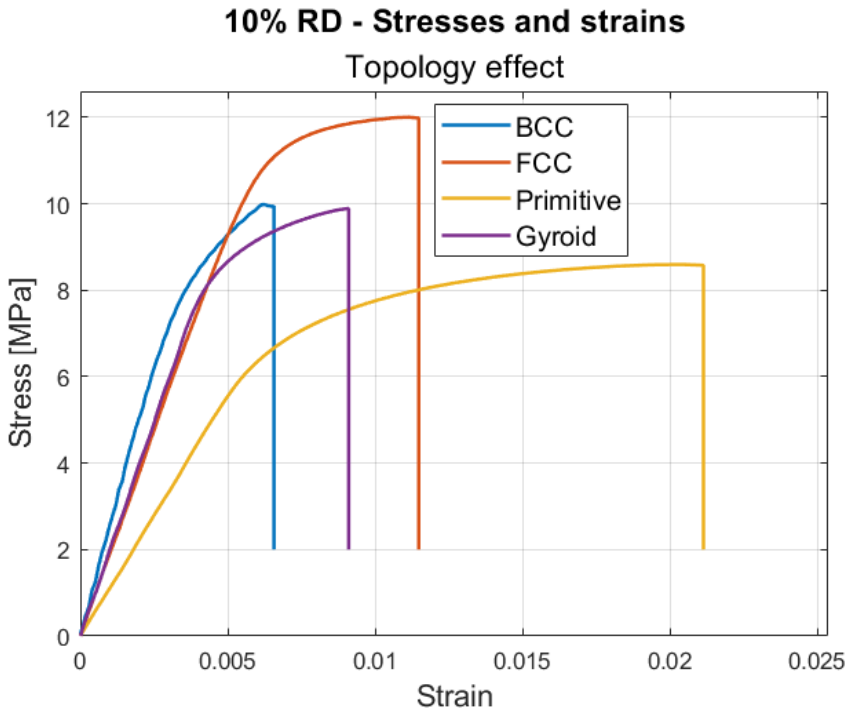

Figure 4.20: Stress and strain curves: impact of different topologies, for 10% rel. density specimens.

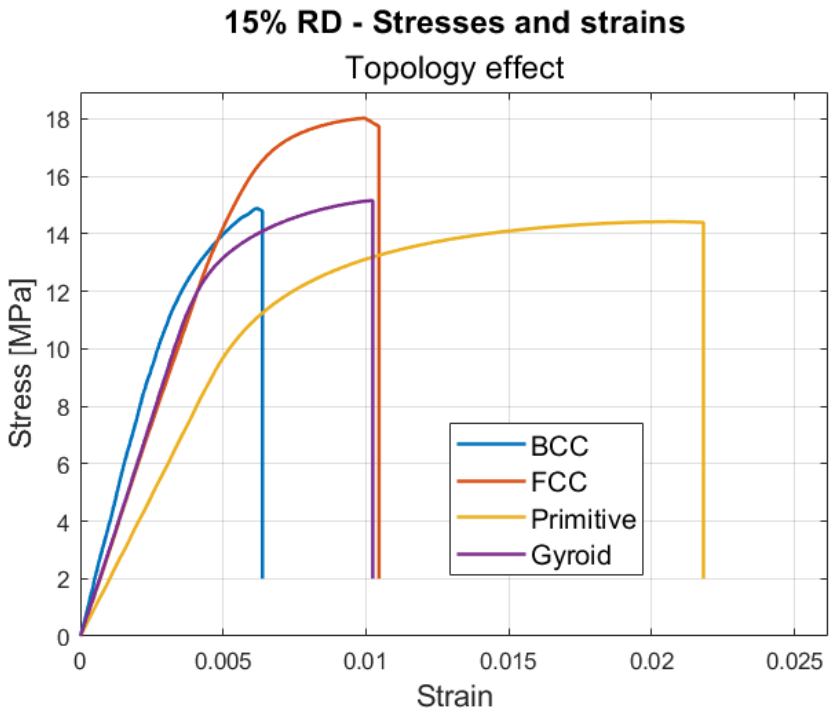

Figure 4.21: Stress and strain curves: impact of different topologies, for 15% rel. density specimens.

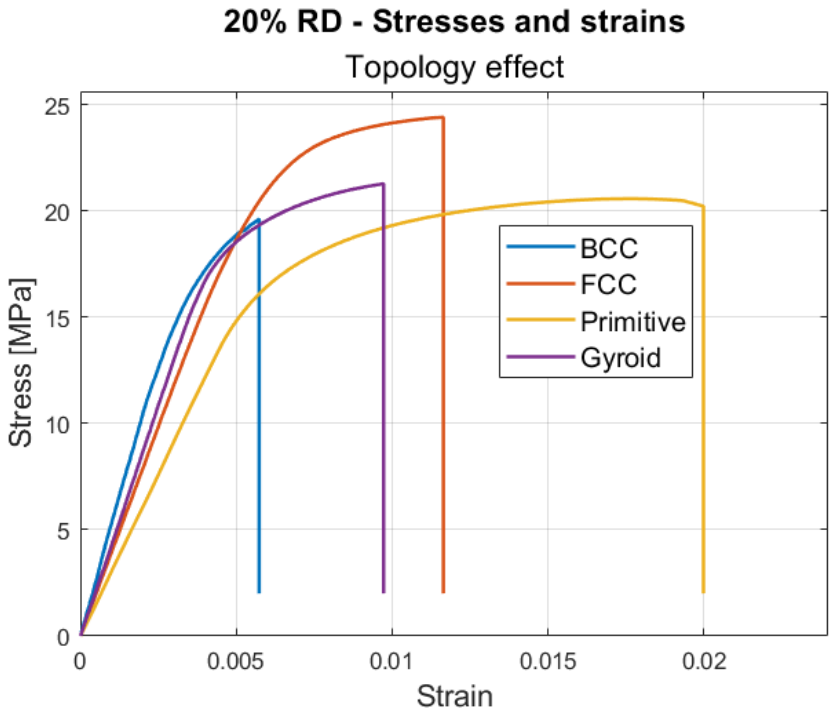

Figure 4.22: Stress and strain curves: impact of different topologies, for 20% rel. density specimens.

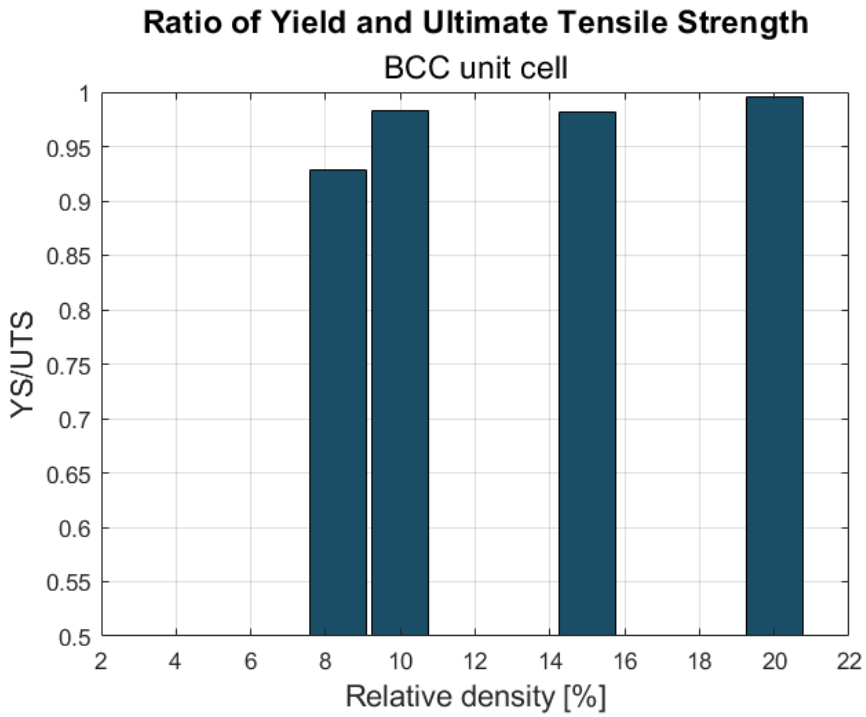

Figure 4.23: Bar charts illustrating the ratio between yield stress and ultimate tensile strength as a function of relative density, for the BCC cell.

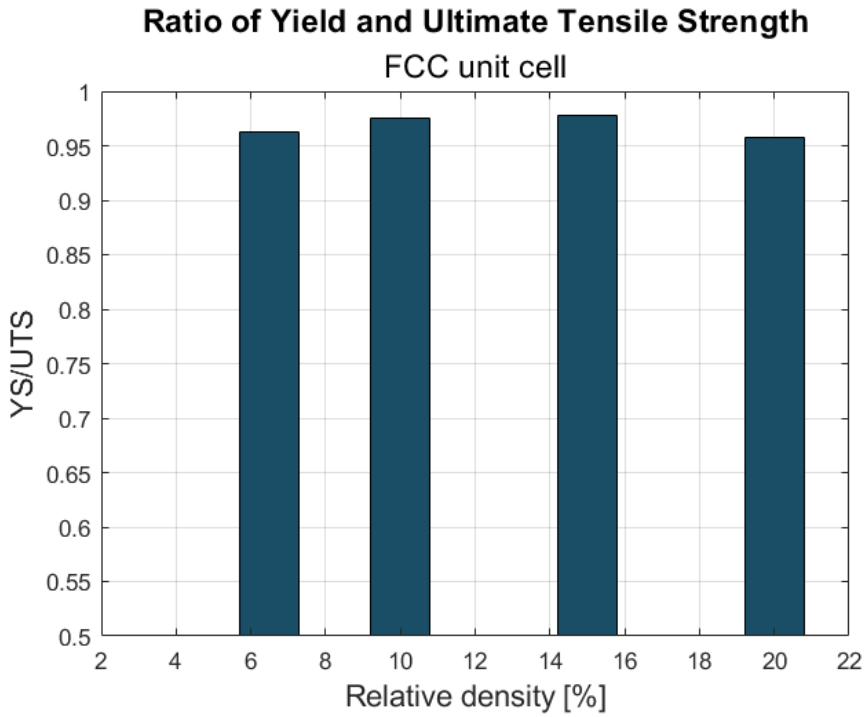

Figure 4.24: Bar charts illustrating the ratio between yield stress and ultimate tensile strength as a function of relative density, for the FCC cell.

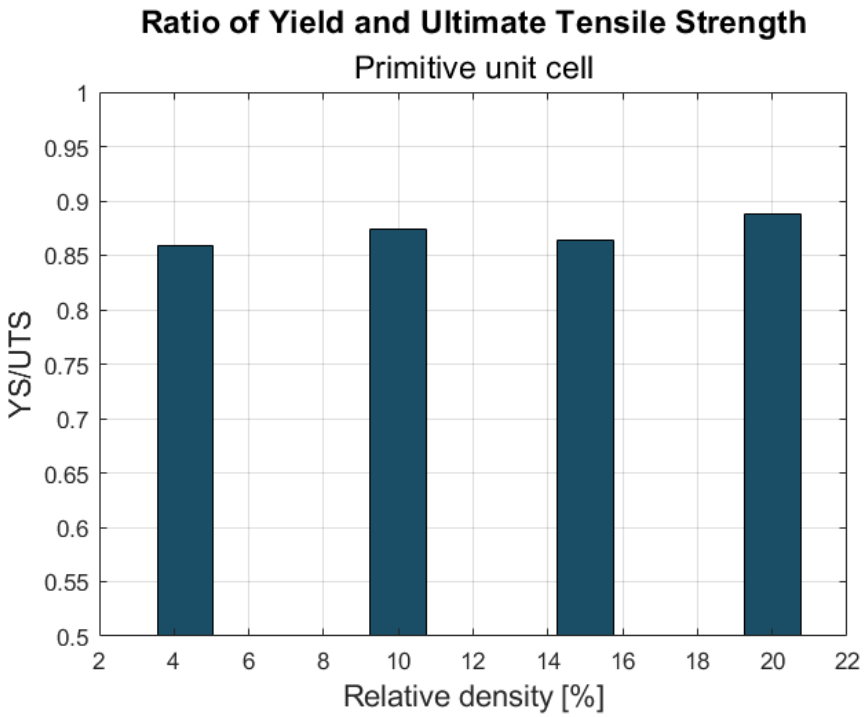

Figure 4.25: Bar charts illustrating the ratio between yield stress and ultimate tensile strength as a function of relative density, for the Primitive cell.

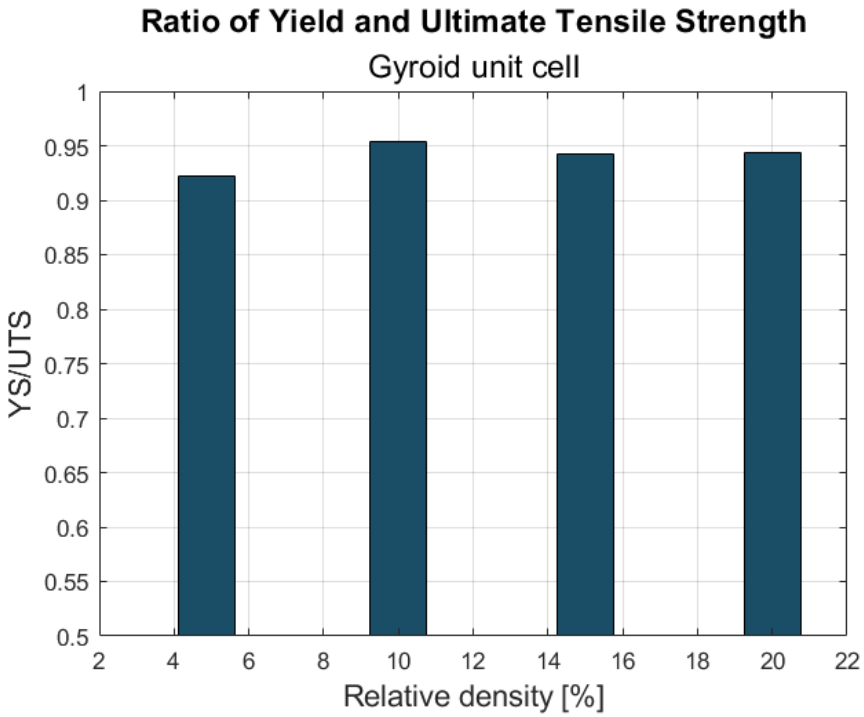

Figure 4.26: Bar charts illustrating the ratio between yield stress and ultimate tensile strength as a function of relative density, for the Gyroid cell.

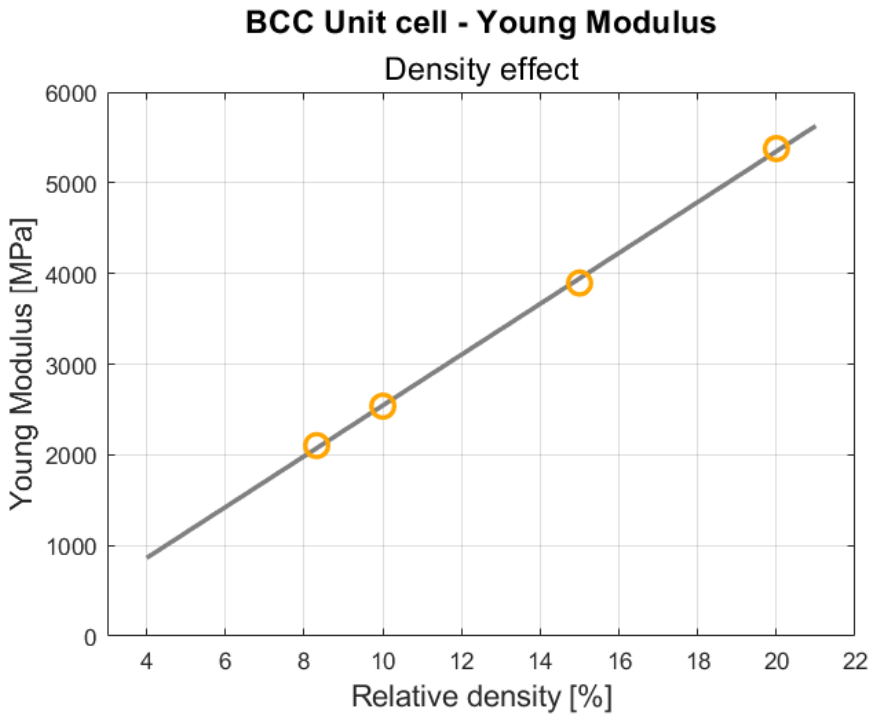

Figure 4.27: Young's modulus as a function of relative density: graphical representation of the dependency, for the BCC cell.

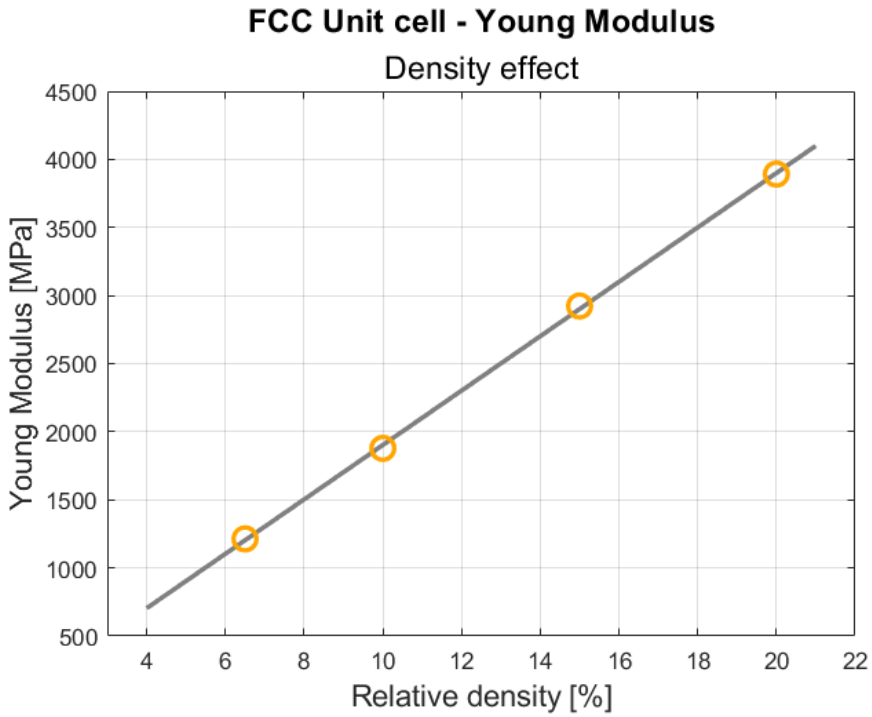

Figure 4.28: Young's modulus as a function of relative density: graphical representation of the dependency, for the FCC cell.

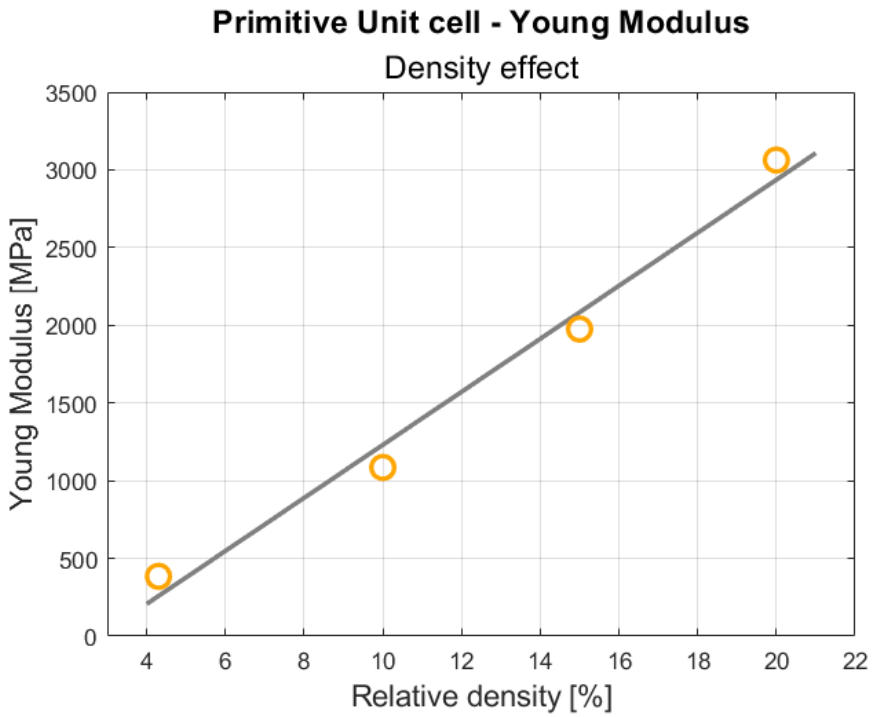

Figure 4.29: Young's modulus as a function of relative density: graphical representation of the dependency, for the Primitive cell.

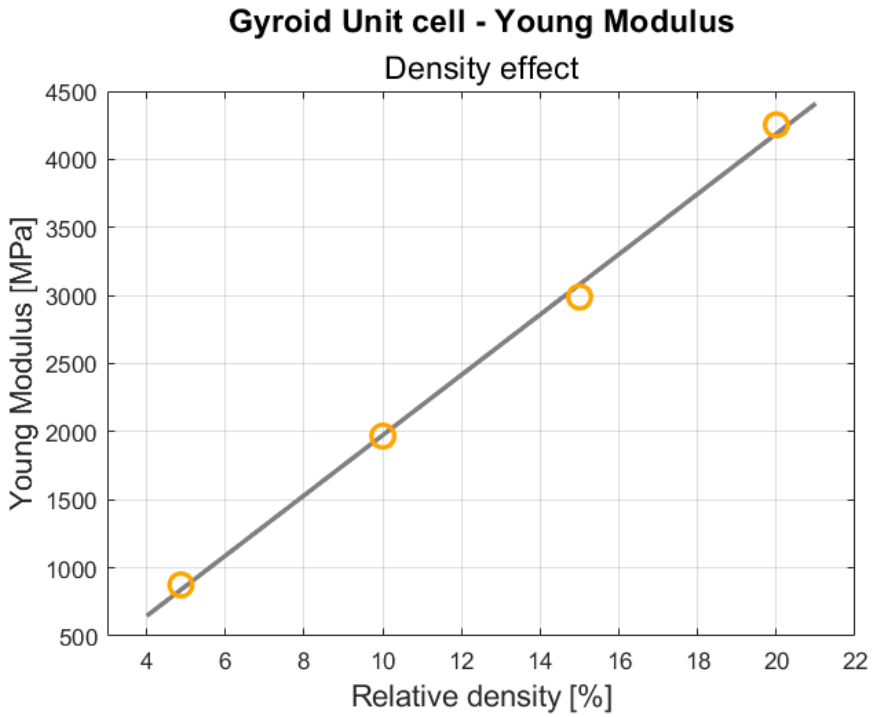

Figure 4.30: Young's modulus as a function of relative density: graphical representation of the dependency, for the Gyroid cell.

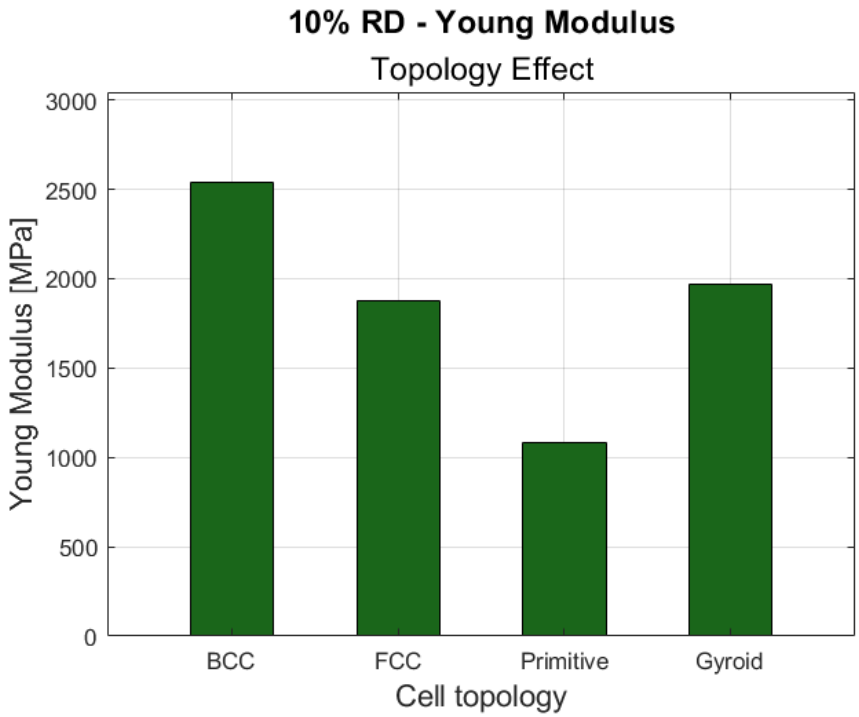

Figure 4.31: Bar charts depicting the influence of lattice topology on Young's modulus at the common relative density levels, for 10% rel. density specimens.

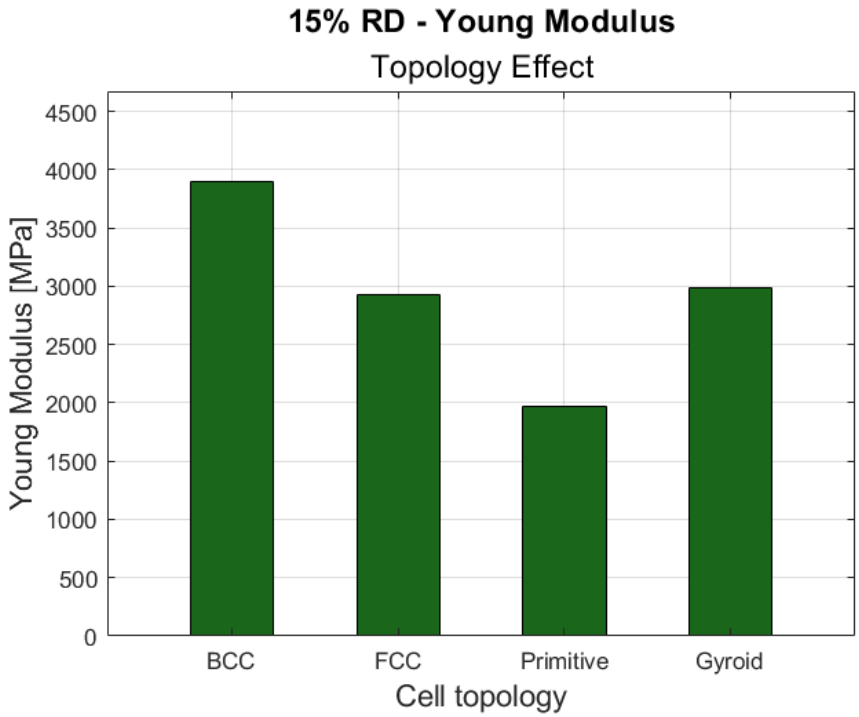

Figure 4.32: Bar charts depicting the influence of lattice topology on Young's modulus at the common relative density levels, for 15% rel. density specimens.

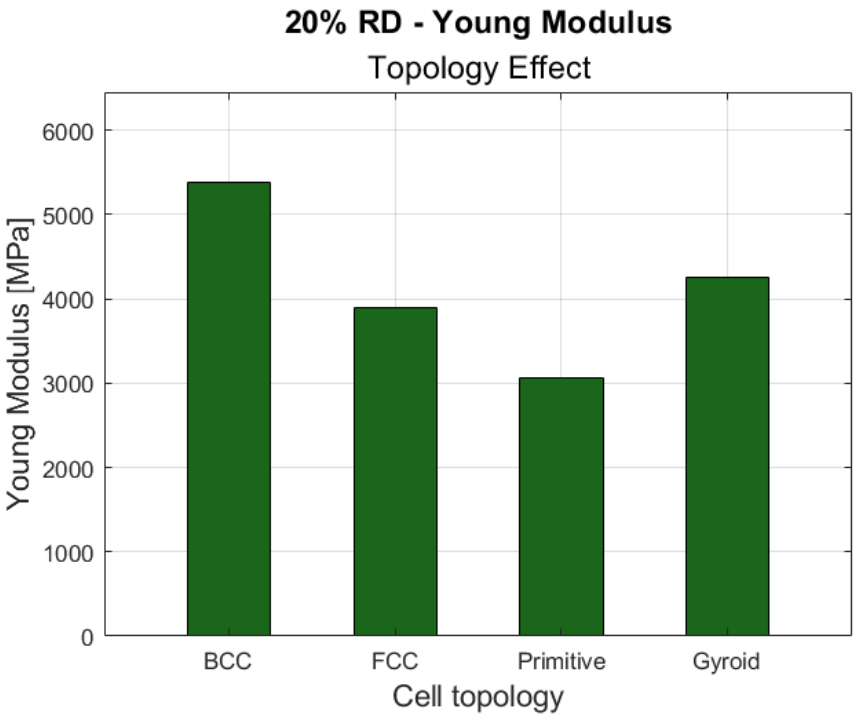

Figure 4.33: Bar charts depicting the influence of lattice topology on Young's modulus at the common relative density levels, for 20% rel. density specimens.

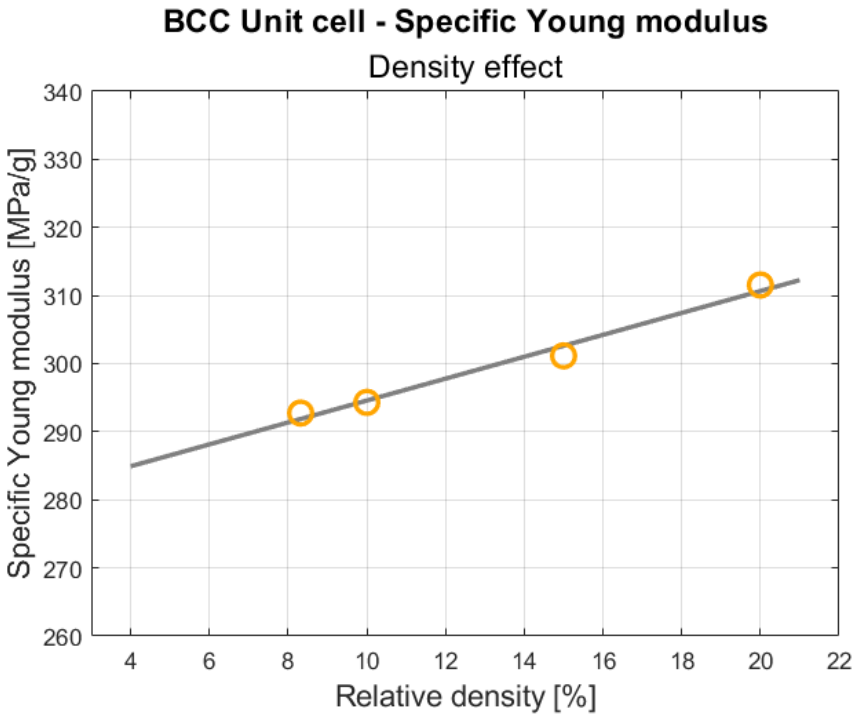

Figure 4.34: Specific Young's modulus as a function of relative density: graphical representation of the dependency, for the BCC cell.

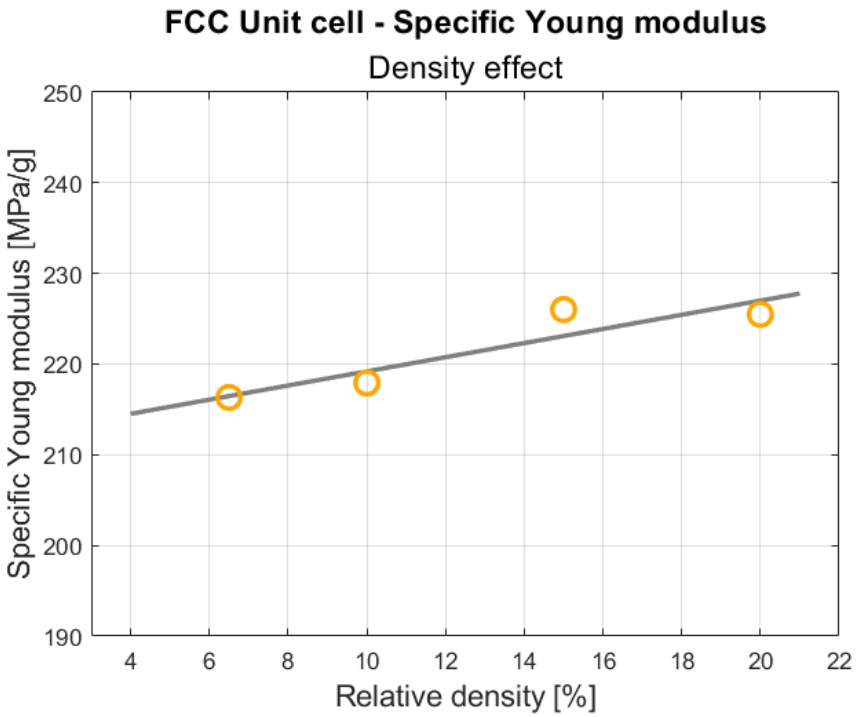

Figure 4.35: Specific Young's modulus as a function of relative density: graphical representation of the dependency, for the FCC cell.

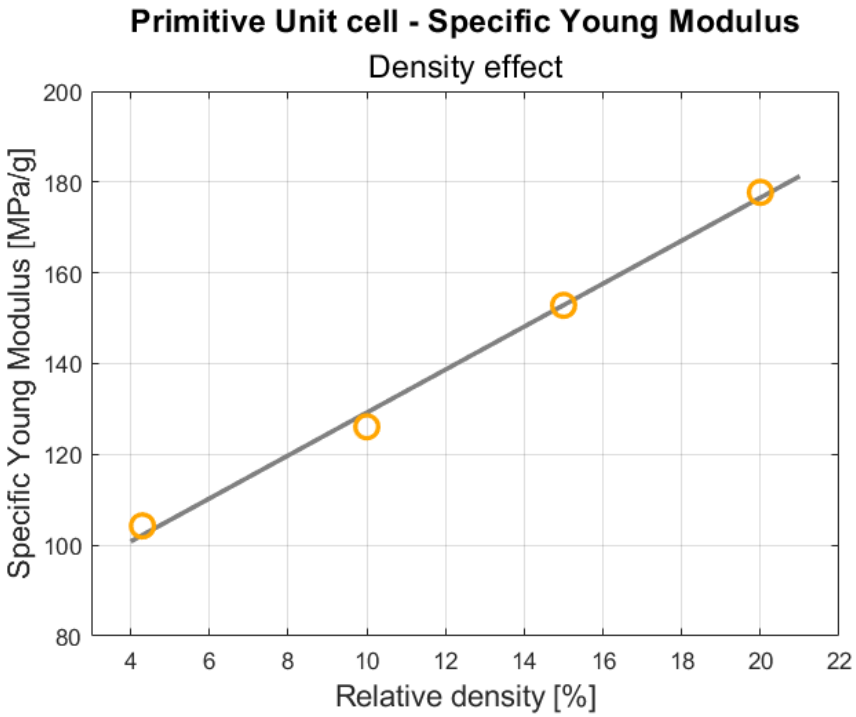

Figure 4.36: Specific Young's modulus as a function of relative density: graphical representation of the dependency, for the Primitive cell.

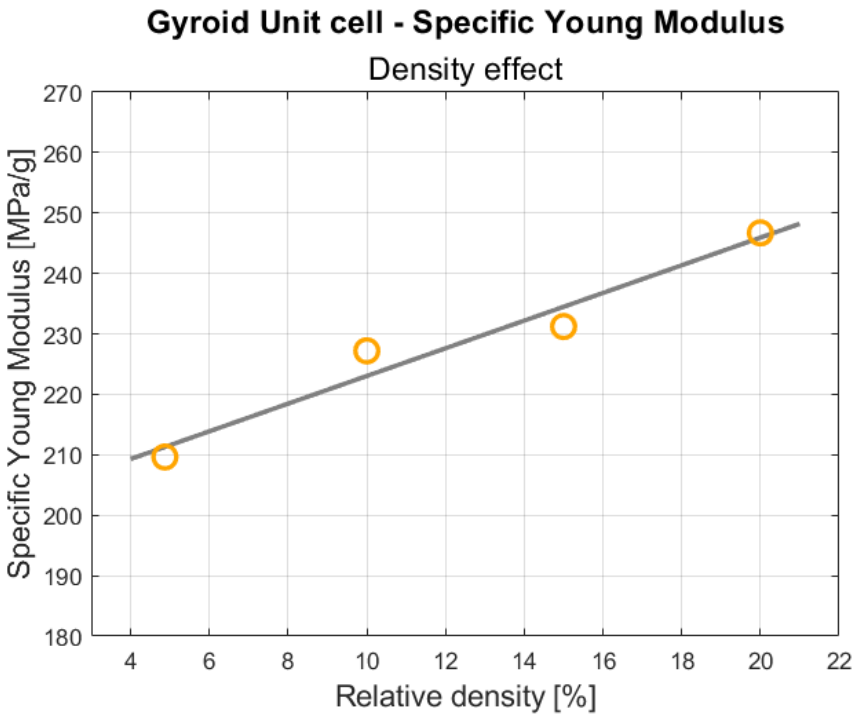

Figure 4.37: Specific Young's modulus as a function of relative density: graphical representation of the dependency, for the Gyroid cell.

CELL	**Rel. Density** [%]	**Mass** [g]	**Young Modulus** [MPa]	**Spec. Young Mod.** [MPa/g]
BCC	8.32	7.179	2102	292.7
	10.0	8.618	2536	294.3
	15.0	12.934	3895	301.1
	20.0	17.260	5377	311.5
FCC	6.50	5.608	1213	216.3
	10.0	8.617	1878	217.9
	15.0	12.933	2923	226.0
	20.0	17.260	3892	225.5
Primitive	4.30	3.690	385	104.3
	10.0	8.608	1085	126.1
	15.0	12.924	1975	152.8
	20.0	17.233	3063	177.7
Gyroid	4.87	4.175	875	209.6
	10.0	8.661	1968	227.2
	15.0	12.930	2990	231.2
	20.0	17.240	4253	246.7

Table 4.5: Mass values and Young's moduli determined from the tensile simulations.

4.3.2 Yield and Ultimate Tensile Strength

In this paragraph, the yield strength (YS) and ultimate tensile strength results are presented. As it is common practice for materials that do not exhibit a clearly defined yield point, a residual plastic strain of 0.2% has been considered to identify its value. Accordingly, the yield strength is determined as the intersection between the stress–strain curve and a line whose slope corresponds to the Young's modulus, determined at Par. 4.3.1, and which intersects the x-axis at $(0.002, 0)$. Finally, the UTS is obtained as the maximum force reached during the simulation divided by the nominal cross-sectional area of the specimen.

As can be observed from Fig. 4.38 - 4.45, the increase in relative density benefits both the yield and ultimate tensile strength, independently of the cell topology. Moreover, a linear relationship between these two characteristic stresses and the volume ratio is observed. In contrast, the specific mechanical properties are almost independent of the volume fraction, as can be seen in Fig. 4.46 - 4.53. These results agree with Alagha et al. [11]. Indeed, the authors reported that the specific strength is independent of relative density for the TPMS Diamond cell, while only a weak influence was observed for the plate-based SC–BCC–FCC hybrid cell. In this thesis it has been found that the specific YS is essentially unrelated to the relative density, while the specific UTS shows a weak negative trend for plate-based cells and a weak positive trend for TPMS cells. These opposite trends could be related to the presence of cut-outs which, although simplify manufacturing, they also reduce mechanical properties compared to closed cells. Additionally, due to the sphere-based approach, increases in relative density, and thus plate thickness, are accompanied by larger cut-outs radii, which can weaken the structure. Meanwhile, TPMS architectures benefit from higher volume ratios.

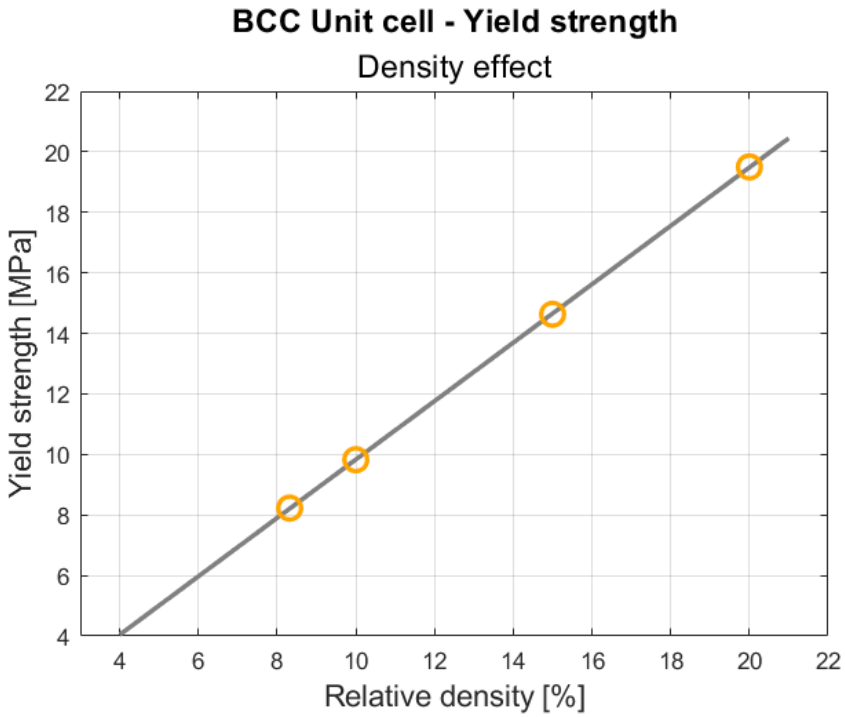

Figure 4.38: Yield strength as a function of relative density: graphical representation of the dependency, for the BCC cell.

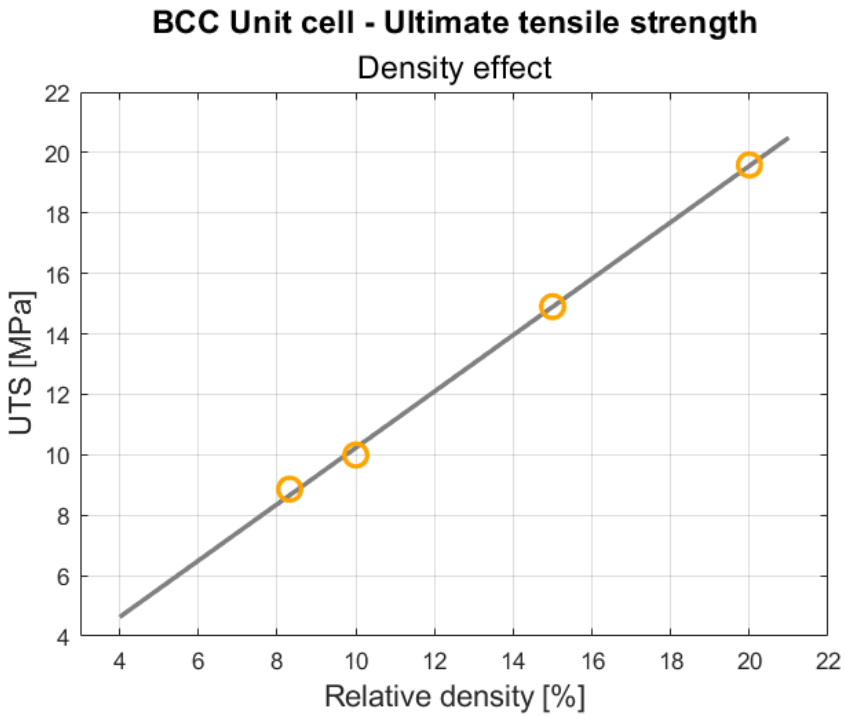

Figure 4.39: Ultimate tensile strength as a function of relative density: graphical representation of the dependency, for the BCC cell.

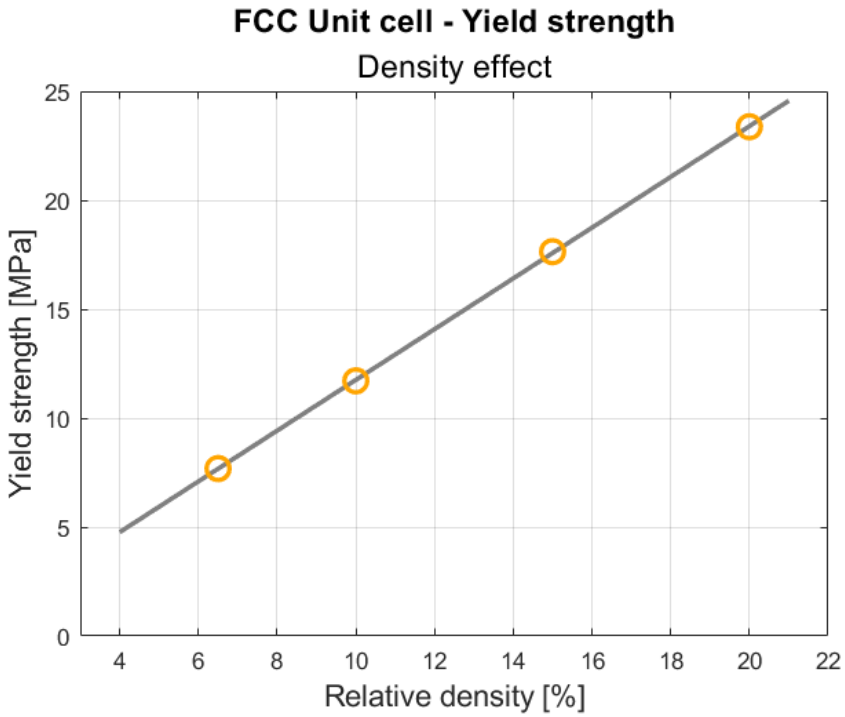

Figure 4.40: Yield strength as a function of relative density: graphical representation of the dependency, for the FCC cell.

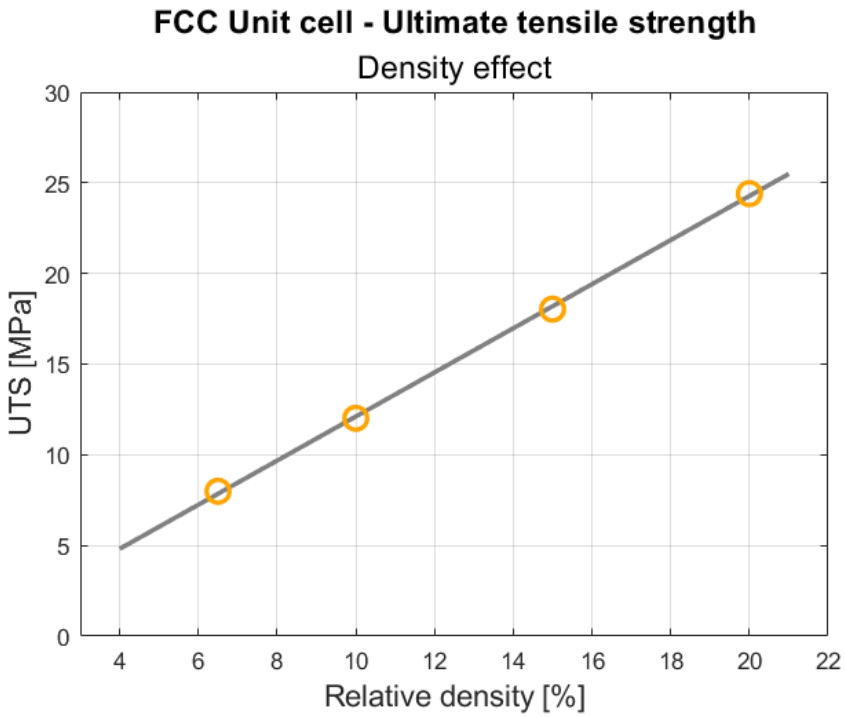

Figure 4.41: Ultimate tensile strength as a function of relative density: graphical representation of the dependency, for the FCC cell.

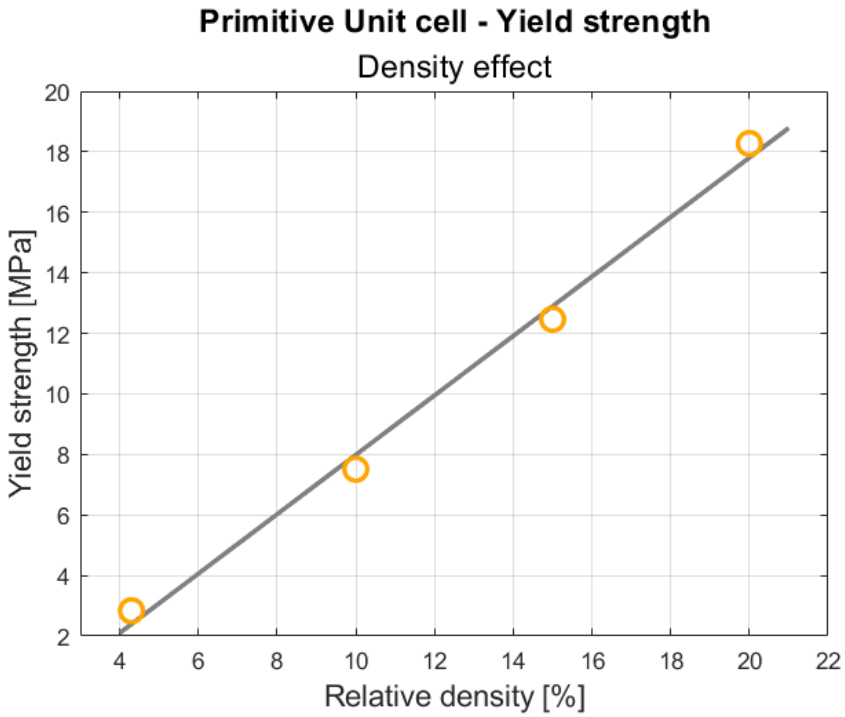

Figure 4.42: Yield strength as a function of relative density: graphical representation of the dependency, for the Primitive cell.

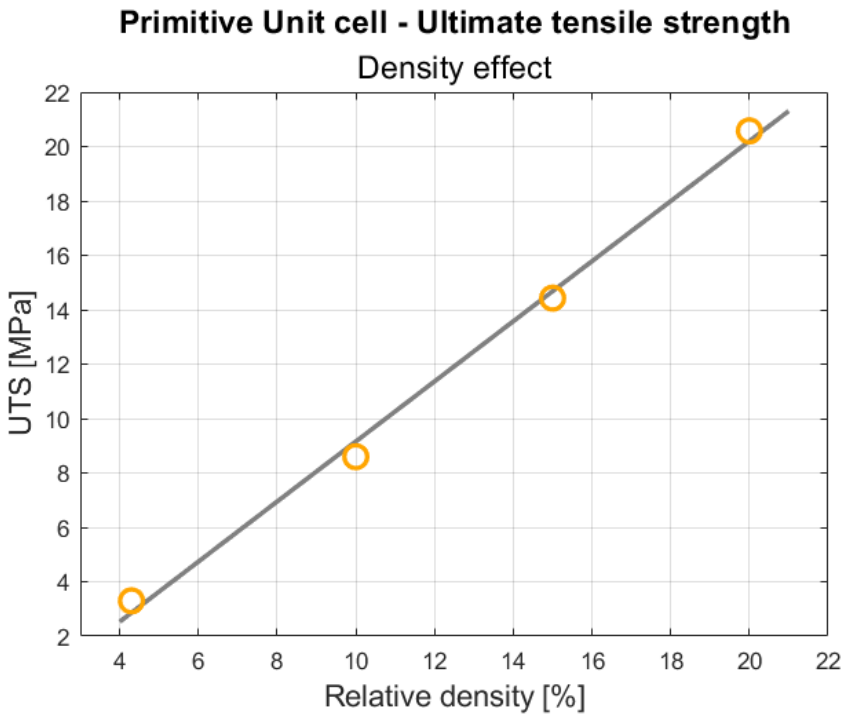

Figure 4.43: Ultimate tensile strength as a function of relative density: graphical representation of the dependency, for the Primitive cell.

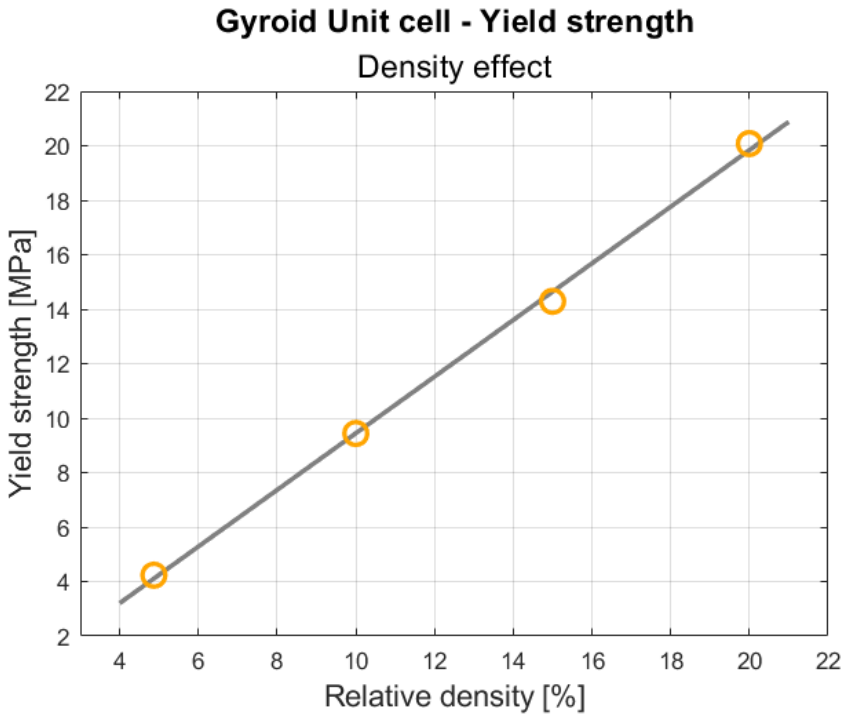

Figure 4.44: Yield strength as a function of relative density: graphical representation of the dependency, for the Gyroid cell.

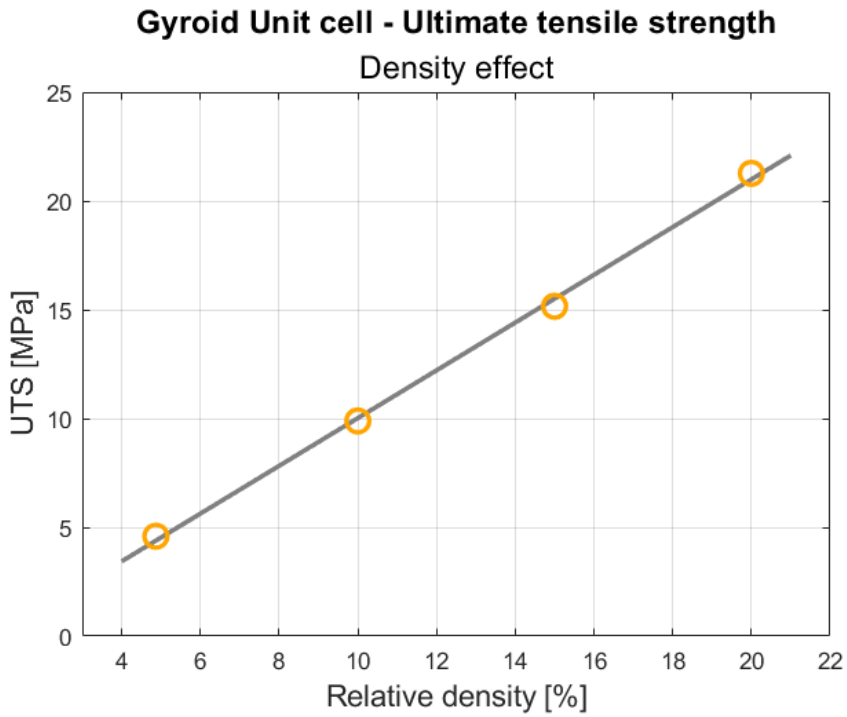

Figure 4.45: Ultimate tensile strength as a function of relative density: graphical representation of the dependency, for the Gyroid cell.

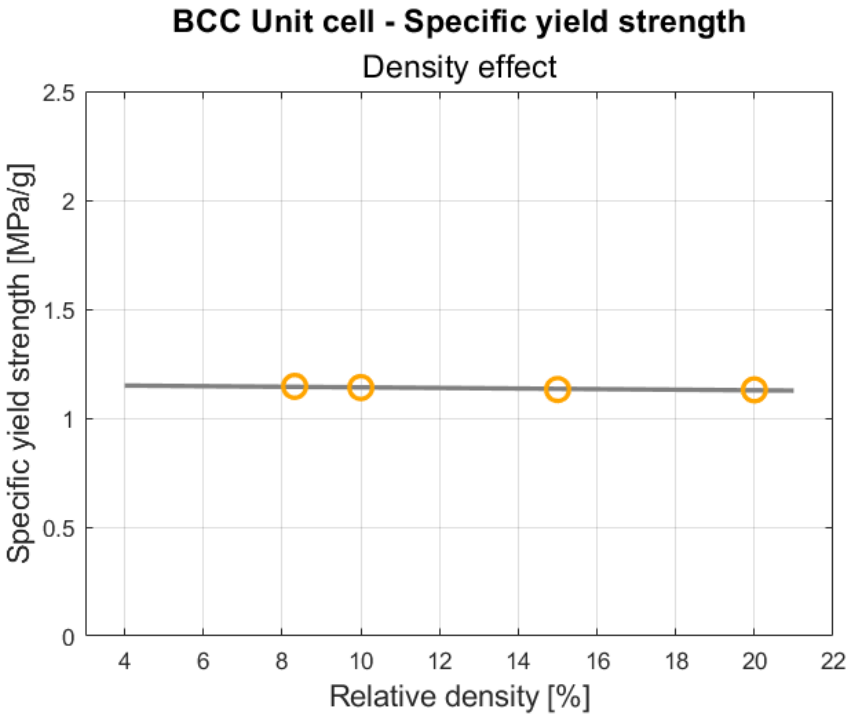

Figure 4.46: Specific yield strength as a function of relative density: graphical representation of the dependency, for the BCC cell.

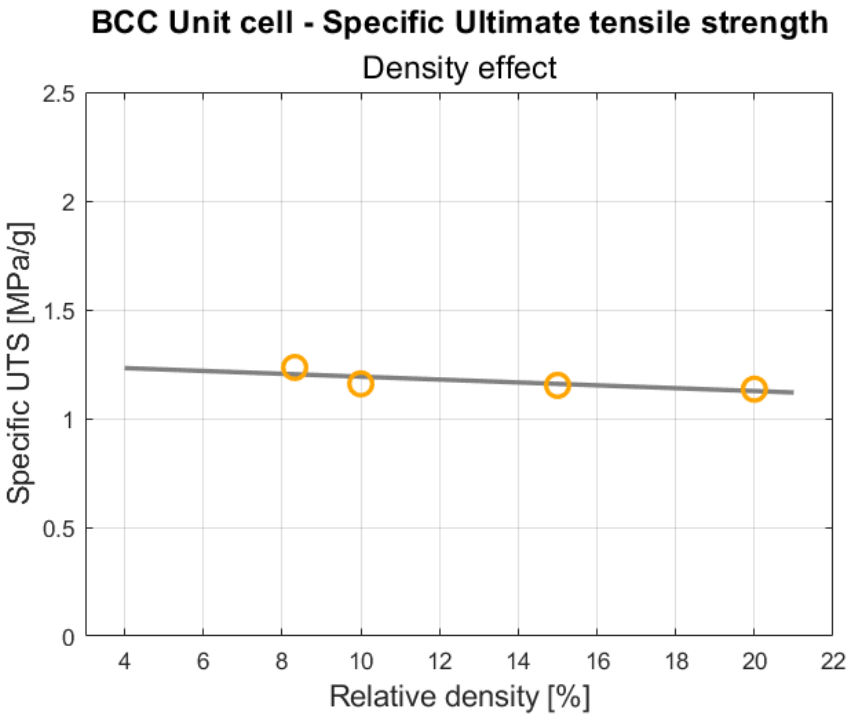

Figure 4.47: Specific ultimate tensile strength as a function of relative density: graphical representation of the dependency, for the BCC cell.

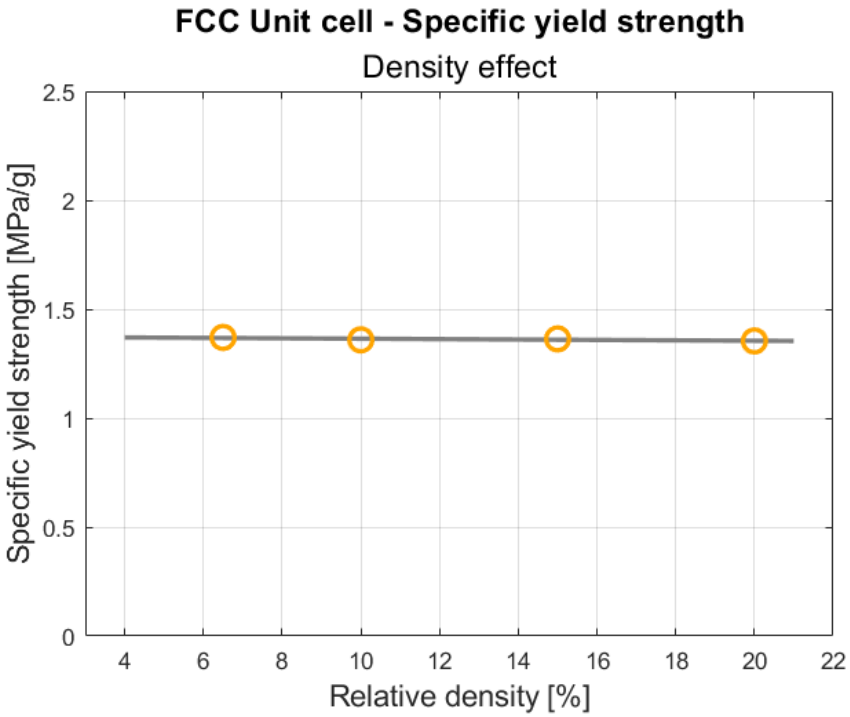

Figure 4.48: Specific yield strength as a function of relative density: graphical representation of the dependency, for the FCC cell.

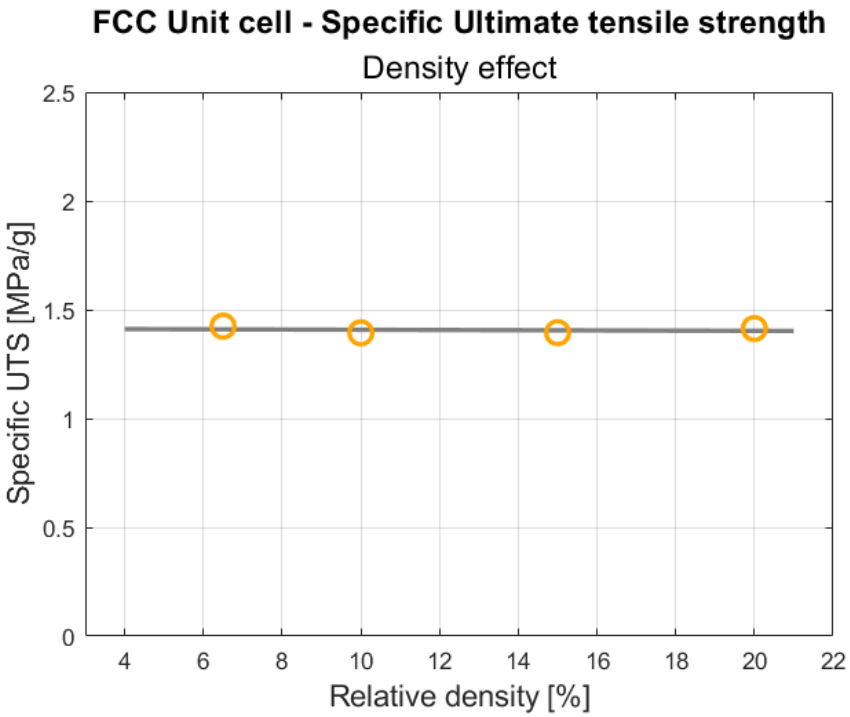

Figure 4.49: Specific ultimate tensile strength as a function of relative density: graphical representation of the dependency, for the FCC cell.

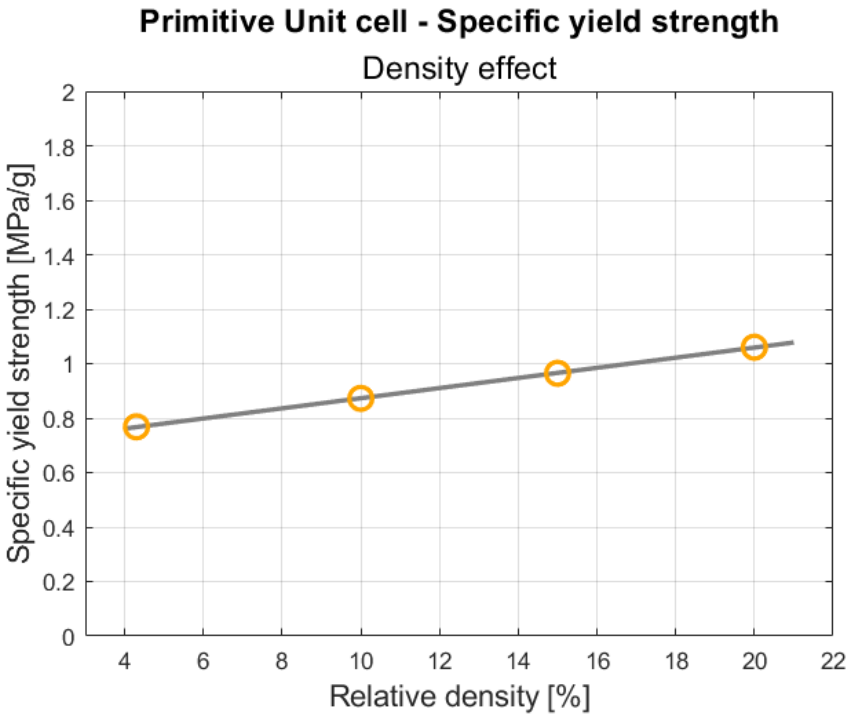

Figure 4.50: Specific yield strength as a function of relative density: graphical representation of the dependency, for the Primitive cell.

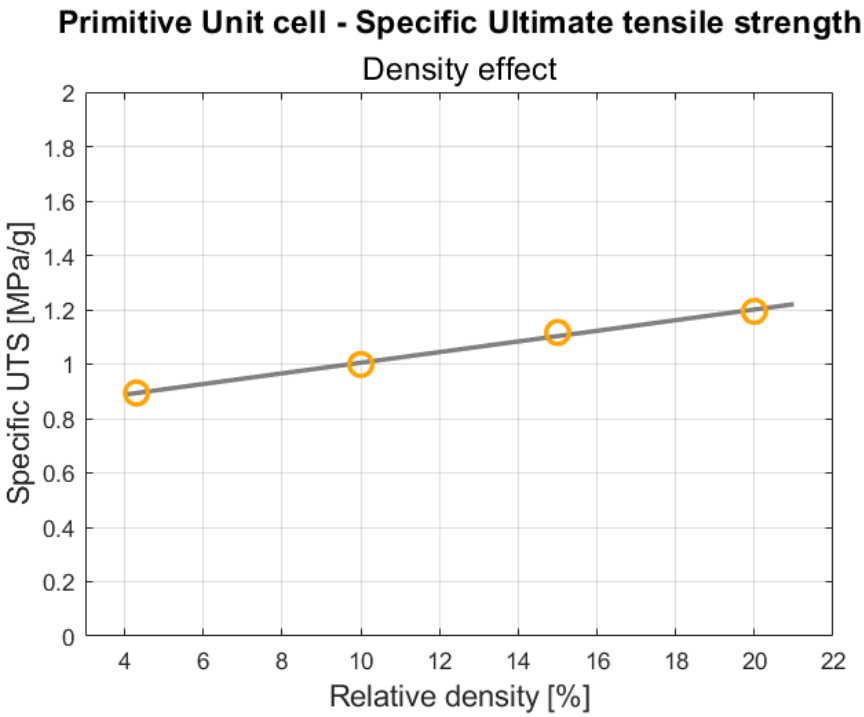

Figure 4.51: Specific ultimate tensile strength as a function of relative density: graphical representation of the dependency, for the Primitive cell.

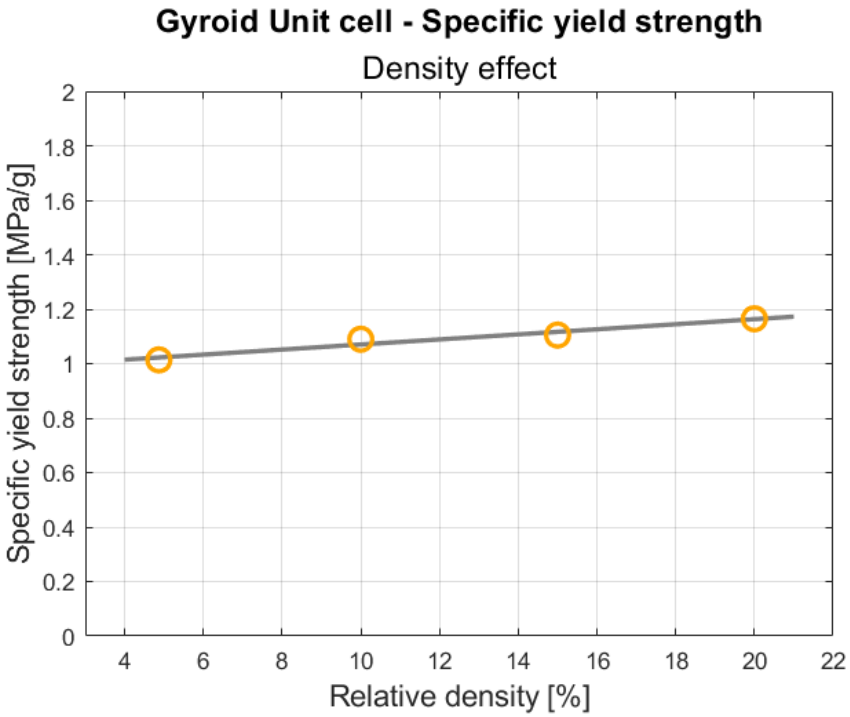

Figure 4.52: Specific yield strength as a function of relative density: graphical representation of the dependency, for the Gyroid cell.

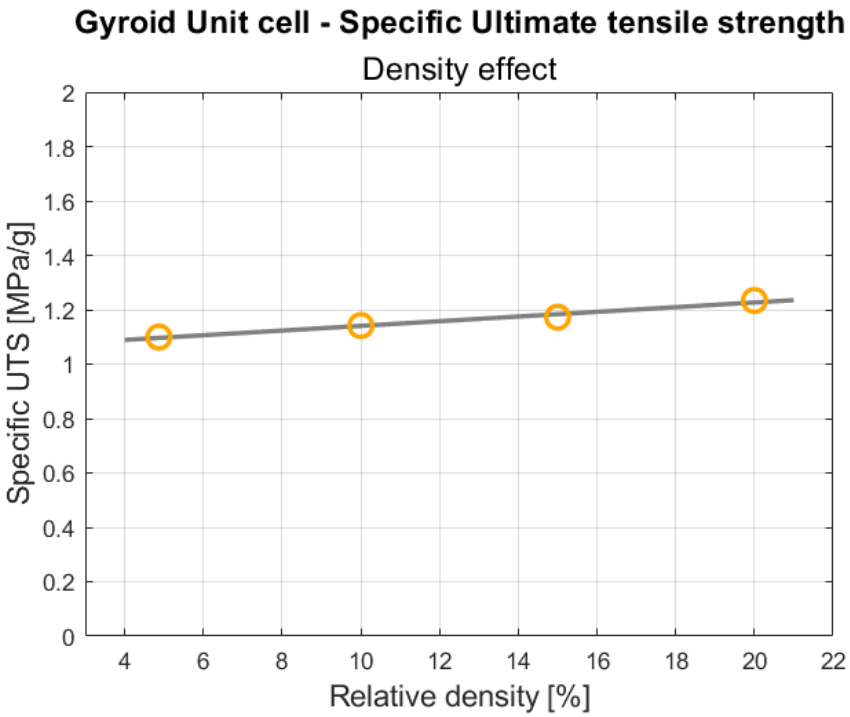

Figure 4.53: Specific ultimate tensile strength as a function of relative density: graphical representation of the dependency, for the Gyroid cell.

It is also noteworthy to examine the bar charts in Fig. 4.23 - 4.26, which have been constructed to analyse the brittle or ductile behaviour of the studied metamaterials. Specifically, the ratios between the yield and ultimate tensile strength have been plotted as a function of relative density and classified according to the cell shape. It can be observed that all the structures, regardless of porosity or architecture, exhibit a very brittle behaviour, since the maximum stress the structure can withstand is only slightly higher than the yield point. Upon closer inspection, the higher ductility of the Primitive cell, compared to the other cells, which was already highlighted based on the stress–strain curves, is again evident. This cell exhibits the lowest yield-to-ultimate tensile strength ratio. Qualitatively, the Gyroid geometry follows, then the FCC cell, while the BCC architecture is generally the most brittle. No clear trend or dependence on relative density is apparent.

Finally, by comparing the different topologies at a given relative density, and with the support of Fig. 4.54 - 4.56, the following conclusions can be drawn. At every studied porosity, the FCC unit cell exhibits the highest yield stress and ultimate tensile strength, aligning with [22, 24], whereas the Primitive architecture almost always displays the lowest mechanical properties. Nevertheless, the influence of cell shape is also affected by the volume ratio. Indeed, while at 10% relative density the BCC cell has the second-highest mechanical performance, at 15% its UTS is lower than that of the Gyroid cell, and at 20% it is lower than both the Gyroid and Primitive cells. For instance, at 10% volume fraction, the FCC UTS is approximately 1.20 times that of the Gyroid cell, decreasing to 1.15 at 20%. It is possible that at even higher densities, this trend could lead to a switch in the most resistant cell. These results highlight the importance, in practical applications, of selecting the metamaterial according to the loading conditions of the expected operative life, since different conditions may affect and alter the optimal configuration.

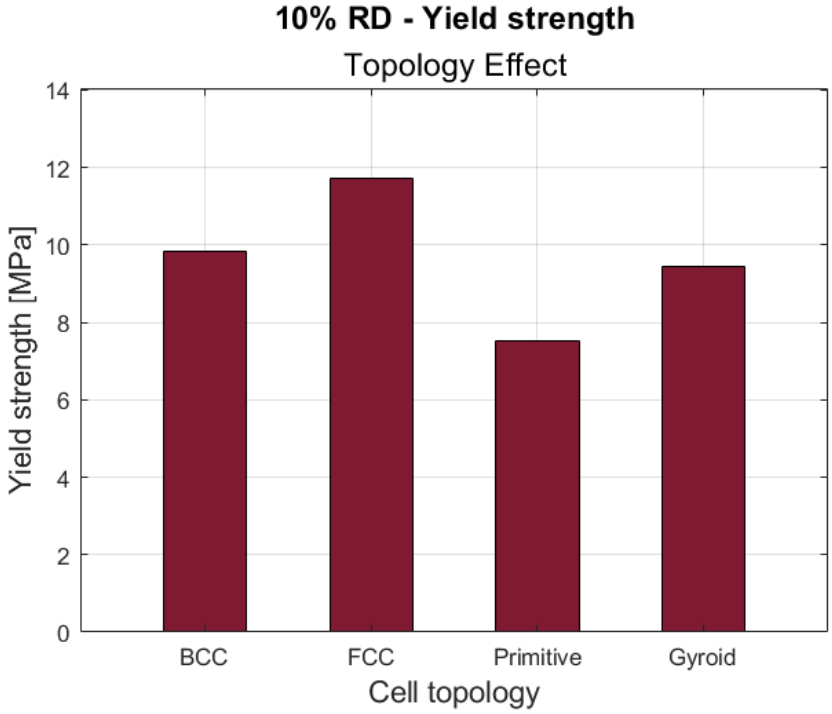

(a) Yield strength.

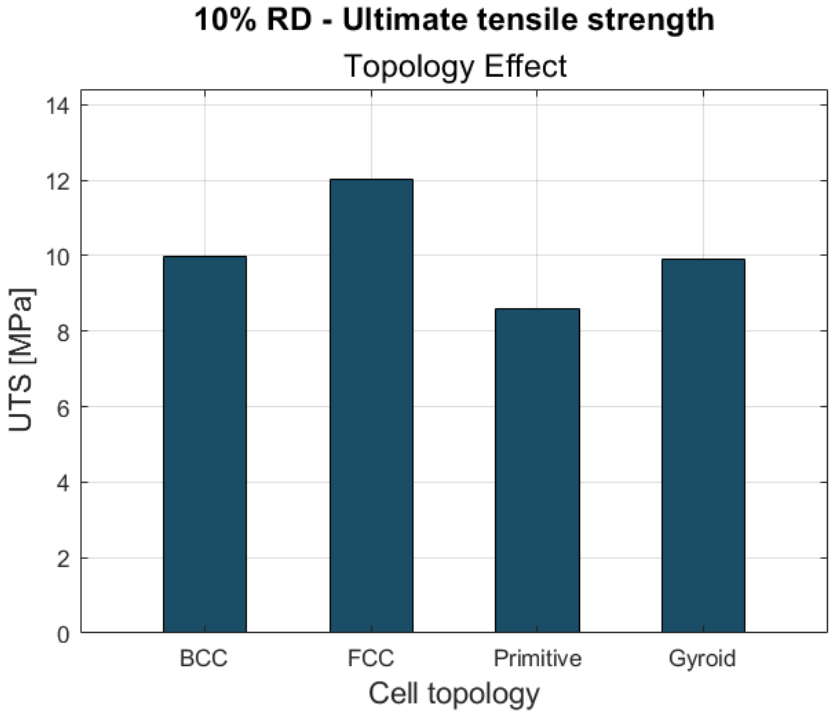

(b) Ultimate tensile strength.

Figure 4.54: Bar charts depicting the influence of lattice topology on yield and ultimate tensile strength, for 10% rel. density specimens.

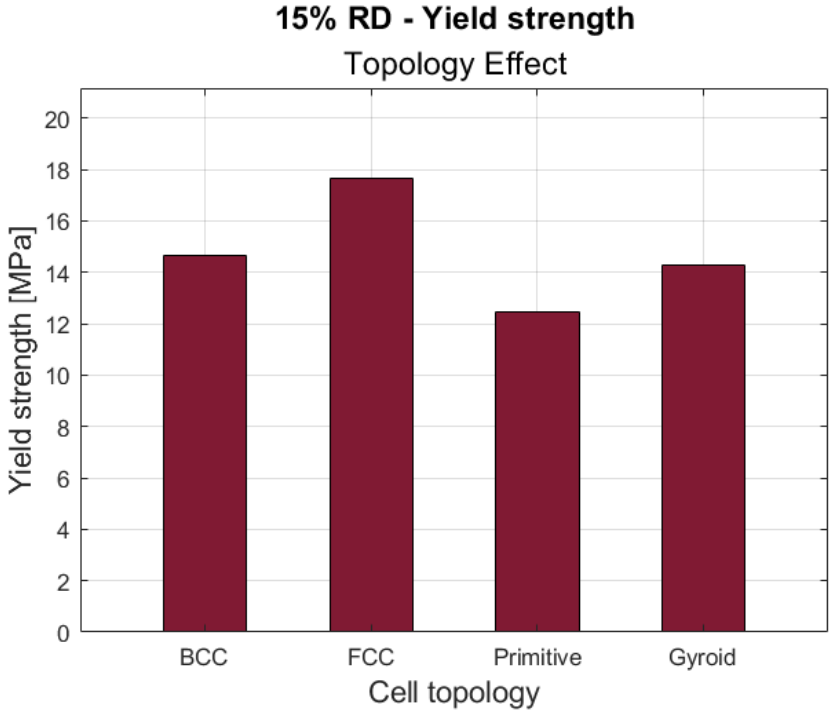

(a) Yield strength.

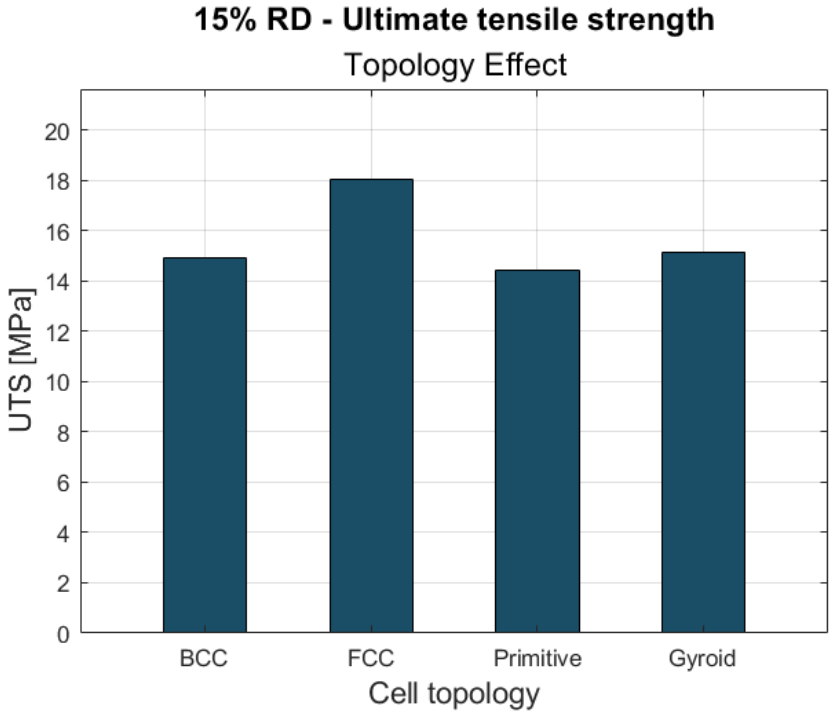

(b) Ultimate tensile strength.

Figure 4.55: Bar charts depicting the influence of lattice topology on yield and ultimate tensile strength, for 15% rel. density specimens.

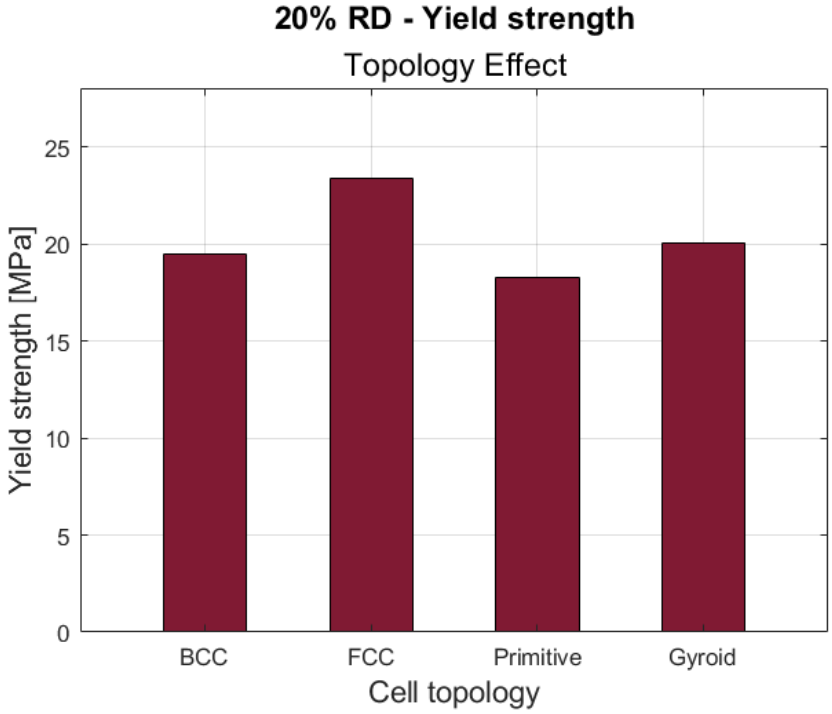

(a) Yield strength.

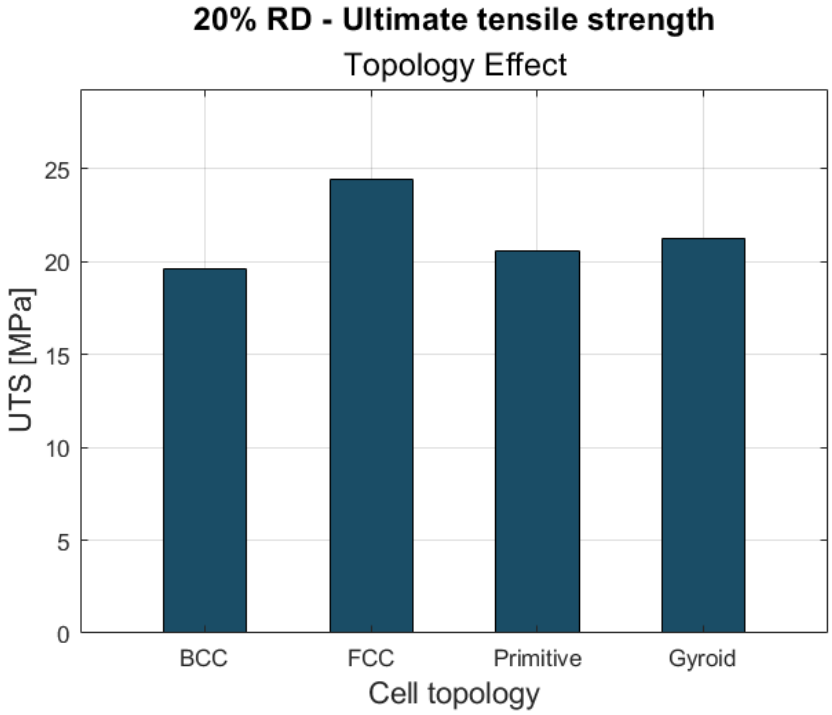

(b) Ultimate tensile strength.

Figure 4.56: Bar charts depicting the influence of lattice topology on yield and ultimate tensile strength, for 20% rel. density specimens.

CELL	Rel. Density [%]	Yield S. [Mpa]	UTS [Mpa]	Spec. Yield S. [Mpa/g]	Spec. UTS [Mpa/g]
BCC	8.32	8.226	8.863	1.146	1.235
	10.0	9.826	9.992	1.140	1.159
	15.0	14.632	14.905	1.131	1.152
	20.0	19.499	19.590	1.130	1.135
FCC	6.50	7.685	7.988	1.370	1.424
	10.0	11.711	12.011	1.359	1.394
	15.0	17.636	18.033	1.364	1.394
	20.0	23.372	24.401	1.354	1.414
Primitive	4.30	2.834	3.298	0.768	0.894
	10.0	7.510	8.596	0.872	0.999
	15.0	12.465	14.427	0.964	1.116
	20.0	18.274	20.577	1.060	1.194
Gyroid	4.87	4.233	4.590	1.014	1.099
	10.0	9.436	9.889	1.089	1.142
	15.0	14.287	15.161	1.105	1.173
	20.0	20.08	21.269	1.165	1.234

Table 4.6: Yield and ultimate tensile strength determined from the tensile simulations.

4.3.3 Fractures shape and location

In this paragraph, the fracture shapes and locations within the specimens, across the different topologies and porosities, are presented. Before providing a brief description of each specimen's behaviour, it is worth noting that both topology and porosity influence the type of failure, as will be highlighted. To improve readability while preserving the completeness of the thesis, only images illustrating failure mode and initiation are reported in this paragraph, whereas those showing failure localisation within the specimen are included in App. D. Moreover, to obtain the most informative images, displacements and plastic strains are used for the screenshots. Fracture shapes are well highlighted by displacement, as the separated portions exhibit markedly different values, producing a clear colour map. Additionally, the implemented Johnson-Cook damage model is based on plastic strain, so the best way to identify the equivalent of stress concentration is by displaying the *plastic strain equivalent* (PEEQ), which indicates the positions of incipient failures. Supporting this approach, Jiang et al. [28] reported a strong correlation between areas of stress concentration and regions exhibiting larger strain.

The failure locations confirm, for every cell shape and relative density, the correctness of the specimen design, as all failures occur within the test section. Failures in specimens relying on BCC cells, are slightly biased towards the top of the specimen for all porosities, except for the 20% sample. The distance from the grips varies slightly, from four layers of cells for the heaviest specimen to six layers for the lightest. For FCC and Primitive lattices, failures also occur slightly towards the top, except for the 15% relative density specimens. In FCC architectures, the distance from the grips ranges from five to seven layers of cells (with seven corresponding to the very middle). The same pattern is observed for the Primitive cell. The Gyroid cases behave differently, with failures occurring slightly towards the bottom, except for the 20% relative density sample. The distance from the grips ranges from five to seven layers.

Bobbert et al. [29] observed that failure modes depend on the geometry of the unit cell, and

similar results are reported in this thesis. In addition, failures are also influenced by loading conditions. For instance, the Gyroid typically undergoes 45° shear failure under compressive loads, but fails along planes perpendicular to the loading direction under fully-reverse cyclic stress [14].

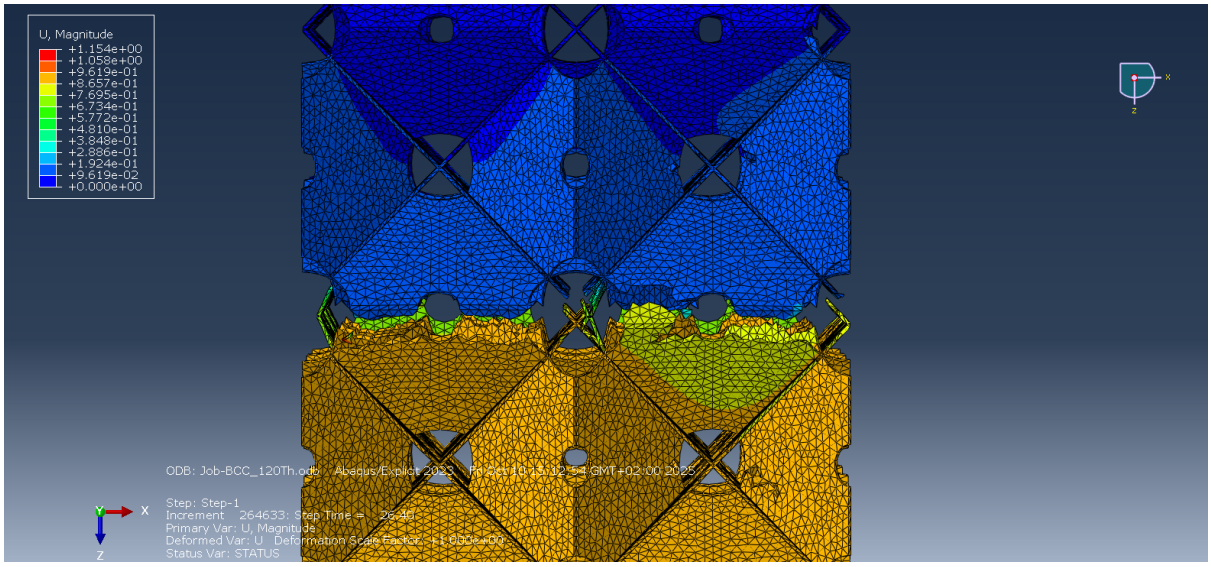

(a) Failure shape.

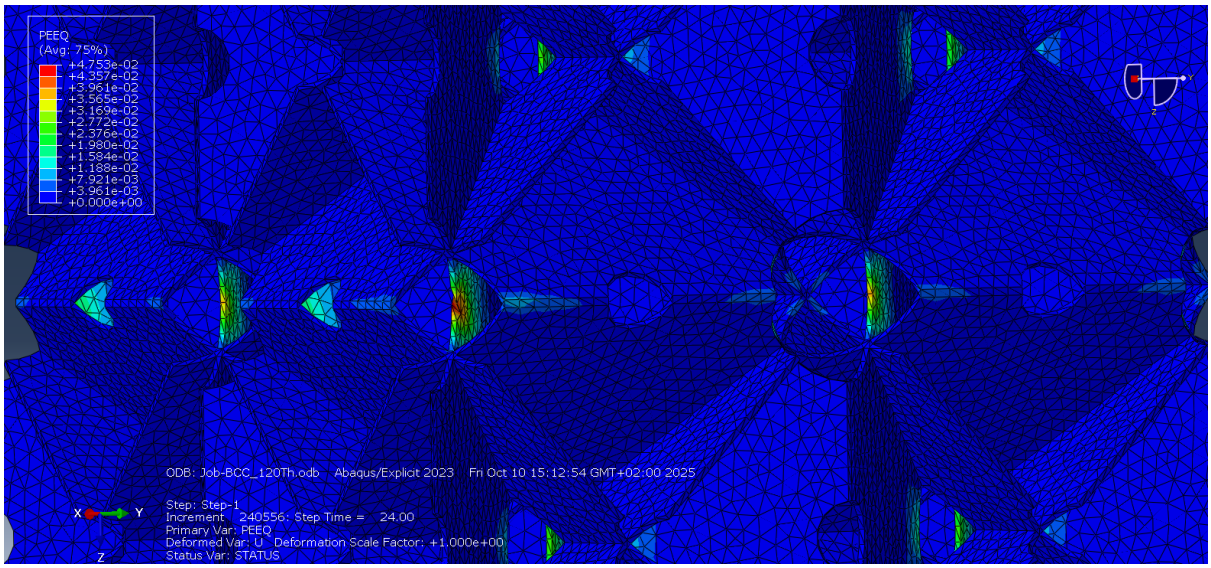

(b) Fracture initiation.

Figure 4.57: BCC unit cell: failure mode and fracture initiation, for 8.32% rel. density specimen.

The failure characteristics of the BCC architectures are shown in Fig. 4.57 - 4.60. As already mentioned, the failure is guided by the vertex extruded cuts. Indeed, plastic strains concentrate in these locations, particularly on the vertical plates. Here, the first mesh elements fail, initiating crack propagation that ultimately leads to complete specimen failure. For this architecture, failure occurs perpendicular to the loading direction for all relative density values. It is also noteworthy to examine the failure mechanism, which, due to the BCC geometric configuration, is clearly visible in the sequence of images in Fig. 4.61 - 4.62 and which shows the same behaviour described by Ashby and Gibson for both in-plane honeycomb deformation and foams' tensile

behaviour. In this process, failure begins with the partial or complete failure of one or more cells (but not all), leading to stress redistribution on neighbouring walls. Consequently, these walls are subjected to higher stress and the load-bearing capacity of the structure decreases until fracture propagation results in a fully broken specimen [1]. Once the vertical plates fail first, and the inclined plates tend to align with the loading direction in an attempt to increase resistance to the applied loads. In FCC and TPMS cells, this mechanism is not evident, except for the slight elongation of the quasi-circular cavity along the loading direction, which occurs in the Primitive architecture.

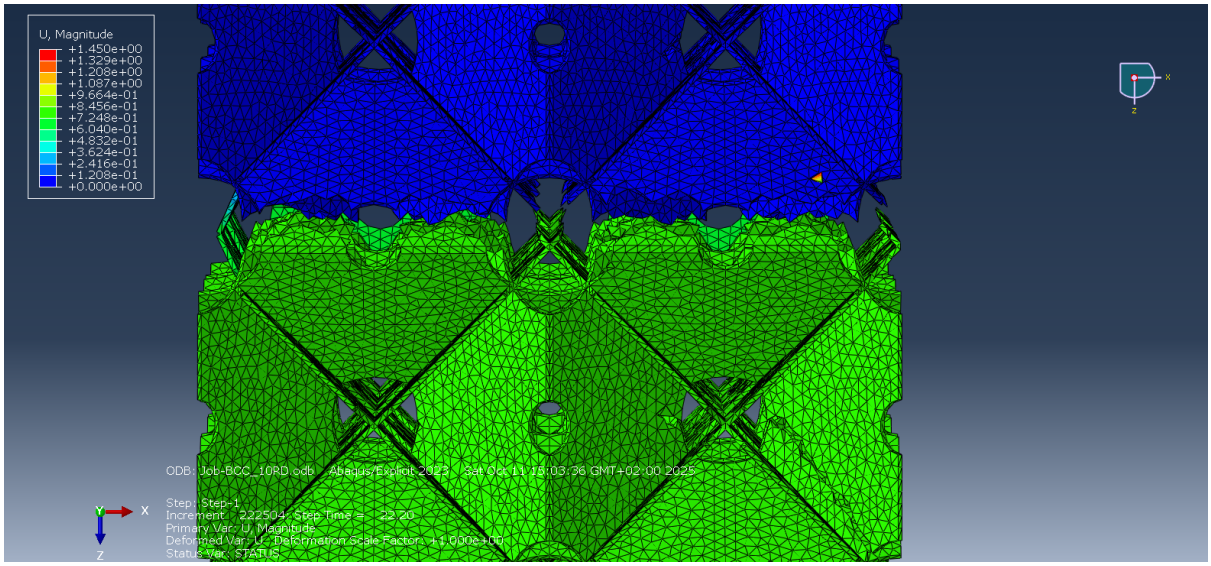

(a) Failure shape.

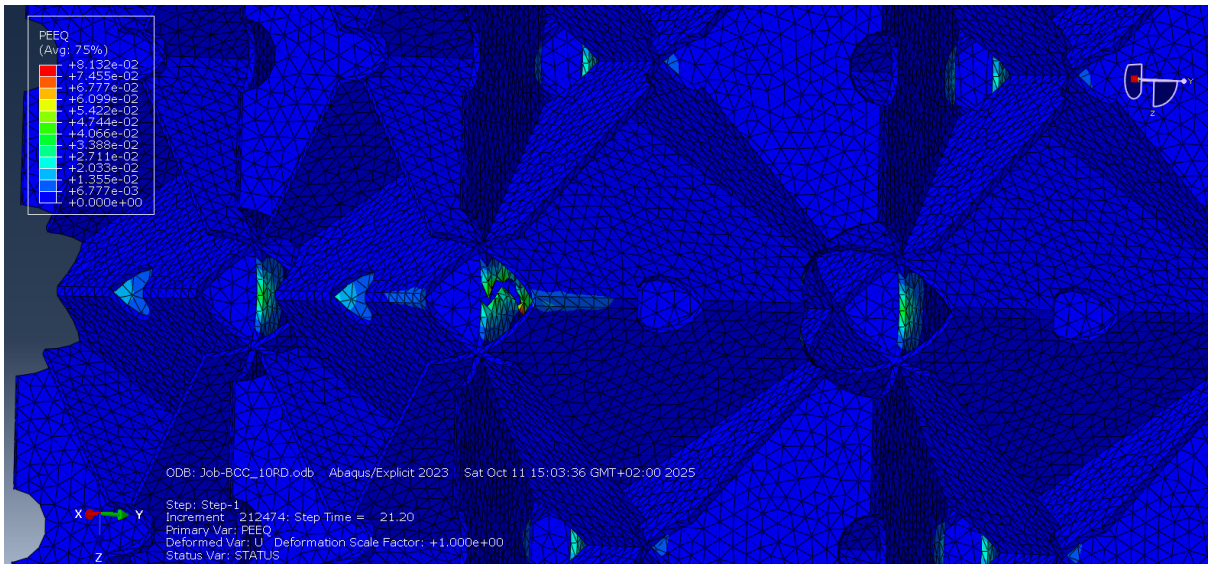

(b) Fracture initiation.

Figure 4.58: BCC unit cell: failure mode and fracture initiation, for 10% rel. density specimen.

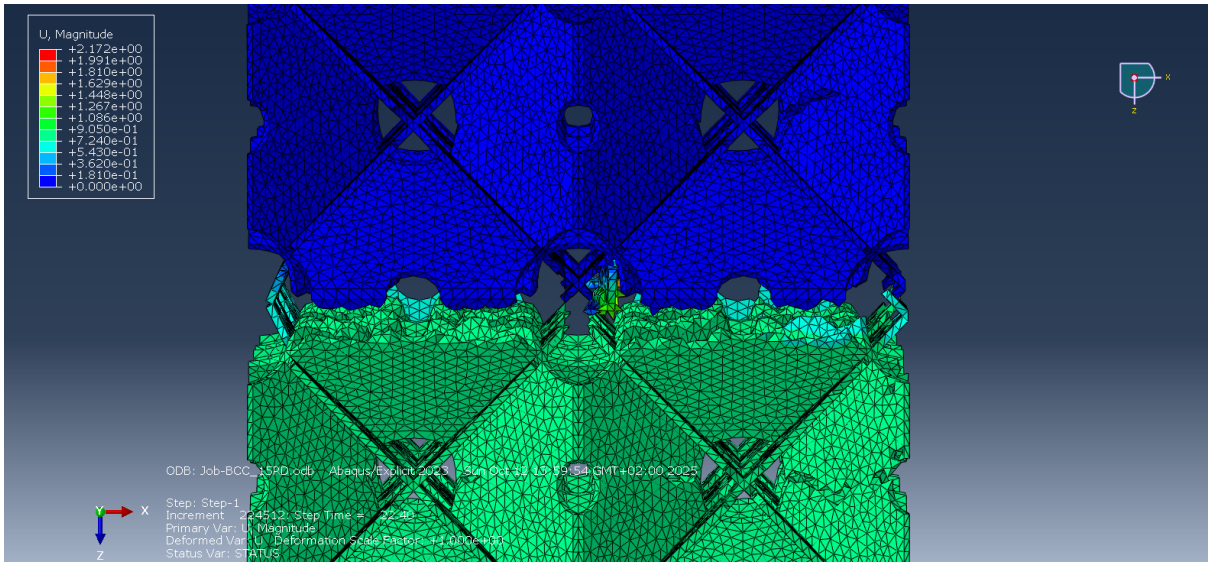

(a) Failure shape.

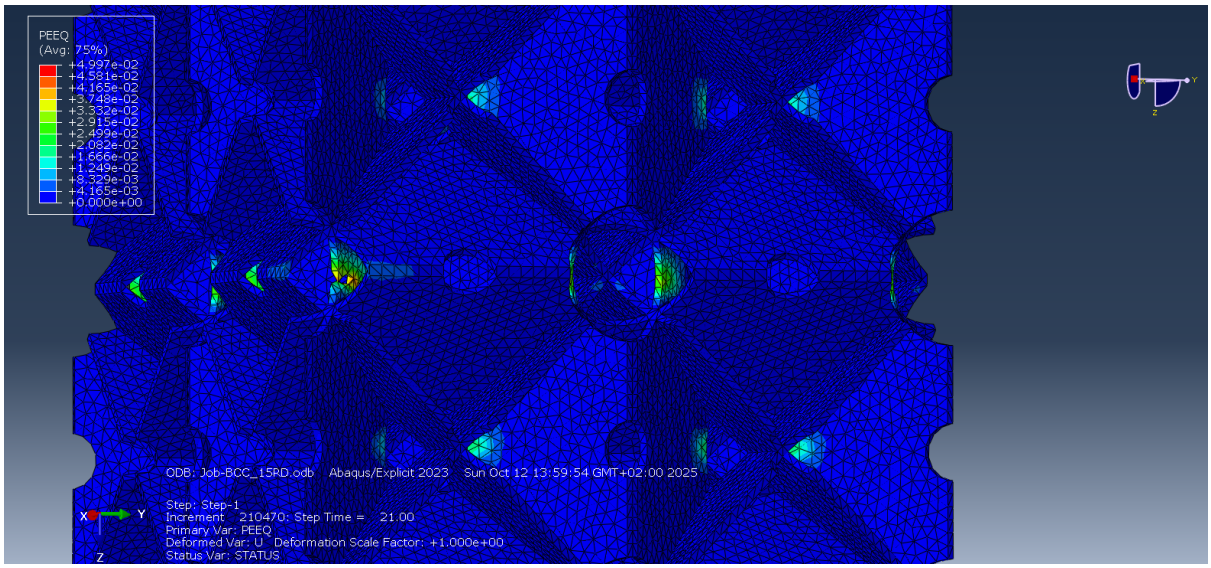

(b) Fracture initiation.

Figure 4.59: BCC unit cell: failure mode and fracture initiation, for 15% rel. density specimen.

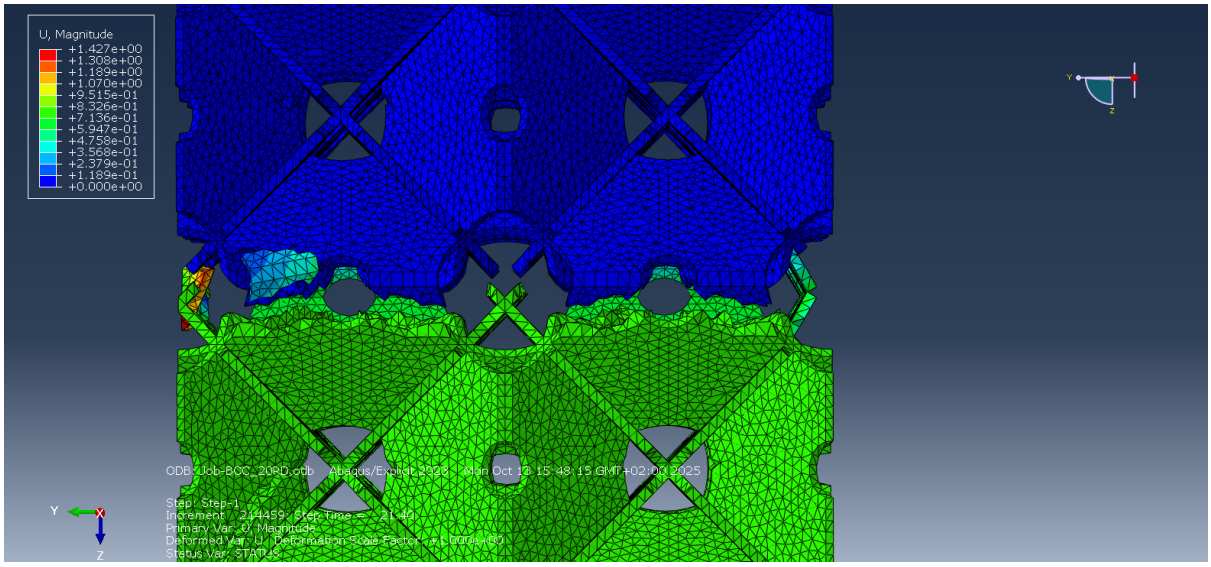

(a) Failure shape.

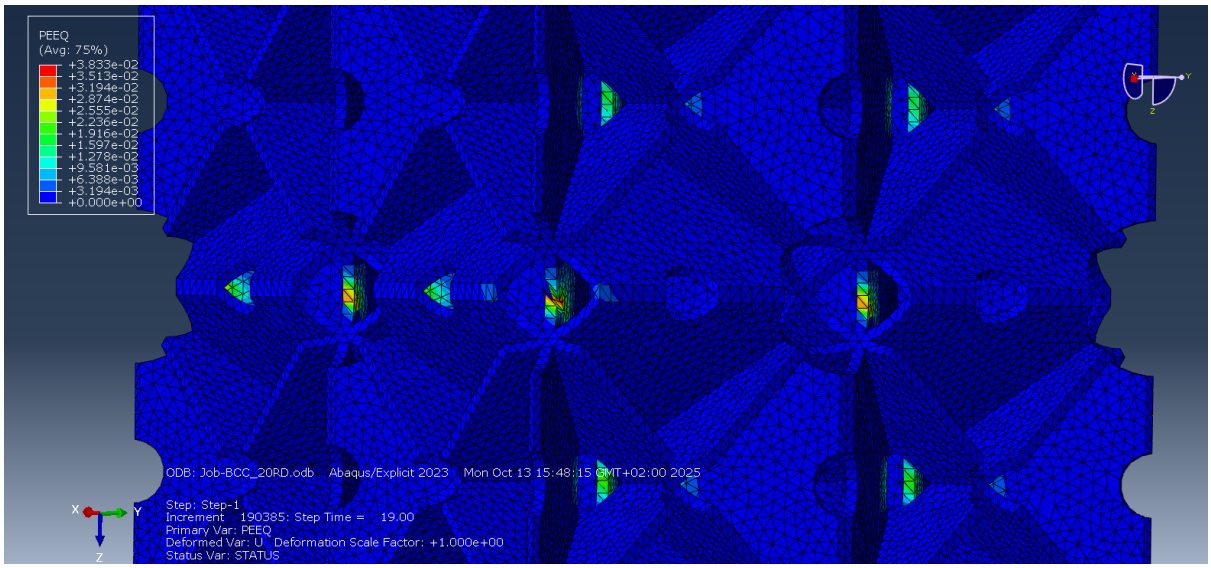

(b) Fracture initiation.

Figure 4.60: BCC unit cell: failure mode and fracture initiation, for 20% rel. density specimen.

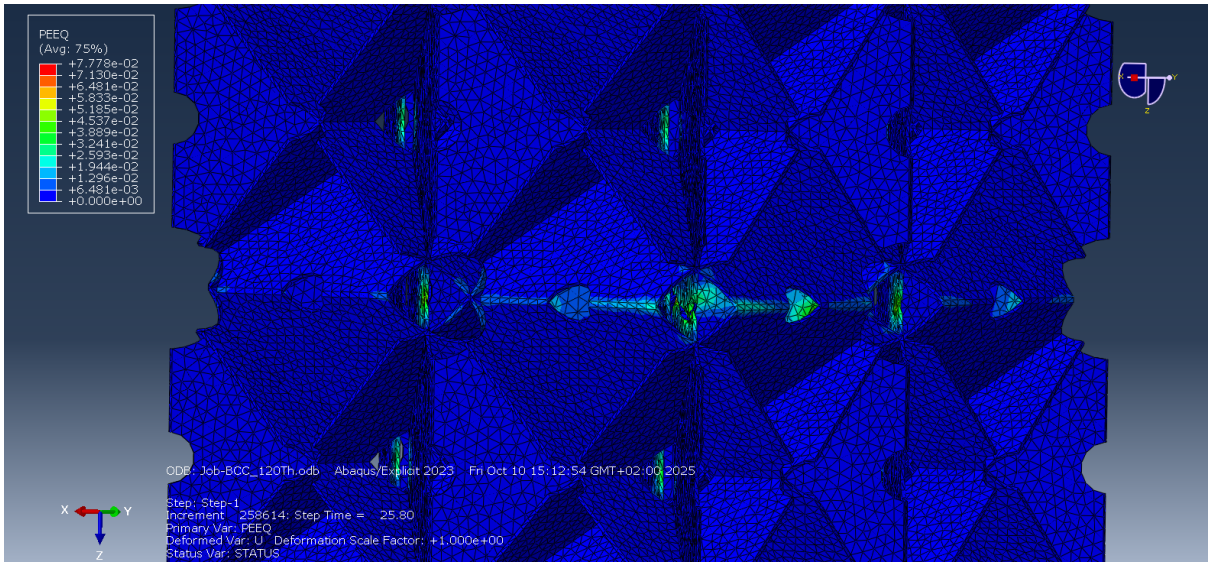

(a) Equivalent plastic strain distribution. Step time 25.80s.

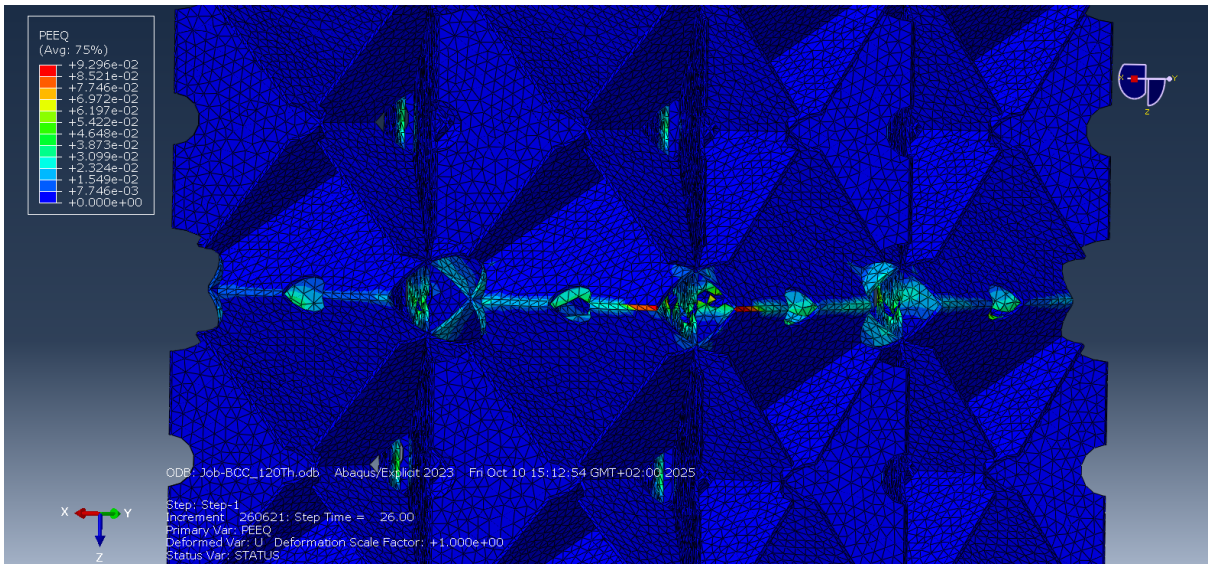

(b) Equivalent plastic strain distribution. Step time 26.00s.

Figure 4.61: BCC unit cell - 8.32% rel. density: sequence of failure - Part 1.

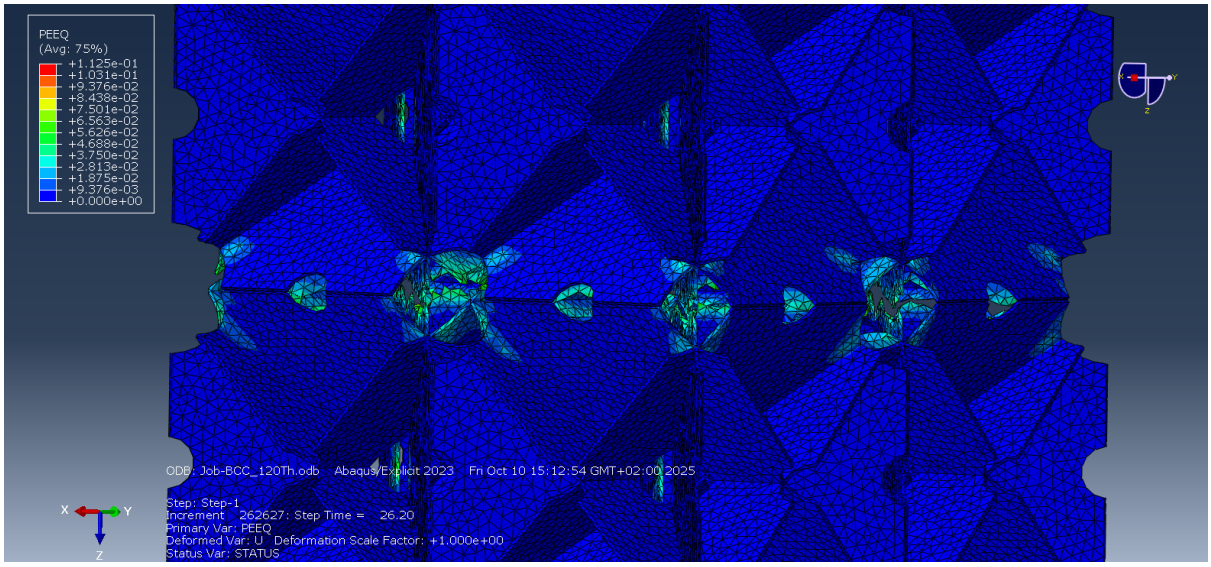

(a) Equivalent plastic strain distribution. Step time 26.20s.

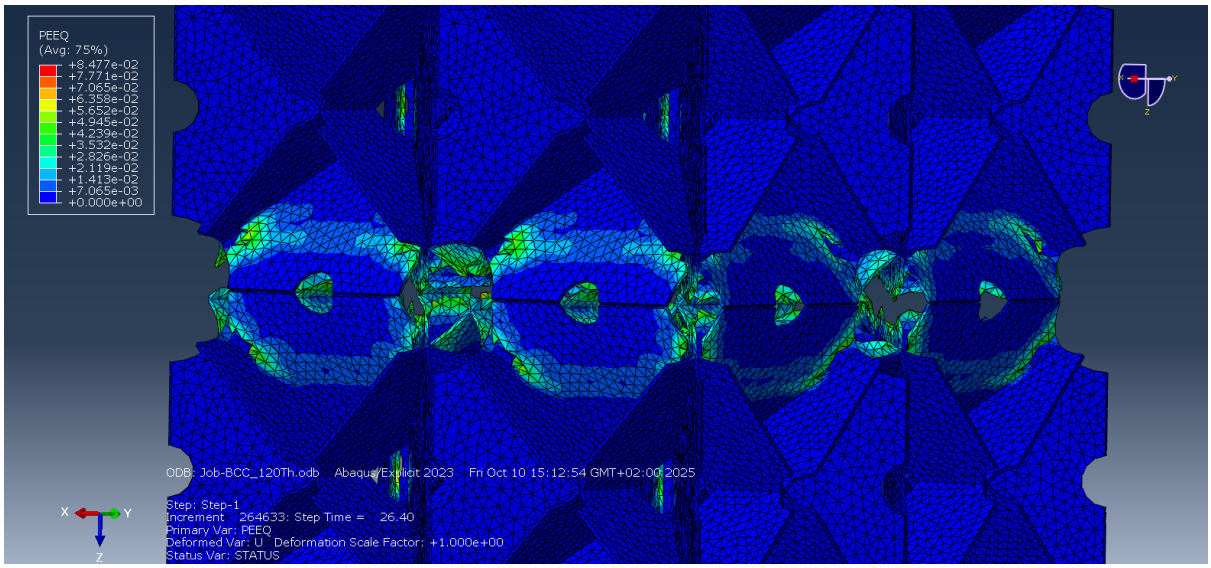

(b) Equivalent plastic strain distribution. Step time 26.40s.

Figure 4.62: BCC unit cell - 8.32% rel. density: sequence of failure - Part 2.

In the description of FCC architectures failure mechanisms under tensile conditions, the images in Fig. 4.63 - 4.66 are particularly useful. The behaviour is not as straightforward as for the other plate-based lattices analysed and also depends on relative density. At very low density, corresponding to the minimum achievable, the fracture surface is inclined at 45° with respect to the loading direction. A more detailed examination of the plastic strains distribution highlights that they concentrate at the touching edges within the individual tetrahedrons. These locations fail first, initiating the failure of the entire specimen. As the porosity decreases, these locations are less stressed, and the contact surfaces between different tetrahedrons become more critical. In this regard, it is observed that the 10% and 15% specimens exhibit failure lines both within individual tetrahedrons and between different ones.

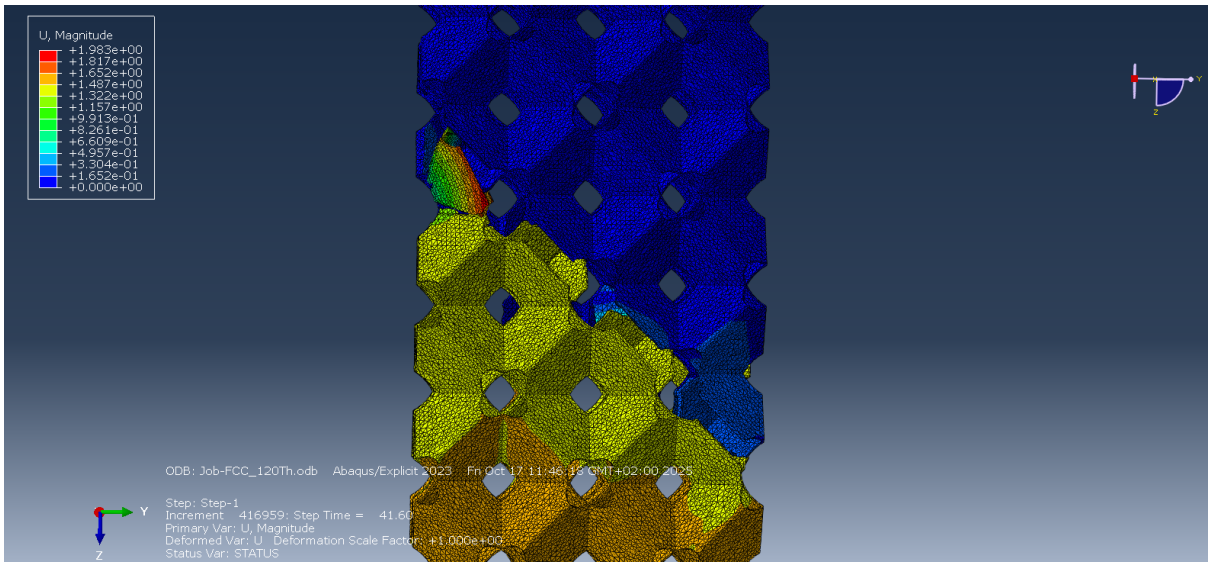

(a) Failure shape.

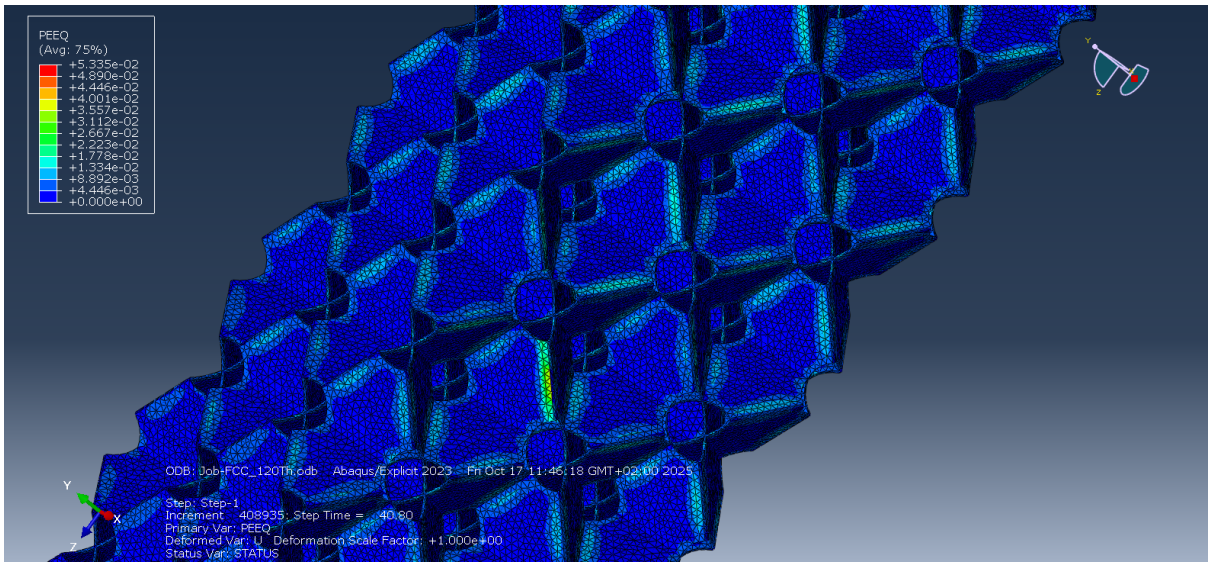

(b) Fracture initiation.

Figure 4.63: FCC unit cell: failure mode and fracture initiation, for 6.50% rel. density specimen.

Finally, in the configuration with 20% relative density, failure produces fracture surfaces perpendicular to the loading direction, showing a fracture pattern opposite to that of the 6.50% sample, with the individual tetrahedrons remaining almost intact. Bonatti et al. [13] reported a similar trend for shell-TPMS structures, observing different deformation modes for porosities below 80% or above 90%. These fracture surfaces illustrate how, even though the applied external deformation is uniaxial, it is internally translated into more complex local stress states, as also proposed by Soro et al. [32].

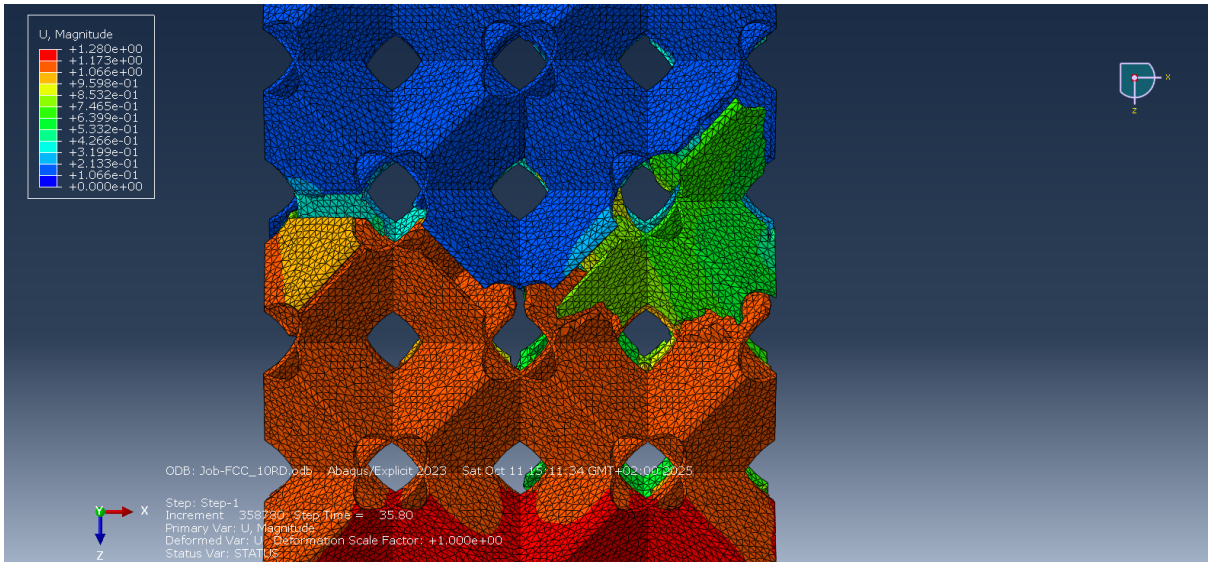

(a) Failure shape.

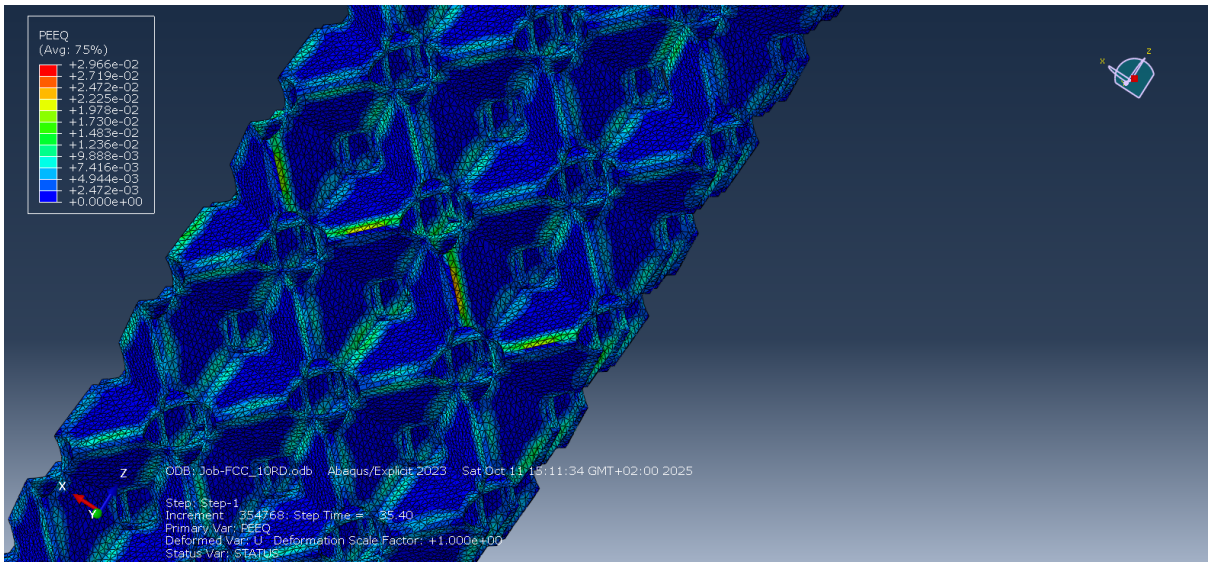

(b) Fracture initiation.

Figure 4.64: FCC unit cell: failure mode and fracture initiation, for 10% rel. density specimen.

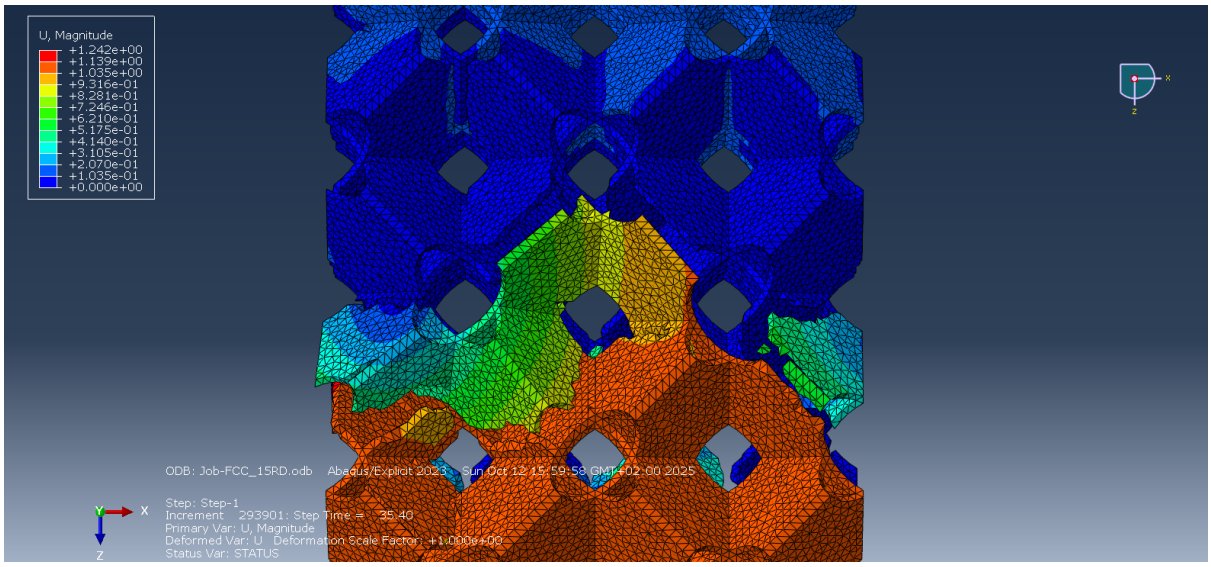

(a) Failure shape.

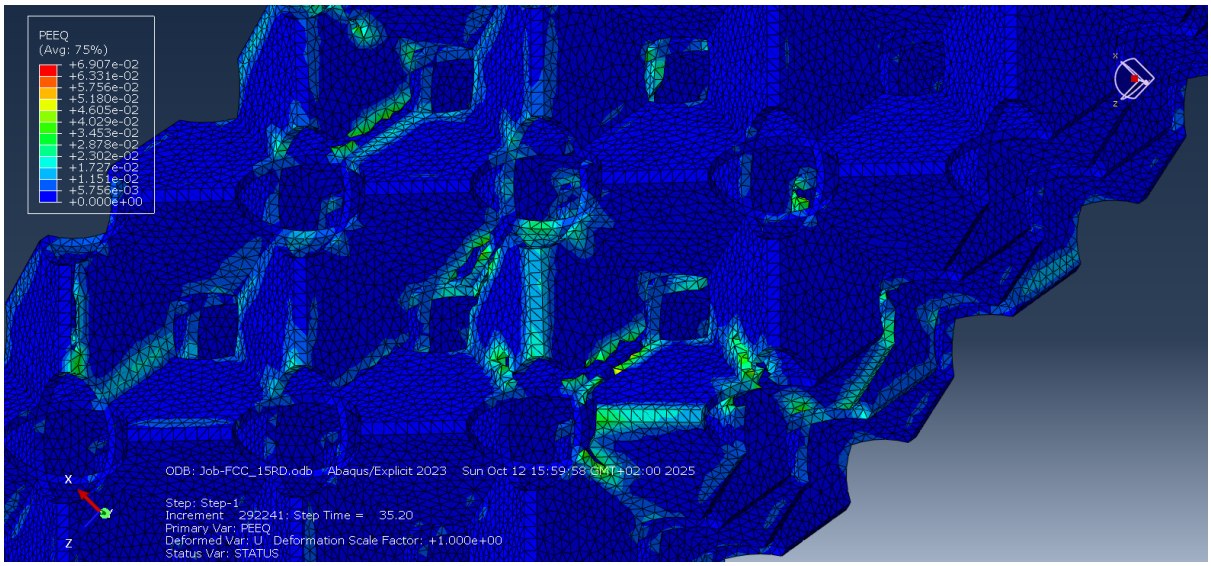

(b) Fracture initiation.

Figure 4.65: FCC unit cell: failure mode and fracture initiation, for 15% rel. density specimen.

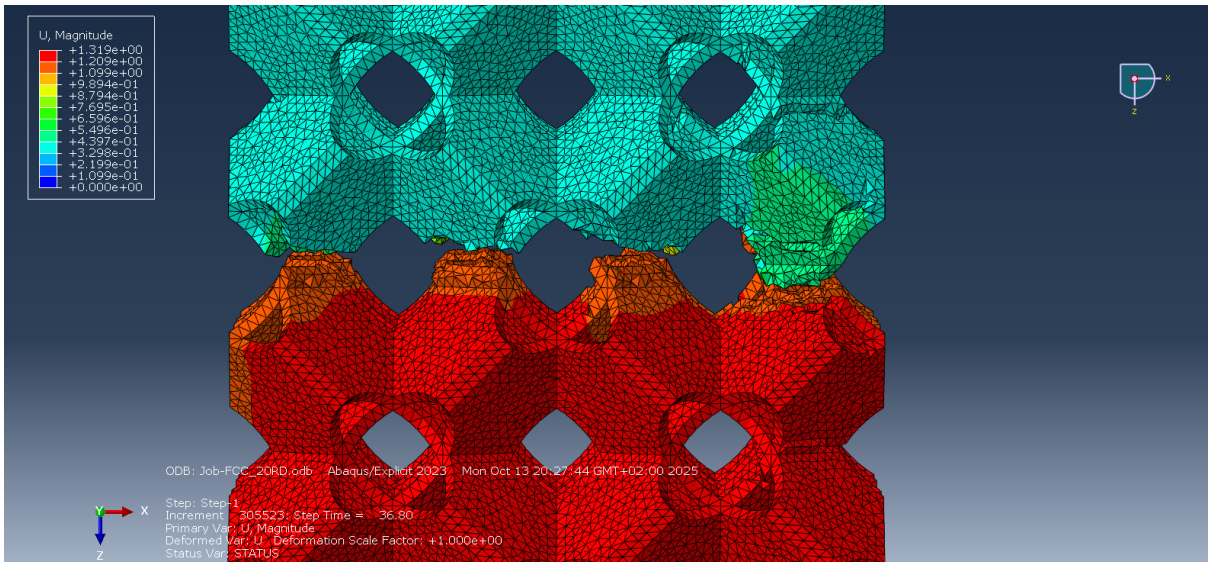

(a) Failure shape.

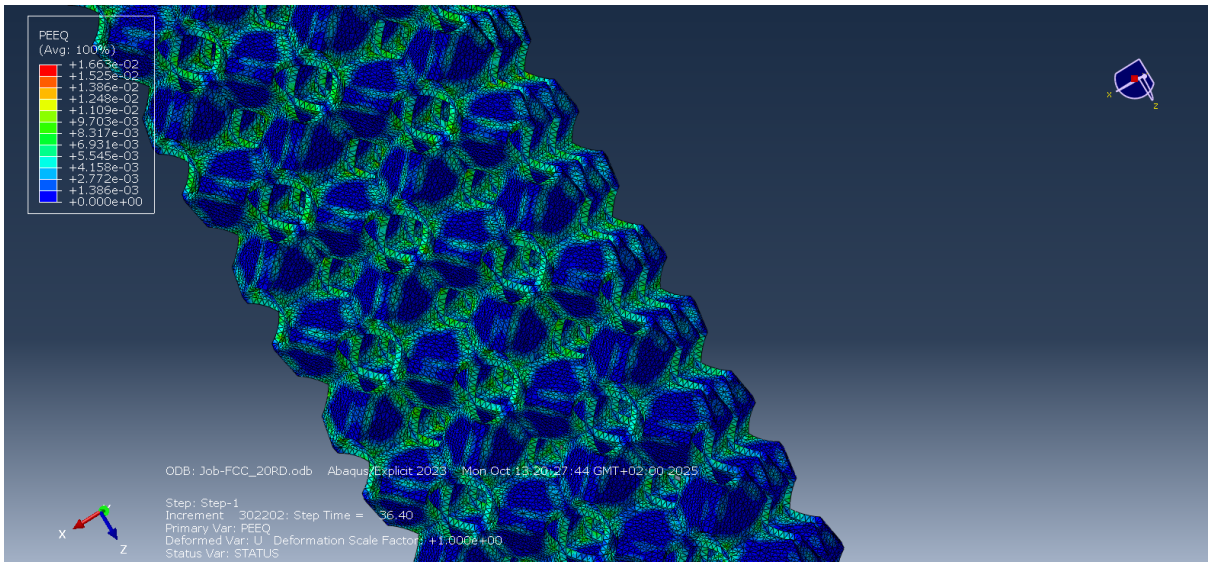

(b) Fracture initiation.

Figure 4.66: FCC unit cell: failure mode and fracture initiation, for 20% rel. density specimen.

Primitive unit cells are characterised by the emergence of deformed zones, highlighted in green and red in the images on the right side of Fig. 4.67 - 4.70. At every density, failure initiates inside the cell from these locations and propagates, ultimately splitting the specimen into two main parts. However, it can be observed that the planes in which these fractures occur are not identical for each cell or each half-cell. Fractures are perpendicular to the loading direction, as reported by some authors [32], but they do not lie on the same plane. The specimens with 4.30% and 15% relative density exhibit final fracture surfaces inclined, in steps, at approximately 45°, while the remaining two are almost perpendicular to the loading direction.

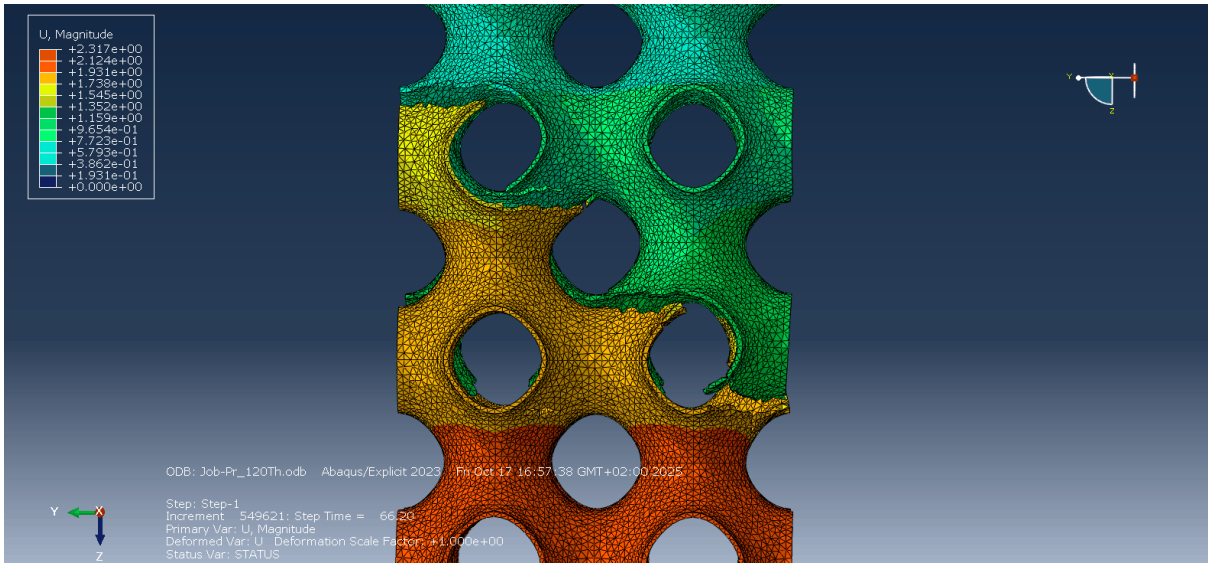

(a) Failure shape.

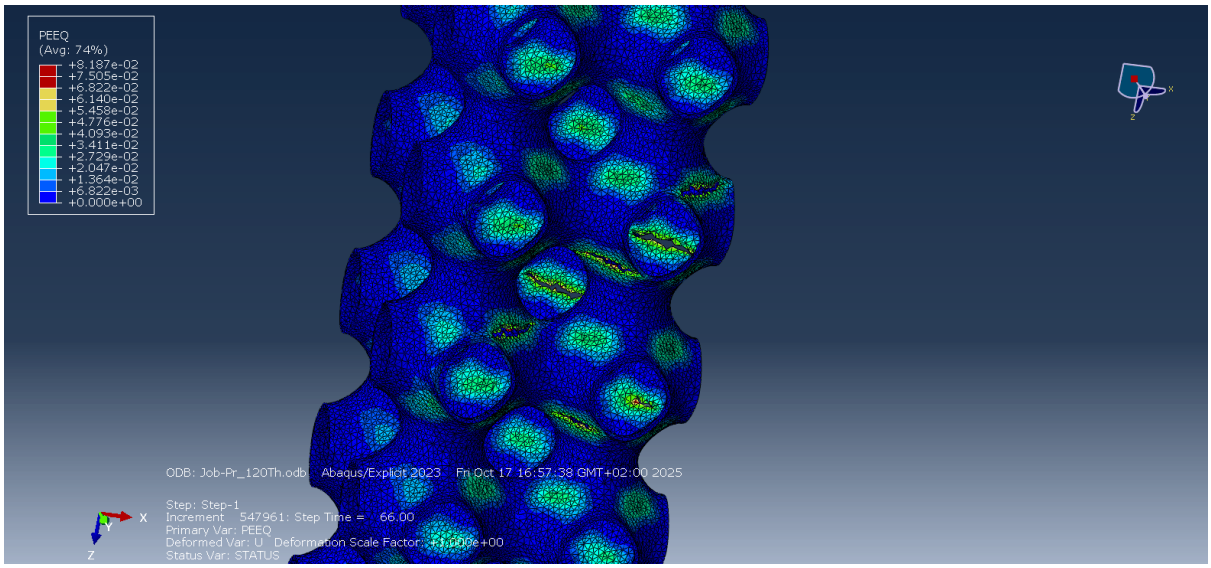

(b) Fracture initiation.

Figure 4.67: Primitive unit cell: failure mode and fracture initiation, for 4.30% rel. density specimen.

Additionally, the 10% specimen is characterised by the failure of the inner pillar, on a plane parallel to but distinct from that of the outer fractures. This behaviour was also reported by Zheng et al. [34], who investigated the static tensile, compressive, and bending characteristics of Primitive unit cells, finding that under tensile conditions fractures are predominantly localised at the connection points between the pillars of the solid lattice structure. These locations approximately correspond to those presenting the largest plastic strain. Indeed, these same locations (again, not on the same plane) lead to failure in the other porosities as well, with some differences in the heaviest sample, where failure occurs both at these locations and along the horizontal symmetry plane of the cell.

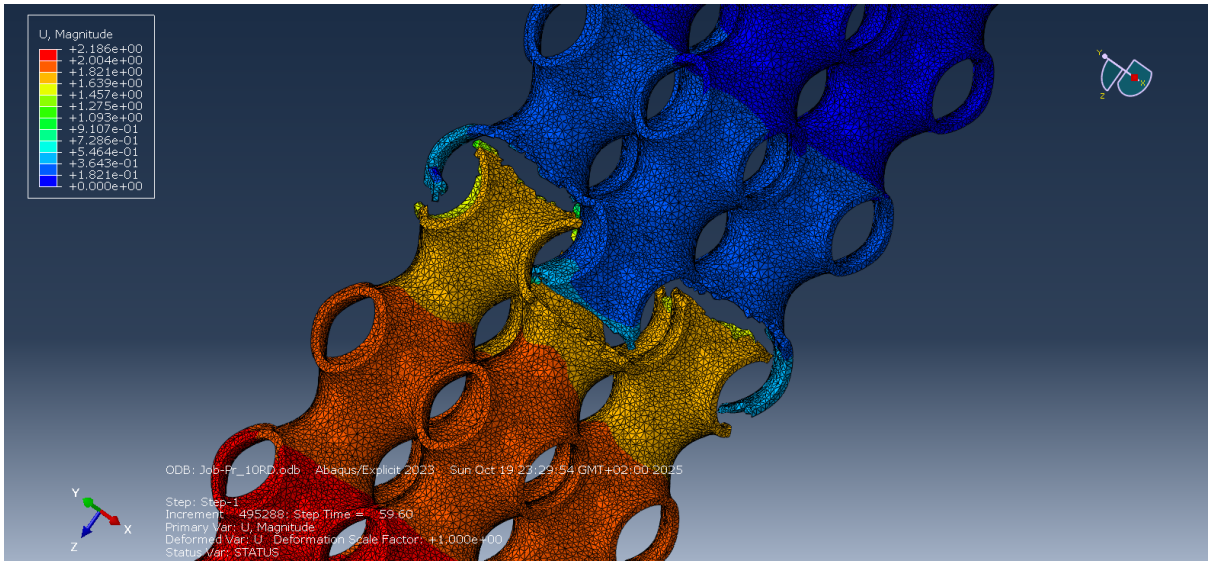

(a) Failure shape.

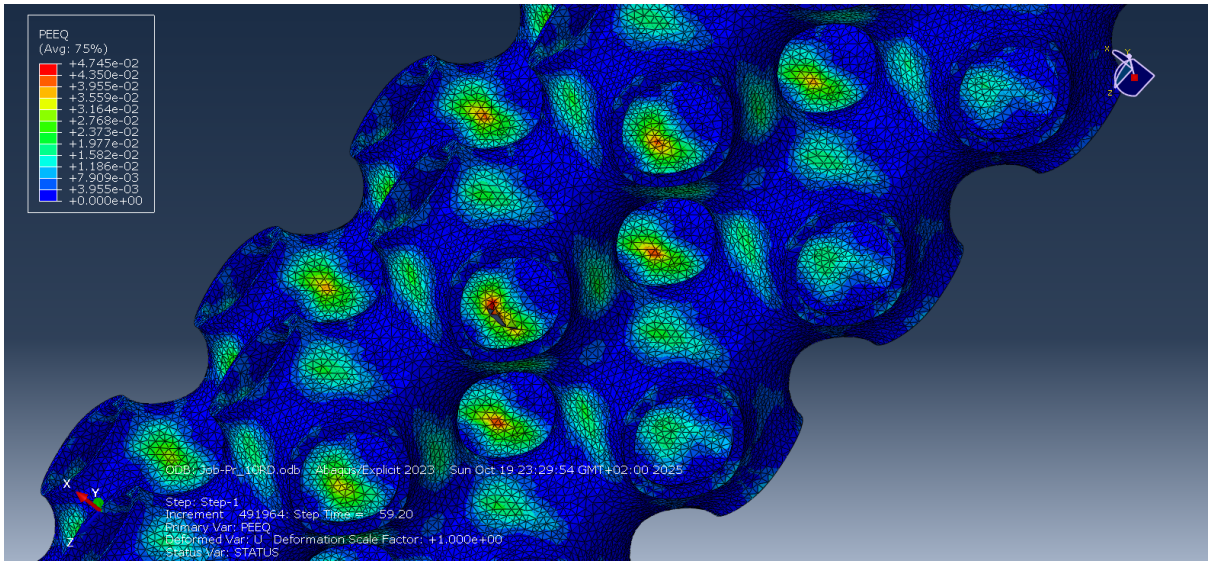

(b) Fracture initiation.

Figure 4.68: Primitive unit cell: failure mode and fracture initiation, for 10% rel. density specimen.

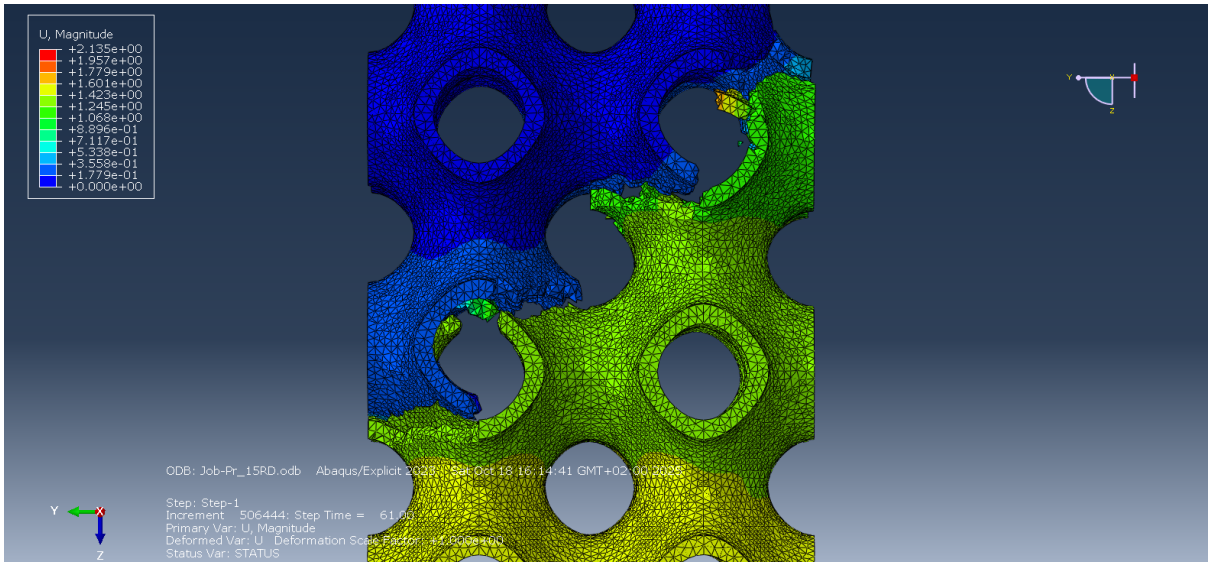

(a) Failure shape.

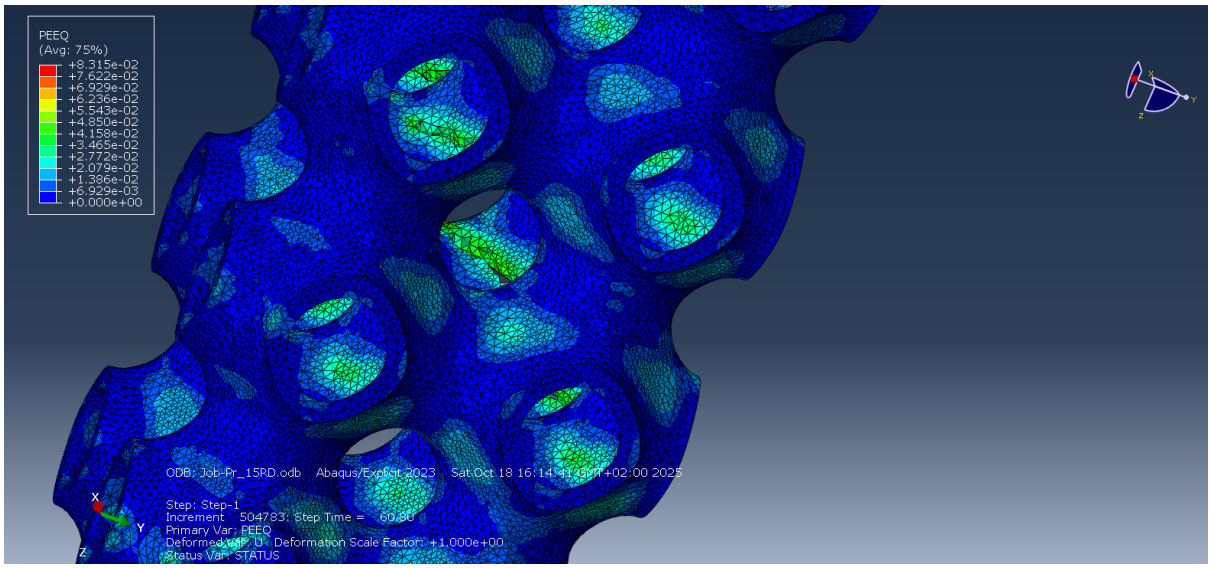

(b) Fracture initiation.

Figure 4.69: Primitive unit cell: failure mode and fracture initiation, for 15% rel. density specimen.

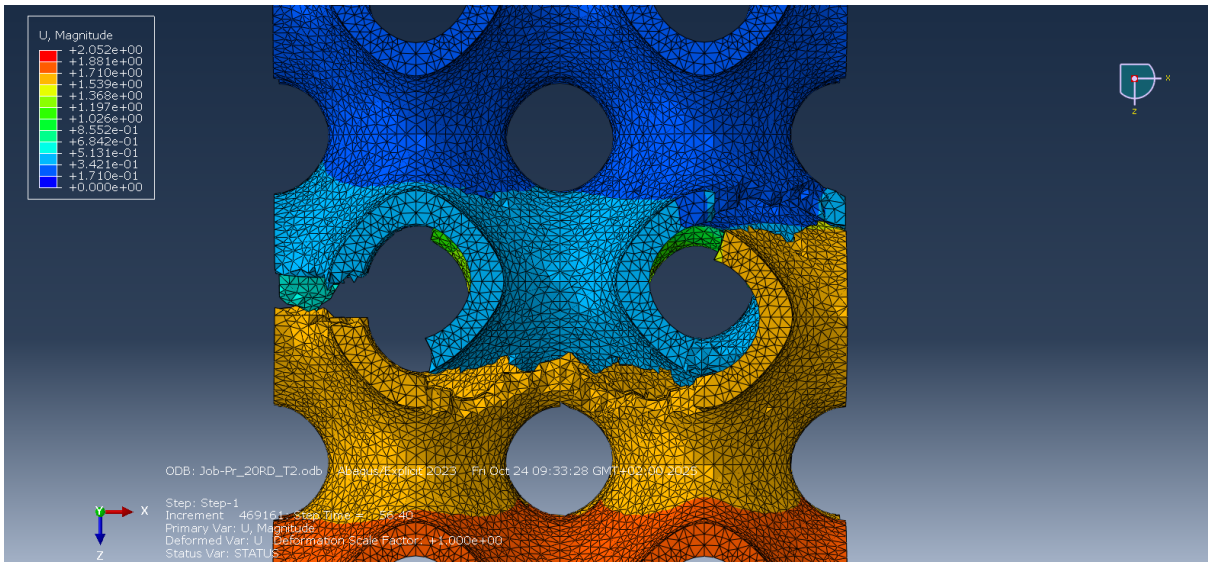

(a) Failure shape.

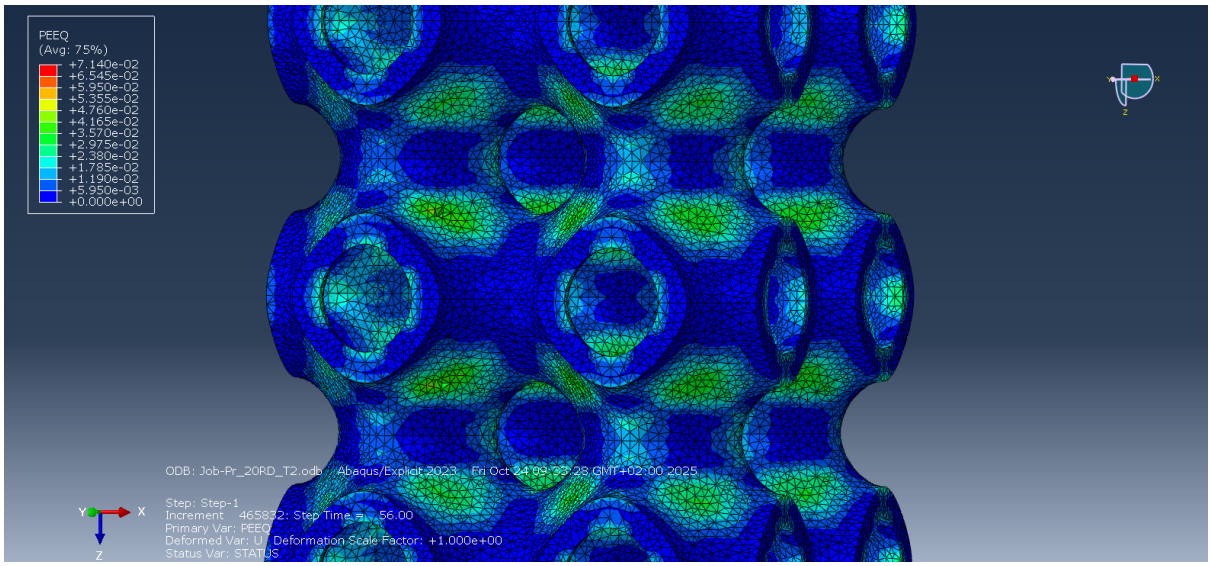

(b) Fracture initiation.

Figure 4.70: Primitive unit cell: failure mode and fracture initiation, for 20% rel. density specimen.

Finally, the Gyroid architecture exhibits features similar to those previously described, as can be seen in Fig. 4.71 - 4.74. At lower densities, the fracture surface is inclined at 45°, consistent with the findings of Soro et al. [32] on skeletal Gyroid structures. For the heaviest sample, the fracture is nearly perpendicular to the loading direction on one face and slightly inclined on the adjacent face sheet, although less pronounced than at lower densities. It is worth noting that different results have been reported in literature. Feng et al. [106] (China), who investigated the quasi-static compressive behaviour of Gyroid and Diamond unit cells made of PLA via fused deposition modelling (FDM), found no significant influence of relative density on the deformation characteristics. In contrast, Novak et al. [109] (Slovenia, UAE, Croatia), who studied the quasi-static and dynamic compressive behaviour of sheet-based TPMS, observed that the volume ratio affects the deformation pattern of Gyroid structures.

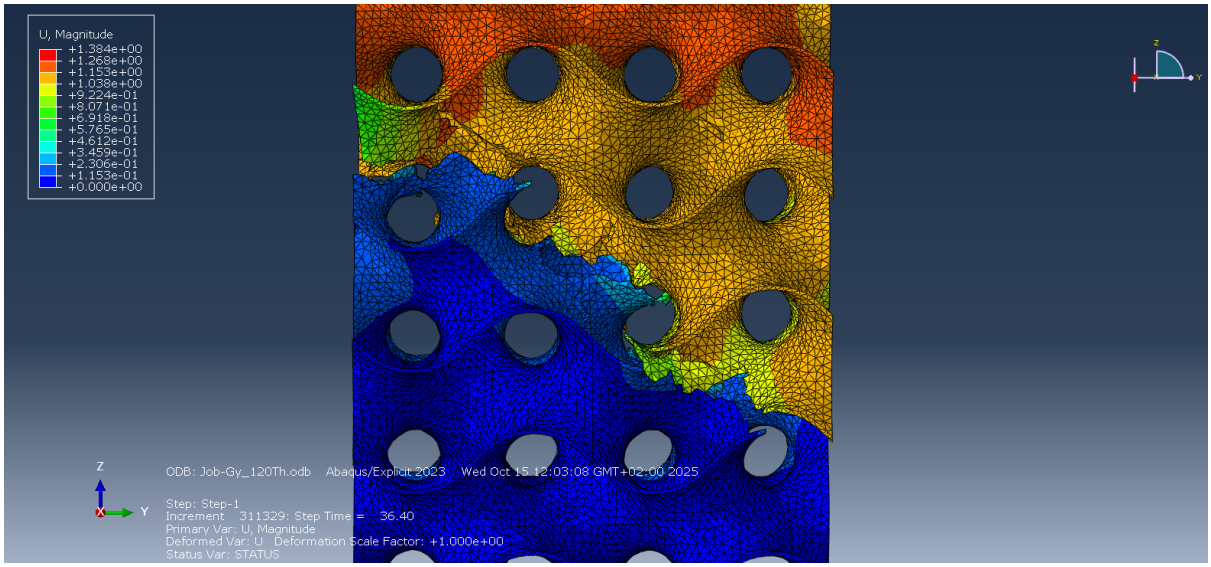

(a) Failure shape.

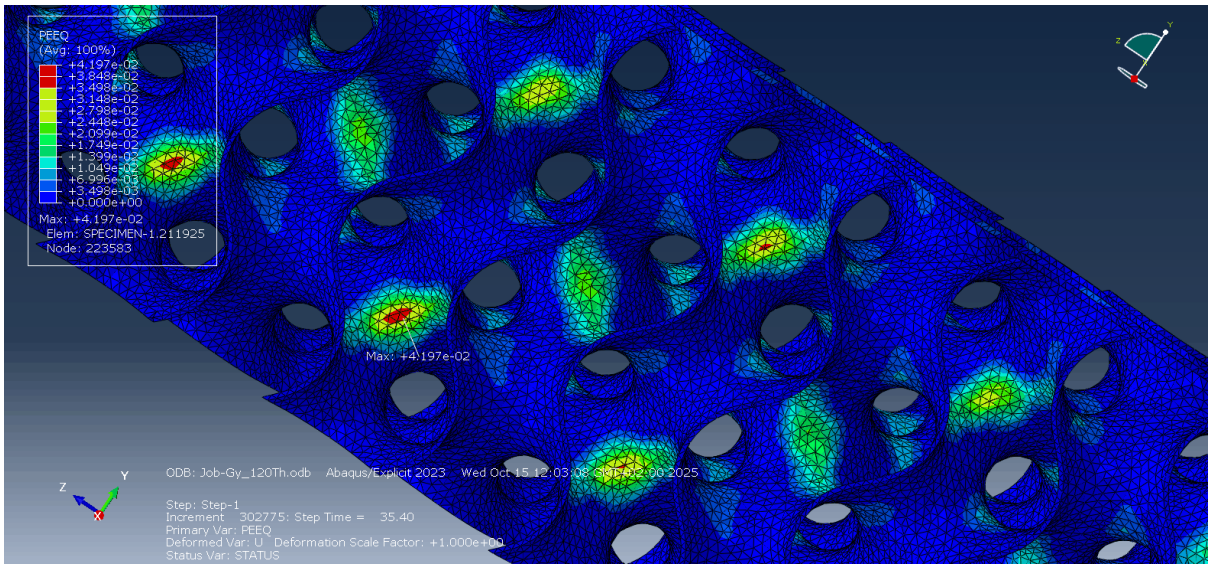

(b) Fracture initiation.

Figure 4.71: Gyroid unit cell: failure mode and fracture initiation, for 4.87% rel. density specimen.

Nevertheless, it is important to consider that the limited research on the tensile behaviour of these metamaterials requires comparisons across different materials and loading conditions; therefore, these considerations, although informative, cannot serve as a definitive basis for evaluating the quality or validity of the results obtained in this thesis, except to a very limited extent.

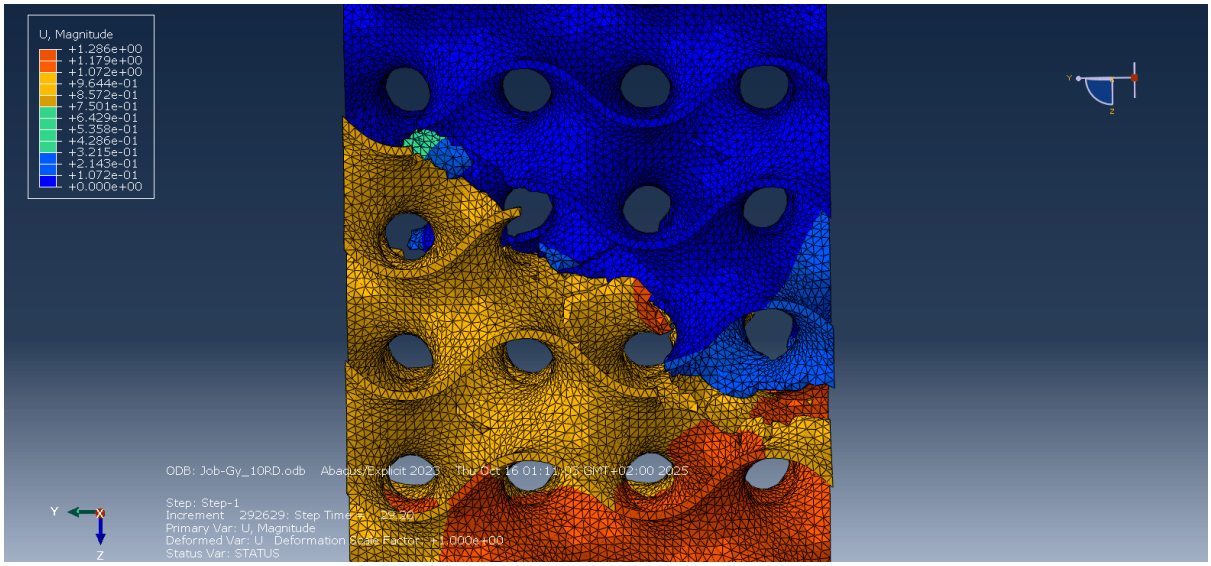

(a) Failure shape.

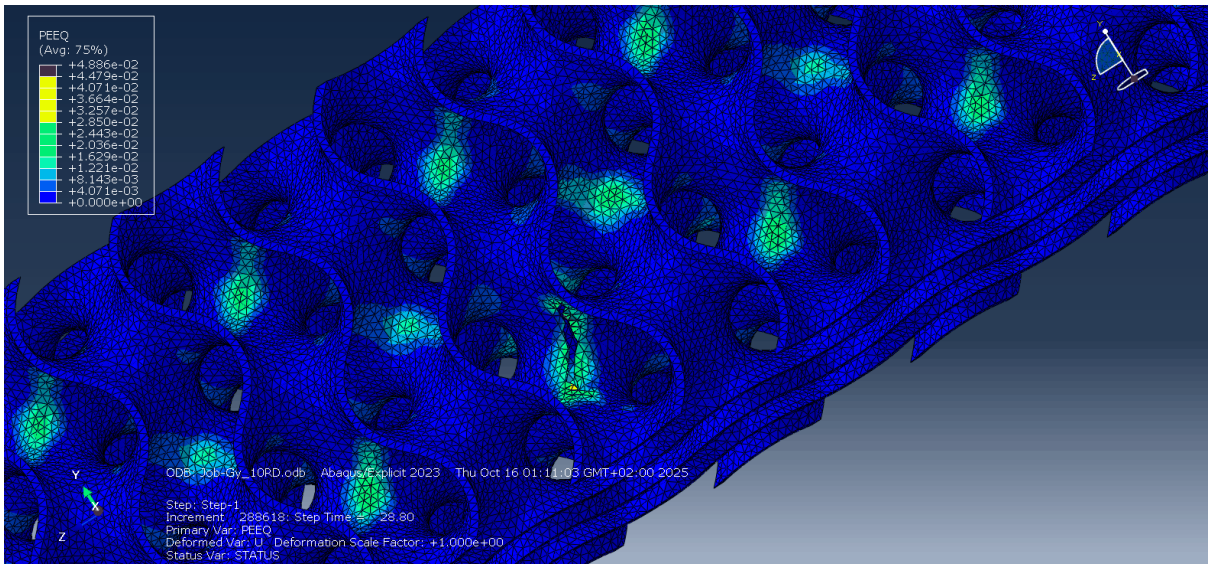

(b) Fracture initiation.

Figure 4.72: Gyroid unit cell: failure mode and fracture initiation, for 10% rel. density specimen.

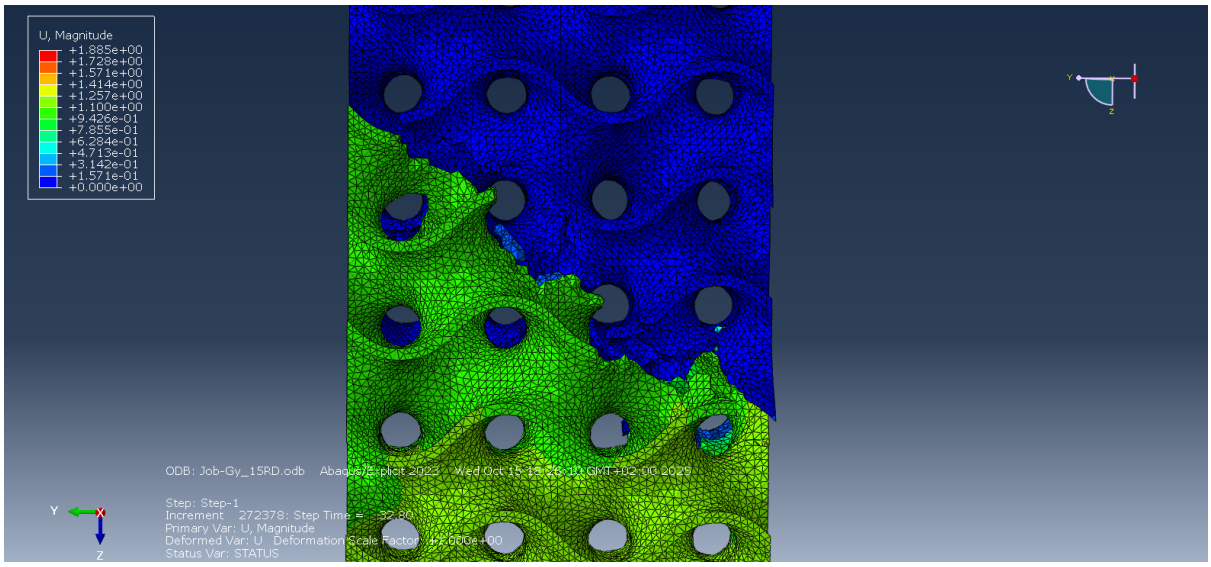

(a) Failure shape.

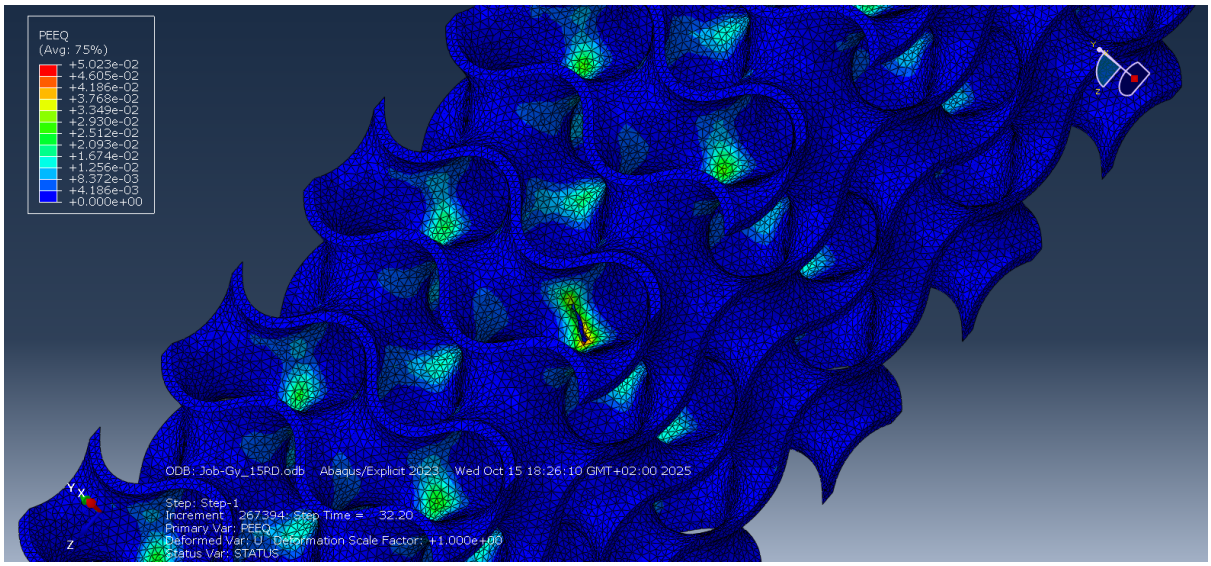

(b) Fracture initiation.

Figure 4.73: Gyroid unit cell: failure mode and fracture initiation, for 15% rel. density specimen.

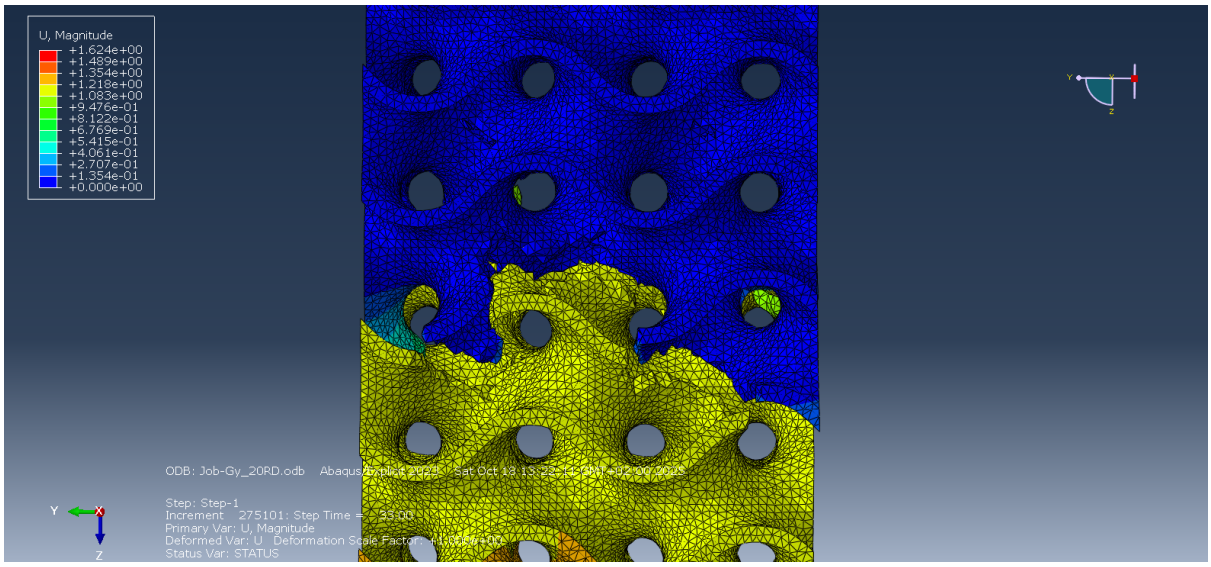

(a) Failure shape.

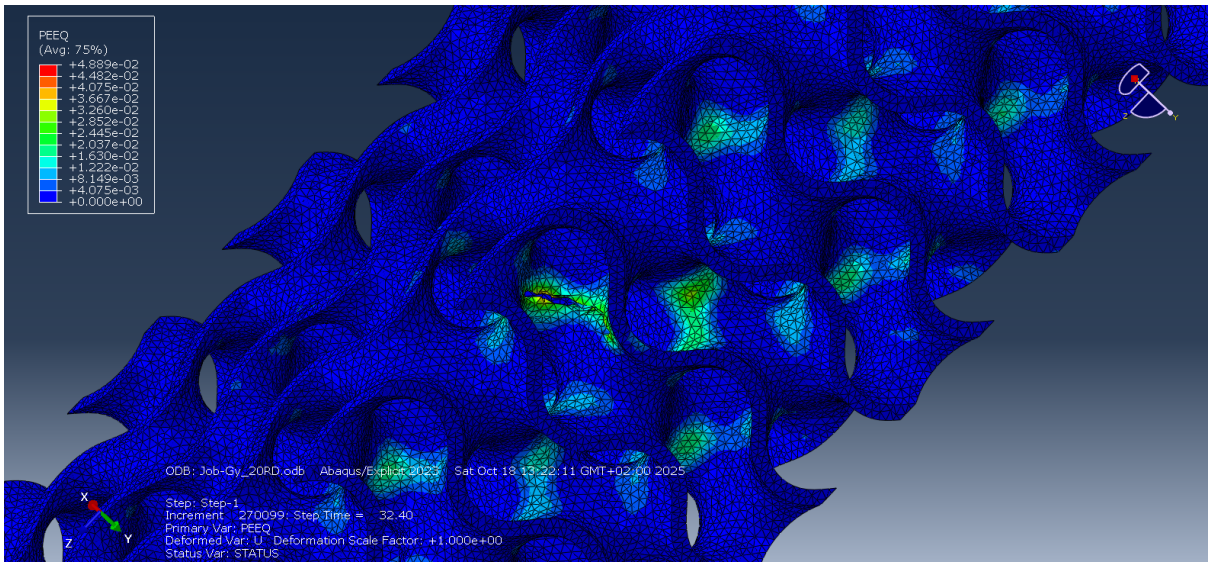

(b) Fracture initiation.

Figure 4.74: Gyroid unit cell: failure mode and fracture initiation, for 20% rel. density specimen.

Chapter 5

Design of fatigue tests by using the static FE model

5.1 Methodology and theoretical background

The specimen design was chosen to allow its use in both quasi-static tensile experimental tests and fatigue analyses under tensile-tensile or tensile-compressive loading conditions. Numerical simulations have confirmed that the specimen design is correct, namely that fracture is predicted to occur within the test section, as prescribed by ASTM standards. In this regard, the same failure locations are expected for both quasi-static and fatigue tests, as Soul et al. [35] observed that similar fracture patterns characterised monotonic and fatigue tests in the lattice structures they studied.

As reported by Xin et al. [14], the primary methods for determining the fatigue life of metallic lattice materials are predominantly empirical and rely on S–N curve fitting. The fatigue life, N_f, is defined as the number of cycles leading to specimen failure under given loading conditions [110]. However, these laboratory activities are costly in terms of both money (mainly fabrication and testing equipment) and time. Therefore, it is necessary to optimise them. Predicting the fatigue life of these structures under different load conditions is essential to identify a range of applicable nominal stresses that allow effective study of fatigue, ensuring that failure does not occur before 10^3 cycles or after 10^6-10^7 cycles. This theoretical preparation helps to avoid conducting unnecessary tests and was also explicitly employed by Zhuo et al. [108].

Based on these considerations, theoretical Wöhler and Haigh curves have been plotted to support the design of experimental cyclic loading configurations. Several studies have demonstrated that the Basquin equation can be employed to construct Wöhler curves for lattice materials [14], while Lietaert et al. [48] have already developed Haigh diagrams based on local stresses. This procedure has also been applied in this thesis. To draw the Wöhler curve for high-cycle fatigue (HCF), the following parameters are of interest: the force at which a stress exceeding 50% of the UTS of the bulk material first appears in the specimen and the force at which 90% of the UTS is reached, as prescribed by the *Bach criterion* [111]. The former provides an estimate of the material's fatigue limit, although for aluminium alloys a true fatigue limit generally does not exist, as fatigue failures can occur at every stress amplitude [110]. For this reason, the concept of *fatigue resistance*[1] is typically used instead, defined as the stress level that produces failure for a given high number of cycles, such as 10^6 or 10^7. No universally recognised value exists:

[1] In this thesis, the terms *fatigue limit* and *fatigue resistance* are used synonymously. However, the term *fatigue limit* is mainly used to accurately reflect the terminology employed by the authors of the referenced works, while *fatigue resistance* is generally used when describing the results obtained in this thesis.

Soro et al. [32] set the failure criterion at 10^6 cycles, Zhuo et al. [108] and Lei et al. [112] (China, Belgium, UK) to $2 * 10^6$, Van Hooreweder et al. [113] (Belgium) at $4 * 10^6$ cycles, while Soul et al. [35] chose 10^7 cycles. During an eventual experimental campaign, once the failure criterion is selected, it may be convenient to start from this force value and decrease it if the specimen fails before reaching the anticipated fatigue life. This approach, unlike the opposite strategy (starting lower and increasing), minimises material consumption. Indeed, this methodology is also suggested by Lei et al. [112]. The authors, during compression-compression fatigue experiments on Ti6Al4V, started applying a force equivalent to 50% the plauteu stress and then decreased it until the sample was able to last for the chosen fatigue life. The 90% UTS stress corresponds to a predicted fatigue life of 1000 cycles, which will be denoted as σ_{1000}. The identification of these loading conditions has been carried out based on maximum principal stresses, using an averaging method of 75%, which is the default in Abaqus. Averaging is necessary because results are calculated at nodes and when graphically displaying results on elements, which are influenced by all the nodes defining them, it is necessary to average the contributions [103]. In this thesis, the fatigue resistance, denoted as σ_D, has been chosen so that when a stress amplitude σ_D is applied, fatigue failure is supposed to happen after $2 * 10^6$ cycles (which is the corresponding fatigue life). This number of cycles corresponds to the average patient walking activity during a year [29][2].

5.2 Results

5.2.1 Wöhler curves

The Wöhler diagrams have been drawn to describe the fatigue life of specimens subjected to alternating stress. Specifically, the number of cycles to failure is reported on the x-axis, while on the y-axis the applied stress amplitude, σ_a, is. In addition, the x-axis is generally plotted on a logarithmic scale [111]. The stress amplitude (or alternating stress) is defined by eq.(5.1) and corresponds to half the difference between the maximum and minimum applied stress. Wöhler diagrams are constructed for a given mean stress, σ_m (half the sum of the maximum and minimum applied stress) [110], and are generally used for *fully reversed* loading cycles, where $\sigma_m = 0$ and the stress ratio $R = -1$. This methodology was also selected here.

$$\sigma_a = \frac{\sigma_{max} - \sigma_{min}}{2} \tag{5.1}$$

$$\sigma_m = \frac{\sigma_{max} + \sigma_{min}}{2} \tag{5.2}$$

$$R = \frac{\sigma_{max}}{\sigma_{min}} \tag{5.3}$$

The fatigue resistance is reported in detail in Tab. 5.1. It has been determined observing the stress distribution within the test section: the first time the maximum principal stress overpass the 50% of AlSi10Mg UTS, which is equal to 208 MPa as the UTS adopted in the simulations is 416 MPa, the reaction force developed by the specimen in that moment is written down. Then, it is divided by the nominal specimen cross section area ($A_0 = 400$ mm^2), to obtain the corresponding nominal stress. This last value is adopted as the estimation of σ_D.

[2]This paper is one of the rare exceptions in which the choice of the fatigue limit is clearly justified.

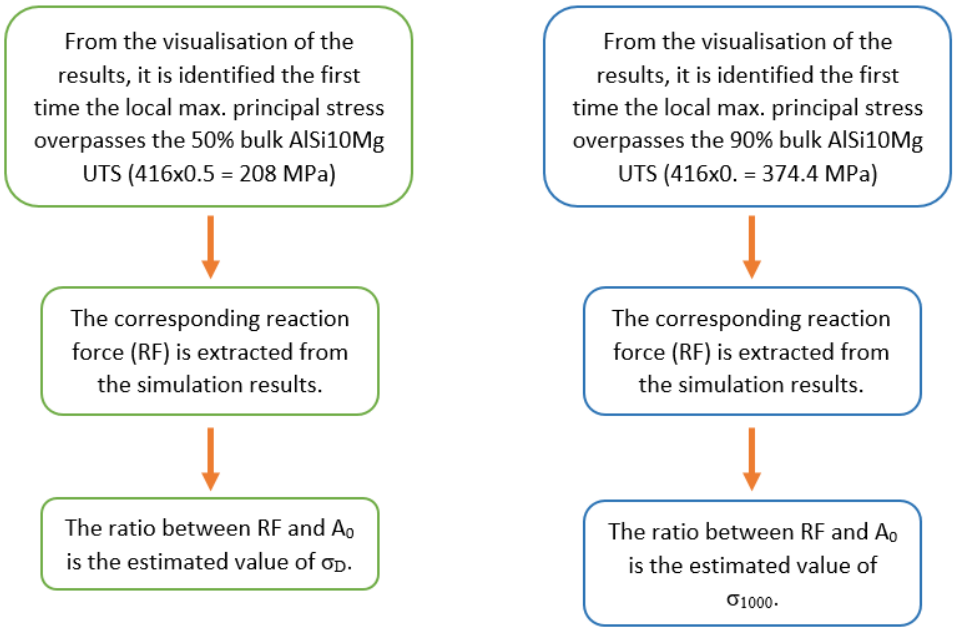

Figure 5.1: Schematic representation of the procedure for determining σ_D and σ_{1000}.

CELL	**Rel. density** [%]	**Fatigue resistance** [MPa]	**Spec. Fatigue resistance** [MPa/g]
BCC	8.32	2.305	0.321
	10.0	2.915	0.338
	15.0	4.335	0.335
	20.0	6.513	0.377
FCC	6.50	1.608	0.287
	10.0	2.290	0.266
	15.0	2.995	0.232
	20.0	6.018	0.349
Primitive	4.30	2.138	0.579
	10.0	3.243	0.377
	15.0	4.900	0.379
	20.0	7.708	0.447
Gyroid	4.87	1.655	0.396
	10.0	3.388	0.391
	15.0	6.280	0.486
	20.0	7.055	0.409

Table 5.1: Fatigue resistance values determined from the tensile simulations results.

The same procedure is adopted for the estimation of σ_{1000}, with the only difference that 90% of AlSi10Mg UTS, hence 374.4 MPa, is the threshold to consider. In Fig. 5.1 a schematic representation of this procedure can be seen. Additional observations can be made observing the graphs in Fig. 5.2 - 5.5 and 5.6 - 5.9. In particular, in Ch. 4, the results of the quasi-static tensile numerical simulations showed a beneficial effect of relative density on mechanical

properties, in agreement with previous findings in the literature. These considerations also apply to the fatigue limit, as previously observed by Kelly et al. [26], and hence to the Wöhler diagrams [108]. Although deviations are larger than those found for Young's modulus, also yield and ultimate tensile strength, whose graphs can be seen in Fig. 5.6 - 5.9, show a positive trend for this specimen characteristic, which increases linearly with volume ratio.

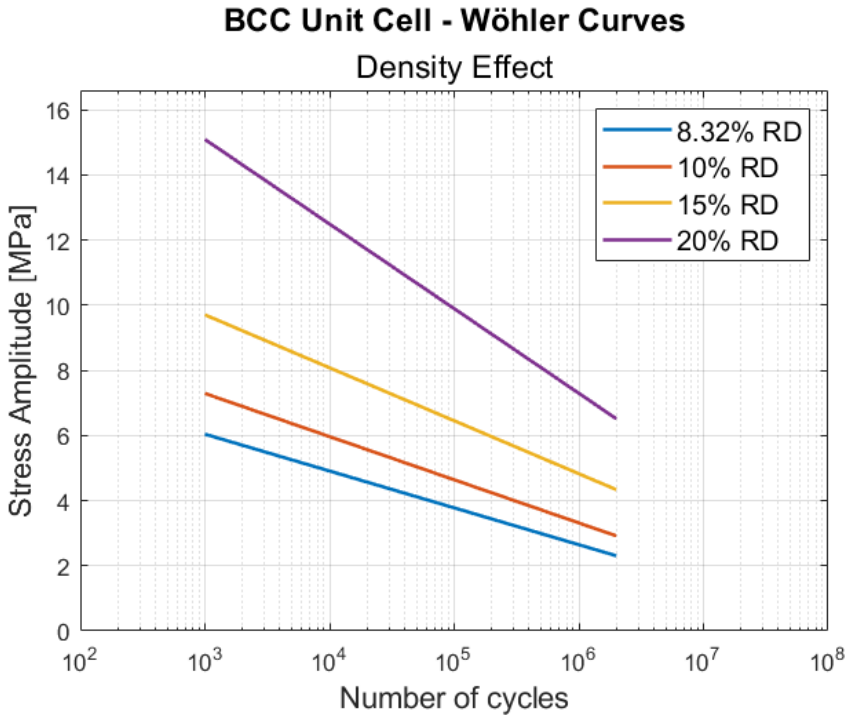

Figure 5.2: BCC unit cell: Wöhler diagram.

At the same time, the specific fatigue resistance values do not display a clear trend, as can be seen in Fig. 5.10 - 5.13. While the grey segments, which approximate the data using a least-squares approach, show a positive trend for all architectures except the Primitive cell, the values are scattered and sometimes increases and sometimes decreases with relative density. Finally, the bar charts in Fig. 5.14 - 5.16 make it easy to observe that the Gyroid architecture has the highest fatigue resistance for 10% and 15% relative densities, whereas the Primitive cell exhibits the highest value at 20% one. Gyroid structures have generally been found to exhibit a very high fatigue life, while the Primitive cell shows one of the shortest [29]. Nevertheless, loading conditions play a significant role in determining lattice performance. In this regard, Jiang et al. [28] investigated the torsional fatigue of several TPMS architectures simulating the mechanical properties of 40 Cr steel. Their simulations showed the Primitive type to perform better and the Gyroid to exhibit the lowest torsion resistance. The results obtained in this thesis do not fully reflect those of Bobbert et al. [29], but a possible explanation could be related to differences between compressive and tensile behaviour. Moreover, plate-based lattices generally exhibit lower fatigue resistance, with the FCC architecture being the weakest.

The same data used for building the Wöhler diagrams, namely the reaction forces linked to the first appearance of stress equivalent to 50% and 90% of the material UTS, have been employed to estimate and visualise the range of applicable stress amplitudes. These are reported in Fig. 5.17 - 5.20 to observe the impact of relative density and in Fig. 5.21 - 5.23 to analyse the effect of topology. For each topology, an increase in relative density leads to a larger stress range. This occurs because the global stress corresponding to 90% of the ultimate tensile strength (UTS)

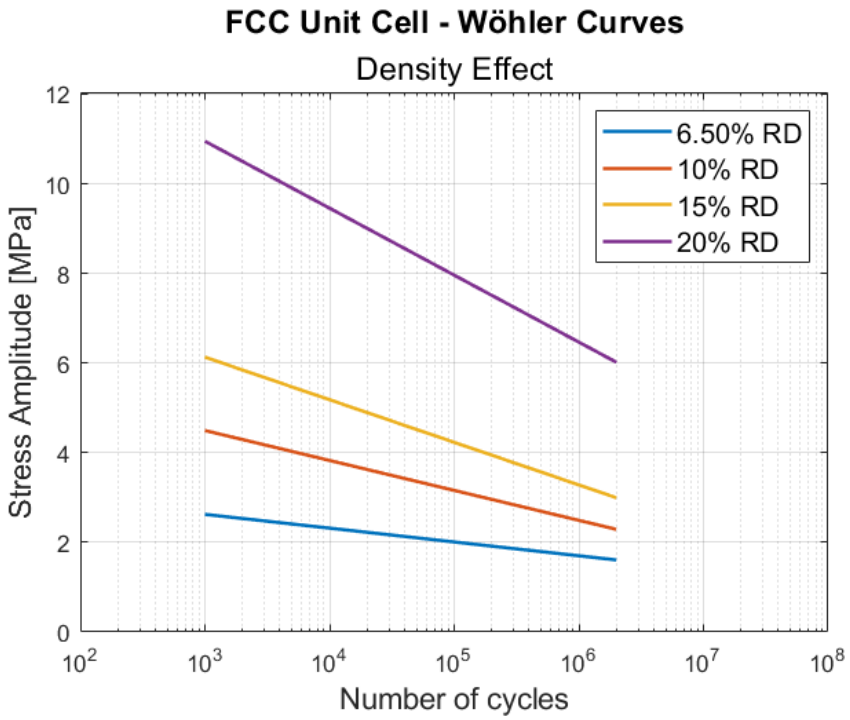

Figure 5.3: FCC unit cell: Wöhler diagram.

increases more significantly than that corresponding to 50% of the UTS. Consequently, the segments in Fig. 5.17 - 5.20 are more extensively stretched. The only exception is represented by the 15% and 20% relative density Gyroid samples, whose ranges are very similar.

More interesting is the comparison of the same relative densities, to study the influence of topology. The FCC architecture is always characterised by narrow stress ranges, with the lowest minimum and maximum applicable stresses. In contrast, the other plate-based architecture, namely BCC, exhibits a very large stress range, although still with a low minimum stress; its maximum is the highest for the 10% samples and one of the highest (approximately equal to that of the Primitive cell) for the 20% samples. The Primitive cell benefits from higher density: its range is narrow and the maximum stress is low, except for the heaviest specimen, condition in which it is large and shows both the highest minimum and maximum applicable stresses. Finally, the Gyroid cell presents one of the highest fatigue resistance, and hence high minimum applicable stresses, with its performance reaching a peak at 15% relative density.

Fatigue ratio, also referred to as the fatigue endurance limit, is defined as « *the ratio of the fatigue limit or fatigue strength to the tensile strength for tension-compression fatigue, and as the ratio of fatigue strength to the plateau stress for compression-compression fatigue*» [112]. The value of the fatigue ratio varies among materials, loading conditions, and specimen architectures. For SLM 316L stainless steel, it is typically around 0.19 [112]. Lei et al. [112], who investigated skeletal Gyroid structures with a 15% relative density, additively manufactured via SLM using 316L stainless steel, reported a fatigue ratio of 0.35 for as-built specimens and 0.45 for sandblasted ones. Bobbert et al. [29] cited similar results, reporting that several AM porous biomaterials previously studied (mainly strut-based) are characterised by a ratio between the fatigue limit and the yield (or plateau) stress of approximately 20%. In their study, the authors investigated the fatigue response of sheet-like TPMS structures produced with Ti6Al4V by SLM under compression-compression cyclic loads and found values up to 60% for Diamond cells. Kelly et al. [26] reported a value of 50% for Gyroid structures. As can be easily observed

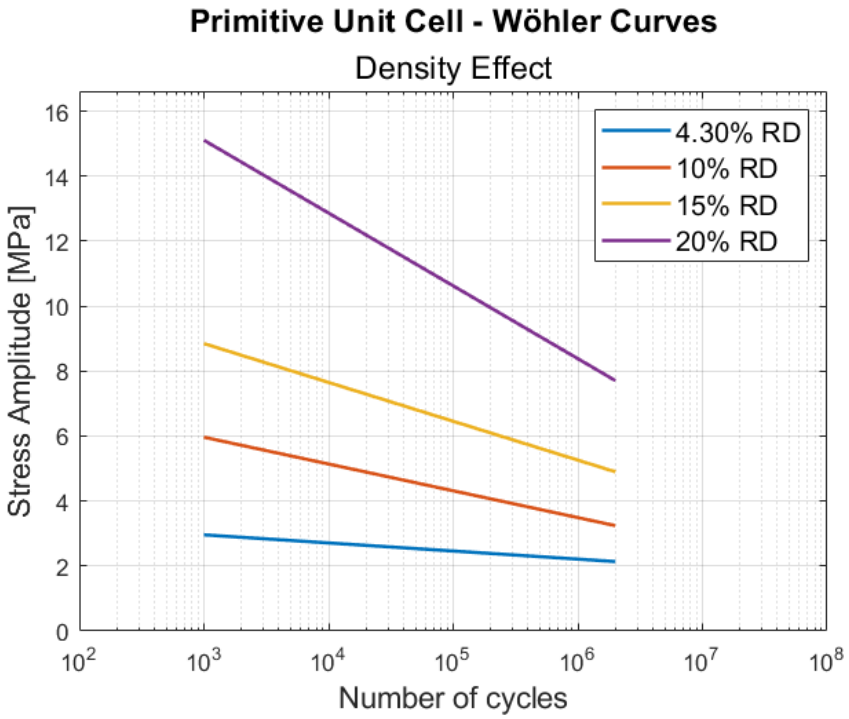

Figure 5.4: Primitive unit cell: Wöhler diagram.

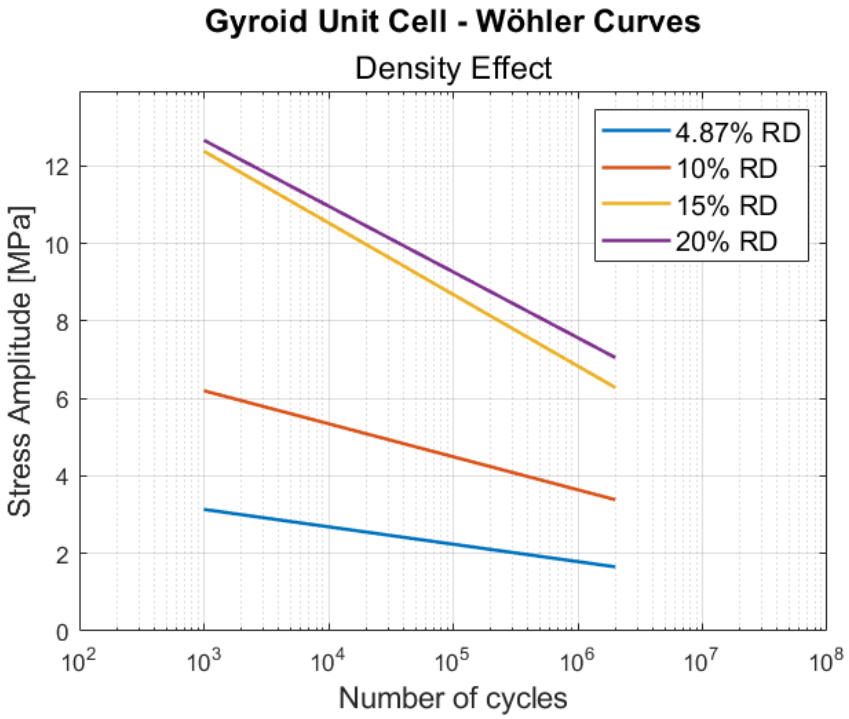

Figure 5.5: Gyroid unit cell: Wöhler diagram.

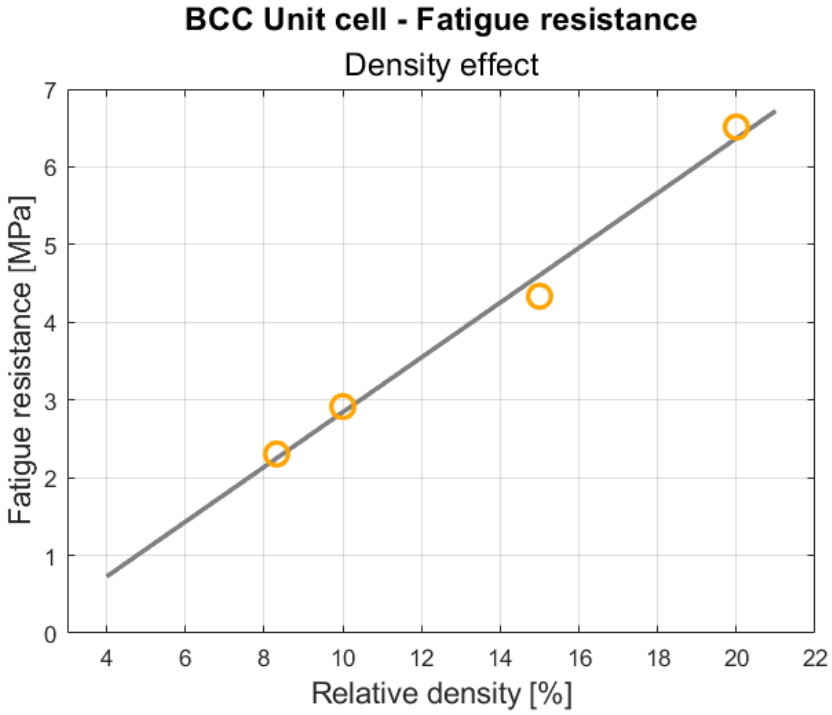

Figure 5.6: Fatigue resistance as a function of relative density: graphical representation of the dependency, for the BCC cell.

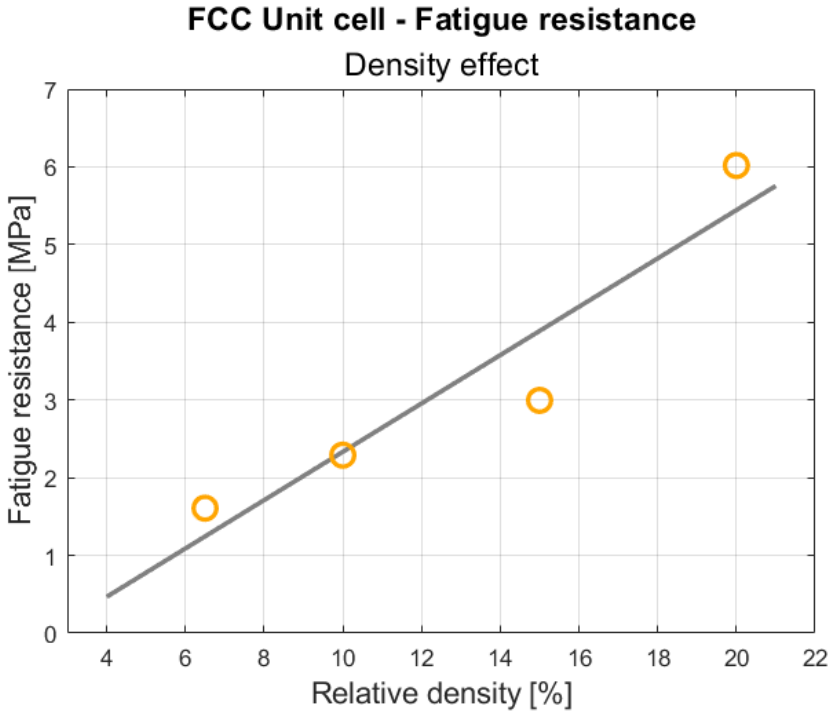

Figure 5.7: Fatigue resistance as a function of relative density: graphical representation of the dependency, for the FCC cell.

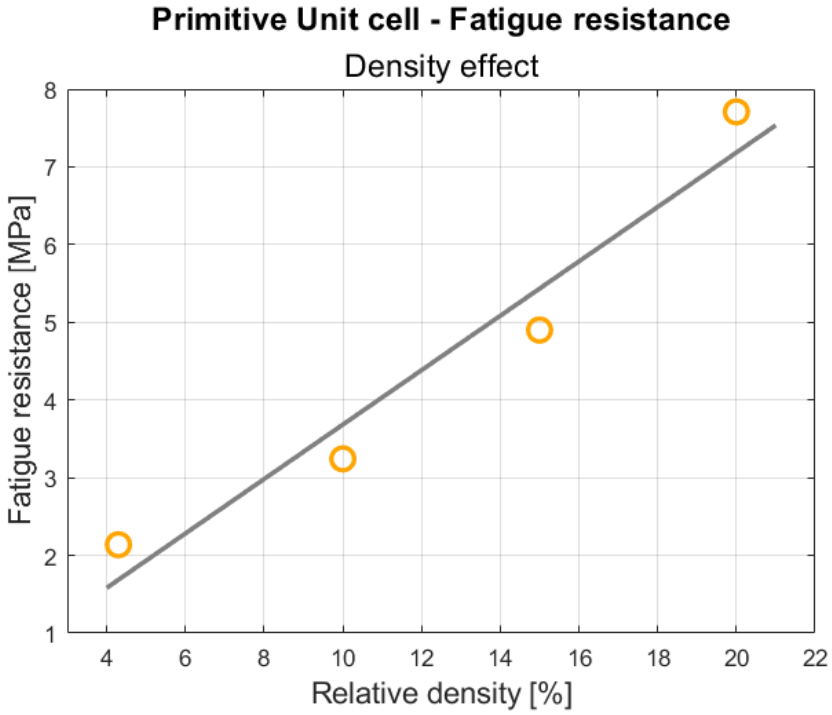

Figure 5.8: Fatigue resistance as a function of relative density: graphical representation of the dependency, for the Primitive cell.

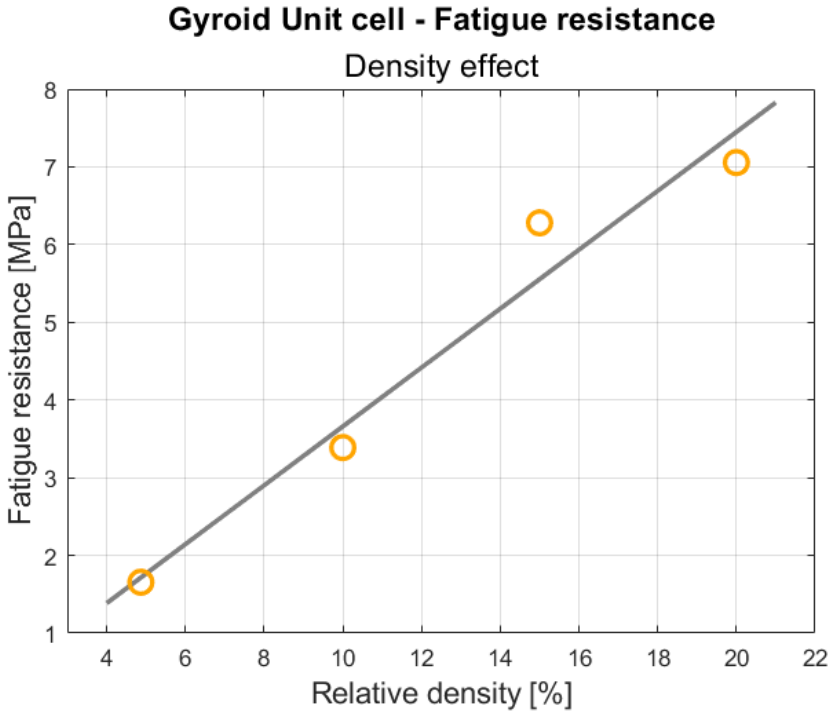

Figure 5.9: Fatigue resistance as a function of relative density: graphical representation of the dependency, for the Gyroid cell.

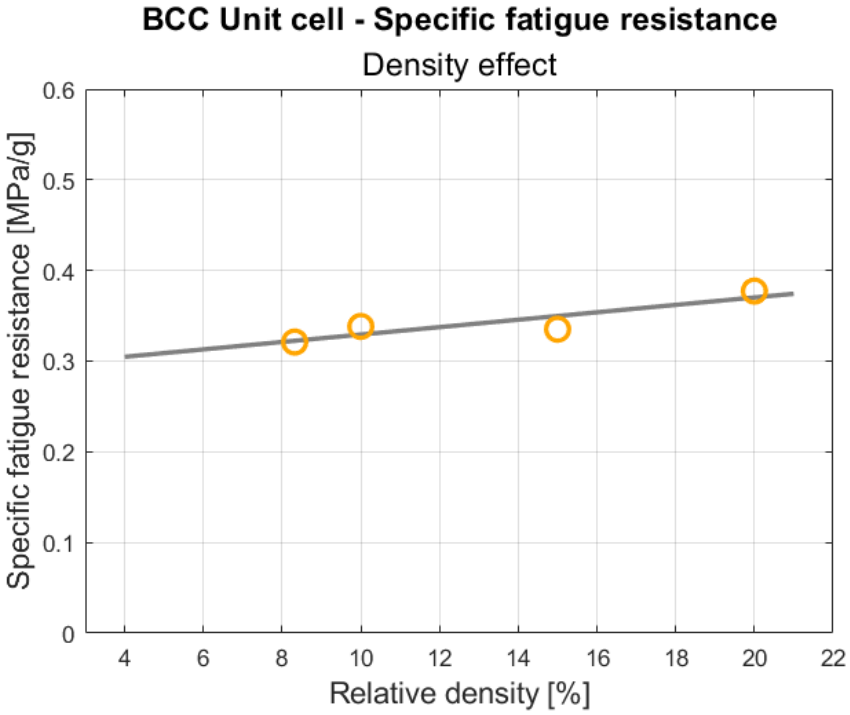

Figure 5.10: Specific fatigue resistance as a function of relative density: graphical representation of the dependency, for the BCC cell.

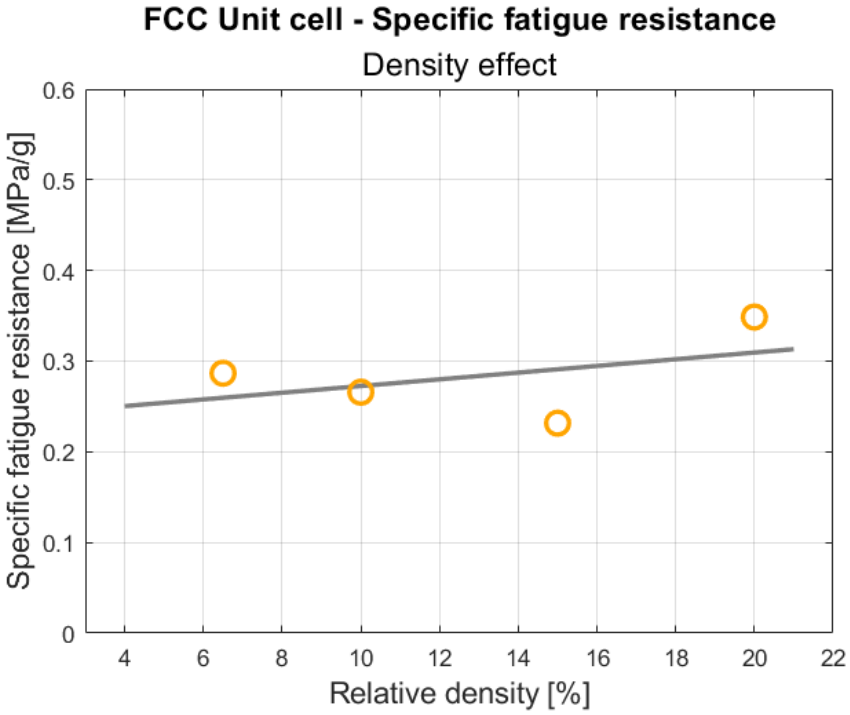

Figure 5.11: Specific fatigue resistance as a function of relative density: graphical representation of the dependency, for the FCC cell.

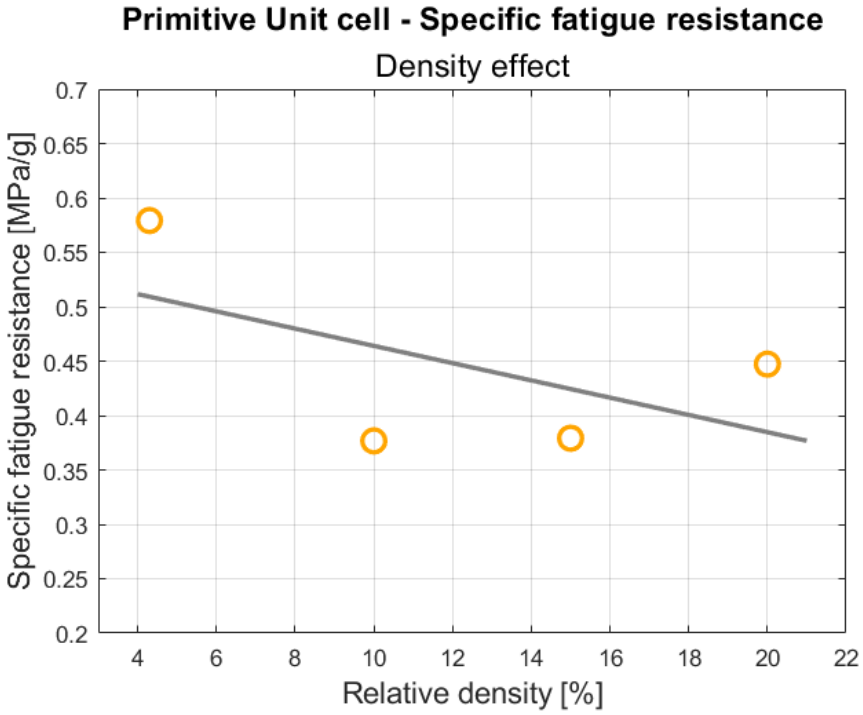

Figure 5.12: Specific fatigue resistance as a function of relative density: graphical representation of the dependency, for the Primitive cell.

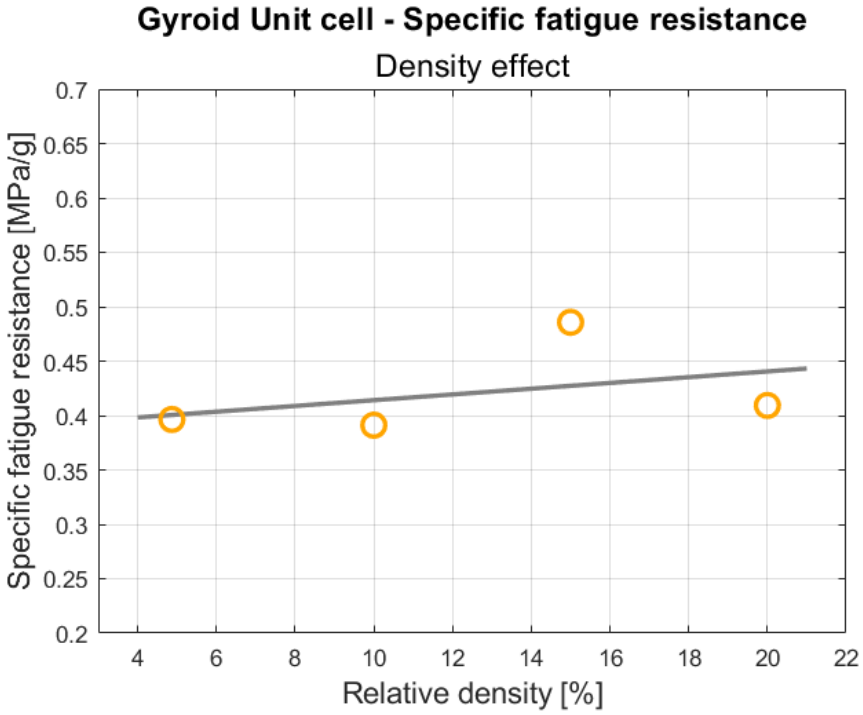

Figure 5.13: Specific fatigue resistance as a function of relative density: graphical representation of the dependency, for the Gyroid cell.

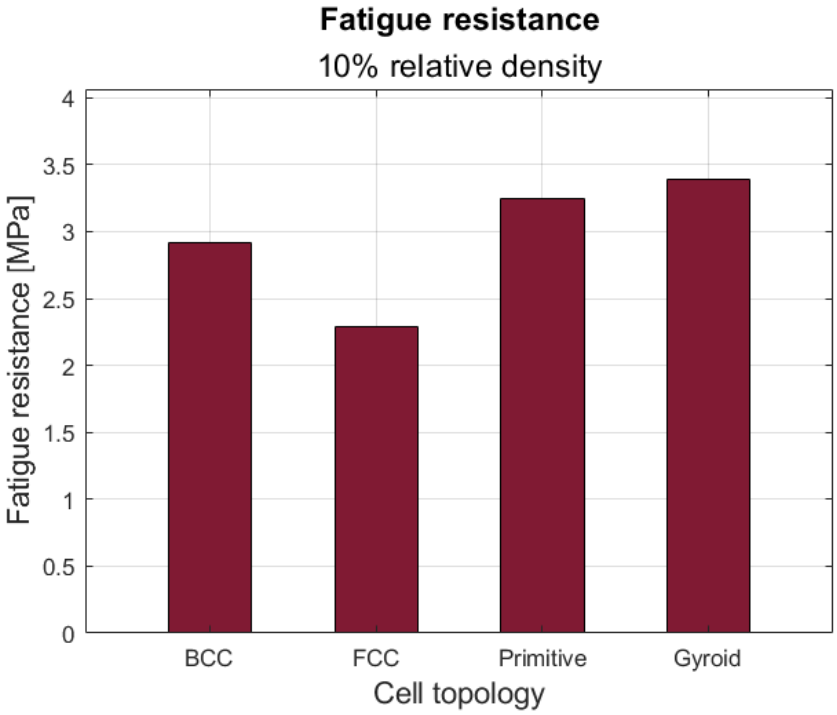

Figure 5.14: Bar charts depicting the influence of lattice topology on fatigue resistance, for 10% rel. density specimens.

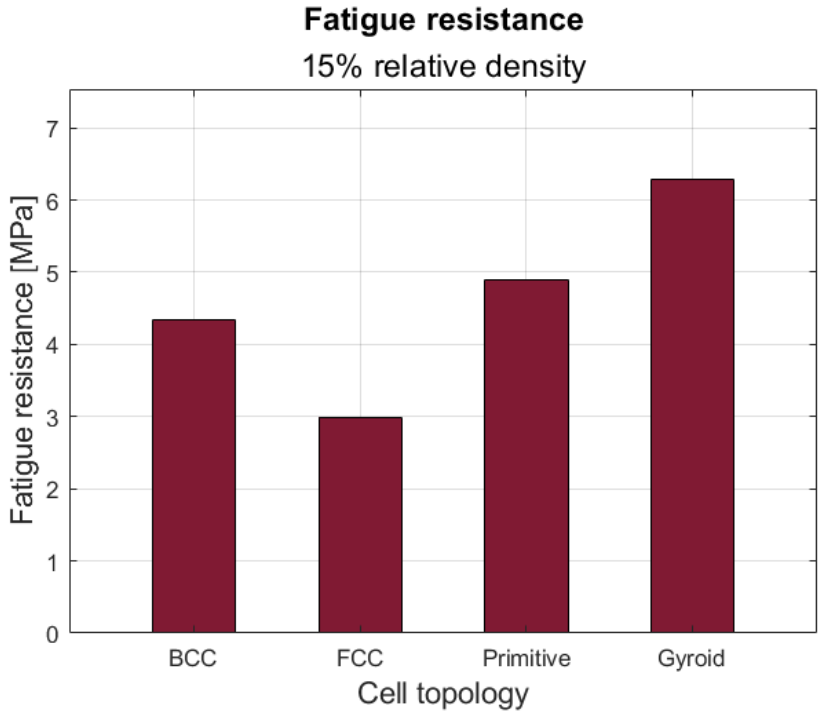

Figure 5.15: Bar charts depicting the influence of lattice topology on fatigue resistance, for 15% rel. density specimens.

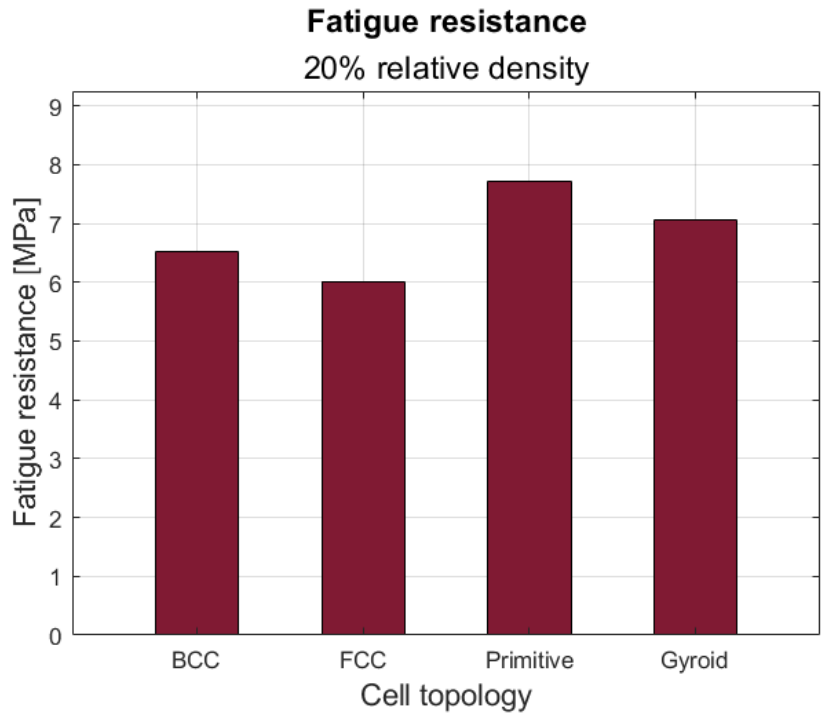

Figure 5.16: Bar charts depicting the influence of lattice topology on fatigue resistance, for 20% rel. density specimens.

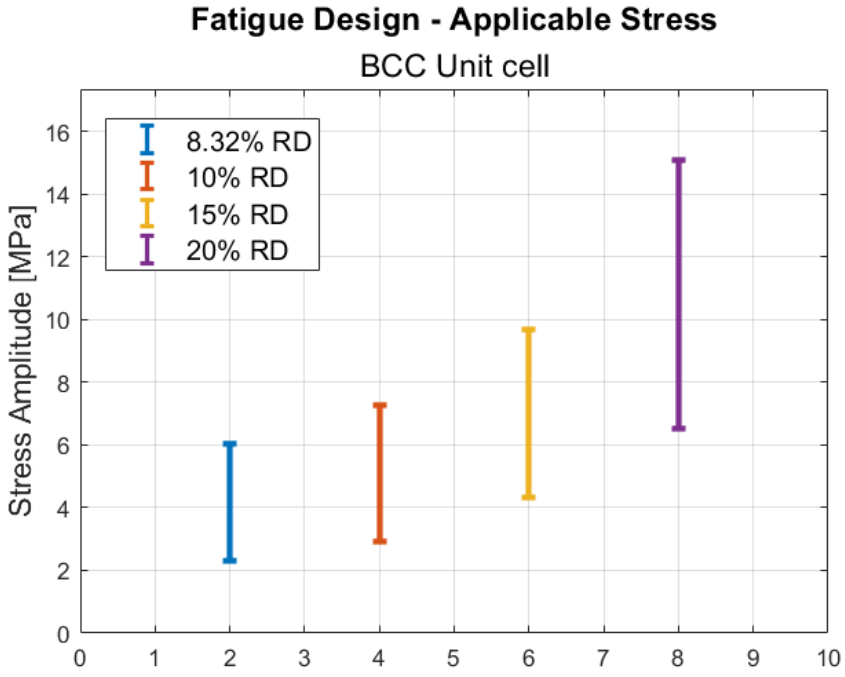

Figure 5.17: Applicable stress amplitude: impact of porosity, for the BCC cell.

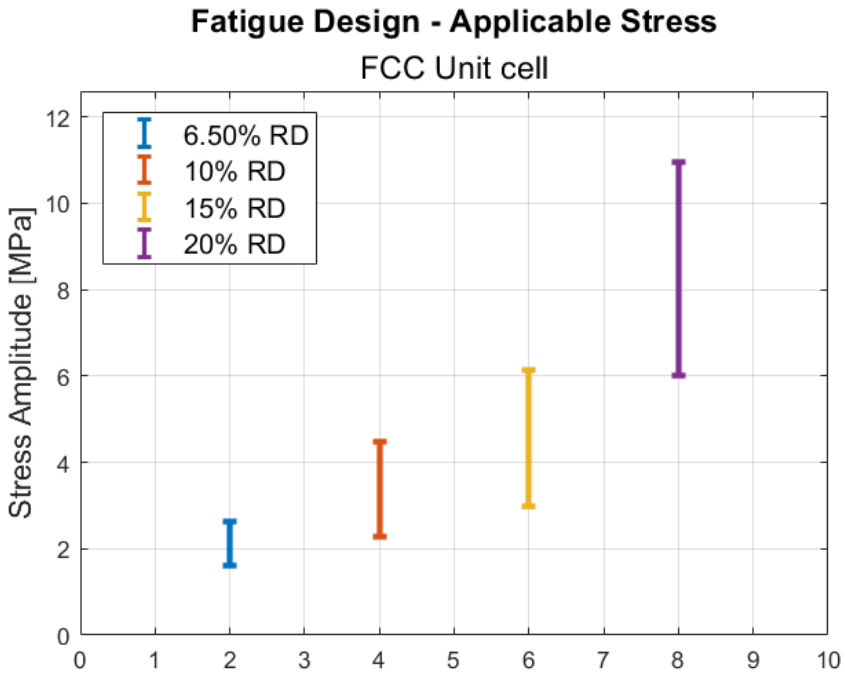

Figure 5.18: Applicable stress amplitude: impact of porosity, for the FCC cell.

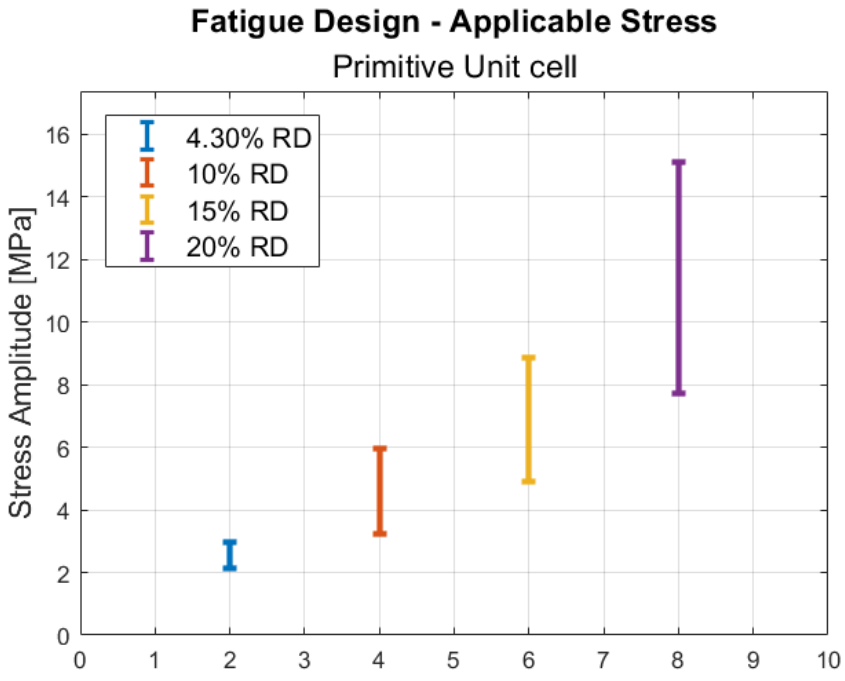

Figure 5.19: Applicable stress amplitude: impact of porosity, for the Primitive cell.

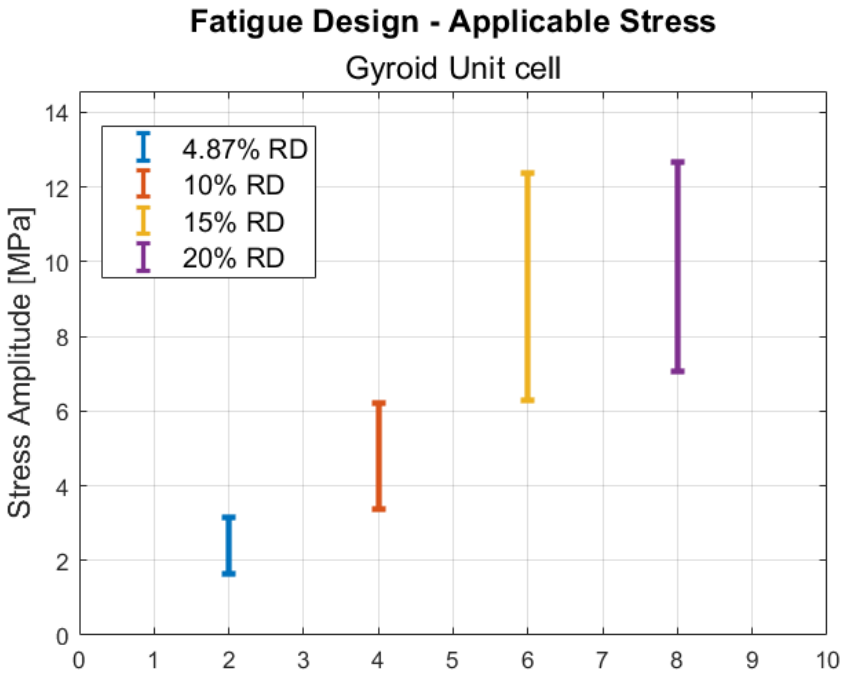

Figure 5.20: Applicable stress amplitude: impact of porosity, for the Gyroid cell.

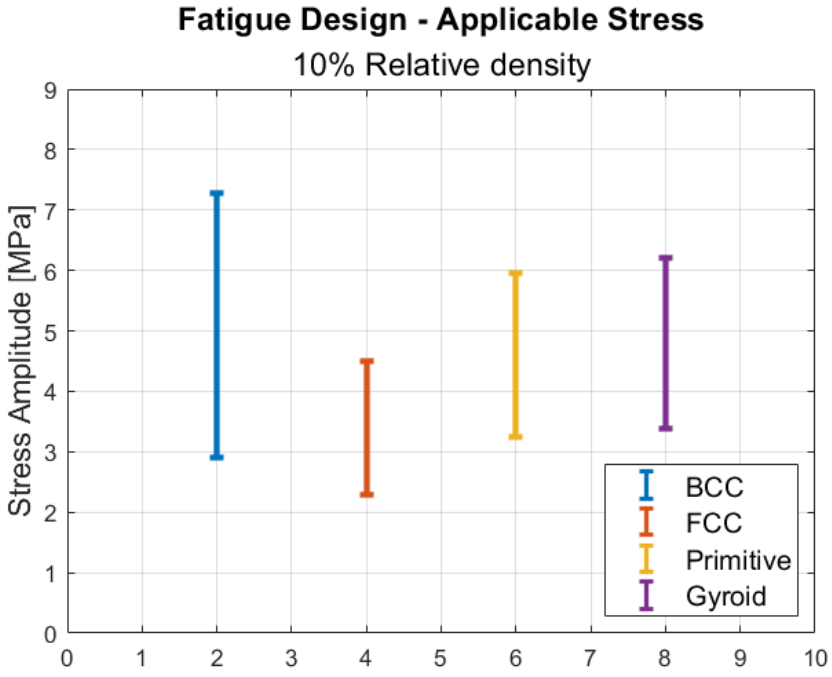

Figure 5.21: Applicable stress amplitude: impact of lattice topology, for 10% rel. density specimens.

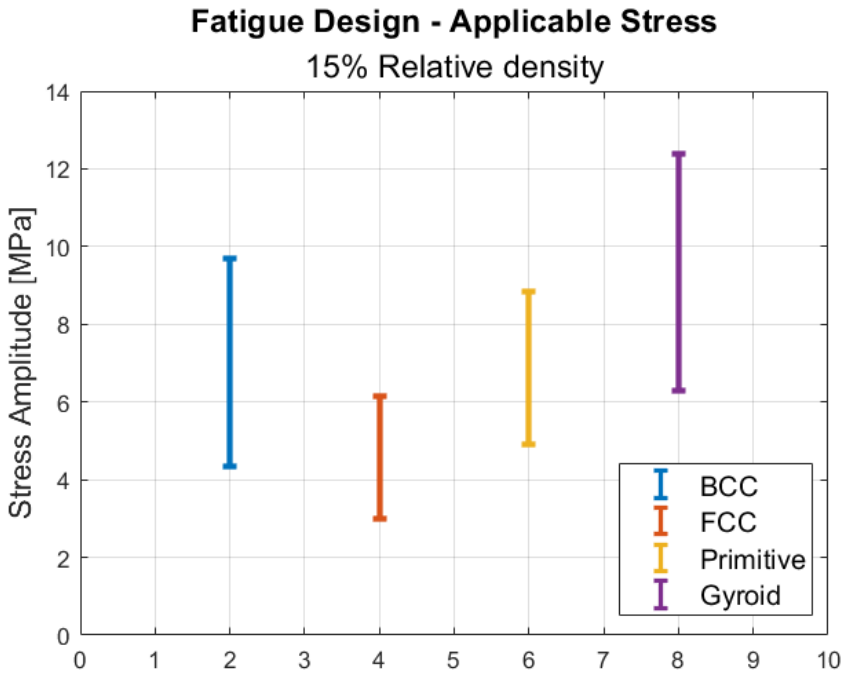

Figure 5.22: Applicable stress amplitude: impact of lattice topology, for 15% rel. density specimens.

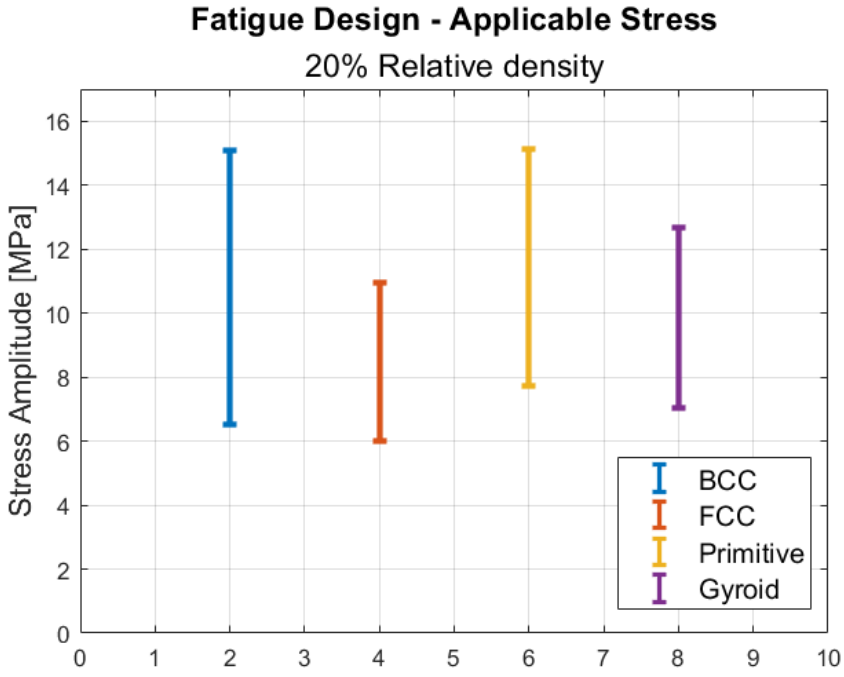

Figure 5.23: Applicable stress amplitude: impact of lattice topology, for 20% rel. density specimens.

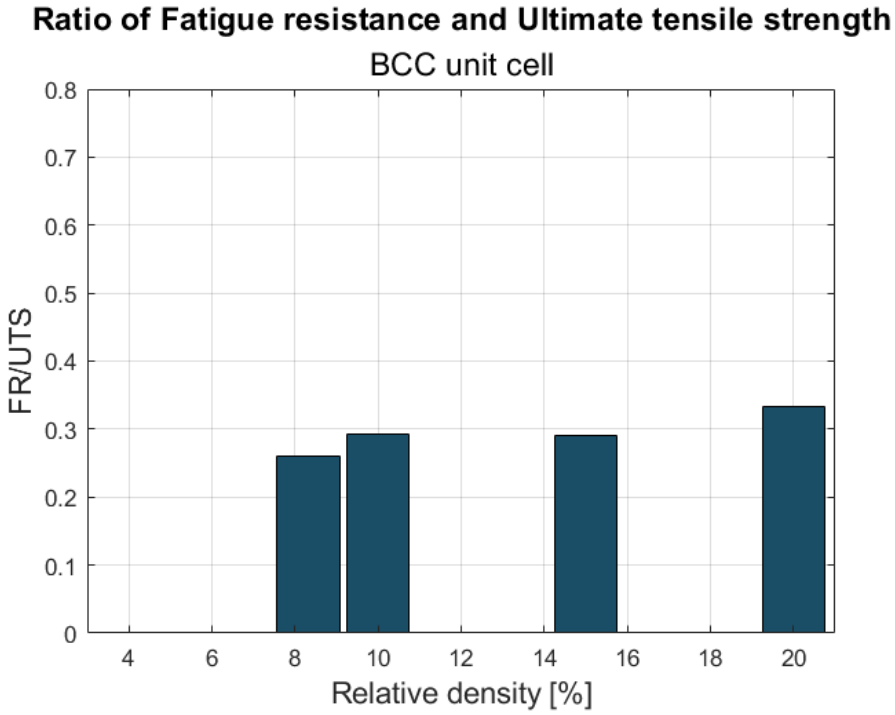

Figure 5.24: Bar charts illustrating the ratio between fatigue resistance and global ultimate tensile strength as a function of relative density, for the BCC cell.

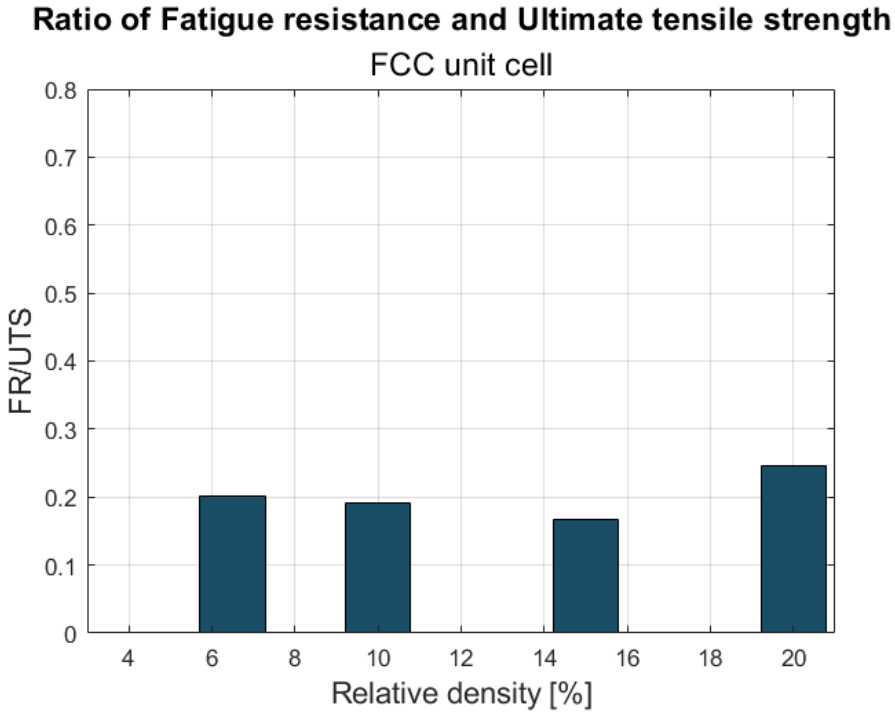

Figure 5.25: Bar charts illustrating the ratio between fatigue resistance and global ultimate tensile strength as a function of relative density, for the FCC cell.

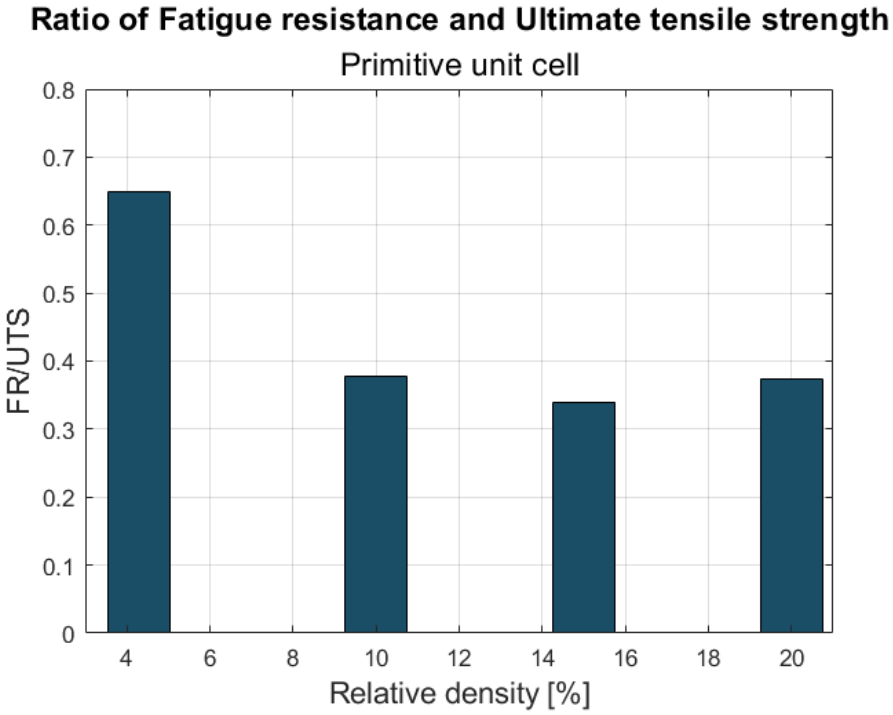

Figure 5.26: Bar charts illustrating the ratio between fatigue resistance and global ultimate tensile strength as a function of relative density, for the Primitive cell.

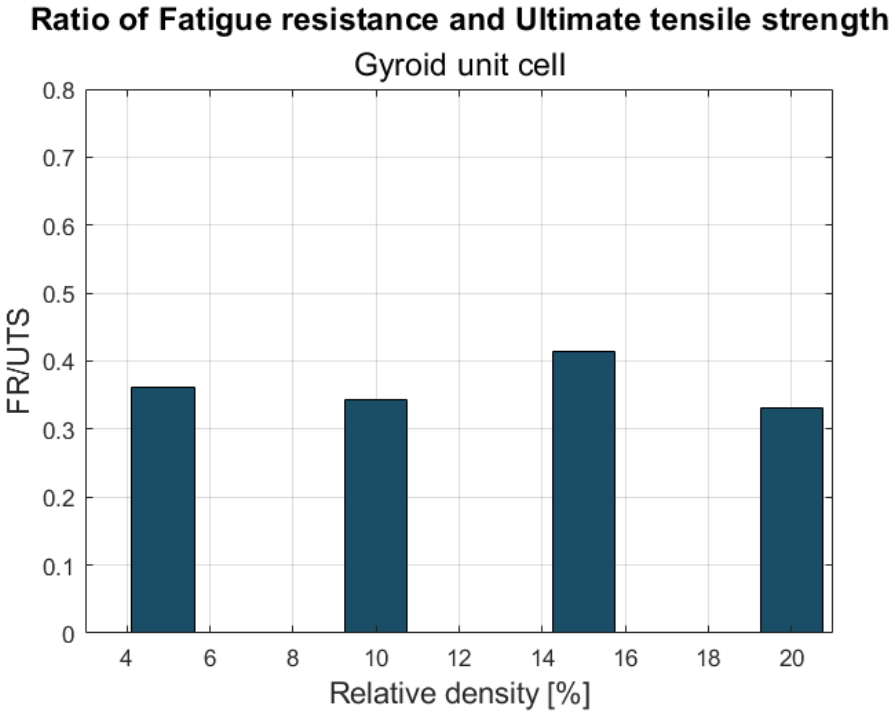

Figure 5.27: Bar charts illustrating the ratio between fatigue resistance and global ultimate tensile strength as a function of relative density, for the Gyroid cell.

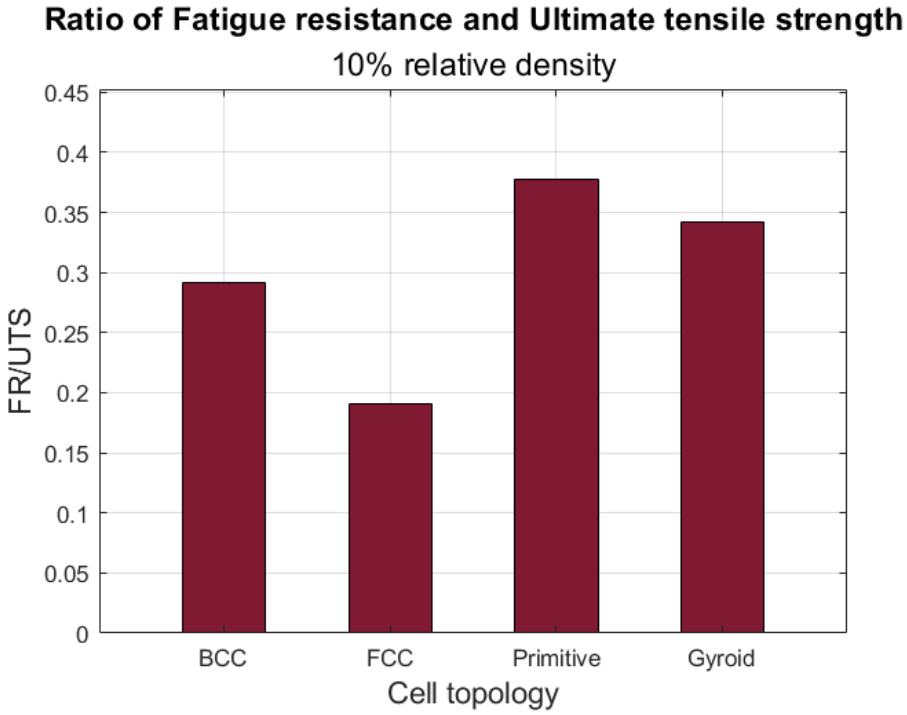

Figure 5.28: Bar charts depicting the influence of lattice topology on fatigue resistance, for 10% rel. density specimens.

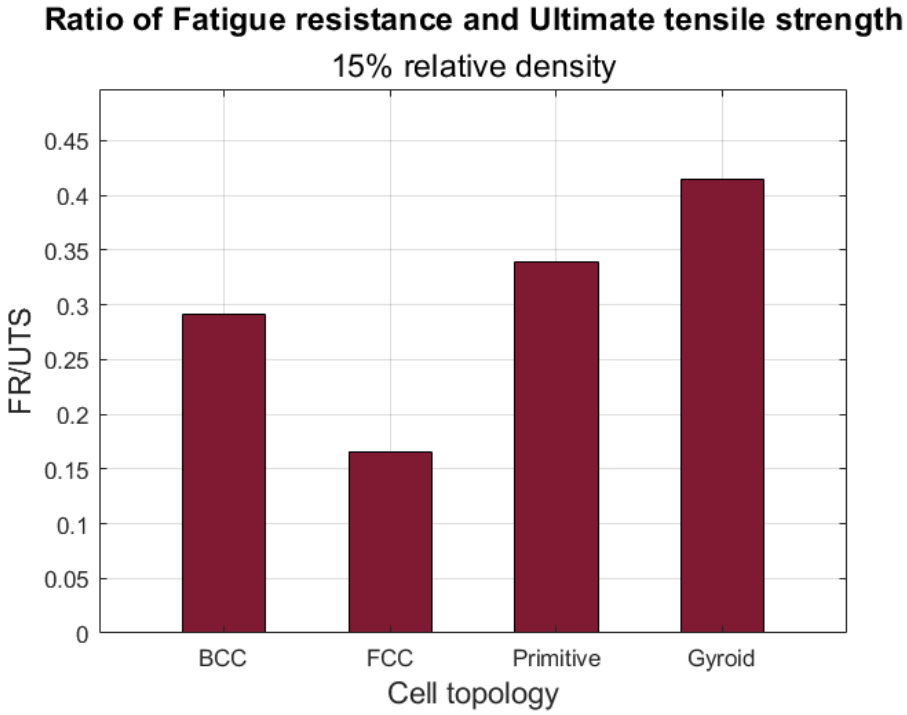

Figure 5.29: Bar charts depicting the influence of lattice topology on fatigue resistance, for 15% rel. density specimens.

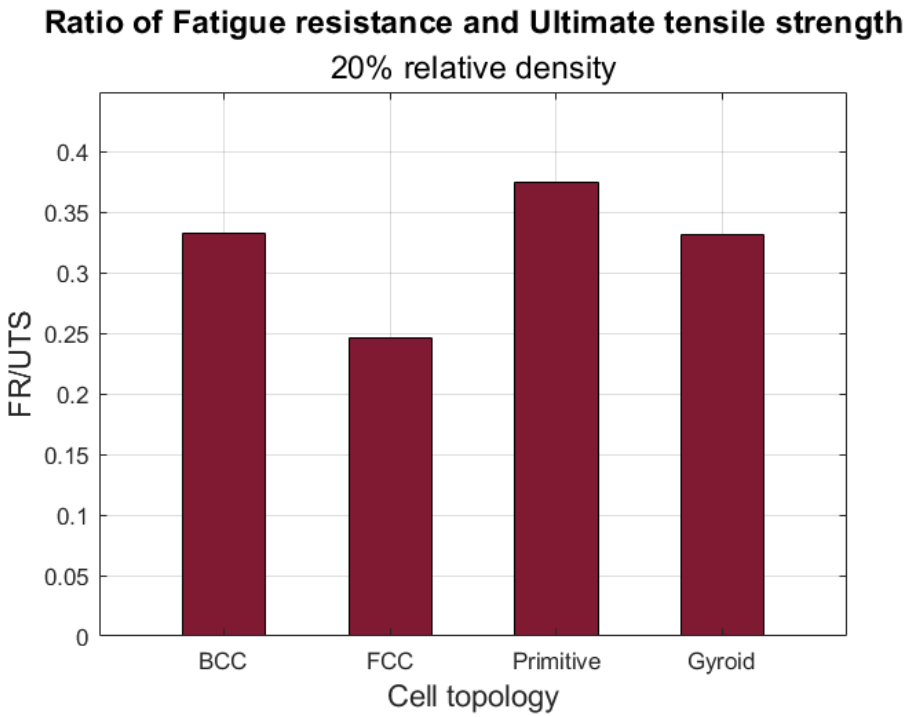

Figure 5.30: Bar charts depicting the influence of lattice topology on fatigue resistance, for 20% rel. density specimens.

from the bar charts in Fig. 5.24 - 5.27 and 5.28 - 5.30, the values obtained in this thesis lie in between. TPMS lattices show higher fatigue performance compared to the plate-based ones, which are expected to suffer significantly from the degradation of mechanical properties due to the cut-outs. Specifically, the FCC architecture consistently shows the lowest fatigue ratio (around 20%), whereas TPMS structures, namely the Primitive and the Gyroid, clearly outperform perforated plate-based lattices, probably due to their smoother stress distribution. TPMS cells exhibit fatigue ratios from 33 to 41, with the lightest Primitive sample almost reaching 80%. It is also possible that this last result is negatively influenced by some mesh issues, potentially linked to the extremely thin walls. The BCC cell exhibits intermediate behaviour and approaches TPMS performance at higher densities, with the 20% specimen having a fatigue ratio of 33%.

5.2.2 Haigh curves

In practical applications, the mean stress is usually different from zero. Consequently, it is necessary to study its influence and the differences in mechanical behaviour it induces compared to the cases described by Wöhler diagrams, in which only stress amplitude is considered and the mean stress is zero [114]. To perform this analysis, Haigh diagrams can be employed. One of the simplest, yet most conservative [114], approaches is known as the *Goodman approach*. The Goodman equation, reported in Eq. (5.4), represents the boundary between safe and unsafe cyclic loading configurations. Considering only the first quadrant, it is the segment connecting the fatigue resistance, σ_D, on the y-axis with the ultimate tensile strength, σ_R, on the x-axis, for a given fatigue life represented by a number N_f of cycles. Therefore, each pair (σ_m, σ_a) along this segment represents a loading condition that would theoretically cause specimen failure in

N_f cycles[3], whereas below this line the components should not fail for that given fatigue life.

$$\frac{\sigma_a}{\sigma_N} + \frac{\sigma_m}{\sigma_R} = 1 \tag{5.4}$$

In order to draw the Haigh curve, it is necessary to obtain the values of the stress amplitude that, when a zero mean tensile stress is applied, lead to failure for a precise, given number of cycles. To obtain these data, the Basquin relation is applied to the known values, specifically to σ_{1000}, defined as the alternating stress (with $R = -1$) that causes specimen failure in approximately 1000 cycles, and to the fatigue resistance σ_D, defined here as the alternating stress, also with $R = -1$, that does not lead to specimen failure for 2×10^6 cycles. These values have already been extracted from the tensile numerical simulations. Hence, the Basquin relation, given by Eq. (5.5) and valid in the HCF regime from 10^3 cycles up to the fatigue resistance, is applied, resulting in a system of two linearly independent equations in two variables, which can then be solved.

$$\sigma_N = A * (N)^b \tag{5.5}$$

$$\text{Eq. } 1 \sigma_{1000} = A * (10^3)^b \tag{5.6}$$

$$\text{Eq. } 2 \sigma_D = A * (2 * 10^6)^b \tag{5.7}$$

The solutions are the following:

$$b = \frac{log \frac{\sigma_D}{\sigma_{1000}}}{3 + log 2} \tag{5.8}$$

$$A = \frac{\sigma_{1000}}{10^{3b}} \tag{5.9}$$

It is important to emphasise that these coefficients are strictly dependent on the specimen, and therefore vary not only with the material, but also with the type of unit cell and the relative density. Consequently, sixteen pairs must be computed, sixteen Basquin relations are written, each applied for five values of N (10^3, 10^4, 10^5, 10^6, 2×10^6), resulting in sixteen curves. The MATLAB scripts used are attached in App. E, the Basquin's coefficients obtained in Tab. 5.2. Finally, in Fig. 5.31 - 5.46 the corresponding Haigh diagrams can be seen.

[3]In real experiments, fatigue data exhibit significant scatter [111]. As a result, Wöhler and Haigh diagrams typically display multiple curves for the same loading conditions, each corresponding to different failure probabilities.

CELL	**Rel. density** [%]	**A** [MPa]	**b**
BCC	8.32	14.4961	−0.1267
	10.0	16.7693	−0.1206
	15.0	20.1876	−0.1060
	20.0	32.3855	−0.1106
FCC	6.50	4.0991	−0.0645
	10.0	8.2969	−0.0887
	15.0	11.7624	−0.0943
	20.0	18.8670	−0.0788
Primitive	4.30	3.9791	−0.0428
	10.0	10.3800	−0.0802
	15.0	15.1371	−0.0777
	20.0	27.8495	−0.0885
Gyroid	4.87	5.6110	−0.0842
	10.0	10.7390	−0.0795
	15.0	22.9404	−0.0893
	20.0	21.5546	−0.0770

Table 5.2: Basquin's coefficients determined for the different specimens.

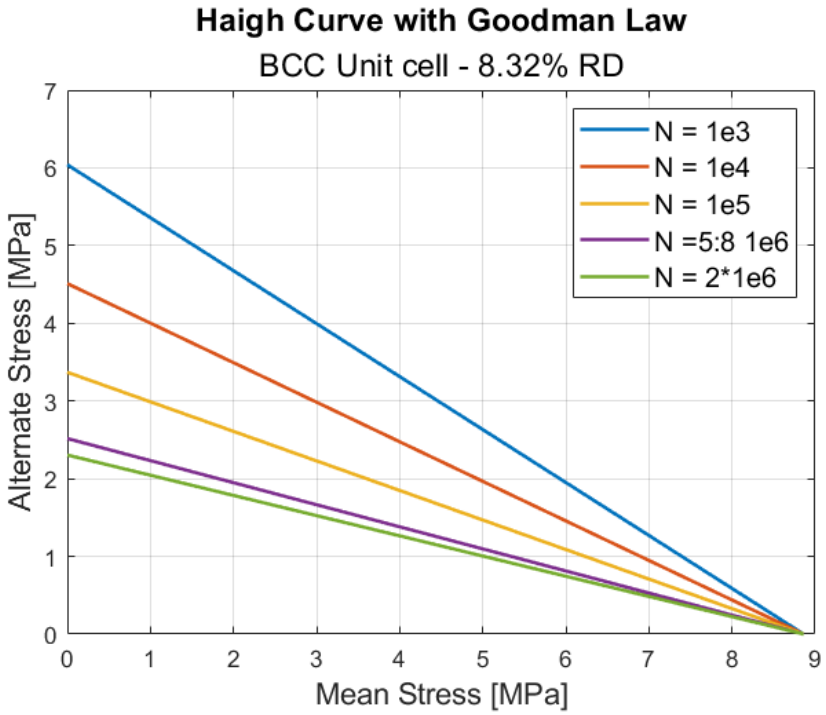

Figure 5.31: Haigh diagrams with the Goodman line representation: BCC unit cell - 8.32% rel. density.

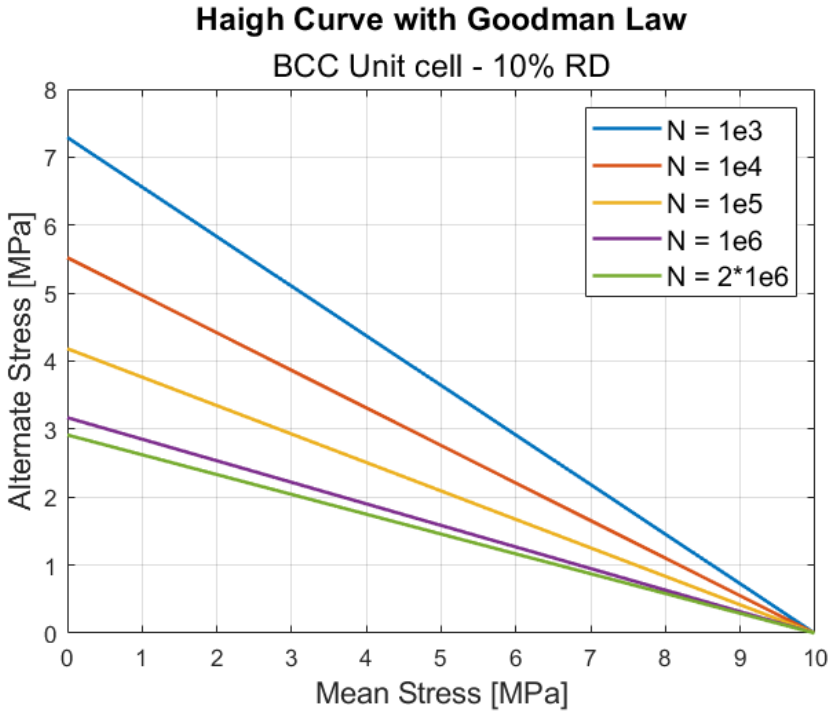

Figure 5.32: Haigh diagrams with the Goodman line representation: BCC unit cell - 10% rel. density.

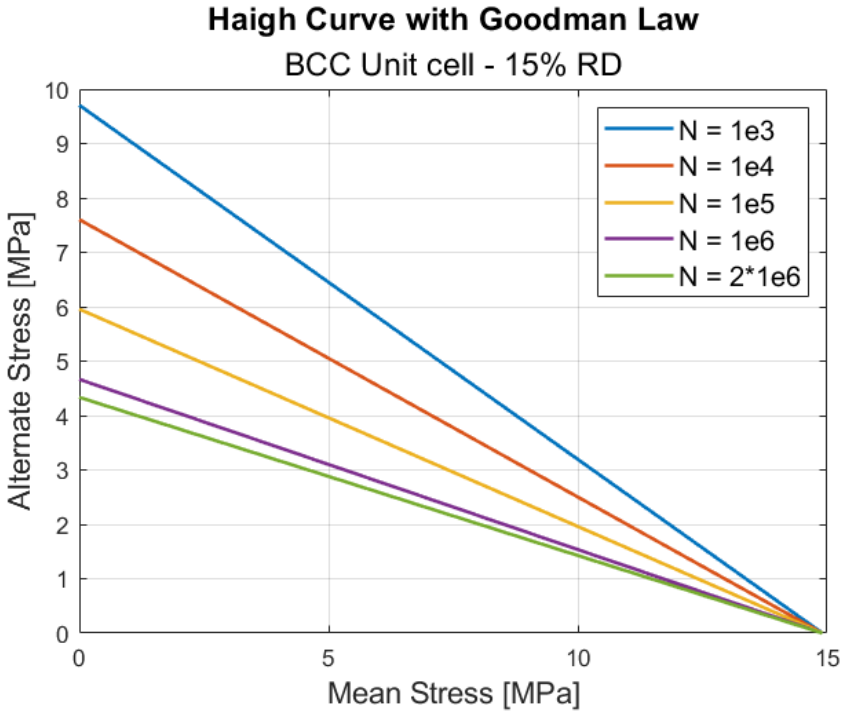

Figure 5.33: Haigh diagrams with the Goodman line representation: BCC unit cell - 15% rel. density.

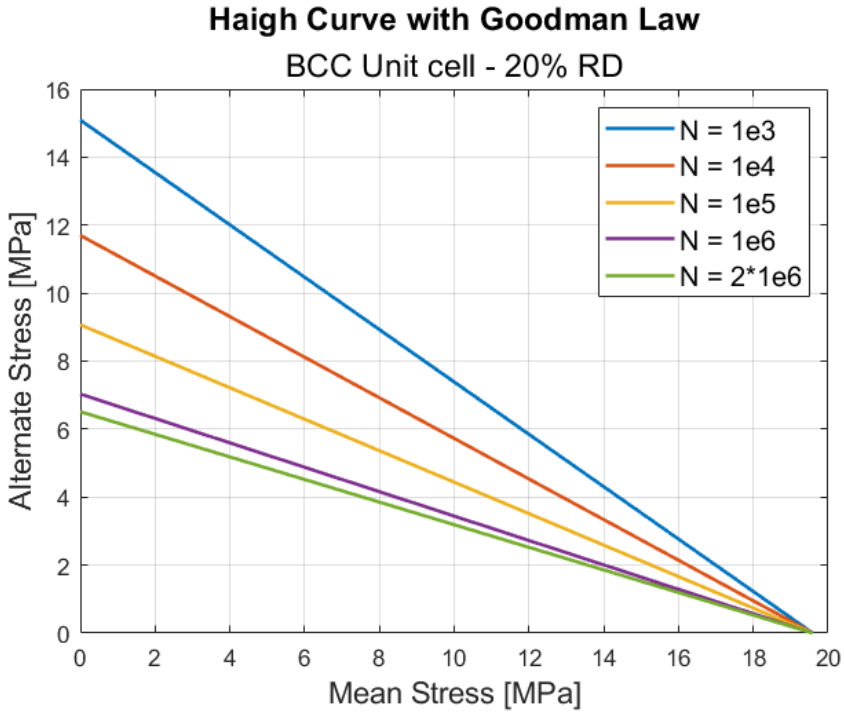

Figure 5.34: Haigh diagrams with the Goodman line representation: BCC unit cell - 20% rel. density.

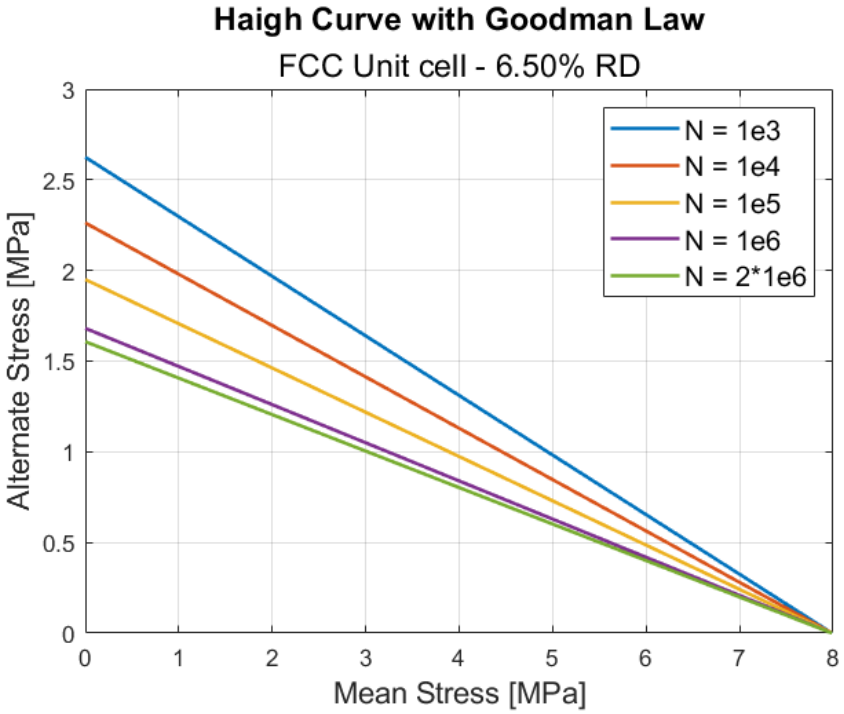

Figure 5.35: Haigh diagrams with the Goodman line representation: FCC unit cell - 6.50% rel. density.

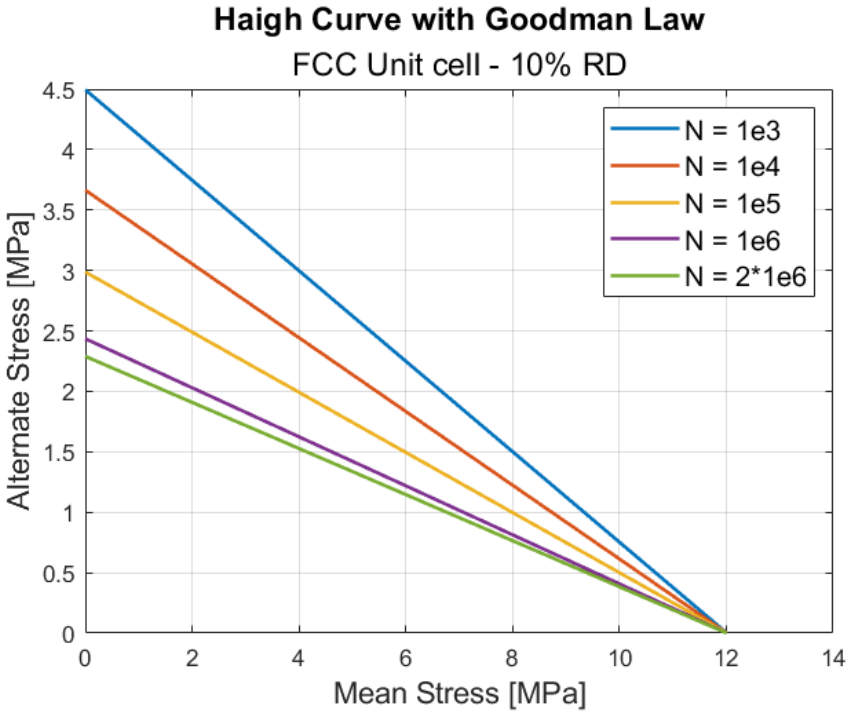

Figure 5.36: Haigh diagrams with the Goodman line representation: FCC unit cell - 10% rel. density.

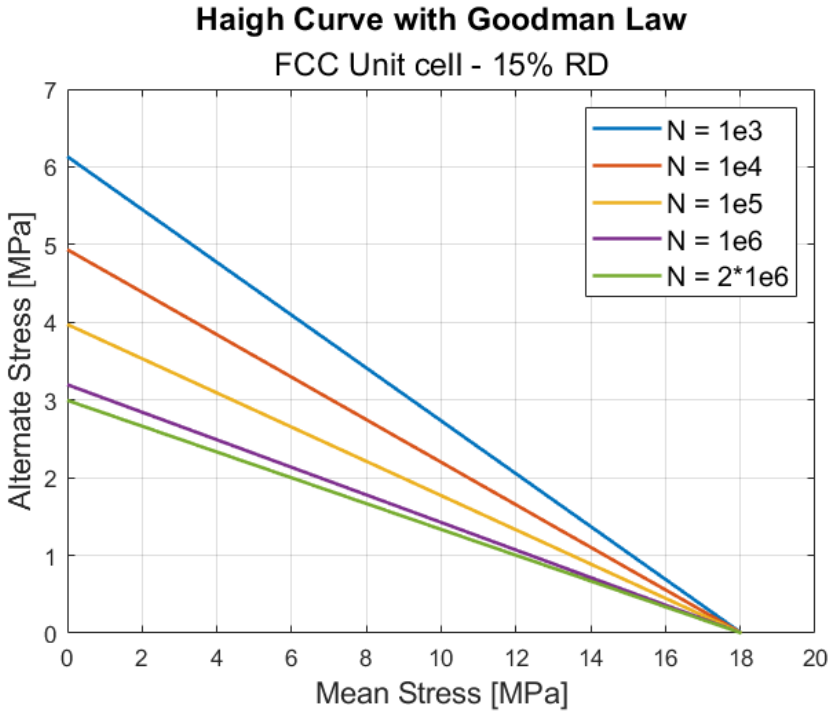

Figure 5.37: Haigh diagrams with the Goodman line representation: FCC unit cell - 15% rel. density.

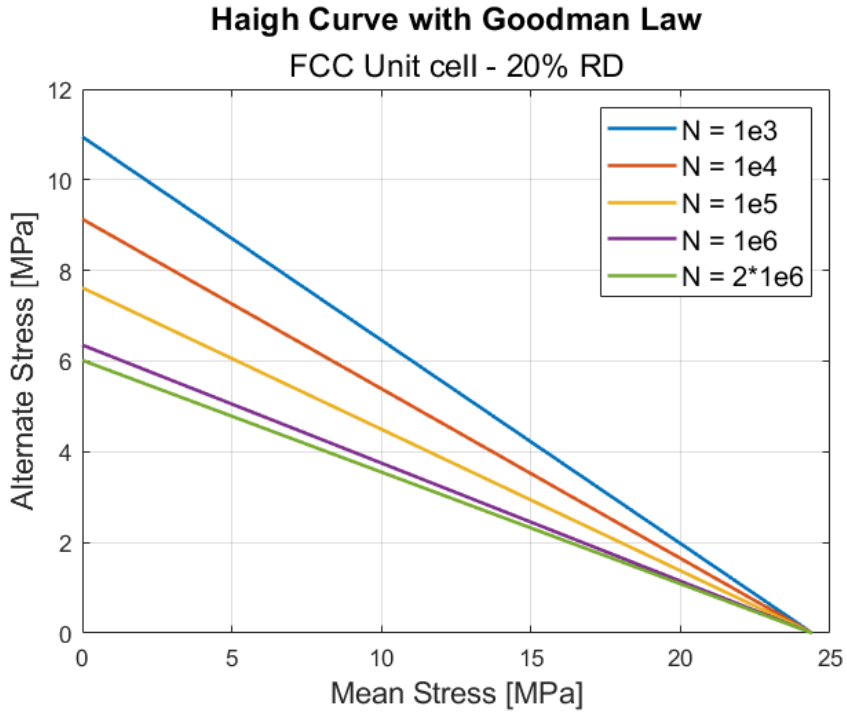

Figure 5.38: Haigh diagrams with the Goodman line representation: FCC unit cell - 20% rel. density.

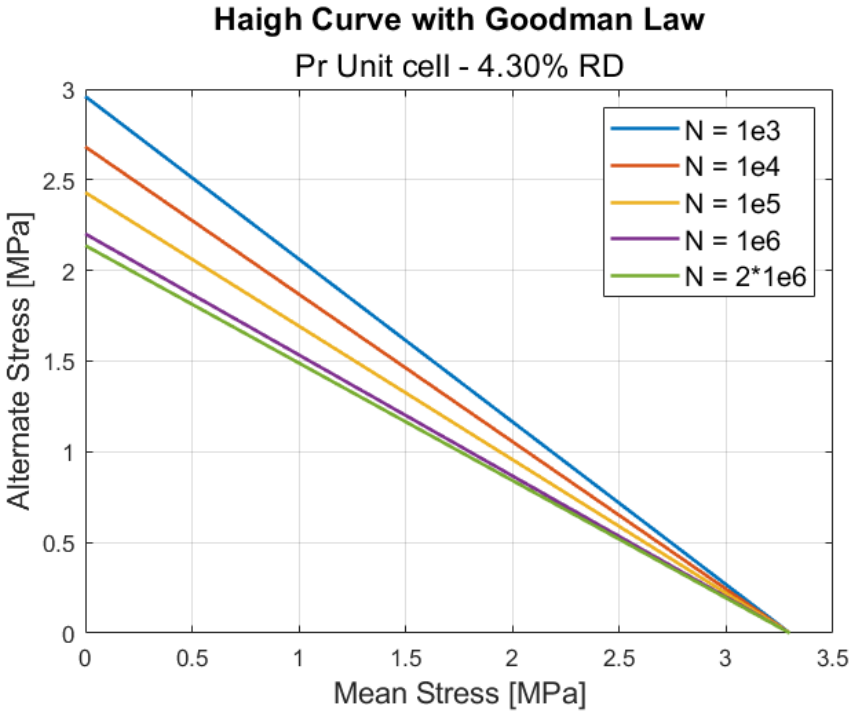

Figure 5.39: Haigh diagrams with the Goodman line representation: Primitive unit cell - 4.30% rel. density.

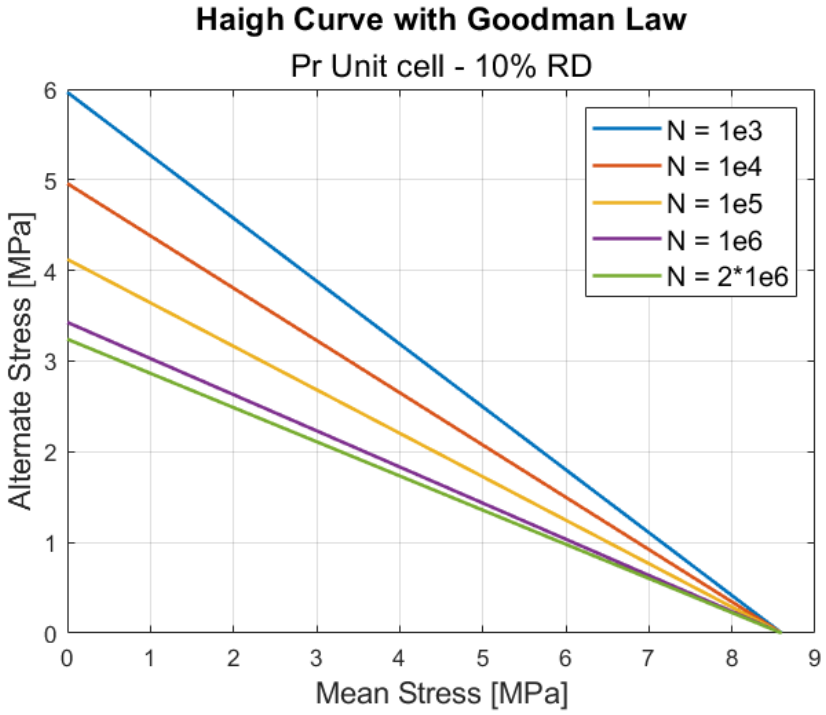

Figure 5.40: Haigh diagrams with the Goodman line representation: Primitive unit cell - 10% rel. density.

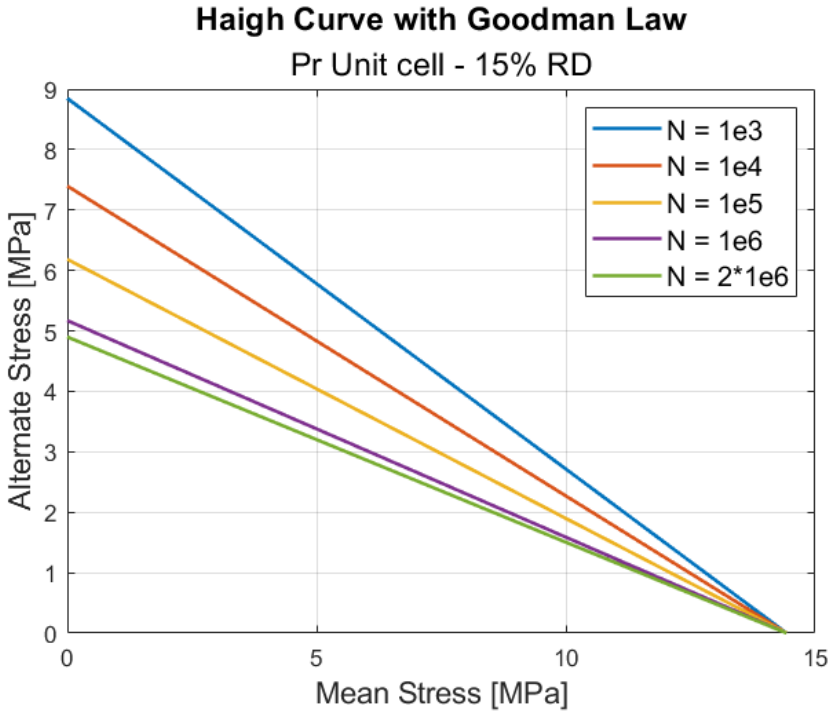

Figure 5.41: Haigh diagrams with the Goodman line representation: Primitive unit cell - 15% rel. density.

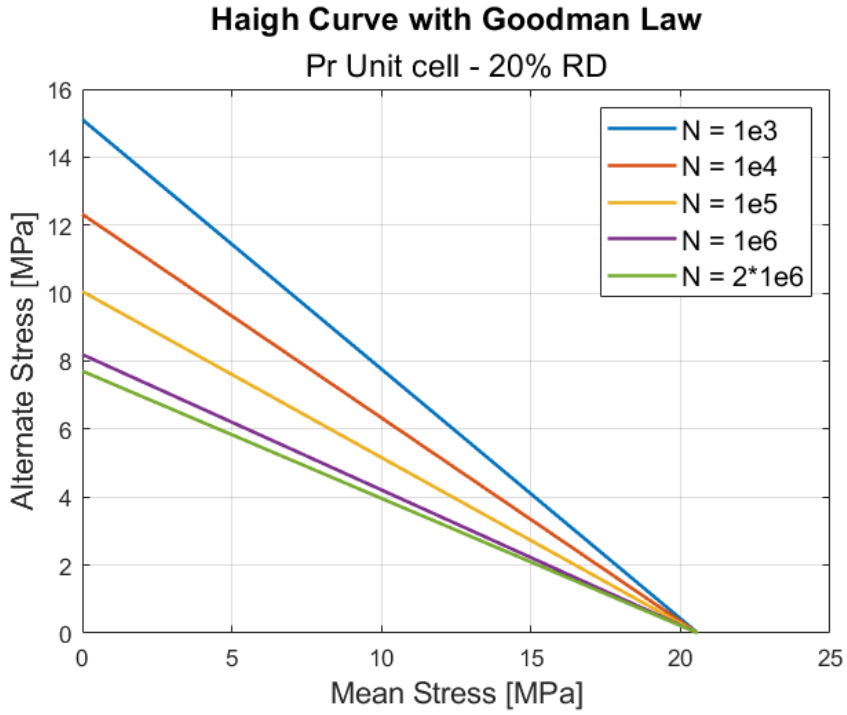

Figure 5.42: Haigh diagrams with the Goodman line representation: Primitive unit cell - 20% rel. density.

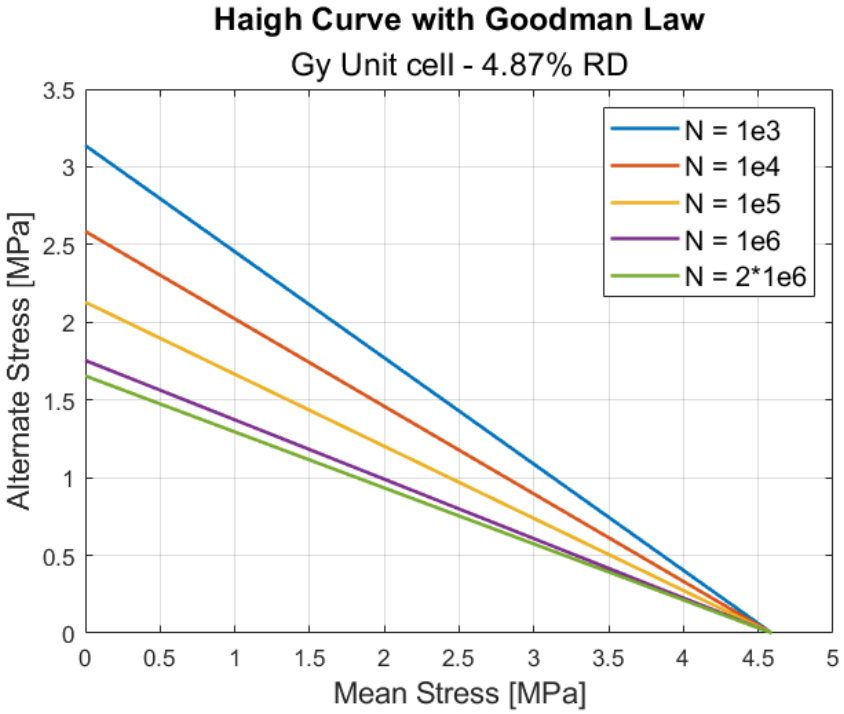

Figure 5.43: Haigh diagrams with the Goodman line representation: Gyroid unit cell - 4.87% rel. density.

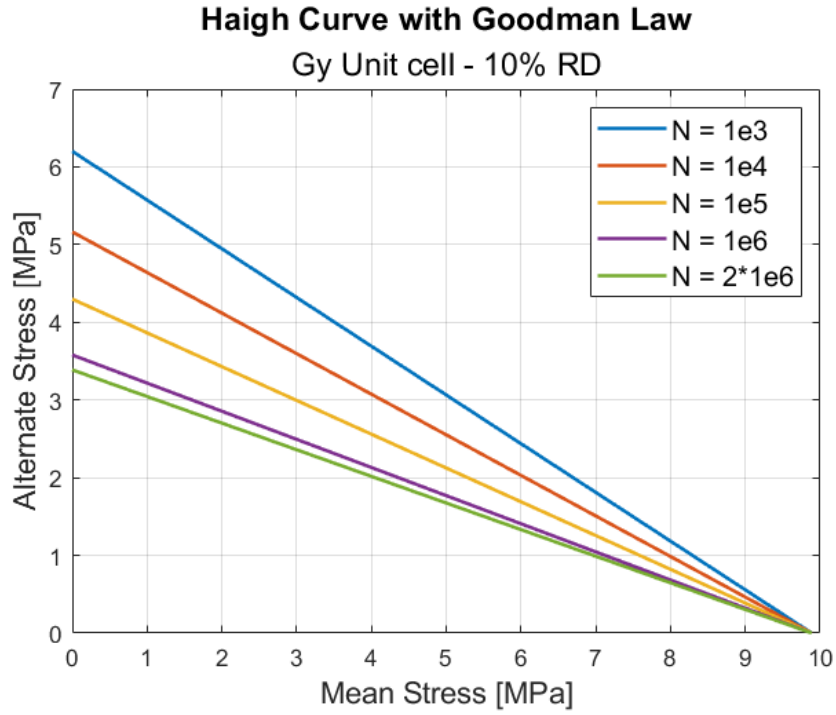

Figure 5.44: Haigh diagrams with the Goodman line representation: Gyroid unit cell - 10% rel. density.

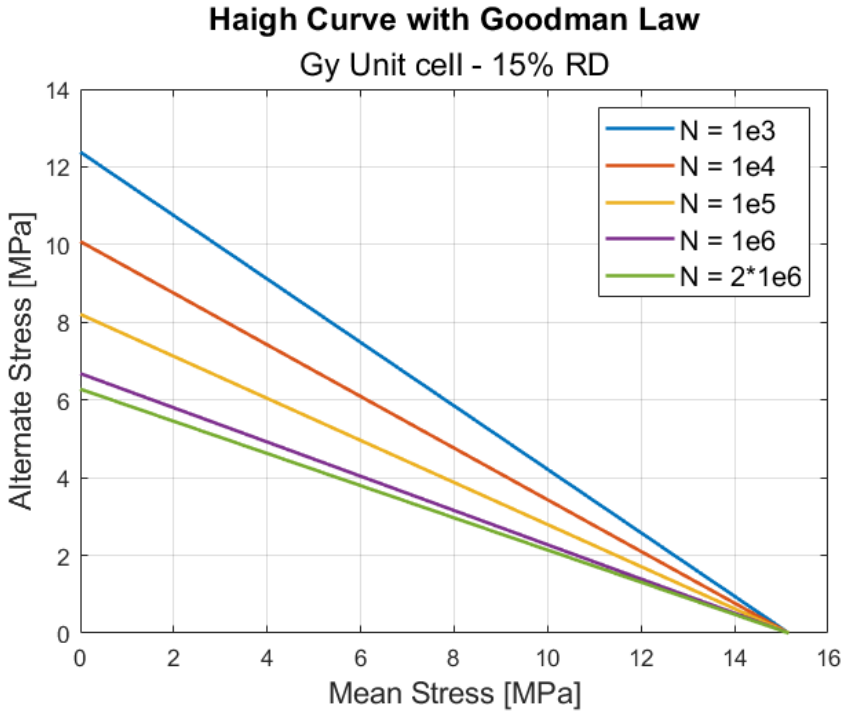

Figure 5.45: Haigh diagrams with the Goodman line representation: Gyroid unit cell - 15% rel. density.

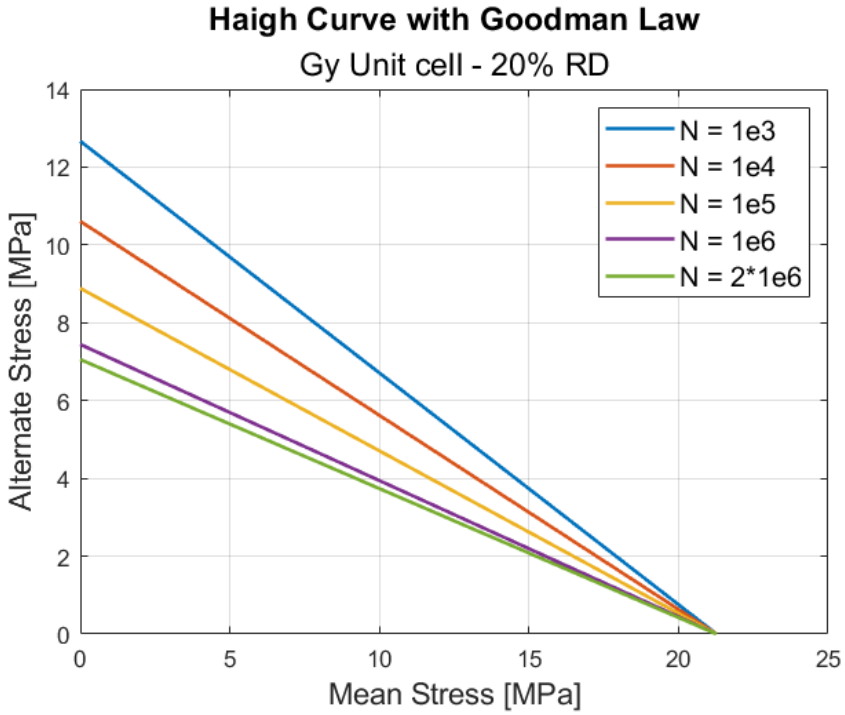

Figure 5.46: Haigh diagrams with the Goodman line representation: Gyroid unit cell - 20% rel. density.

Chapter 6

Conclusions and future works

6.1 Conclusions

This thesis has presented a numerical investigation of the tensile of AlSi10Mg lattice-based metamaterials with different unit cell topologies and relative densities, aimed on the estimation of fatigue performance under cyclic load conditions involving tension. Four representative architectures were considered: the plate-based BCC and FCC structures, and the sheet-TPMS Primitive and Gyroid cells. The relative densities ranged between approximately 4% and 20%: the lowest is the result of the minimum printable thickness and hence depends on the cell geometry, while the common ones are 10, 15 and 20%. The results confirm that the mechanical response of these metamaterials under tensile loading is governed both by density and by topology.

The quasi-static analyses show that stiffness, yield strength, and ultimate tensile strength increase with relative density for all the investigated architectures. However, the rate of increase and the linearity of these trends differ markedly among topologies. Plate-based lattices, exhibit higher mechanical performances, but their margin decreases with relative density, probably because of larger impact of cut-outs. BCC is characterised by higher stiffness, while FCC show higher yield and ultimate tensile strength. Both reach failure in an almost perfect brittle way. Meanwhile, TPMS show lower rigidity that BCC, but higher yield and ultimate tensile strength for 20% relative density, even though they cannot outperform FCC at any of the porosities analysed. Between Primitive and Gyroid, the latter has higher mechanical properties, but the former is more ductile; both are characterised by a high value of yield to ultimate tensile strength ratio, lower than that of plate-based lattices. Finally, the specific mechanical properties follow weak monotonic trends, generally positive, sometimes negative. This suggests that both absolute and density-normalised metrics must be considered in structural design.

The evaluation of fracture mechanisms indicates that crack initiation and propagation strongly depend on the interaction between geometry and relative density. Despite the recurrence of typical fracture patterns, inclined, perpendicular or mixed crack paths, their prevalence varies significantly among the examined unit cells. Plate-based architectures tend to fail with more abrupt, brittle-like surfaces, while TPMS structures show more distributed damage before catastrophic failure. These observations align with part of the existing literature, although discrepancies arise when comparing tensile-based results with compression-dominated studies, highlighting the role of the applied stress state in governing deformation modes.

The fatigue estimation further emphasises the interplay between load amplitude, mean stress and topology. The Wöhler curves obtained from the numerical evaluation of the stresses corresponding to 50% and 90% of the bulk UTS, together with the Haigh diagrams constructed via

the Basquin and Goodman relations, reveal that the fatigue limit increases with relative density, albeit with larger scatter compared to quasi-static properties. TPMS architectures consistently achieve superior fatigue behaviour, with fatigue limits around 40% of the global ultimate tensile strength. Plate-based lattices, particularly FCC, show significantly lower endurance, often close to the 20% threshold commonly reported for conventional strut-based lattices. These results agree with previous experimental findings for Ti6Al4V sheet-based TPMS structures manufactured by SLM, though differences between tensile and compressive fatigue conditions must be taken into account, while the low fatigue performance of plate-based lattices have been attributed to the degradation brought by cut-outs.

Overall, the results demonstrate that the optimal metamaterial configuration depends simultaneously on relative density and expected service loading. The numerical framework developed in this work provides an effective methodology for predicting the mechanical behaviour of complex architectures and serves as a solid foundation for guiding experimental testing. Furthermore, the analyses conducted herein contribute to improving the understanding of the performance–topology relationship in additively manufactured lattice materials, supporting future design strategies in engineering applications.

6.2 Future Work

The findings of this thesis motivate several promising directions for future research. The most immediate step is the experimental validation of the numerical predictions. Tensile tests on additively manufactured specimens would allow direct comparison between simulated and measured stress–strain curves, while fatigue testing under fully reversed or tension–tension loading conditions would confirm the estimated fatigue limits and the Haigh diagrams. High-resolution techniques, such as digital image correlation or *in situ* X-ray computed tomography, would enable detailed observation of strain localisation and crack evolution, providing a more comprehensive understanding of failure mechanisms. Additionally, this procedure would be particularly important, as it could eliminate the doubts that affect the results, which are caused by the hardware limitations previously cited.

A second development concerns the expansion of the design space. Although the present study covers a representative density range, many lattices used in many fields of engineering lie outside these limits. Future work should investigate slightly higher densities (up to 40%), where the differences among the mechanical performance of TPMS and plate-based structures may change. This would require a new way of approaching transition zones and cut-outs because of the highlighted density limits for the designed BCC and FCC cells. Moreover, the effects of manufacturing-induced defects, surface roughness and internal porosity should be incorporated into the analyses, through the implementation of specific models, due to their well known influence on the fatigue behaviour of additively manufactured components

From a modelling standpoint, the adoption of more advanced constitutive laws, to improve the plastic and damage models with in-house obtained data, could significantly enhance predictive accuracy. Extending the simulations to multiaxial or non-proportional loading paths would also provide a more realistic representation of service conditions, in which combined torsion, bending and tension are often present.

Finally, future investigations should consider graded or hybrid structures, where different topologies or density distributions coexist within the same component. These configurations offer the potential for locally tailored stiffness, controlled failure behaviour, or enhanced fatigue performance. The methodologies developed in this thesis provide a solid starting point for analysing and optimising such advanced architected materials.

Acknowledgements

Above all, my deepest gratitude goes to my family, who have supported my life and education from the very beginning, and whose presence and love I feel every single day, far more than I feel for my own life. My parents, sister, grandparents, aunts, uncles and cousins have been an indispensable help and a constant element in my life. Without them, I would not have reached the goals I am now achieving. I hope my sharp character has not caused them irreparable wounds and I hope one day to return at least a great part of the love I have received.

I will always cherish my friends, both old and new, in Italy and abroad, for their presence in my life over these years: collaborating on university projects, supporting and advising me in difficult decisions, offering me job opportunities, sharing adventures, welcoming me as if no time had passed since our last meeting, cooking and living together, travelling, and countless other moments that words cannot fully capture.

Looking back over the past three years, I realize how much I have been able to enrich my life with invaluable experiences. I deeply appreciate everyone who has been part of this journey and contributed to it in various ways.

I owe a special thanks to Polito Sailing Team, who welcomed me warmly, introduced me to the field of structural design and allowed me to gain significant practical experience. They reminded me that hard work pays off, that lectures are just a small part of academic duties and that passion is an endless source of energy.

I am also grateful to everyone who, directly or indirectly, consciously or unconsciously, influenced my decision to go abroad for Erasmus and later for my thesis. Thanks to these experiences, I now have a deeper understanding of the World and its complexity is deeply carved into my thoughts.

I would like to express my appreciation to the people of Germany, particularly those in Sachsen and Hessen, for the high quality of life I was able to experience in their Länder. I am also indebted to TU Dresden and its professors for their patience with my imperfect German and for allowing me to take exams in English, a rare flexibility that I deeply value.

Finally, but by no means least, I sincerely thank my thesis supervisors, Prof. De Pasquale and M.Sc. Milenkovski, as well as Prof. Mittelstedt, for giving me the opportunity to prepare my thesis on a topic I was genuinely interested in, at a university I was glad to visit.

References

[1] Lorna J. Gibson and Micheal F.Ashby. *Cellular solids:Structures and properties - Second Edition*. Cambridge University Press, 1997.

[2] MIT - Massachusetts Institute of Technology - Department of Materials Science and Engineering. *Lorna J. Gibson*. Accessed 29 October 2025. URL: https://dmse.mit.edu/people/faculty/lorna-j-gibson/.

[3] Clare Hall. *Professor Micheal Ashby*. Accessed 29 October 2025. URL: https://www.clarehall.cam.ac.uk/directory/ashby/.

[4] Antonio Coluccia. "Modeling and simulation of lightweight lattice structures for impact energy absorption". MA thesis. Politecnico di Torino, 2021.

[5] Fangxi Ren et al. "Transition boundaries and stiffness optimal design for multi-TPMS lattices". In: *Materials & Design Vol. 210, Art. 110062* (2021). DOI: https://doi.org/10.1016/j.matdes.2021.110062.

[6] Ming Li et al. "Design optimization of interconnected porous structures using extended triply periodic minimal surfaces". In: *Journal of Computational Physics Vol. 425, Art. 109909* (2021). DOI: https://doi.org/10.1016/j.jcp.2020.109909.

[7] Magali E García-Gutiérrez et al. "Numerical investigation of the effective mechanical properties of architected structures: a comparative study of flexural stiffness, omogenization, and elastic anisotropy". In: *Materials Research Express Vol.11, no.11, Art. 115801* (2024). DOI: https://doi.org/10.1088/2053-1591/ad8b99.

[8] Babak Ziaie, Xavier Velay, and Waqas Saleem. "Exploring the optimal mechanical properties of triply periodic minimal surface structures for biomedical applications: A Numerical analysis". In: *journal of the mechanical behavior of biomedical materials Vol. 160, Art. 106757* (2024). DOI: https://doi.org/10.1016/j.jmbbm.2024.106757.

[9] Albert Forés-Garriga, Giovanni Gómez-Gras, and Marco A. Pérez. "Additively manufactured three-dimensional lightweight cellular solids: Experimental and numerical analysis". In: *Materials & Design Vol. 226, Art. 111641* (2023). DOI: https://doi.org/10.1016/j.matdes.2023.111641.

[10] Itkankhya Mahapatra et al. "Evaluation of tensile properties of 3D-printed lattice composites: Experimental and machine learning-based predictive modelling". In: *Composites: Part A Vol. 193, Art. 108823* (2025). DOI: https://doi.org/10.1016/j.compositesa.2025.108823.

[11] Ali N. Alagha1 et al. "Mechanical Behavior and Energy Absorption of TPMS Diamond Structures and Hybrid SC-FCC-BCC Plate-Lattices". In: *Journal of Engineering Mechanics Vol. 150, no. 12, Art. 04024088* (2024). DOI: https://doi.org/10.1061/JENMDT.EMENG-7537.

[12] Jun Wei Chua, Wei Zhai, and Xinwei Li. “Elucidating Structure-Property relationships for optimization of plate lattice sound absorbers”. In: *Materials & Design Vol. 253, Art. 113801* (2025). DOI: https://doi.org/10.1016/j.matdes.2025.113801.

[13] Colin Bonatti and Dirk Mohr. “Smooth-shell metamaterials of cubic symmetry: Anisotropic elasticity, yield strength and specific energy absorption”. In: *Acta Materialia Vol. 164, p. 301-321* (2019). DOI: https://doi.org/10.1016/j.actamat.2018.10.034.

[14] Hao Xin et al. “Fatigue failure mechanisms and life prediction of additive manufactured metallic lattices: a comprehensive review”. In: *Virtual and Physical Prototyping Vol. 20, no.1, Art. e2451124,* (2025). DOI: DOI:10.1080/17452759.2025.2451124.

[15] Numan Khan and Aniello Riccio. “A systematic review of design for additive manufacturing of aerospace lattice structures: Current trends and future directions”. In: *Progress in Aerospace Science Vol. 149, Art. 101021* (2024). DOI: https://doi.org/10.1016/j.paerosci.2024.101021.

[16] Chengxing Yang, Kai Xu, and Suchao Xie. “Comparative Study on the Uniaxial Behaviour of Topology-Optimised and Crystal-Inspired Lattice Materials”. In: *Metals Vol. 10, no. 4, p. 491* (2020). DOI: https://doi.org/10.3390/met10040491.

[17] Bingteng Sun et al. “Energy absorption optimization of parametric plate lattices”. In: *Computers and Structures Vol. 316, Art. 107880* (2025). DOI: https://doi.org/10.1016/j.compstruc.2025.107880.

[18] Marie Pirotais et al. “Ti6Al4V lattices obtained by SLM: characterisation of the heterogeneous high cycle fatigue behaviour of thin walls”. In: *Procedia Structural Integrity Vol. 38, p. 132-140* (2022). DOI: https://doi.org/10.1016/j.prostr.2022.03.014.

[19] Mohamed Abdelmageed et al. “Systematic numerical design of a supported FCC plate lattice with structural reinforcement and gradation for energy absorption”. In: *Composite Structures Vol. 373, Art. 119677* (2025). DOI: https://doi.org/10.1016/j.compstruct.2025.119677.

[20] Fabio Distefano, Salvatore Pasta, and Gabriella Epasto. “Titanium Lattice Structures Produced via Additive Manufacturing for a Bone Scaffold: A Review”. In: *Journal of Functional Biomaterials Vol. 14, no. 3, Art. 125* (2023). DOI: https://doi.org/10.3390/jfb14030125.

[21] N. Shivakumar, T. Ramesh, and S. Muthukumaran. “A short review of molecularly inspired strut-based metal lattice structures”. In: *Materials Today: Proceedings* (2024). DOI: https://doi.org/10.1016/j.matpr.2024.05.080.

[22] Xinwei Li et al. “Microlattice Metamaterials with Simultaneous Superior Acoustic and Mechanical Energy Absorption”. In: *Small Vol. 17, Art. 2100336* (2021). DOI: https://doi.org/10.1002/smll.202100336.

[23] Colin Bonatti and Dirk Mohr. “Mechanical performance of additively-manufactured anisotropic and isotropic smooth shell-lattice materials: Simulations & experiments”. In: *Journal of the Mechanics and Physics of Solids Vol. 122, p.1-26* (2019). DOI: https://doi.org/10.1016/j.jmps.2018.08.022.

[24] Ming Lei et al. “Novel conformal sandwich lattice structures: Design concept, fabrication and mechanical properties”. In: *Thin–Walled Structures Vol. 199, Art. 111806* (2024). DOI: https://doi.org/10.1016/j.tws.2024.111806.

[25] Sermet Demir, Abdurrahim Temiz, and Fatih Pehlivan. “The investigation of printing parameters effect on tensile characteristics for triply periodic minimal surface designs by Taguchi”. In: *Polymer Engineering & Science Vol. 64, p. 1209-1221* (2023). DOI: https://doi.org/10.1002/pen.26608.

[26] Cambre N. Kelly et al. “Fatigue behavior of As-built selective laser melted titanium scaffolds with sheet-based gyroid microarchitecture for bone tissue engineering”. In: *Acta Biomaterialia Vol. 94, p.610-626* (2019). DOI: https://doi.org/10.1016/j.actbio.2019.05.046.

[27] Fatih Pehlivan. “Enhancing tensile properties of polymer-based triply periodic minimal surface metamaterial structures: Investigating the impact of post-curing time and layer thickness via response surface methodology”. In: *Polymer Engineering and Science Vol. 64, p. 5915–5928* (2024). DOI: DOI:10.1002/pen.26958.

[28] Jijun Jiang et al. “Investigation of torsional and fatigue resistance properties based on triply periodic minimal surfaces (TPMS)”. In: *Journal of Physics: Conference Series Vol. 2879 , Art. 012043* (2024). DOI: https://doi.org/10.1088/1742-6596/2879/1/012043.

[29] F.S.L. Bobbert et al. “Additively manufactured metallic porous biomaterials based on minimal surfaces: A unique combination of topological, mechanical, and mass transport properties”. In: *Acta Biomaterialia Vol. 52, p. 572-584* (2017). DOI: https://doi.org/10.1016/j.actbio.2017.02.024.

[30] Paul J.F. Gandy and Jacek Klinowski. “Exact computation of the triply periodic G ‘Gyroid’ minimal surface”. In: *Chemical Physics Letters Vol. 321, p. 363–371* (2000). DOI: https://doi.org/10.1016/S0009-2614(00)00373-0.

[31] Oraib Al-Ketan and Rashid K. Abu Al-Rub. “MSLattice: A free software for generating uniform and graded lattices based on triply periodic minimal surfaces”. In: *Material Design & Processing communications Vol. 3, no. 6, Art. e205* (2020). DOI: DOI:10.1002/mdp2.205.

[32] Nicolas Soro et al. “Quasi-static and fatigue properties of graded Ti–6Al–4V lattices produced by Laser Powder Bed Fusion (LPBF)”. In: *Additive Manufacturing Vol. 37, Art. 101653* (2021). DOI: https://doi.org/10.1016/j.addma.2020.101653.

[33] Mirhan Ozdemir et al. “Experimental and Numerical Modal Characterization for Additively Manufactured Triply Periodic Minimal Surface Lattice Structures: Comparison between Free-Size and Homogenization-Based Optimization Methods”. In: *Advanced Engineering Materials Vol. 25, Art. 2201811* (2023). DOI: https://doi.org/10.1002/adem.202201811.

[34] Qi Zheng et al. “Lightweight design of lattice structure of boron steel prepared by selective laser melting”. In: *Journal of Materials Research and Technology Vol. 30, p.7523–7532* (2024). DOI: https://doi.org/10.1016/j.jmrt.2024.05.160.

[35] Hugo Soul, Patrick Terriault, and Vladimir Brailovski. “The Static and Fatigue Behavior of AlSiMg Alloy Plain, Notched, and Diamond Lattice Specimens Fabricated by Laser Powder Bed Fusion”. In: *Journal of Manufacturing and Material Processing Vol. 2, Art. 25* (2018). DOI: https://doi.org/10.3390/jmmp2020025.

[36] Siqi Wang et al. “Bird strike resistance analysis for engine fan blade filled with triply periodic minimal surface”. In: *Aerospace Science and Technology Vol. 161, Art. 110109* (2025). DOI: https://doi.org/10.1016/j.ast.2025.110109.

[37] Sonu Singh et al. “Evaluation of Fatigue Life of Additively Manufactured Ti6Al4V Neovius Lattices in Simulated Body Fluid for Biomedical Applications”. In: *Advanced Engineering Materials Vol. 27, Art. 2402368* (2025). DOI: https://doi.org/10.1002/adem.202402368.

[38] Agyapal Singh, Abdulrahman Jaber, and Nikolaos Karathanasopoulos. “Fatigue performance of TPMS-based AlSi10Mg architected cellular materials fabricated via hybrid and powder bed fusion methods”. In: *International Journal of Fatigue Vol. 193, Art. 108758* (2025). DOI: https://doi.org/10.1016/j.ijfatigue.2024.108758.

[39] Garvin Schultheiß, Burkhard Heine, and Markus Merkel. “Characterization of flexural fatigue behaviour of additively manufactured (PBF–LB) gyroid structures”. In: *Progress in Additive Manufacturing Vol. 9, p. 1331–1340* (2024). DOI: https://doi.org/10.1007/s40964-024-00607-y.

[40] Stefania Liseni et al. “Numerical method for energy absorption maximization in lattice structures and experimental validation”. In: *17th European Conference on Spacecraft Structures Materials and Environmental Testing (ECSSMET)*. Toulouse, France, Mar. 2023, pp. 1183–1189.

[41] Zhaogui Wang et al. “Isothermal annealing effects on compression performances of polyether-ether-ketone lattice structures prepared via material extrusion additive manufacturing”. In: *Materials Today Communications Vol. 47, Art. 112993* (2025). DOI: https://doi.org/10.1016/j.mtcomm.2025.112993.

[42] Ahsen Sultan Kilic, Hakan Hafizoglu, and Nazim Babacan. “Investigation of ballistic performance of selective laser-melted AlSi10Mg alloy lattice structures by experimental and numerical studies”. In: *Materials Today Communications Vol. 44, Art. 112032* (2025). DOI: https://doi.org/10.1016/j.mtcomm.2025.112032.

[43] Antonio Coluccia et al. “Nonlinear static and dynamic modeling of energy absorption lattice structures behavior”. In: *Mechanics of Advanced Materials and Structures Vol.30, no. 14, p. 2838-2849* (2023). DOI: 10.1080/15376494.2022.2064016.

[44] Avez Shaikha et al. “Towards Gradient Design of TPMS lattices and Laser Powder Bed Fusion Processing – Role of Laser Strategies and Lattice Thickness”. In: *Manufacturing Letters Vol. 41, p. 1046–1054* (2024). DOI: DOI:10.1016/j.mfglet.2024.09.129.

[45] Zahabul Islam et al. “Tensile and compressive response of tungsten g-TPMS lattice structures”. In: *Materials Today Communications Vol. 40, Art. 109606* (2024). DOI: https://doi.org/10.1016/j.mtcomm.2024.109606.

[46] Hossein Doostmohammadi et al. “Experimental and Numerical Analysis of Novel Polycontinuous Triply Periodic Minimal Surface Architectures”. In: *Advanced Engineering Materials Vol. 27, no.9, Art. 2402679* (2025). DOI: https://doi.org/10.1002/adem.202402679.

[47] Marco Pelegatti et al. “Low cycle fatigue behaviour of cellular materials: Experimental comparative study of strut-based and gyroid structures made of additively manufactured 316L steel”. In: *International Journal of Fatigue Vol. 178, Art. 108024* (2024). DOI: https://doi.org/10.1016/j.ijfatigue.2023.108024.

[48] Karel Lietaert et al. “Fatigue life of additively manufactured Ti6Al4V scaffolds under tension-tension, tension-compression and compression-compression fatigue load”. In: *Scientific Reports Vol. 8, no.1, Art. 4957* (2018). DOI: https://doi.org/10.1038/s41598-018-23414-2.

[49] Sihao Han, Chunlei Li, and Yangfan He. "Hierarchically topological design and mechanical performances of TPMS-based biomimetic cellular structures". In: *Materials Today Communications Vol. 44, Art. 111836* (2025). DOI: https://doi.org/10.1016/j.mtcomm.2025.111836.

[50] Antonio Coluccia and Giorgio De Pasquale. "Strain-based method for fatigue failure analysis of truss lattice structures: modeling and experimental setup". In: *17th European Conference on Spacecraft Structures Materials and Environmental Testing (ECSSMET).* Toulouse, France, Mar. 2023, pp. 1190–1194.

[51] Antonio Coluccia and Giorgio De Pasquale. "A multiscale-based methodology for the fatigue failure analysis of additively manufactured lattice structures applied to the four-point-bending test". In: *International Journal of Fatigue Vol. 200, Art. 109122* (2025). DOI: https://doi.org/10.1016/j.ijfatigue.2025.109122.

[52] Anna Falkowska and Andrzej Seweryn. "Fatigue of titanium alloy Ti6Al4V with diamond structure obtained by Laser Power Bed Fusion method". In: *International Journal of Fatigue Vol. 163, Art. 107079* (2022). DOI: https://doi.org/10.1016/j.ijfatigue.2022.107079.

[53] Ali Mulhi et al. "Dimensional assessment of uniformly periodic porosity primitive TPMS lattices using additive manufacturing laser powder bed fusion technique". In: *The International Journal of Advanced Manufacturing Technology Vol. 124, p. 2127–2148* (2023). DOI: https://doi.org/10.1007/s00170-022-10578-5.

[54] Jian Liu et al. "Optimization of Triply Periodic Minimal Surface Heat Exchanger to Achieve Compactness, High Efficiency, and Low-Pressure Drop". In: *Energies Vol. 17, Art. 5141* (2024). DOI: https://doi.org/10.3390/en17205141.

[55] Ashish Kumar Mishra, Hrushikesh Chavan, and Arvind Kumar. "Effect of cell size and wall thickness on the compression performance of triply periodic minimal surface based AlSi10Mg lattice structures". In: *Thin–Walled Structures Vol. 193, Art. 111214* (2023). DOI: https://doi.org/10.1016/j.tws.2023.111214.

[56] Antonio Coluccia and Giorgio De Pasquale. "Strain-based method for fatigue failure prediction of additively manufactured lattice structures". In: *Nature Scientific Reports Vol. 13, Art. 22775* (2023). DOI: DOI:10.1038/s41598-023-49846-z.

[57] Zhitong Li et al. "Mechanical properties of triply periodic minimal surface (TPMS) scaffolds: considering the influence of spatial angle and surface curvature". In: *Biomechanics and Modeling in Mechanobiology Vol. 22, p. 541–560* (2023). DOI: https://doi.org/10.1007/s10237-022-01661-7.

[58] Ahmad Baroutaji et al. "The Influence of Atmospheric Oxygen Content on the Mechanical Properties of Selectively Laser Melted AlSi10Mg TPMS-Based Lattice". In: *Materials Vol. 16, Art. 430* (2023). DOI: https://doi.org/10.3390/ma16010430.

[59] T.H.G. Megson. *Aircraft Structures for Engineering Students - Sixth Edition.* Butterworth-Heinemann, 2020.

[60] Aurelio Burdese. *Manuale di metallurgia.* Unione tipografico-editrice torinese, 1969.

[61] Johannes Schneider and S. Kumar. "Comparative performance evaluation of microarchitected lattices processed via SLS, MJ, and DLP 3D printing methods: Experimental investigation and modelling". In: *Journal of Materials Research and Technology Vol. 26, p.7182-7198* (2023). DOI: https://doi.org/10.1016/j.jmrt.2023.09.061.

[62] Na Qiu et al. “Experimental and numerical studies on mechanical properties of TPMS structures”. In: *International Journal of Mechanical Sciences Vol. 261, Art. 108657* (2024). DOI: https://doi.org/10.1016/j.ijmecsci.2023.108657.

[63] Dalia Mahmoud, Kassim S. Al-Rubaie, and Mohamed A. Elbestawi. “The influence of selective laser melting defects on the fatigue properties of Ti6Al4V porosity graded gyroids for bone implants”. In: *International Journal of Mechanical Sciences Vol. 193, Art. 106180* (2021). DOI: https://doi.org/10.1016/j.ijmecsci.2020.106180.

[64] Dayue Jiang and Fuda Ning. “Physical-mechanical behaviors of stainless steel plate-lattice built by material extrusion additive manufacturing”. In: *Journal of Materials Processing Tech. Vol. 309, Art. 117739* (2022). DOI: https://doi.org/10.1016/j.jmatprotec.2022.117739.

[65] Yuan Zhang et al. “A systematic study on the energy absorption performance of plate-lattices: performance, design, and optimization”. In: *Acta Mechanica Sinica/Lixue Xuebao Vol. 42, no. 7, Art. 424493* (2026). DOI: https://doi.org/10.1007/s10409-025-24493-x.

[66] nTopology Inc. *Website*. Accessed 30 October 2025. URL: https://www.ntop.com/.

[67] Mansoureh Rezapourian et al. “Selective laser melted Ti6Al4V split-P TPMS lattices for bone tissue engineering”. In: *International Journal of Mechanical Sciences Vol. 251, Art. 108353* (2023). DOI: https://doi.org/10.1016/j.ijmecsci.2023.108353.

[68] Giorgio De Pasquale and Daniela Barra. *nTop5 User Guide: Comprehensive Reference Manual for Beginners and Intermediate Users with Step-by-Step Design-Based Approach.* 2025.

[69] Jing Zhang et al. “Study on isotropic design of triply periodic minimal surface structures under an elastic modulus compensation mechanism”. In: *Composite Structures Vol. 342, Art.118266* (2024). DOI: https://doi.org/10.1016/j.compstruct.2024.118266.

[70] Dr. Oraib Al-Ketan. *Dr. Oraib Al-Ketan - Biography*. Accessed 30 October 2025. URL: https://www.oraibkhitan.com/.

[71] Nicolas Martin et al. “Reactor physics characterization of triply periodic minimal surface-based nuclear fuel lattices”. In: *Progress in Nuclear Energy Vol. 165, Art. 104895* (2023). DOI: https://doi.org/10.1016/j.pnucene.2023.104895.

[72] Mauricio Ivan Tenorio-Suárez et al. “MaSMaker: An open-source, portable software to create and integrate maze-like surfaces into arbitrary geometries”. In: *SoftwareX Vol. 19, Art. 101203* (2022). DOI: https://doi.org/10.1016/j.softx.2022.101203.

[73] James Pérez-Barrera et al. “Version [2.0]- [MaSMaker: An open-source, portable software to create and integrate maze-like surfaces into arbitrary geometries”. In: *SoftwareX Vol. 26, Art. 101683* (2024). DOI: https://doi.org/10.1016/j.softx.2024.101683.

[74] A. Sabik et al. “Evaluation of PLA gyroid scaffold for long bone fracture treatment: numerical and experimental study”. In: *Journal of the Mechanical Behavior of Biomedical Materials Vol. 170, Art. 101710* (2025). DOI: https://doi.org/10.1016/j.jmbbm.2025.107110.

[75] Ornelas-Ramón Luis Guillermo et al. “Computational analysis and engineering modeling for the heat transfer and fluid flow through the gyroid TPMS structure”. In: *Applied Thermal Engineering Vol. 268, Art. 125865* (2025). DOI: https://doi.org/10.1016/j.applthermaleng.2025.125865.

[76] Wang Guo et al. “3D printed TPMS structural PLA/GO scaffold: Process parameter optimization, porous structure, mechanical and biological properties”. In: *Journal of the Mechanical Behavior of Biomedical Materials, Vol.142, Art. 105848* (2023). DOI: https://doi.org/10.1016/j.jmbbm.2023.105848.

[77] Lingbo Li et al. “Mechanisms of low-frequency bandgap formation and energy absorption of three-dimensional nested hybrid lattice structures”. In: *Composite Part B Vol. 291, Art. 112045* (2025). DOI: https://doi.org/10.1016/j.compositesb.2024.112045.

[78] Yacob Medhin1 et al. “Effect of material ductility on the post buckling plateau and specific energy absorption of additively manufactured hybrid plate lattice structures”. In: *Progress in Additive Manufacturing* (2025). DOI: https://doi.org/10.1007/s40964-025-01345-5.

[79] Mahan Ghosh et al. “Scalability in SLA lattice through lattice orientation and hybrid frame and plate architectures”. In: *Journal of Materials Research and Technology Vol. 35, p. 645-659* (2025). DOI: https://doi.org/10.1016/j.jmrt.2024.12.155.

[80] Rui Xue et al. “Mechanical design and energy absorption performances of novel dual scale hybrid plate-lattice mechanical metamaterials”. In: *Extreme Mechanics Letters Vol. 40, Art. 100918* (2020). DOI: https://doi.org/10.1016/j.eml.2020.100918.

[81] Julian N. Heidenreich et al. “Design of isotropic porous plates for use in hierarchical plate-lattices”. In: *Materials & Design Vol. 212, Art. 110218* (2021). DOI: https://doi.org/10.1016/j.matdes.2021.110218.

[82] Michał Doroszko and Andrzej Seweryn. “Cyclic behaviour modelling of additively manufactured Ti-6Al-4V lattice structures”. In: *International Journal of Mechanical Sciences Vol. 273, Art. 109219* (2024). DOI: https://doi.org/10.1016/j.ijmecsci.2024.109219.

[83] BSI. “BS EN 3987:2009. Aerospace series - Test methods for metallic materials - Constant amplitude force-controlled high cycle fatigue testing”. In: *British Standards Institution* (2009).

[84] ASTM Committee E08. “E606/E606M-21: Standard Test Method for Strain-Controlled Fatigue Testing”. In: *ASTM International* (2021). DOI: https://doi.org/10.1520/E0606_E0606M-21.

[85] ASTM Committee E08. “E466-21: Standard Practice for Conducting Force Controlled Constant Amplitude Axial Fatigue Tests of Metallic Materials”. In: *ASTM International* (2021). DOI: https://doi.org/10.1520/E0466-21.

[86] ISO Technical Committee 164. “BS ISO 1099:2017. Metallic materials - Fatigue testing - Axial force-controlled method”. In: *British Standards Institution* (2017). DOI: https://doi.org/10.1520/E0466-21.

[87] Dr. S. Roy Swanson, ed. *Handbook of Fatigue Testing*. American Society for Testing and Materials, 1974.

[88] Miguel Araya et al. “Assessing the compressive and tensile properties of TPMS-Gyroid and stochastic Ti64 lattice structures: A study on laser powder bed fusion manufacturing for biomedical implants”. In: *Journal of Science: Advanced Materials and Devices Vol. 9, Art. 100663* (2024). DOI: https://doi.org/10.1016/j.jsamd.2023.100663.

[89] L. Boniotti et al. “Experimental and numerical investigation on fatigue damage in micro-lattice materials by Digital Volume Correlation and CT-based finite element models”. In: *Engineering Fracture Mechanics Vol. 266, Art. 108370* (2022). DOI: https://doi.org/10.1016/j.engfracmech.2022.108370.

[90] ASTM Committee D20. "D638-22: Standard Test Method for Tensile Properties of Plastics". In: *ASTM International* (2022). DOI: https://doi.org/10.1520/D0638-22.

[91] ASTM Committee D20. "D638-14: Standard Test Method for Tensile Properties of Plastics". In: *ASTM International* (2014). DOI: https://doi.org/10.1520/D0638-14.

[92] ASTM Committee D20. "D695-15: Standard Test Method for Compressive Properties of Rigid Plastics". In: *ASTM International* (2015). DOI: https://doi.org/10.1520/D0695-15.

[93] Math Industries Srl. *Integrale triplo per il volume dell'intersezione di due cilindri*. Accessed 10 November 2025. URL: https://www.youmath.it/forum/sezione-speciale-per-i-topic-a-pagamento/72360-integrale-triplo-per-il-volume-dellintersezione-di-due-cilindri.html.

[94] EOS GmbH. *EOS Aluminium AlSi10Mg. Material Data Sheet*. Accessed 13 November 2025. URL: https://www.eos.info/metal-solutions/metal-materials/data-sheets/mds-eos-aluminium-alsi10mg.

[95] Dassault Systèmes. *Abaqus Materials Guide - 2023*. URL: https://www.3ds.com/support/documentation/user-guides.

[96] Gianni Jiang. "Modeling and simulation of elasto-plastic lattice structures for energy absorption". MA thesis. Politecnico di Torino, 2021.

[97] Junyan He et al. "LatticeOPT: a heuristic topology optimization framework for thin-walled, 2D extruded lattices". In: *Structural and Multidisciplinary Optimization Vol. 65, Art. 308* (2022). DOI: https://doi.org/10.1007/s00158-022-03397-5.

[98] J. Noronha et al. "Ti-6Al-4V hollow-strut lattice materials by laser powder bed fusion". In: *Additive Manufacturing Vol. 72, Art. 103637* (2023). DOI: https://doi.org/10.1016/j.addma.2023.103637.

[99] Yan Chunze et al. *Triply Periodic Minimal Surface Lattices Additively Manufactured by Selective Laser Melting*. Academic Press, 2021.

[100] Zhiqiang Liu, He Gong, and Jiazi Gao. "Enhancement in the fatigue resistances of triply periodic surfaces-based scaffolds". In: *International Journal of Mechanical Sciences Vol.245, Art. 108119* (2023). DOI: https://doi.org/10.1016/j.ijmecsci.2023.108119.

[101] Dassault Systèmes. *Abaqus Constraints Guide - 2023*. URL: https://www.3ds.com/support/documentation/user-guides.

[102] Stefania Liseni. "Modeling and validation of lightweight lattice structures for high specific energy absorption". MA thesis. Politecnico di Torino, 2022.

[103] Dassault Systèmes. *Abaqus/CAE User's Guide - 2023*. URL: https://www.3ds.com/support/documentation/user-guides.

[104] ASTM Committee E28. "E8/E8M-25: Standard Test Methods for Tension Testing of Metallic Materials". In: *ASTM International* (2025). DOI: https://doi.org/DOI:10.1520/E0008_E0008M-25.

[105] Dassault Systèmes. *Abaqus Analysis Guide - 2023*. URL: https://www.3ds.com/support/documentation/user-guides.

[106] Genzhu Feng et al. "Mechanical properties and deformation behavior of functionally graded TPMS structures under static and dynamic loading". In: *International Journal of Impact Engineering Vol. 176, Art. 104554* (2023). DOI: https://doi.org/10.1016/j.ijimpeng.2023.104554.

[107] Inc. The MathWorks. *Smooth response data*. Accessed 25 November 2025. URL: https://it.mathworks.com/help/curvefit/smooth.html.

[108] Zhuo Xu et al. "Evaluating quasi-static and fatigue performance of IN718 gyroid lattice structures fabricated via LPBF: Exploring relative densities". In: *International Journal of Fatigue Vol. 178, Art. 108028* (2024). DOI: https://doi.org/10.1016/j.ijfatigue.2023.108028.

[109] Nejc Novak et al. "Quasi-static and dynamic compressive behaviour of sheet TPMS cellular structures". In: *Composite Structures Vol. 266, Art. 113801* (2021). DOI: https://doi.org/10.1016/j.compstruct.2021.113801.

[110] William D. Callister Jr. and David G. Rethwisch. *Scienza ed Ingegneria dei Materiali, IV edizione*. EdiSES, 2019.

[111] Giorgio De Pasquale. "Fatica: diagramma di Wöhler". Material projected during the lecture. Fondamenti di meccanica strutturale, Bachelor's degree course in Biomedical Engineering. Politecnico di Torino. 2023-2024.

[112] Lei Yang et al. "Compression–compression fatigue behaviour of gyroid-type triply periodic minimal surface porous structures fabricated by selective laser melting". In: *Acta Materialia Vol. 181, p. 49–66* (2019). DOI: https://doi.org/10.1016/j.actamat.2019.09.042.

[113] Brecht Van Hooreweder et al. "Improving the fatigue performance of porous metallic biomaterials produced by Selective Laser Melting". In: *Acta Biomaterialia Vol. 47, p. 193-202* (2017). DOI: https://doi.org/10.1016/j.actbio.2016.10.005.

[114] Giorgio De Pasquale. "Fatica: effetto della tensione media". Material projected during the lecture. Fondamenti di meccanica strutturale, Bachelor's degree course in Biomedical Engineering. Politecnico di Torino. 2023-2024.

Appendix A

MSLattice and MaSMaker, a very brief description.

A.1 MSLattice very short description

MSLattice is a MATLAB-based tool, projected by Dr. Oraib Al-Ketan, scientist at New York University Abu Dhabi [70]. The software can perform the main tasks for TPMS modelling: it already includes the equations for the most common architectures, such as Primitive, Gyroid, Diamond, Neovius, but also less famous such as Fischer-Koch S, F-RD and PMY. In addition, it has a dedicated section, denoted as *Implicit Function*, which, given an arbitrary level-set implicit function [31] in the shape $F(x, y, z) - C(x, y, z) = 0$, draws the corresponding sample. Sheet and solid networks are both possible, as well as cuboid, cylindrical and spherical samples. Gradation is only limited to the first two volume shapes, and can be referred to the relative density or to the cell size. The parameters whose input is given by the user are the start and end relative density (a single value when density gradation is not imposed), the initial and final cell size (a single value when cell dimension is kept constant), the sample length, width, height or radius, and finally the mesh density points. Upon clicking on plot, the lattice could be displayed and then exported as an .stl file for the purpose of numerical simulations or 3D printing [31]. Detailed description of the software is reported in a dedicated paper [31].

A.2 MaSMaker very short description

MaSMaker, differently from MSLattice, relies on Python programming language [71], but it is pretty similar to the latter from the user viewpoint. The first version of the software only included Gyroid architecture [72], while the new one, MaSMaker 2.0, has expanded the range to Schwarz P, Diamond, Split-P, Neovius, and Lidinoid. Once selected the desired shape (cell type and sample shape among cuboid, cylindrical and spherical, but shell networks only), the user can set the sample's length, width, height and/or radius, and the cell size. The relative density is substituted by the volume fraction, which, when considering uniform homogeneous materials, leads to a conceptual but not real difference. Gradation is possible only in the sense of volume fraction and for cuboid samples. There is also the possibility to generate hybrid lattice along the longitudinal direction, with two different TPMS architectures. Finally, integration of the TPMS-based lattice into an external geometry, which must be imported, is another feature available. The resolution is set in terms of voxel; Pérez-Barrera et al. [73] suggest guidelines for this choice. As it happens with MaSMaker, samples can be plotted and exported as .stl files. Its functions are explored by Pérez-Barrera et al. [73] (Mexico), in a dedicated paper.

Appendix B

BCC unit cell: Vertex cut radius calculation through MATLAB

The following *script* computes the radius of vertex cut-outs for BCC-plate-based lattices. The user must select the radius *Rsp*, in order to allow the implementation of the sphere-approach, and the thickness t of the structure he is modelling. He also has to choose an initial guess x_0, which is required by the MATLAB function *fsolve*. It is possible to use the rough result obtained from the graphic method to optimise the choice of this value.

```
clear
close all
clc

t = 1.0;
Rsp = 0.50;

%% Graphic method

Rv = linspace(1.5,3.0,1000);

R2a = sqrt(Rv.^2 + (0.5*t)^2);
Ep = 0.25*pi - atan(0.5) - atan(t./(2*Rv));
R2b = Rsp./sin(Ep);

figure(1)
plot(Rv,R2a)
grid on
hold on
plot(Rv,R2b)

%% Iterative method

x0 = 2;             % I can exploit the graphic method for getting the starting guess

fun = @(x) (x.^2)*(sin(0.25*pi - atan(0.5) - atan(0.5*t./x))).^2 + ...
    (0.25*t^2)*(sin(0.25*pi - atan(0.5) - atan(0.5*t./x))).^2 - Rsp^2;

[Rv] = fsolve(fun,x0);
```

Appendix C

Plate-based unit cell: Determination of geometrical parameters for transition zones.

The following *scripts* and *functions* are programmed to compute the geometrical parameters for the correct modelling of the transition regions of plate-based specimens. Specifically, in case of BCC architectures, both the required thickness and vertex cut-outs radius are provided, while for FCC configurations only the thickness is required. The user must select the radius *Rsp*, in order to allow the implementation of the sphere-approach, the initial *ID* and final *FD* relative density, the number of layers *NC*, the size cell *Sz*, the lattice type (BCC or FCC) and finally an initial value of thickness t_0 and an initial guess x_0 for the vertex cut out radius, which is required by the MATLAB function *fsolve*. All dimensions are in millimetres. The script recalls different functions, here reported as well. The code also implements error messages, to prevent the user from committing unwanted mistakes.

```
clear
close all
clc

% User's data

ID = 0;              % Initial density

FD = 20;             % Final density

NC = 1;              % Number of layers (how many different thickness you want)

t0 = 0.080;          % Initial thickness [mm]. It must be LOWER than the lowest one
                     % you are computing. However, the closer it is,
                     % the more efficient the function.

x0 = 2;              % Initial guess for Rv, it generally works with 2 with
                     % 10mm cell size

Rsp = 0.50;          % Sphere radius (for cut outs sphere-approach)

Sz = 10;             % Cell size

FCC = 0;             % Put 1 if you want to do the calculation for FCC (only thickness)
                     % !! It is not possible to compute both at the same
                     % time. One must be mandatorly 0 and the other 1.

BCC = 1;             % Put 1 if you want to do the calculation for BCC (thickness and vertex radius)

% Check of the correctness

if FD ≤ ID
    error('Final density must be higher than the initial one')
end

if BCC == FCC
    error('BCC and FCC must have different values. Only one type of calculation per time is ...
```

```
        allowed')
end

if BCC ≠ 0 && BCC ≠ 1
    error('BCC value must be 0 or 1')
end

if FCC ≠ 0 && FCC ≠ 1
    error('FCC value must be 0 or 1')
end

if FCC == 1 && (ID > 24.6294 || FD > 24.6294)
    warning('FCC has a maximum relative density around 24.6294%. ...
    If this limit is excedeed, the function is not going to converge')
end

% Mathematical function

if BCC == 1
    [t,Rv,err_ex,err_de] = BCC_tRv(ID,FD,NC,t0,Rsp,Sz,x0);
end

if FCC == 1
    t = FCC_tRv(ID,FD,NC,t0,Rsp,Sz);
    % t = FCC_tRv_high(ID,FD,NC,t0,Rsp,Sz);          % To be used for 15%
    % t = FCC_tRv_superhigh(ID,FD,NC,t0,Rsp,Sz);     % To be used for 20%

end
```

The function *BCC_tRv*, is the real worker that does the required calculations in case of BCC architecture. Its mechanism is described at Par.3.4. This function implements another one, called *calc_Rv*, which is reported as well.

```
function [t,Rv,err_ex,err_de] = BCC_tRv(ID,FD,NC,t0,Rsp,Sz,x0)

t_ex = zeros(NC,1);

Rv_ex = zeros(NC,1);
Rv_de = zeros(NC,1);

err_ex = zeros(NC,1);
err_de = zeros(NC,1);
step = (FD-ID)/NC;

k = 0;
t = t0;
L = Sz;

BCC_idensity = 0;
BCC_density = (ID+step:step:FD)';
BCC_density_ex = zeros(NC,1);
BCC_density_de = zeros(NC,1);


sqr2 = sqrt(2);
sqr3 = sqrt(3);
sqr6 = sqrt(6);

for i = 1:NC

    while BCC_idensity < BCC_density(i) && k < 20000

        % Transformations and similar

        Rs = sqr2*Rsp + t/2;     % Radius of the side holes (just one wall)
        Rc = Rs;                 % Radius of the centre holes (the one at the
```

```
                        % centre of facesheets, where two walls intersect).
Rv = calcRv(t,Rsp,x0);

%%% Mathematical section - BCC VOLUME without cutouts.

BCC_volume_NH = 2*sqr2*t*(3*L^2 - 6*sqr2*L*t + 8*t^2);
BCC_density_NH = BCC_volume_NH/L^3;

%%% Mathematical section - CENTRAL HOLES  - There are generally six of these holes.

Vch = pi*Rc^2*t - (8/3)*(Rc^3 - sqrt((Rc^2 - t^2/4)^3));

%%% Mathematical section - SIDE HOLES  - There are generally twelve of these holes.

cir = @(y) sqrt(Rs^2 - y.^2);
xf = cir(t/2);

sigma = pi - 2*atan(t/(2*xf));

Vsh = 0.5*sigma*Rs^2*t + (4/3)*(Rs^3 - (Rs^2 + t^2/8)*(sqrt(Rs^2 - t^2/4)));


%%% Mathematical section - VERTEX HOLES  - There are generally sixteen of
%    these holes (eight vertex plus eight which created the big hole located at the
%    very centre of the unit cell).

% Mathematical section

cal_cil = @(x,y) sqrt(Rv^2 - x.^2 - 0*y);

y_min_1 = @(x) x;

V_cil = integral2(cal_cil,0,t/2,y_min_1,t/2);

Vv = 0.25*pi*Rv^2*t - 2*V_cil;               %% Volume of one single element

%%% Common parts

% Cube

V_cube = (t^3*sqr2/4);

% Square-base pyramids (Attention! Already considered two of them)

V_sq_pyramid = t^3*sqrt(2)/6;

% Trianglular-base pyramid 1 (big below)

V_tr1_pyramid = t^3*sqr3/9*cos(atan(1/sqr2));

% Trianglular-base pyramid 2 (smaller above)

V_tr2_pyramid = t^3*sqr2/18;

% Portion under the cylinders' intersection. This formula is quiete exact, but not 100%. ...
    (It is neglect the fact that the external cylinder surface is not the same for all ...
    cylinders.)
% Very small approximations lead to extremely low errors.

m1 = -sqr3;
m2 = -1/m1;

y_min = @(x) m2*x;
y_max = @(x) m1*x;

Cil1 = @(x,y) sqrt(Rv^2 - y.^2);

V_sf = 4*integral2(Cil1,-t/2,0,y_min,y_max);

V_sf = V_sf - t^3*sqr2;
```

```
        V_hole = V_cube + V_sq_pyramid + V_tr1_pyramid + V_tr2_pyramid + V_sf;

        %%% Volume of the exa.

        m_exa = sqrt(1/3);

        y_min_exa = @(x)  -m_exa*x;
        y_max_exa = @(x)   m_exa*x;

        V_exa = 6*integral2(Cil1,0,t/2,y_min_exa ,y_max_exa);

        V_exa_pyramid = t^3*sqr2/24;        % Already considered three

        h_exa = t*sqrt6/3;

        V_exa = V_exa - h_exa*sqr3*(t^2)/2 + 5*V_cube/6 + V_exa_pyramid;

        % Total volume of the hole

        Vvh = 3*Vv - 3*V_hole + V_exa;

        %%% Mathematical section - BCC VOLUME without cutouts.

        BCC_volume = BCC_volume_NH - 6*Vch - 12*Vsh - 16*Vvh;
        BCC_idensity = 100*BCC_volume/(L^3);

        t = t + 0.001;
        k = k+1;
    end

    if k == 20000
        error('The counter has reached its maximum value (20000 thickness increments) and has ...
            not converged!')
    end

    t_ex(i) = t - 0.001;
    BCC_density_ex(i) = BCC_idensity;
    Rv_ex(i) = Rv;
    err_ex(i) = abs(BCC_density_ex(i) - BCC_density(i))/(BCC_density(i));
end

t_de = t_ex - 0.001;

for i = 1:NC

    t = t_de(i);

    Rs = sqr2*Rsp + t/2;     % Radius of the side holes (just one wall)
    Rc = Rs;                 % Radius of the centre holes
                             % (the one at the centre of facesheets)
    Rv = calcRv(t,Rsp,x0);

    %%% Mathematical section - BCC VOLUME without cutouts.

    BCC_volume_NH = 2*sqr2*t*(3*L^2 - 6*sqr2*L*t + 8*t^2);
    BCC_density_NH = BCC_volume_NH/L^3;

    %%% Mathematical section - CENTRAL HOLES  - There are generally six of these holes.

    Vch = pi*Rc^2*t - (8/3)*(Rc^3 - sqrt((Rc^2 - t^2/4)^3));


    %%% Mathematical section - SIDE HOLES  - There are generally twelve of these holes.

    cir = @(y) sqrt(Rs^2 - y.^2);
    xf = cir(t/2);

    sigma = pi - 2*atan(t/(2*xf));
```

```
Vsh = 0.5*sigma*Rs^2*t + (4/3)*(Rs^3 - (Rs^2 + t^2/8)*(sqrt(Rs^2 - t^2/4)));


%%% Mathematical section - VERTEX HOLES  - There are generally sixteen of
%    these holes (eight vertex plus eight which created the big hole located at the
%    very centre of the unit cell).

% Mathematical section

cal_cil = @(x,y) sqrt(Rv^2 - x.^2 - 0*y);

y_min_1 = @(x) x;

V_cil = integral2(cal_cil,0,t/2,y_min_1,t/2);

Vv = 0.25*pi*Rv^2*t - 2*V_cil;               %% Volume of one single element

%%% Common parts

% Cube

V_cube = (t^3*sqr2/4);

% Square-base pyramids (Attention! Already considered two of them)

V_sq_pyramid = t^3*sqrt(2)/6;

% Trianglular-base pyramid 1 (big below)

V_tr1_pyramid = t^3*sqr3/9*cos(atan(1/sqr2));

% Trianglular-base pyramid 2 (smaller above)

V_tr2_pyramid = t^3*sqr2/18;

% Portion under the cylinders' intersection. This formula is quiete exact, but not 100%. (It ...
   is neglect the fact that the external cylinder surface is not the same for all cylinders.)
% Very small approximations lead to extremely low errors.

m1 = -sqr3;
m2 = -1/m1;

y_min = @(x) m2*x;
y_max = @(x) m1*x;

Cil1 = @(x,y) sqrt(Rv^2 - y.^2);

V_sf = 4*integral2(Cil1,-t/2,0,y_min,y_max);

V_sf = V_sf - t^3*sqr2;

V_hole = V_cube + V_sq_pyramid + V_tr1_pyramid + V_tr2_pyramid + V_sf;

%%% Volume of the exa.

m_exa = sqrt(1/3);

y_min_exa = @(x)  -m_exa*x;
y_max_exa = @(x)   m_exa*x;

V_exa = 6*integral2(Cil1,0,t/2,y_min_exa ,y_max_exa);

V_exa_pyramid = t^3*sqr2/24;        % Already considered three

h_exa = t*sqrt6/3;

V_exa = V_exa - h_exa*sqr3*(t^2)/2 + 5*V_cube/6 + V_exa_pyramid;

% Total volume of the hole
```

```
    Vvh = 3*Vv - 3*V_hole + V_exa;

    %%% Mathematical section - BCC VOLUME without cutouts.

    BCC_volume = BCC_volume_NH - 6*Vch - 12*Vsh - 16*Vvh;
    BCC_density_de(i) = 100*BCC_volume/(L^3);
    Rv_de(i) = Rv;
    err_de(i) = abs(BCC_density_de(i) - BCC_density(i))/(BCC_density(i));
end

t = zeros(NC,1);
Rv = zeros(NC,1);

for i = 1:NC
    if err_de(i) < err_ex(i)
        Rv(i) = Rv_de(i);
        t(i) = t_de(i);
    else
        Rv(i) = Rv_ex(i);
        t(i) = t_ex(i);
    end
end

end
```

The function *calc_Rv* implements the iterative part of the script of App.B, simply inside a *function* environment.

```
function Rv = calcRv(t,Rsp,x0)

fun = @(x) (x.^2)*(sin(0.25*pi - atan(0.5) - atan(0.5*t./x))).^2 + ...
    (0.25*t^2)*(sin(0.25*pi - atan(0.5) - atan(0.5*t./x))).^2 - Rsp^2;

[Rv] = fsolve(fun,x0);

end
```

The function *FCC_tRv*, is the real worker that does the required calculations in case of FCC architecture. Its mechanism is described at Par.3.4. This function has three different versions: *FCC_tRv* - for 6.50 and 10% relative density, *FCC_tRv_high* for 15% and *FCC_tRv_superhigh* for 20%. The first and the second versions differ just for a line (it is properly highlighted so not to report a almost identical code), because the cut outs shape does not change, simply each cell has 3 and not 4 holes, which respectively corresponds to 72 and not 96 fundamental cuts. The third one is different, not in the approach but in the formula implemented, as the cut outs design is completely different.

```
function  t = FCC_tRv(ID,FD,NC,t0,Rsp,Sz)

% Geometrical data

t_ex = zeros(NC,1);

err_ex = zeros(NC,1);
err_de = zeros(NC,1);
step = (FD-ID)/NC;

k = 0;
t = t0;
L = Sz;

FCC_idensity = 0;
FCC_density = (ID+step:step:FD)';
FCC_density_ex = zeros(NC,1);
```

```
FCC_density_de = zeros(NC,1);

alfa = acos(1/3);
beta = pi/3;

sqr3 = sqrt(3);

for i = 1:NC

    while FCC_idensity < FCC_density(i) && k < 20000

        %%% Mathematical transformations

        Indent_cut = t/(2*sin(alfa/2));

        %%% Mathematical section - FCC VOLUME without cutouts.

        FCC_volume_NH = 2*sqr3*t*(2*L^2 - 3*sqr3*L*t + 5*t^2);
        FCC_density_NH = 100*FCC_volume_NH/L^3;

        %%% Mathematical section - Holes

        l1 = t/(2*cos(alfa/2));           % Length of the side created by chamfering (half of it)
        l2 = t/(2*sin(alfa/2));           % Length of the sloped cause by the loft (=Indent_cut)
        Rv = 3*Rs + t/tan(alfa/ 2);       % Radius of the cut
        Sn1 = t*tan(alfa/2);
        Sn2 = t/tan(alfa/2);

        Xv = 0;                           % Coordinates of the vertex
        Yv = 0;

        Vi = sqrt(Xv^2 + Yv^2);           % Distance origin - vertex

        %%% Volumes calculation

        % Volume 1

        dy1 = Sn1/2;
        dx1 = sqrt(Rv^2 - (Yv + dy1)^2);
        R12 = dx1 - (sqr3/2)*Sn1 - Xv;

        Atg1 = 0.5*Sn1*R12;                    % It is not divided by two (hence it is 2*Atg1)
                                               % This is more efficient for the next steps
        h1 = Atg1/Rv;
        gamma1 = asin(h1/Sn1);

        V1 = ((gamma1)*(Rv^2) - Atg1)*t/4;

        % Volume 2  (similar to a slice of circumference, but it is not, the smaller one)

        dy2 = Sn2/2;
        dx2 = sqrt(Rv^2 - (Yv + dy2)^2);
        R22 = dx2 - (sqr3/2)*Sn2 - Xv;

        Atg2 = 0.5*Sn2*R22;                    % It is not divided by two (hence it is 2*Atg2).
                                               % It is more efficient for the next steps
        h2 = Atg2/Rv;
        gamma2 = asin(h2/Sn2);

        V2 = ((gamma2)*(Rv^2) - Atg2)*t/4;

        % Volume 3 - Three steps - Side with the bigger triangle (Sn2)

        %%% Step a

        V3_a = (sqr3/24)*Sn1*dy1*t;

        %%% Step b

        V3_b = dy1*R12*t/4;
```

```
        %%% Step c

        Xff = sqrt(Rc^2 - Yv^2);
        y_max = @(x) sqrt(Rc^2 - x.^2);
        Δ1 = pi/2 - alfa/2;
        z1 = @(x,y) (y-Yv)*tan(Δ1) +0*x;

        V3_c = integral2(z1,dx1,Xff,Yv,y_max);

        % Volume 4 - Three steps - Side with the smaller triangle (Sn)

        %%% Step a

        V4_a = (sqr3/24)*Sn2*dy2*t;

        %%% Step b

        V4_b = dy2*R22*t/4;

        %%% Step c

        Δ2 = alfa/2;
        z2 = @(x,y) (y-Yv)*tan(Δ2) +0*x;

        V4_c = integral2(z2,dx2,Xff,Yv,y_max);

        %%% Total Volume

        V3 = V3_a + V3_b + V3_c;
        V4 = V4_a + V4_b + V4_c;

        V_tot = 2*(V1+V2+V3+V4);

        %%% Mathematical section - FCC VOLUME with cutouts.

        %  k = k+1;
        FCC_volume = FCC_volume_NH - 96*V_tot;
        % FCC_volume = FCC_volume_NH - 72*V_tot;        % Use this for 15\% specimens
        FCC_idensity = 100*FCC_volume/(L^3);

        t = t + 0.001;
        k = k+1;
    end

    if k == 20000
        error('The counter has reached its maximum value (20000 thickness increments) and has ...
            not converged!')
    end

    t_ex(i) = t-0.001;
    FCC_density_ex(i) = FCC_idensity;
    err_ex(i) = abs(FCC_density_ex(i) - FCC_density(i))/(FCC_density(i));
end

t_de = t_ex - 0.001;

for i = 1:NC

    t = t_de(i);

        %%% Mathematical transformations

        Indent_cut = t/(2*sin(alfa/2));

        %%% Mathematical section - FCC VOLUME without cutouts.

        FCC_volume_NH = 2*sqr3*t*(2*L^2 - 3*sqr3*L*t + 5*t^2);
        FCC_density_NH = 100*FCC_volume_NH/L^3;
```

```
%%% Mathematical section - Holes

l1 = t/(2*cos(alfa/2));           % Length of the side created by chamfering (half of it)
l2 = t/(2*sin(alfa/2));           % Length of the sloped cause by the loft (=Indent_cut)
Rv = 3*Rs + t/tan(alfa/ 2);       % Radius of the cut
Sn1 = t*tan(alfa/2);
Sn2 = t/tan(alfa/2);

Xv = 0;                           % Coordinates of the vertex
Yv = 0;

Vi = sqrt(Xv^2 + Yv^2);           % Distance origin - vertex

%%% Volumes calculation

% Volume 1

dy1 = Sn1/2;
dx1 = sqrt(Rv^2 - (Yv + dy1)^2);
R12 = dx1 - (sqr3/2)*Sn1 - Xv;

Atg1 = 0.5*Sn1*R12;                    % It is not divided by two (hence it is 2*Atg1)
                                       % This is more efficient for the next steps
h1 = Atg1/Rv;
gamma1 = asin(h1/Sn1);

V1 = ((gamma1)*(Rv^2) - Atg1)*t/4;

% Volume 2  (similar to a slice of circumference, but it is not, the smaller one)

dy2 = Sn2/2;
dx2 = sqrt(Rv^2 - (Yv + dy2)^2);
R22 = dx2 - (sqr3/2)*Sn2 - Xv;

Atg2 = 0.5*Sn2*R22;                    % It is not divided by two (hence it is 2*Atg2).
                                       % It is more efficient for the next steps
h2 = Atg2/Rv;
gamma2 = asin(h2/Sn2);

V2 = ((gamma2)*(Rv^2) - Atg2)*t/4;

% Volume 3 - Three steps - Side with the bigger triangle (Sn2)

%%% Step a

V3_a = (sqr3/24)*Sn1*dy1*t;

%%% Step b

V3_b = dy1*R12*t/4;

%%% Step c

Xff = sqrt(Rc^2 - Yv^2);
y_max = @(x) sqrt(Rc^2 - x.^2);
Δ1 = pi/2 - alfa/2;
z1 = @(x,y) (y-Yv)*tan(Δ1) +0*x;              % Pay attention to the different angles!

V3_c = integral2(z1,dx1,Xff,Yv,y_max);

% Volume 4 - Three steps - Side with the smaller triangle (Sn)

%%% Step a

V4_a = (sqr3/24)*Sn2*dy2*t;

%%% Step b

V4_b = dy2*R22*t/4;
```

```
        %%% Step c

        Δ2 = alfa/2;
        z2 = @(x,y) (y-Yv)*tan(Δ2) +0*x;

        V4_c = integral2(z2,dx2,Xff,Yv,y_max);

        %%% Total Volume

        V3 = V3_a + V3_b + V3_c;
        V4 = V4_a + V4_b + V4_c;

        V_tot = 2*(V1+V2+V3+V4);

        %%% Mathematical section - FCC VOLUME with cutouts.

        FCC_volume = FCC_volume_NH - 96*V_tot;
        % FCC_volume = FCC_volume_NH - 72*V_tot;        % Use this for 15\% specimens
        FCC_density_de(i) = 100*FCC_volume/(L^3);
        err_de(i) = abs(FCC_density_de(i) - FCC_density(i))/(FCC_density(i));
end

for i = 1:NC
    if err_de(i) < err_ex(i)
        t(i) = t_de(i);
    else
        t(i) = t_ex(i);
    end
end

end
```

```
function  t = FCC_tRv_superhigh(ID,FD,NC,t0,Rsp,Sz)

% Geometrical data

t_ex = zeros(NC,1);

err_ex = zeros(NC,1);
err_de = zeros(NC,1);
step = (FD-ID)/NC;

k = 0;
t = t0;
L = Sz;

FCC_idensity = 0;
FCC_density = (ID+step:step:FD)';
FCC_density_ex = zeros(NC,1);
FCC_density_de = zeros(NC,1);

alfa = acos(1/3);
beta = pi/3;

sqr3 = sqrt(3);

for i = 1:NC

    while FCC_idensity < FCC_density(i) && k < 20000

        %%% Mathematical section - FCC VOLUME without cutouts.

        FCC_volume_NH = 2*sqr3*t*(2*L^2 - 3*sqr3*L*t + 5*t^2);
        FCC_density_NH = 100*FCC_volume_NH/L^3;

        %%% Mathematical section - FCC VOLUME with cutouts.
```

```
        V_hole = pi*(Rsp^2)*t;

        FCC_volume = FCC_volume_NH - 32*V_hole;
        FCC_idensity = 100*FCC_volume/(L^3);

        t = t + 0.001;
        k = k+1;
    end

    if k == 20000
        error('The counter has reached its maximum value (20000 thickness increments) and has ...
            not converged!')
    end

    t_ex(i) = t-0.001;
    FCC_density_ex(i) = FCC_idensity;
    err_ex(i) = abs(FCC_density_ex(i) - FCC_density(i))/(FCC_density(i));
end

t_de = t_ex - 0.001;

for i = 1:NC

    t = t_de(i);

        %%% Mathematical section - FCC VOLUME without cutouts.

        FCC_volume_NH = 2*sqr3*t*(2*L^2 - 3*sqr3*L*t + 5*t^2);
        FCC_density_NH = 100*FCC_volume_NH/L^3;

        %%% Mathematical section - FCC VOLUME with cutouts.

        V_hole = pi*(Rsp^2)*t;

        FCC_volume = FCC_volume_NH - 32*V_hole;
        FCC_density_de(i) = 100*FCC_volume/(L^3);
        err_de(i) = abs(FCC_density_de(i) - FCC_density(i))/(FCC_density(i));
end

for i = 1:NC
    if err_de(i) < err_ex(i)
        t(i) = t_de(i);
    else
        t(i) = t_ex(i);
    end
end

end
```

Appendix D

Results: supplementary graphs and figures.

The single stress and strain curves, which constitute part of the outcome of the tensile test simulations described at Ch.4, are reported here for completeness.

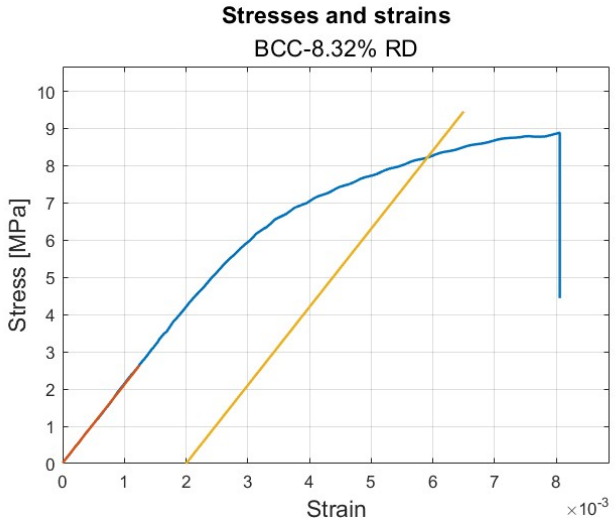

(a) Specimen with 8.32% rel. density.

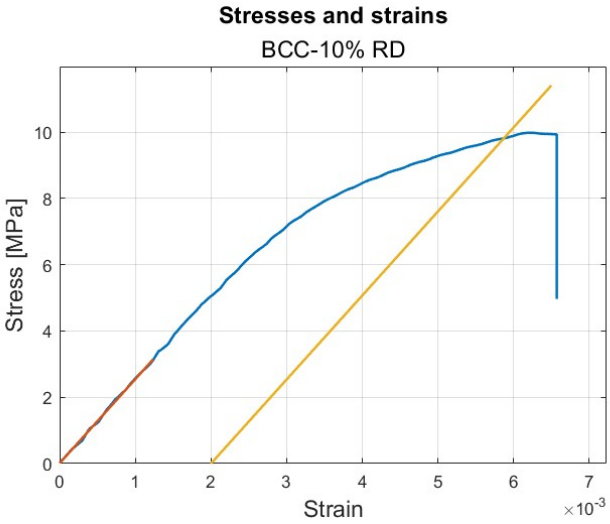

(b) Specimen with 10% rel. density.

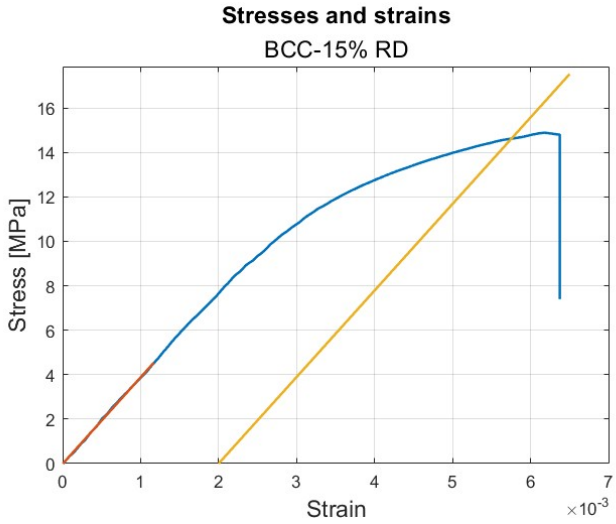

(c) Specimen with 15% rel. density.

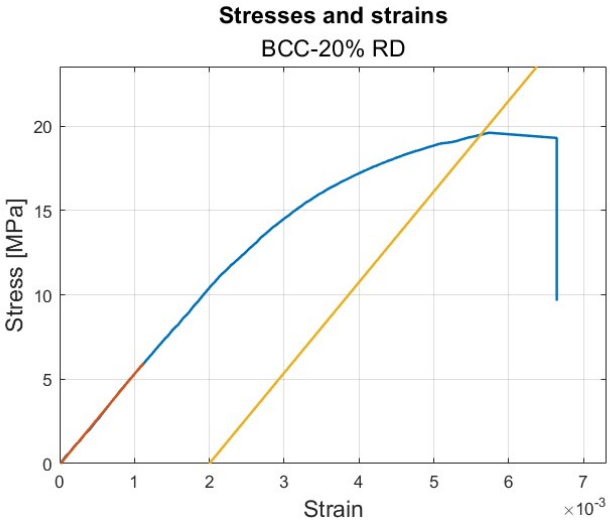

(d) Specimen with 20% rel. density.

Figure D.1: BCC unit cell: stress and strain curves.

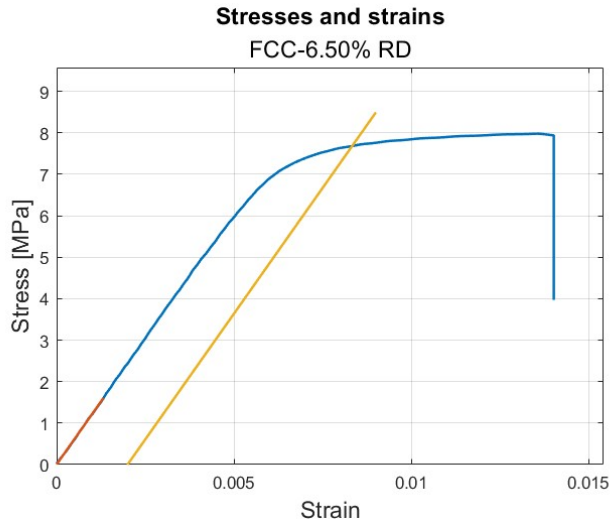

(a) Specimen with 6.50% rel. density.

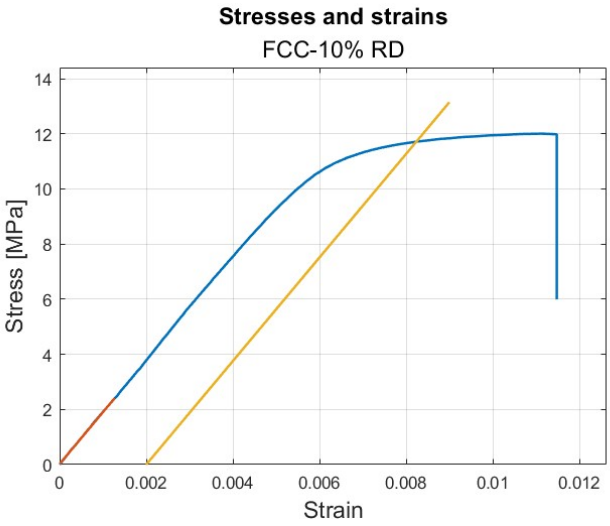

(b) Specimen with 10% rel. density.

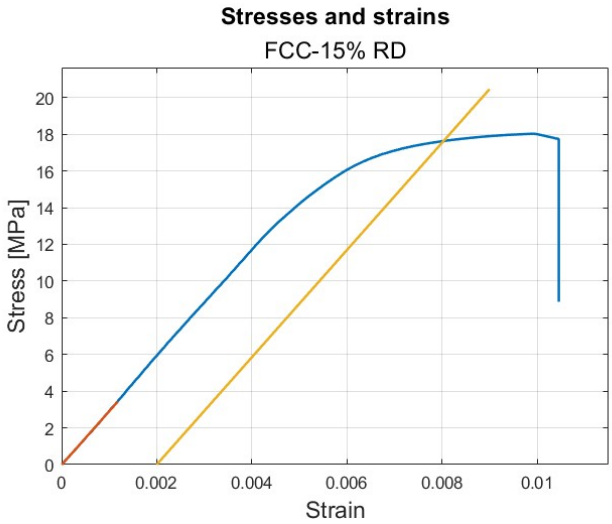

(c) Specimen with 15% rel. density.

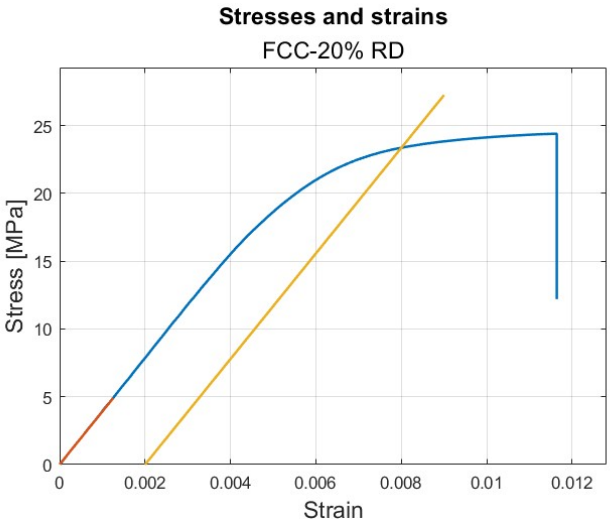

(d) Specimen with 20% rel. density.

Figure D.2: FCC unit cell: stress and strain curves.

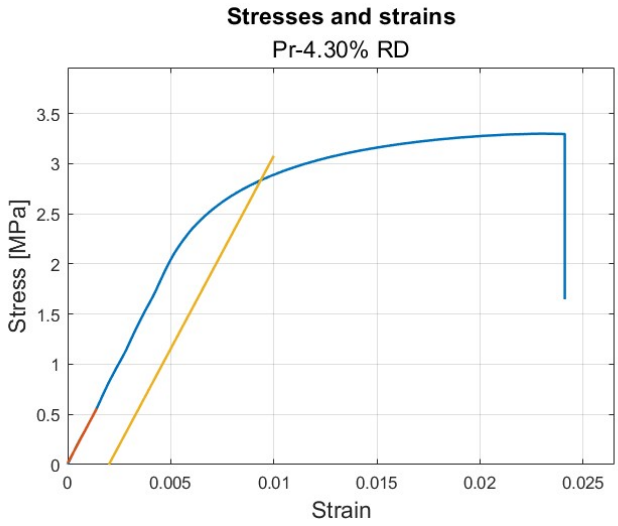

(a) Specimen with 4.30% rel. density.

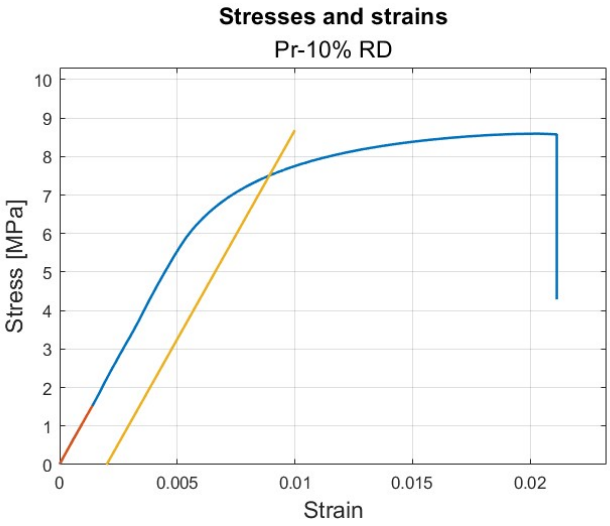

(b) Specimen with 10% rel. density.

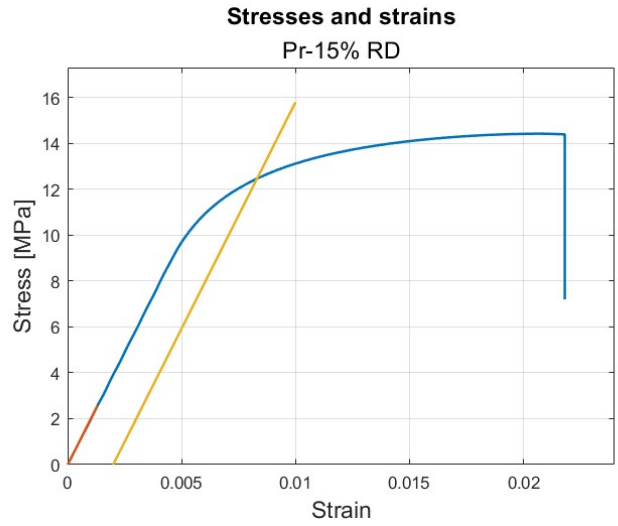

(c) Specimen with 15% rel. density.

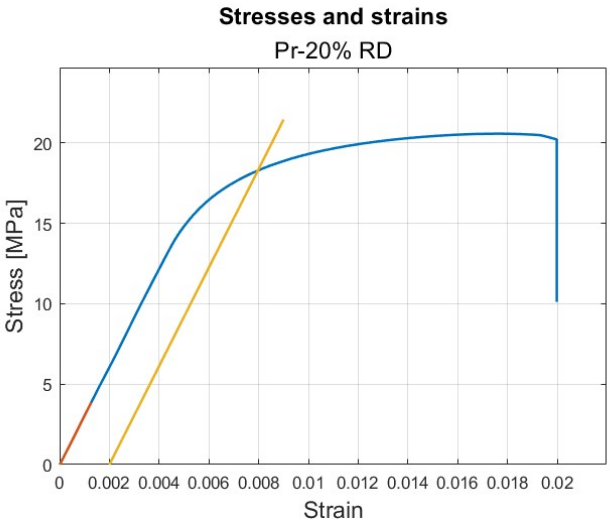

(d) Specimen with 20% rel. density.

Figure D.3: Primitive unit cell: stress and strain curves.

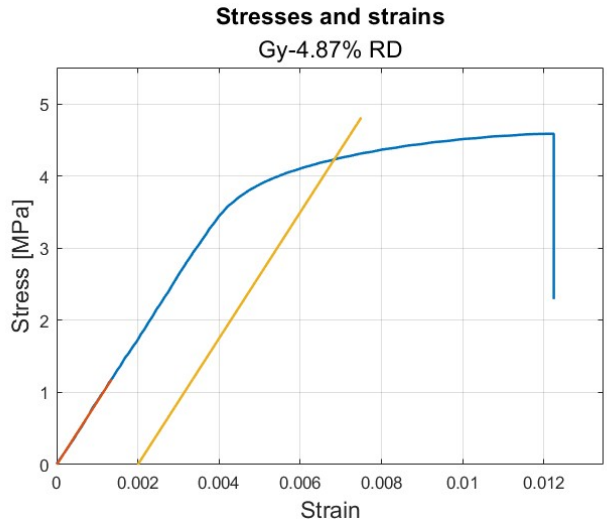

(a) Specimen with 4.87% rel. density.

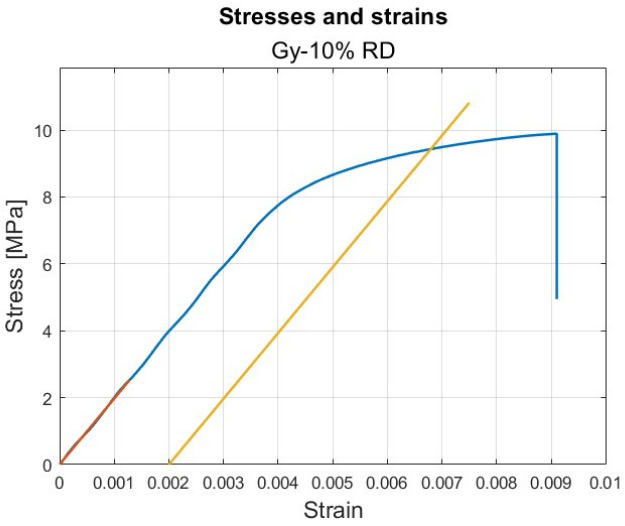

(b) Specimen with 10% rel. density.

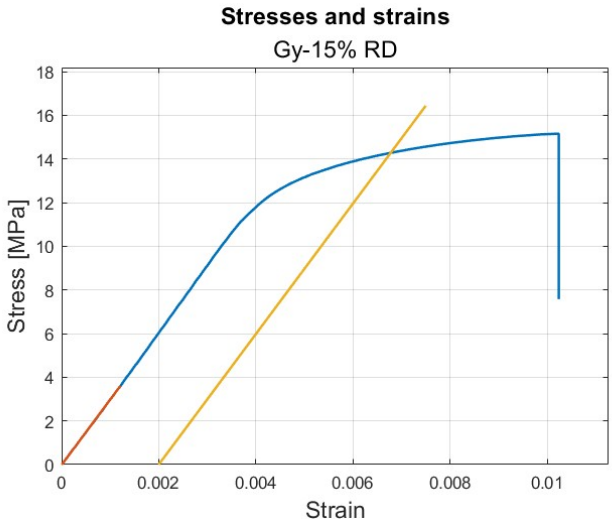

(c) Specimen with 15% rel. density.

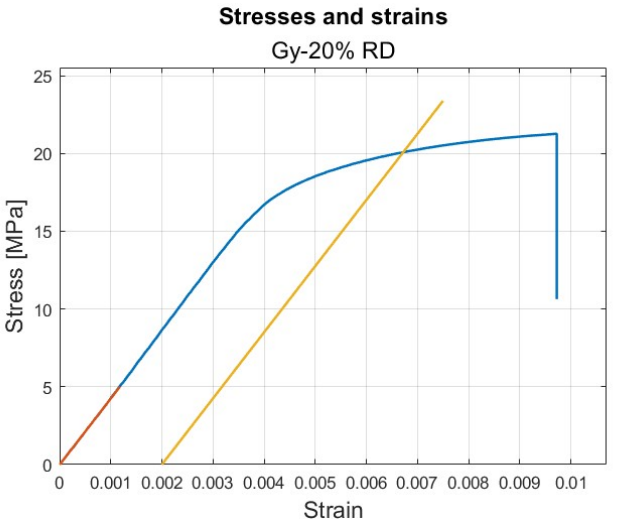

(d) Specimen with 20% rel. density.

Figure D.4: Gyroid unit cell: stress and strain curves.

The images showing the failure location within each single specimen, are reported here. As previously mentioned, these have been excluded from the main text at Ch.4 to enhance readability and maintain the flow of the narrative.

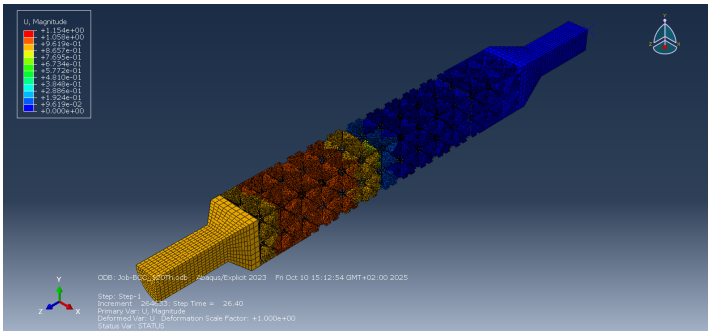

(a) Specimen with 8.32% rel. density.

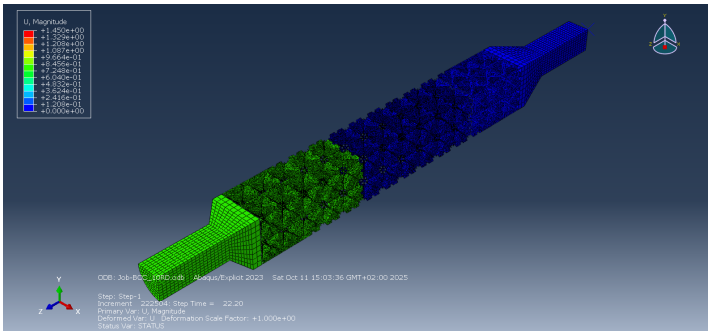

(b) Specimen with 10% rel. density.

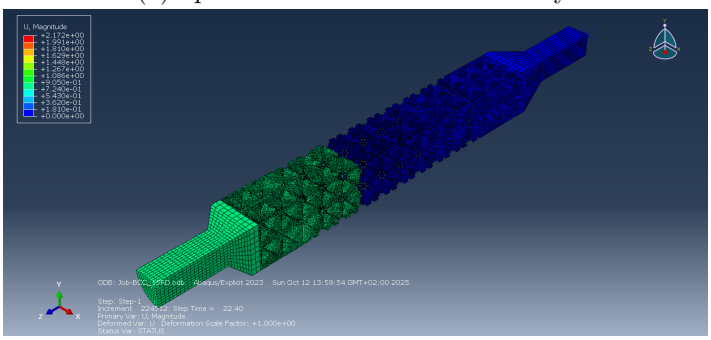

(c) Specimen with 15% rel. density.

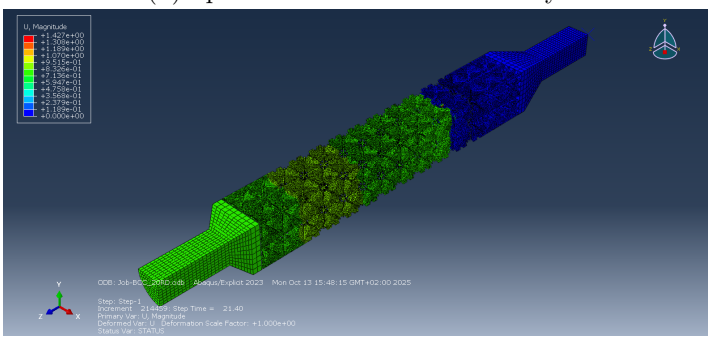

(d) Specimen with 20% rel. density.

Figure D.5: BCC unit cell: failure location in the specimen.

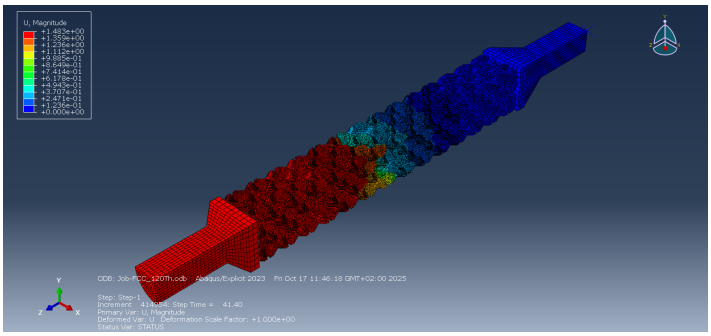

(a) Specimen with 6.50% rel. density.

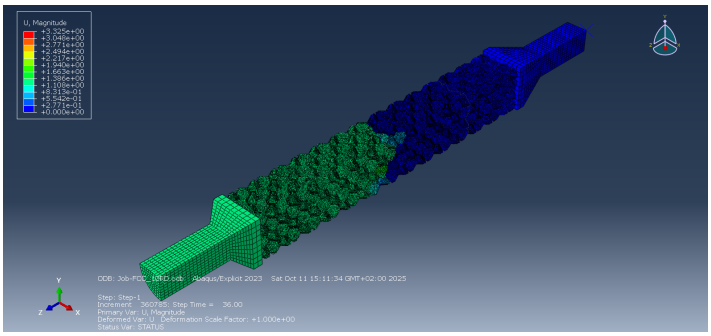

(b) Specimen with 10% rel. density.

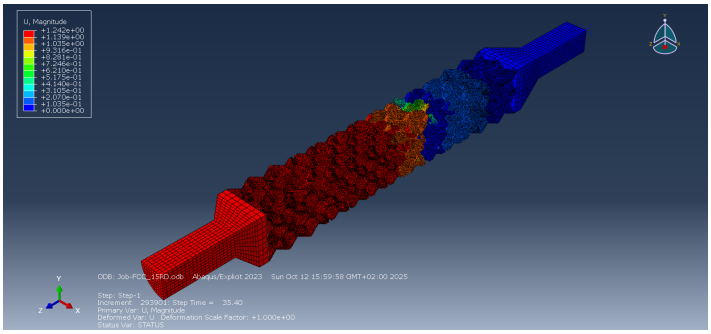

(c) Specimen with 15% rel. density.

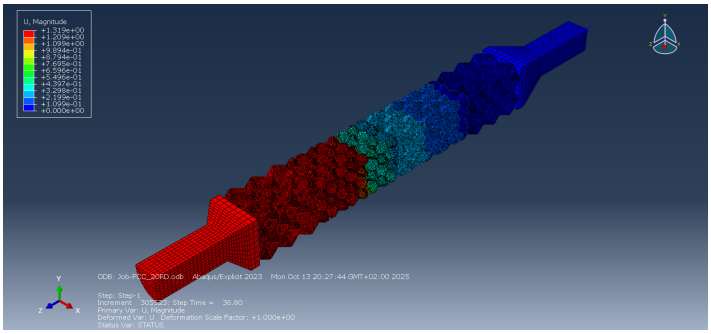

(d) Specimen with 20% rel. density.

Figure D.6: FCC unit cell: failure location in the specimen.

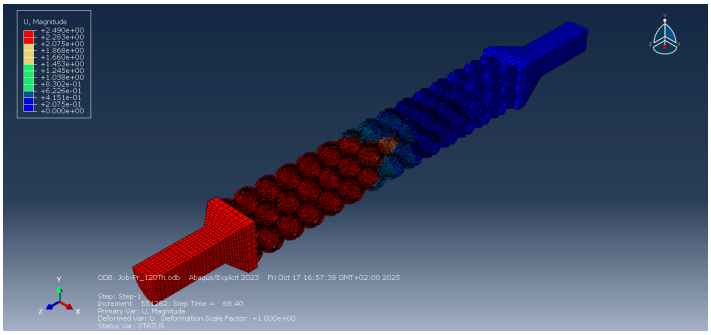

(a) Specimen with 4.30% rel. density.

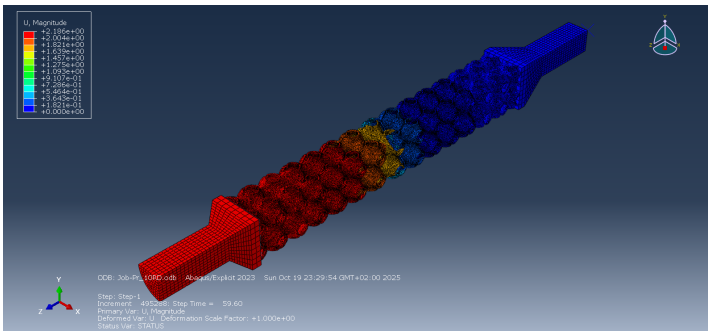

(b) Specimen with 10% rel. density.

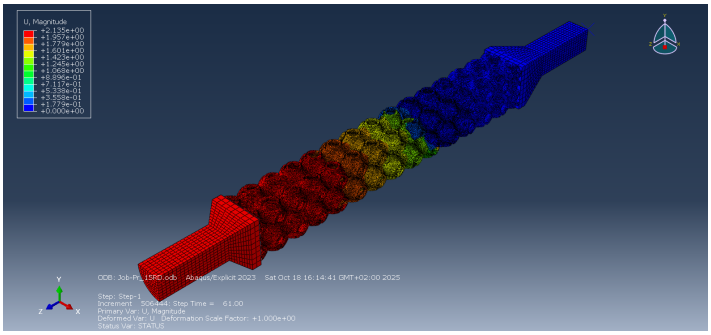

(c) Specimen with 15% rel. density.

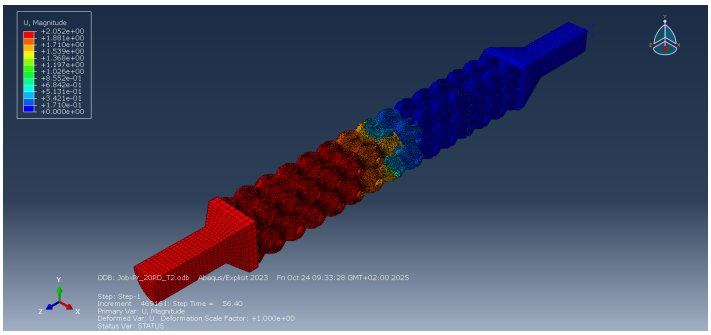

(d) Specimen with 20% rel. density.

Figure D.7: Primitive unit cell: failure location in the specimen.

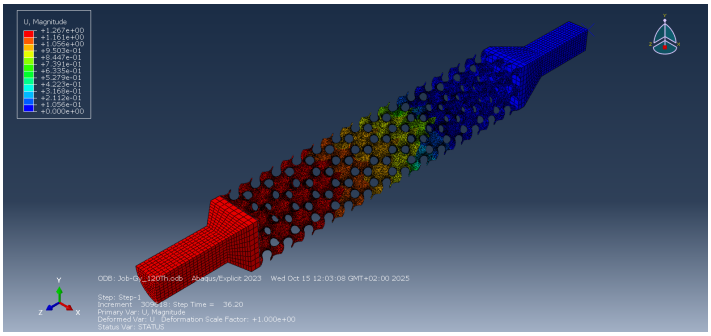

(a) Specimen with 4.87% rel. density.

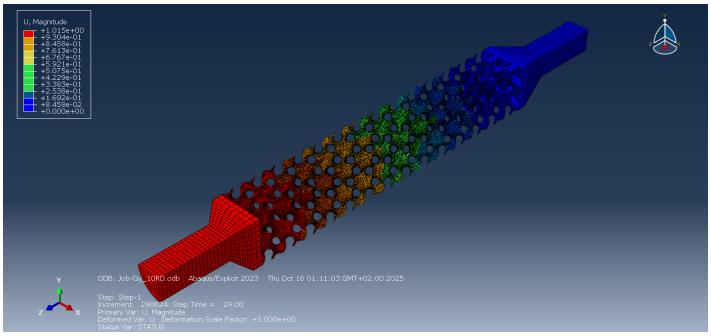

(b) Specimen with 10% rel. density.

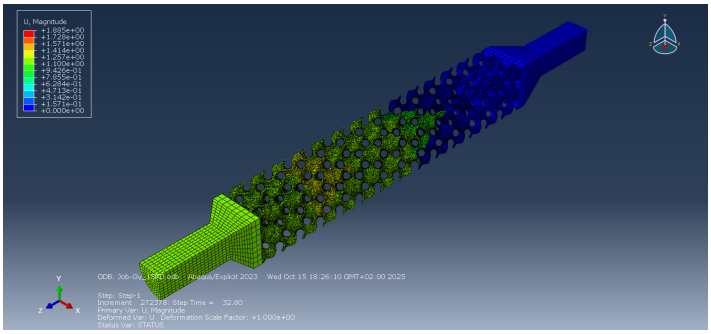

(c) Specimen with 15% rel. density.

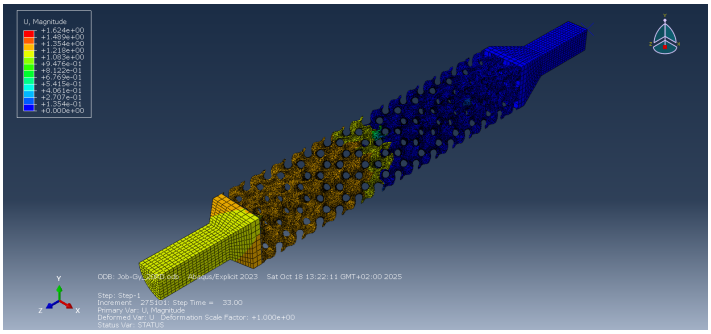

(d) Specimen with 20% rel. density.

Figure D.8: Gyroid unit cell: failure location in the specimen.

Appendix E

Wöhler and Haigh curves, code implemented in MATLAB.

The Wöhler curves are built through the following MATLAB code.

```
%%% Wohler Curve_Average_75%

clear
close all
clc

data = readmatrix("Fatigue_data_Matlab_75.txt"); % The first column contains the force to get
                                                 % 50% UTS, the second column to get 90% UTS.
data = 2.5*data;                                 % The factor 2.5 transforms kN into MPa
data(:,[1 2]) = data(:, [2 1]);                  % Exchange the columns (plottig is easier)

BCC = data(1:4,[1 2]);                           % The first column contains the force to get
                                                 % 90% UTS, the second column to get 50% UTS.
FCC = data(5:8,[1 2]);                           % Rows 1 to 4 for BCC, 5 to 8 for FCC, and so on
Pr = data(9:12,[1 2]);                           % Rows 1,5,9,13 for minimum relative density,
                                                 % 2,6,10,14 for 10% RD and so on.
Gy = data(13:end,[1 2]);

N = [1e3 2*1e6 1e8];

figure (1)

for i = 1:4
    semilogx(N,[BCC(i,:) BCC(i,2)],'LineWidth',1.5)
    grid on
    hold on
end
xlim([1e3 1e8])
ylim([0 1.1*BCC(4,1)]);
legend('8.32% RD', '10% RD', '15% RD', '20% RD','Fontsize',12)
xlabel('Number of cycles','Fontsize',13)
ylabel('Stress Amplitude [MPa]','Fontsize',13)
title("BCC Unit Cell - Wohler Curves",'Density Effect','FontSize',14)

figure (2)

for i = 1:4
    semilogx(N,[FCC(i,:) FCC(i,2)],'LineWidth',1.5)
    grid on
    hold on
end
xlim([1e3 1e8])
ylim([0 1.1*FCC(4,1)]);
legend('6.50% RD', '10% RD', '15% RD', '20% RD','Fontsize',12)
xlabel('Number of cycles','Fontsize',13)
ylabel('Stress Amplitude [MPa]','Fontsize',13)
title("FCC Unit Cell - Wohler Curves",'Density Effect','Fontsize',14)
```

```
figure (3)

for i = 1:4
    semilogx(N,[Pr(i,:) Pr(i,2)],'LineWidth',1.5)
    grid on
    hold on
end
xlim([1e3 1e8])
ylim([0 1.1*Pr(4,1)]);
legend('4.30% RD', '10% RD', '15% RD', '20% RD','Fontsize',12)
xlabel('Number of cycles','Fontsize',13)
ylabel('Stress Amplitude [MPa]','Fontsize',13)
title("Primitive Unit Cell - Wohler Curves",'Density Effect','FontSize',14)

figure (4)

for i = 1:4
    semilogx(N,[Gy(i,:) Gy(i,2)],'LineWidth',1.5)
    grid on
    hold on
end
xlim([1e3 1e8])
ylim([0 1.1*Gy(4,1)]);
legend('4.87% RD', '10% RD', '15% RD', '20% RD','Fontsize',12)
xlabel('Number of cycles','Fontsize',13)
ylabel('Stress Amplitude [MPa]','Fontsize',13)
title("Gyroid Unit Cell - Wohler Curves",'Density Effect','FontSize',14)
```

The Haigh curves are built through the following MATLAB code.

```
%%% Haigh Fatigue Curve

clear
close all
clc

data = readmatrix('Fatigue_data_Matlab_75.txt');     % Data has 16 rows: BCC,FCC,Pr,Gy,
                                                     %four for each unit cell
                                                     % Every 4 rows have the following scheme:
                                                     % minimum/10/15/20 relative density

data = 2.5*data;                                     % The factor 2.5 transforms kN into MPa
data(:, [1 2]) = data(:, [2 1]);                     % Exchange the columns (plottig is easier)

RF = data(:,3);
BCC = data(1:4,[1 2]);
FCC = data(5:8,[1 2]);
Pr = data(9:12,[1 2]);
Gy = data(13:end,[1 2]);

% Determination of Basquin coefficients for every geometry and density
% ATTENTION log = ln; log10 = log;

f = @(A,b,N) A.*(N.^b);

b = zeros(size(data,1),1);
A = zeros(size(data,1),1);
Z = [1e4 1e5 1e6];
sigma_N = zeros(size(data,1),length(Z));

% BCC

for i = 1:4
    b(i) = (log10(data(i,2)/(data(i,1))))/(3+log10(2));
    A(i) = data(i,1)/10^(3*b(i));
```

```
    for k = 1:length(Z)
        sigma_N(i,k) = f(A(i),b(i),Z(k));
    end
end

% FCC

for i = 5:8
    b(i) = log10(data(i,2)/(data(i,1)))/(3+log10(2));
    A(i) = data(i,1)/10^(3*b(i));
    for k = 1:length(Z)
        sigma_N(i,k) = f(A(i),b(i),Z(k));
    end
end

% Primitive

for i = 9:12
    b(i) = log10(data(i,2)/(data(i,1)))/(3+log10(2));
    A(i) = data(i,1)/10^(3*b(i));
    for k = 1:length(Z)
        sigma_N(i,k) = f(A(i),b(i),Z(k));
    end
end

% Gyroid

for i = 13:16
    b(i) = log10(data(i,2)/(data(i,1)))/(3+log10(2));
    A(i) = data(i,1)/10^(3*b(i));
    for k = 1:length(Z)
        sigma_N(i,k) = f(A(i),b(i),Z(k));
    end
end

%%% Haigh Curves

sigma_M = [zeros(size(data,1),1) RF];
sigma_N = [data(:,1) sigma_N data(:,2)];
N = [1e3 Z 2*1e6];

% BCC Unit cell

figure(1)
for i = 1:length(N)
    plot(sigma_M(1,:), [sigma_N(1,i) 0],'LineWidth',1.5)
    grid on
    hold on
end
xlabel('Mean Stress [MPa]','FontSize',13)
ylabel('Alternate Stress [MPa]','FontSize',13)
legend('N = 1e3','N = 1e4','N = 1e5','N =5:8 1e6','N = 2*1e6' ,'Fontsize',12)
title('Haigh Curve with Goodman Law', 'BCC Unit cell - 8.32% RD','FontSize',14)

figure(2)
for i = 1:length(N)
    plot(sigma_M(2,:), [sigma_N(2,i) 0],'LineWidth',1.5)
    grid on
    hold on
end
xlabel('Mean Stress [MPa]','FontSize',13)
ylabel('Alternate Stress [MPa]','FontSize',13)
legend('N = 1e3','N = 1e4','N = 1e5','N = 1e6','N = 2*1e6' ,'Fontsize',12)
title('Haigh Curve with Goodman Law', 'BCC Unit cell - 10% RD','FontSize',14)

figure(3)
for i = 1:length(N)
    plot(sigma_M(3,:), [sigma_N(3,i) 0],'LineWidth',1.5)
    grid on
    hold on
```

```
end
xlabel('Mean Stress [MPa]','FontSize',13)
ylabel('Alternate Stress [MPa]','FontSize',13)
legend('N = 1e3','N = 1e4','N = 1e5','N = 1e6','N = 2*1e6' ,'Fontsize',12)
title('Haigh Curve with Goodman Law', 'BCC Unit cell - 15% RD','FontSize',14)

figure(4)
for i = 1:length(N)
    plot(sigma_M(4,:), [sigma_N(4,i) 0],'LineWidth',1.5)
    grid on
    hold on
end
xlabel('Mean Stress [MPa]','FontSize',13)
ylabel('Alternate Stress [MPa]','FontSize',13)
legend('N = 1e3','N = 1e4','N = 1e5','N = 1e6','N = 2*1e6' ,'Fontsize',12)
title('Haigh Curve with Goodman Law', 'BCC Unit cell - 20% RD','FontSize',14)

% FCC Unit cell

figure(5)
for i = 1:length(N)
    plot(sigma_M(5,:), [sigma_N(5,i) 0],'LineWidth',1.5)
    grid on
    hold on
end
xlabel('Mean Stress [MPa]','FontSize',13)
ylabel('Alternate Stress [MPa]','FontSize',13)
legend('N = 1e3','N = 1e4','N = 1e5','N = 1e6','N = 2*1e6' ,'Fontsize',12)
title('Haigh Curve with Goodman Law', 'FCC Unit cell - 6.50% RD','FontSize',14)

figure(6)
for i = 1:length(N)
    plot(sigma_M(6,:), [sigma_N(6,i) 0],'LineWidth',1.5)
    grid on
    hold on
end
xlabel('Mean Stress [MPa]','FontSize',13)
ylabel('Alternate Stress [MPa]','FontSize',13)
legend('N = 1e3','N = 1e4','N = 1e5','N = 1e6','N = 2*1e6' ,'Fontsize',12)
title('Haigh Curve with Goodman Law', 'FCC Unit cell - 10% RD','FontSize',14)

figure(7)
for i = 1:length(N)
    plot(sigma_M(7,:), [sigma_N(7,i) 0],'LineWidth',1.5)
    grid on
    hold on
end
xlabel('Mean Stress [MPa]','FontSize',13)
ylabel('Alternate Stress [MPa]','FontSize',13)
legend('N = 1e3','N = 1e4','N = 1e5','N = 1e6','N = 2*1e6' ,'Fontsize',12)
title('Haigh Curve with Goodman Law', 'FCC Unit cell - 15% RD','FontSize',14)

figure(8)
for i = 1:length(N)
    plot(sigma_M(8,:), [sigma_N(8,i) 0],'LineWidth',1.5)
    grid on
    hold on
end
xlabel('Mean Stress [MPa]','FontSize',13)
ylabel('Alternate Stress [MPa]','FontSize',13)
legend('N = 1e3','N = 1e4','N = 1e5','N = 1e6','N = 2*1e6' ,'Fontsize',12)
title('Haigh Curve with Goodman Law', 'FCC Unit cell - 20% RD','FontSize',14)

% Primitive Unit cell

figure(9)
for i = 1:length(N)
    plot(sigma_M(9,:), [sigma_N(9,i) 0],'LineWidth',1.5)
    grid on
    hold on
```

```
end
xlabel('Mean Stress [MPa]','FontSize',13)
ylabel('Alternate Stress [MPa]','FontSize',13)
legend('N = 1e3','N = 1e4','N = 1e5','N = 1e6','N = 2*1e6' ,'Fontsize',12)
title('Haigh Curve with Goodman Law', 'Pr Unit cell - 4.30% RD','FontSize',14)

figure(10)
for i = 1:length(N)
    plot(sigma_M(10,:), [sigma_N(10,i) 0],'LineWidth',1.5)
    grid on
    hold on
end
xlabel('Mean Stress [MPa]','FontSize',13)
ylabel('Alternate Stress [MPa]','FontSize',13)
legend('N = 1e3','N = 1e4','N = 1e5','N = 1e6','N = 2*1e6' ,'Fontsize',12)
title('Haigh Curve with Goodman Law', 'Pr Unit cell - 10% RD','FontSize',14)

figure(11)
for i = 1:length(N)
    plot(sigma_M(11,:), [sigma_N(11,i) 0],'LineWidth',1.5)
    grid on
    hold on
end
xlabel('Mean Stress [MPa]','FontSize',13)
ylabel('Alternate Stress [MPa]','FontSize',13)
legend('N = 1e3','N = 1e4','N = 1e5','N = 1e6','N = 2*1e6' ,'Fontsize',12)
title('Haigh Curve with Goodman Law', 'Pr Unit cell - 15% RD','FontSize',14)

figure(12)
for i = 1:length(N)
    plot(sigma_M(12,:), [sigma_N(12,i) 0],'LineWidth',1.5)
    grid on
    hold on
end
xlabel('Mean Stress [MPa]','FontSize',13)
ylabel('Alternate Stress [MPa]','FontSize',13)
legend('N = 1e3','N = 1e4','N = 1e5','N = 1e6','N = 2*1e6' ,'Fontsize',12)
title('Haigh Curve with Goodman Law', 'Pr Unit cell - 20% RD','FontSize',14)

% Gyroid Unit cell

figure(13)
for i = 1:length(N)
    plot(sigma_M(13,:), [sigma_N(13,i) 0],'LineWidth',1.5)
    grid on
    hold on
end
xlabel('Mean Stress [MPa]','FontSize',13)
ylabel('Alternate Stress [MPa]','FontSize',13)
legend('N = 1e3','N = 1e4','N = 1e5','N = 1e6','N = 2*1e6' ,'Fontsize',12)
title('Haigh Curve with Goodman Law', 'Gy Unit cell - 4.87% RD','FontSize',14)

figure(14)
for i = 1:length(N)
    plot(sigma_M(14,:), [sigma_N(14,i) 0],'LineWidth',1.5)
    grid on
    hold on
end
xlabel('Mean Stress [MPa]','FontSize',13)
ylabel('Alternate Stress [MPa]','FontSize',13)
legend('N = 1e3','N = 1e4','N = 1e5','N = 1e6','N = 2*1e6' ,'Fontsize',12)
title('Haigh Curve with Goodman Law', 'Gy Unit cell - 10% RD','FontSize',14)

figure(15)
for i = 1:length(N)
    plot(sigma_M(15,:), [sigma_N(15,i) 0],'LineWidth',1.5)
    grid on
    hold on
end
xlabel('Mean Stress [MPa]','FontSize',13)
```

```
ylabel('Alternate Stress [MPa]','FontSize',13)
legend('N = 1e3','N = 1e4','N = 1e5','N = 1e6','N = 2*1e6' ,'Fontsize',12)
title('Haigh Curve with Goodman Law', 'Gy Unit cell - 15% RD','FontSize',14)

figure(16)
for i = 1:length(N)
    plot(sigma_M(16,:), [sigma_N(16,i) 0],'LineWidth',1.5)
    grid on
    hold on
end
xlabel('Mean Stress [MPa]','FontSize',13)
ylabel('Alternate Stress [MPa]','FontSize',13)
legend('N = 1e3','N = 1e4','N = 1e5','N = 1e6','N = 2*1e6' ,'Fontsize',12)
title('Haigh Curve with Goodman Law', 'Gy Unit cell - 20% RD','FontSize',14)
```